

**SoLID (Solenoidal Large Intensity Device)
Preliminary Conceptual Design Report**

The SoLID Collaboration

July 8, 2014

Contents

1	Introduction and Overview of SoLID Experimental Programs	1
1.1	SoLID Project Introduction/Overview	1
1.1.1	Base Equipment Description	1
1.1.2	Dependencies to Base Equipment	1
1.1.3	Experiment-specific Dependencies	2
1.1.4	Research Program	2
1.2	SIDIS Program with SoLID	3
1.2.1	Introduction	3
1.2.2	Transverse Structure and Semi-Inclusive Deep Inelastic Scattering	4
1.2.3	The Phenomenology TSSAs and TMDs	7
1.2.4	Overview of SIDIS program with SoLID	8
1.2.5	Beam Time and Projections	9
1.3	PVDIS Program with SoLID	15
1.3.1	Motivation for PVDIS	15
1.3.2	Review of the Theory	16
1.3.3	Charge Symmetry Violation	17
1.3.4	Higher Twist	18
1.3.5	Data Sample and analysis	18
1.3.6	Beam Time Request	19
1.4	J/Ψ Program	20
1.4.1	Motivation	20
1.4.2	Program Overview	22
1.4.3	Beam Time and Projection	23
2	Technical Requirements and Experimental Setup	36
2.1	Summary of Requirements	36
2.2	SoLID- ^3He -SIDIS Experiments	41
2.3	SoLID-proton-SIDIS Experiment	45
2.4	SoLID-PVDIS Experiment	47
2.5	SoLID- J/ψ Experiment	49
3	Simulation	54
3.1	Framework	54
3.2	Generators	55
3.3	GEM Digitization	55
3.4	Future Plans	56
3.5	Background and Radiation damage estimates	57
3.5.1	Radiation damage to GEM electronics	57
3.5.2	Power deposited	57
3.5.3	Estimates for radiation damage in the Hall	58
4	Magnet	73
4.1	Requirements	73
4.2	SoLID magnet	73
4.3	Planned modifications	74

5	Targets	77
5.1	Polarized ^3He Target	77
5.2	Transversely Polarized Proton Target for SoLID	77
5.3	Cryogenic Target for PVDIS (SOLID)	80
6	Baffles	84
7	GEM Tracker	87
7.1	GEM tracker R&D	91
7.1.1	GEM chamber R&D program in UVa	91
7.1.2	GEM chamber R&D programs in China	94
8	Light Gas Čerenkov	99
8.1	Design	99
8.1.1	Tank and Čerenkov Gas	99
8.1.2	Mirrors	100
8.1.3	PMTs	100
8.1.4	Magnetic Shielding and Winston Cones	101
8.2	Tank Support	101
8.3	Simulations	103
8.3.1	Collection Efficiencies	103
8.3.2	Background Rates	103
8.3.3	Pion Rejection	103
9	Heavy Gas Čerenkov	108
9.1	Optical System Design	108
9.2	Simulation	108
9.2.1	Photon Electron Yield	108
9.2.2	Pion Detection Efficiency and Kaon Rejection Factor	109
9.3	Performance of the PMTs in Magnetic Field	110
9.4	Support Conceptual Design	111
10	Electromagnetic Calorimeter	113
10.1	Overview	113
10.2	Shower Detector Design Considerations	116
10.2.1	Total Length of the Calorimeter	116
10.2.2	Sampling Ratio of the Shower Detector	116
10.2.3	Lateral Size of the Calorimeter Module	117
10.3	Preshower Detector	118
10.4	Layout and Support	120
10.5	Light Readout	120
10.6	Radiation Effect	122
10.7	Performance	124
10.7.1	Intrinsic electron-pion separation	125
10.7.2	PID performance under realistic background simulation	126
10.7.3	Trigger capability	129
10.7.4	EC trigger rate	131
10.7.5	Shower Position Measurement	133

10.8	Supplemental Information: PID Selection Cuts	134
10.9	Scintillator Pad Detector for SIDIS Experiments	136
11	MRPC	139
11.1	Structure of the MRPC prototype	139
11.2	Cosmic ray test	140
11.3	Beam test at Hall A	140
11.4	Beam test Results	142
11.4.1	HV Scan	142
11.4.2	Rate Scan	144
11.5	Conclusions	144
12	Data Acquisition	150
12.1	Introduction	150
12.2	Jefferson Laboratory Hall D Flash ADC	150
12.3	PVDIS	151
12.3.1	Single electron Calorimeter trigger for PVDIS	151
12.3.2	Gas Cerenkov trigger	153
12.4	SIDIS and J/Ψ	154
12.4.1	SIDIS	154
12.4.2	J/Ψ	155
12.4.3	Implementation SIDIS and J/Ψ	156
12.4.4	MRPC readout	157
12.5	GEM readout	157
12.5.1	Background and GEM event size	158
12.5.2	PVDIS GEM rates	158
12.5.3	SIDIS GEM rates	159
12.6	Event size from FADC	159
12.7	Data rates,event size and L3 Farm	160
12.8	Experiment switch over	160
12.9	Hall DAQ installation	160
12.10	Cabling and rack	161
12.11	Pre R&D and tests	161
13	Software and Tracking	165
13.1	Software Framework	165
13.2	Track Reconstruction	165
13.3	Simulation Results	167
13.3.1	GEM Occupancies	169
13.3.2	Track Reconstruction & Efficiency	169
14	Electron Beam Polarimetry	172
14.1	Compton Polarimetry	172
14.2	The Hall A Compton Polarimeter Baseline Upgrade	172
14.3	Upgrades Beyond the Baseline	174
14.3.1	Laser System and Luminosity	175
14.3.2	Alternative Laser System	177
14.3.3	Chicane Magnet Modification	179

14.3.4	Photon Detection	179
14.4	Systematic Uncertainties	180
14.4.1	Sources of Correlated Error	180
14.4.2	Systematic Errors for the Electron Detector	180
14.4.3	Systematic Errors for the Photon Detector	183
14.5	Summary of Compton Polarimetry	184
14.6	Møller Polarimetry	184
14.7	The Hall A Upgrade: “High Field” Iron Foil Targets	185
14.7.1	Ferromagnetic Foil Targets	186
14.7.2	Simplified Møller Scattering Target Assembly	188
15	Supports and Infrastructure	193
15.1	Magnet Support	193
15.2	Endcap Support Structure and Motion Mechanism	193
15.3	Support Structure for Equipment Located Inside Cryostat Bore	193
15.4	Power Requirements	193
16	Installation	195
16.1	Experimental Layout	195
16.2	Magnet Moving and Placement	195
16.3	Helium Dewar Support and Upper Access Platform	199
16.4	Endcap Forward Angle Detector Package Installation Structure	199
16.5	Large Angle Detector and Baffle Installation Mechanism	199
16.6	Light Gas Cherenkov Installation Structure	200
17	Integration, Calibration, and Systematics	201
17.1	Assembly and PID Integration	201
17.2	Kinematics, Resolution and Calibration for PVDIS with SoLID	201
17.2.1	Introduction	201
17.2.2	Approximate Method	201
17.3	Uniform field case	201
17.4	Realistic Case	203
17.4.1	Resolution	204
17.4.2	Calibration	204
18	Project Status and Proposed Management Organization	206
18.1	Collaboration and Organization	206
18.2	Cost estimation	208
	Appendices	209
	Appendix A Summary of Subsystems	209
A.1	Magnet	209
A.2	GEM	209
A.3	Light Gas Čerenkov	210
A.4	Heavy Gas Čerenkov	210
A.5	Electromagnetic Calorimeter and Scintillator-Pad Detector	210
A.6	MRPC	211
A.7	DAQ	211

Appendix B Rates and Background Simulation	213
B.1 DIS e^- and π^-/e^- ratio	213
B.2 GEM Background Rates	213
Appendix C Magnet Choice	217

1 Introduction and Overview of SoLID Experimental Programs

1.1 SoLID Project Introduction/Overview

1.1.1 Base Equipment Description

The SoLID (Solenoidal Large Intensity Device) project will develop a large acceptance spectrometer/detector system capable of handling very high rates. It is designed to satisfy the requirements of five approved high-scientific rated experiments, four A and one A-, as well as to become base equipment for a continued program of physics in the 12 GeV era at Jefferson Lab that requires both high luminosity and large acceptance. The base equipment composing the SoLID project includes two configurations: the “SIDIS” (Semi-Inclusive Deep Inelastic Scattering) configuration and the “PVDIS” (Parity-Violating Deep Inelastic Scattering) configuration. Although the geometrical layouts for the detectors are not the same in the two configurations, the following items are common:

1. A solenoidal magnet with a power supply and cryogenic system, now identified as the CLEO-II magnet. With some modifications as described in the magnet section, this magnet meets the experimental requirements. The transportation of the CREO-II magnet to JLab will be arranged separately (see next section on Dependencies to Base Equipment).
2. An electromagnetic calorimeter for electron identification. (In the SIDIS configuration, it is separated into two sectors, a forward sector and a large-angle sector).
3. A light gas Cherenkov detector for electron identification.
4. A heavy gas Cherenkov detector for pion (hadron) identification. This is for the SIDIS configuration only.
5. A set of baffles. This is for the PVDIS configuration only.
6. A data acquisition system (DAQ). Part of the DAQ electronics, mainly FADCs, will be from the JLab Physics Division Shared Electronics Pool (see next section on Dependencies to Base Equipment).
7. Supporting structures for the magnet and the detectors.
8. Requisite Hall A infrastructure to accommodate the functioning of the above cooling, cabling, and the like.

1.1.2 Dependencies to Base Equipment

The following items are requisite outside contributions to the SoLID base equipment:

1. GEM detectors for tracking: These are planned to be provided by a SoLID Chinese Collaboration. Five Chinese institutions (USTC, CIAE, Tsinghua, Lanzhou and IMP), in collaboration with UVa (Nilanga Liyanage group), have committed to perform R&D and are applying for full funding from the Chinese funding agencies to construct the full set of GEMs for the SoLID project.
2. A MRPC (Multi-Gap Resistive Plate Chamber) detector serving as a time-of-flight (TOF) detector for pion (hadron) identification: Two Chinese groups (Tsinghua and Huangshan University) have committed to perform R&D and apply for full funding to construct the required MRPC detector for the SoLID project. The Chinese groups, in collaboration with US institutions, will also apply for a separate funding for MRPC electronics.

3. DAQ electronics: JLab intends to have an electronics pool to share basic DAQ electronics among the four experimental halls. Some of these electronics, mainly FADCs, will be utilized by SoLID.
4. Magnet: JLab has formally requested the CLEO-II magnet and has received a positive response from Cornell University. JLab, in coordination with Cornell, plans to have this magnet be transported to JLab approximately around Summer 2016.
5. Beamline: The Hall A beam line with standard instrumentation is assumed to be in operational condition and is not included in the SoLID base equipment.

1.1.3 Experiment-specific Dependencies

The five approved experiments in the SoLID research program would require the SoLID base equipment, as well as the development of components outside the base equipment of the SoLID project. The following lists such additional equipment that is either standard and existing at JLab or that will be available for experiments planned before the SoLID experiments:

1. For SIDIS transverse ^3He and longitudinal ^3He : The existing polarized ^3He target with performance already achieved from the 6 GeV transversity (E06-010) experiment is required. However, modifications to the stand, supports, and service may be required to accommodate integration into SoLID.
2. For J/Ψ the standard cryogenic LH2 target system is assumed. This is standard Hall A equipment, however the SoLID SIDIS configuration will require re-arrangement of the detector system for the target and there may be significant modifications required for both to accommodate integration into SoLID.
3. For PVDIS: A Compton polarimeter and a super-conducting Moller polarimeter (both also required by MOLLER and to be employed for PREX also) are assumed to be available.

For completeness, though not as general dependencies for SoLID base equipment, the following experiment-specific items which will require additional resource/funding are listed:

1. For PVDIS: a custom, high-power cryotarget is required. ESR2 is assumed to be available (required by the Moller project).
2. For SIDIS transverse proton: a transversely polarized proton target will need development. An initial study has been performed by Oxford which concluded that such a target is feasible.

1.1.4 Research Program

The five currently-approved, high-impact experiments approved for the SoLID project are as follows:

1. SIDIS-transverse ^3He : Semi-inclusive deep-inelastic-scattering of electron beam on a transversely polarized ^3He target. It is focusing on charged pion production to study transverse spin (transversity) and other transverse momentum dependent parton distributions (TMDs). It will provide a 4-d (x, z, P_T, Q^2) mapping of the Collins, Sivers and pretzelocity asymmetries of the neutron in the valance quark region with high precision. Combined with the SIDIS measurement on the proton and the world e^+e^- data, the Collins asymmetries will allow for an extraction of one of the fundamental properties of the nucleon, the tensor charge of the

u and d quarks to better than 10%, providing a benchmark test of lattice QCD. The Siverson and Pretzelosity asymmetries will allow an extraction of the Siverson function and pretzelosity function, providing crucial information on the quark orbital motion.

2. SIDIS-longitudinal ^3He : Semi-inclusive deep-inelastic-scattering of electron beam on a longitudinally polarized ^3He target. It is focusing on charged pion production to study TMDs. Combined with transversely polarized ^3He target experiment, it will provide a precision 4-d (x, z, P_T, Q^2) mapping of the two worm-gear asymmetries of the neutron in the valence quark region, allowing an extraction of the two so-called worm-gear TMDs (g_{1T} , longi-transversity and h_{1L}^\perp , trans-helicity) with high precision, providing crucial information on the quark orbital motion and the spin-orbital correlations.
3. SIDIS-transverse proton: Same as in 1) but on the proton.
4. PVDIS on the deuteron and the proton: PVDIS on the deuteron will provide a precision test of the standard model. It provides the best measurement of the C_2 coupling and also provides a precision measurement of the $\sin^2 \theta_W$ at an intermediate value of Q^2 . The broad kinematical range enables the separation of the testing of the standard model and the study of fundamental hadron properties, including a precision measurement of possible charge symmetry violation at the partonic level and a unique measurement of the higher-twist effect (twist-4 term). The proton measurement provides a clean measurement of the d-quark over u-quark ratio in the high- x region without nuclear effects.
5. J/Ψ production near threshold: This fully exclusive measurement of the electroproduction of J/Ψ mesons from protons near threshold will be sensitive to the non-perturbative gluonic interaction between the J/ψ and nucleon, and might reveal an enhancement of the cross section just above the production threshold. This in turn could be a manifestation of the important role of the conformal anomaly. A further consequence is whether or not J/ψ -nuclear bound states would exist in nature. This experiment could open a new window to study QCD in the non-perturbative region using charmonium in a multi-phase program.

All proposals are available at

http://www.jlab.org/exp_prog/generated/12GeV/halla.html

1.2 SIDIS Program with SoLID

1.2.1 Introduction

Deep inelastic lepton-nucleon scattering (DIS) experiments have played a fundamental role in describing the partonic momentum structure of hadrons. The unpolarized parton distribution functions (PDF) have been extracted with excellent precision over a large range of x and Q^2 from DIS, Drell-Yan and other processes after several decades of experimental and theoretical efforts. The comparison of the structure functions in the large Q^2 range with QCD evolution equations has provided one of the best tests of QCD.

When the target and/or beam are polarized the essential properties of spin-angular momentum structure of hadrons is probed. Three decades of intensive experimental and theoretical investigation have resulted in a great deal of knowledge on the partonic origin of the nucleon spin structure. Motivated by the ‘‘spin crisis’’ from the European Muon Collaboration experiment in the 1980s [1], the longitudinal polarized parton distribution functions have been determined with significantly improved precision over a large region of x and Q^2 from polarized deep-inelastic (DIS) experiments

carried out at CERN, SLAC, DESY in the last two decades, and more recently at JLab and at RHIC from polarized proton-proton scattering (see [2, 3] for reviews and compilation of references). In particular, considerable knowledge has been gained from inclusive DIS experiments on the longitudinal structure – the x -dependence and the helicity distributions – in terms of the unpolarized (denoted $q^a(x)$ or $f_1^a(x)$) and helicity (denoted $\Delta q^a(x)$ or $g_1^a(x)$) parton distribution functions for the various flavors (indicated by a).

In more recent experimental and theoretical studies, it has become evident that precise knowledge of the transverse structure of partons is essential to unfold the full momentum and spin structure of the nucleon. This concerns in particular the investigations of the chiral-odd transversely polarized quark distribution function or transversity [4] (denoted as $\delta q(x)$, $h_1(x)$ or also $\Delta_T q(x)$) which is probed in transverse spin polarization experiments. Like the axial charge $\Delta q^a = \int_0^1 dx (g_1^a(x) + g_1^{\bar{a}}(x))$, the tensor charge $\delta q^a = \int_0^1 dx (h_1^a(x) - h_1^{\bar{a}}(x))$ is a basic property of the nucleon. The essential role of the transversity distribution function emerges from a systematic extension of the QCD parton model to include transverse momentum and spin degrees of freedom. In this context, semi-inclusive deep-inelastic lepton nucleon scattering (SIDIS) has emerged as an essential tool to probe both the longitudinal and transverse momentum and spin structure of the nucleon. The azimuthal dependence in the scattering of leptons off transversely polarized nucleons is explored through the analysis of transverse single spin asymmetries (TSSAs). Recent work [5, 6, 7] predicts that these observables are factorized convolutions of leading-twist transverse momentum dependent parton distributions (TMDs) and fragmentation functions (FFs) at low transverse momentum. These functions provide *essential non-perturbative* information on the partonic sub-structure of the nucleon; they offer a rich understanding of the motion of partons inside the nucleon, of the quark orbital properties, and of spin-orbit correlations. They also provide essential information on multi-parton correlations at leading-twist, allowing us to explore and uncover the dynamics of the quark-gluon structure of the nucleon.

At leading twist if we integrate over the transverse momenta of quarks, the three quark distribution functions remain: the unpolarized parton distribution f_1 , the longitudinal polarized parton distribution g_1 , and the quark transversity distribution h_1 . Besides f_1 , g_1 and h_1 , there are five more transverse momentum dependent distribution functions [5, 6]. Fig. 1 tabulates all these eight TMDs according to the polarizations of the quark (f, g, h) and nucleon (U, L, T). Since these TMDs provide the description of the parton distributions beyond the collinear approximation, they depend not only on the longitudinal momentum fraction x , but also on the transverse momentum, k_T . An intuitive interpretation of the k_T dependent transversity distribution, h_1 , is that it gives the probability of finding a transversely polarized parton inside a transversely polarized nucleon with certain longitudinal momentum fraction x and transverse momentum k_T . The JLab 12 GeV upgrade provides a unique opportunity to extend our understanding of nucleon spin and momentum structure by carrying out multi-dimensional precision studies of longitudinal and transverse spin and momentum degrees of freedom from SIDIS experiments with high luminosity in combination with large acceptance detectors. Such a program will provide the much needed kinematic reach to unfold the momentum and flavor structure of the nucleon. In the next section, we summarize the essential role that transverse polarization studies play in unfolding this structure in SIDIS.

1.2.2 Transverse Structure and Semi-Inclusive Deep Inelastic Scattering

The transverse spin and momentum structure of the nucleon was first discussed in 1970s [8, 9] followed by renewed interest in late 1980s [4, 10]. The transversity function is a chirally odd quark distribution function, and the least known among the three leading twist parton distribution functions. It describes the net quark transverse polarization in a transversely polarized nucleon [10]. In

the non-relativistic limit, the transversity distribution function $h_1(x, Q^2)$ is the same as the longitudinal quark polarization distribution function, $g_1(x, Q^2)$. Therefore, the transversity distribution function probes the relativistic nature of the quarks inside the nucleon.

Leading Twist TMDs  : Nucleon Spin  : Quark Spin

		Quark polarization		
		Un-Polarized (U)	Longitudinally Polarized (L)	Transversely Polarized (T)
Nucleon Polarization	U	$f_1 = \text{circle with red dot}$		$h_1^\perp = \text{circle with red dot and arrow up} - \text{circle with red dot and arrow down}$ Boer-Mulder
	L		$g_1 = \text{circle with red arrow right} - \text{circle with red arrow left}$ Helicity	$h_{1L}^\perp = \text{circle with red arrow right and arrow up} - \text{circle with red arrow left and arrow up}$
	T	$f_{1T}^\perp = \text{circle with red dot and arrow up} - \text{circle with red dot and arrow down}$ Sivers	$g_{1T}^\perp = \text{circle with red arrow right and arrow up} - \text{circle with red arrow left and arrow up}$	$h_{1T} = \text{circle with red dot and arrow up} - \text{circle with red dot and arrow down}$ Transversity $h_{1T}^\perp = \text{circle with red arrow right and arrow up} - \text{circle with red arrow left and arrow up}$

Figure 1: Leading twist TMDs classified according to the polarizations of the quark (f, g, h) and nucleon (U, L, T).

There are several interesting properties of the quark transversity distribution. First it does not mix with gluons; that is, it evolves as a non-singlet distribution [11] and doesn't mix with gluons under evolution and thus has valence-like behavior [12]. Secondly in the context of the parton model it satisfies the Soffer bound [13], which is an inequality among the three leading twist distributions, $|h_1^q| \leq \frac{1}{2}(f_1^q + g_1^q)$, based on unitarity and parity conservation. QCD evolution of transversity was studied in Ref. [14], where it was shown that Soffer's inequality holds up to next to leading order (NLO) QCD corrections. In the past [15] and more recently [16], studies have been performed that consider the violation of this bound. Therefore, it is interesting to experimentally test the Soffer's inequality as a function of Q^2 . Lastly, the lowest moment of h_1^q is the tensor charge, which has been calculated from lattice QCD [17] and various models [18, 19, 20, 21, 22, 23]. Due to the valence-like nature of the transversity distribution, measuring transversity in the high- x region (JLab kinematics) is crucial to determine tensor charge of quarks. The experimental determination of the transversity function is challenging - it is not accessible in polarized inclusive DIS measurements when neglecting quark masses - h_1 decouples at leading twist in an expansion of inverse powers of the hard scale in inclusive deep-inelastic scattering due to the helicity conserving property of the QCD interactions. However, paired with another hadron in the initial state *e.g.* double polarized Drell-Yan processes (two transversity distributions) [9], or in the final state, *e.g.* semi-inclusive deep-inelastic [24] scattering (transversity and Collins fragmentation function), leading twist h_1 can be accessed without suppression by a hard scale.

The most feasible way to access the transversity distribution function is via an azimuthal single spin asymmetry, in semi-inclusive deep-inelastic lepto-production of mesons on a transversely

polarized nucleon target, $eN^\uparrow \rightarrow e\pi X$. In this case the chiral-odd partner is the Collins fragmentation function, H_1^\perp [24], which has been extracted from charged pion pair production from e^+e^- annihilation [25]. Assuming factorization, schematically this transverse single spin asymmetry (TSSA) contains h_1 and H_1^\perp , $A_{UT} \sim h_1 \otimes H_1^\perp$ ($U \equiv$ unpolarized lepton beam, $T \equiv$ transversely polarized target) [6].

The first evidence of non-trivial transverse spin effects in SIDIS has been observed in the transverse single spin asymmetries measured by the HERMES [26, 27, 28], and the COMPASS [29, 30] experiments from a transversely polarized proton or deuteron target, where an unpolarized lepton beam is scattered off $lp^\uparrow \rightarrow l'hX$. Besides the non-zero Collins asymmetry, which contains h_1 and H_1^\perp discussed previously, another non-zero asymmetry (Sivers asymmetry), was also observed. The Sivers asymmetry is associated with a naive T-odd transverse momentum dependent (TMD) parton distribution function [31]. More recently, results on Collins and Sivers asymmetries on neutron were reported for the first time using a polarized ^3He target at Jefferson Lab [32]. In contrast to inclusive deep-inelastic lepton-nucleon scattering where transverse momentum is integrated out, these processes are sensitive to the transverse-momentum scale, P_T , which is on the order of the intrinsic quark momentum, k_T ; that is $P_T \sim k_T$. This is evident by considering the generic structure of the TSSA for a transversely polarized nucleon target which is characterized by interference between helicity flip and helicity non-flip amplitudes $A_{UT} \sim \text{Im}(f^{*+}f^-)$. In the collinear limit of QCD, partonic processes conserve helicity and Born amplitudes are real [33]. For this structure to be non-zero at leading twist we must go beyond the collinear limit where such a reaction mechanism requires a recoil scale sensitive to the intrinsic quark transverse momentum. This is roughly set by the confinement scale $k_T \sim \Lambda_{\text{QCD}}$ [34]. Because strongly interacting processes conserve parity transverse spin asymmetries are described by T-odd correlations between transverse spin \mathcal{S}_T , longitudinal momentum \mathbf{P} and intrinsic quark momentum \mathbf{k}_T [31, 24], which are depicted by the generic vector product $i\mathcal{S}_T \cdot (\mathbf{P} \times \mathbf{k}_\perp)$. These correlations imply a leading twist reaction mechanism which is associated with a naive T-odd transverse momentum dependent (TMD) parton distribution [31] and fragmentation [24] function (PDF & FF).

A crucial theoretical breakthrough [35, 36, 37] was that the reaction mechanism is due to non-trivial phases arising from the color gauge invariant property of QCD. This leads to the picture that TSSAs arise from initial and final state interactions [38, 39, 40] (ISI/FSI) of the active quark with the soft distribution or fragmentation remnant in SIDIS, which manifests itself as a gauge link that links the bilocal quark configuration. This gauge link gives rise to the final state gluonic interactions between the active quark and target remnant. Thus, T-odd TMDs are of crucial importance because they possess transverse spin polarization structure as well as the necessary phases to account for TSSAs at leading twist. Further work on factorization theorems for SIDIS indicate that there are two leading twist T-odd TMDs; the Sivers function, denoted as f_{1T}^\perp describing the probability density of finding unpolarized partons inside a transversely polarized proton, is one of these functions. All these aforementioned ingredients (TMD, FF, gauge link) enter the factorized [7] hadronic tensor for semi-inclusive deep-inelastic scattering.

Exploring the transverse spin structure of the TMD PDFs reveals evidence of a rich spin-orbit structure of the nucleon. When the transverse spin and momentum correlations are associated with the nucleon, where the quark remains *unpolarized*, the Sivers function [31] describes the helicity flip of the nucleon target in a helicity basis. Since the quark is unpolarized in the Sivers function, the orbital angular momentum of the quarks must come into play to conserve overall angular momentum in the process [41, 42]. Indeed a partonic description of the Sivers and Boer-Mulders functions requires wave function components with nonzero orbital angular momentum and thus provides information about the correlation between the quark orbital angular momentum (OAM) and the nucleon/quark spin, respectively [38, 43].

Unlike the Siverson function, which provides a clean probe of the QCD FSI, the functions g_{1T} and h_{1L}^\perp are (naive) T-even, and thus do not require FSI to be nonzero. Nevertheless, they also require interference between wave function components that differ by one unit of OAM and thus require OAM to be nonzero. Recently, a first ever determination of g_{1T} was reported [44] using a polarized ^3He target at Jefferson Lab, in which a positive azimuthal asymmetry for π^- production on ^3He and the neutron was observed, while the π^+ asymmetries are consistent with zero. Finally, the pretzelosity h_{1T}^\perp requires interference between wave function components that differ by two units of OAM (e.g. p-p or s-d interference). Combining the wealth of information from all these functions could be invaluable for disentangling the spin orbit correlations in the nucleon wave function, thus providing important information about the quark orbital angular momentum.

Complementary to Generalized Parton distributions (or Impact Parameter Dependent distributions), which describe the probability of finding a parton with certain longitudinal momentum fraction and at certain transverse position b (1-D momentum space and 2-D coordinate space), TMDs give a description of the nucleon structure in 3-D momentum space. Furthermore, by including the transverse momentum of the quark, the TMDs reveal important information about the nucleon/parton spin-orbital angular momentum correlations.

1.2.3 The Phenomenology TSSAs and TMDs

All eight leading twist TMDs can be accessed in SIDIS. The transversity, Siverson, and pretzelosity TMDs can be accessed through a transversely polarized target. There are three mechanisms which can lead to the single (transversely polarized target) spin azimuthal asymmetries, which are the Collins asymmetry, the Siverson asymmetry, and the pretzelosity asymmetry. As mentioned previously, the quark transversity function in combination with the chiral-odd Collins fragmentation function [24] gives rise to an azimuthal (Collins) asymmetry in $\sin(\phi_h + \phi_S)$, where azimuthal angles of both the hadron (pion) (ϕ_h) and the target spin (ϕ_S) are with respect to the virtual photon axis and relative to the lepton scattering plane. The Siverson asymmetry [45, 31, 46] refers to the azimuthal asymmetry in $\sin(\phi_h - \phi_S)$ due to the correlation between the transverse target polarization of the nucleon and the transverse momentum of the quarks, which involves the orbital angular momentum of the unpolarized quarks [38, 41]. The pretzelosity asymmetry is similar to Collins asymmetry except it is due to quarks polarized perpendicularly to the nucleon spin direction in the transverse plane in a transversely polarized nucleon. It has an azimuthal angular dependence of $\sin(3\phi_h - \phi_S)$. One can disentangle these angular distributions by taking the azimuthal moments of the asymmetries as has been done by the HERMES Collaboration [28], the COMPASS Collaboration [30], and most recently by the Jefferson Lab E06-010 collaboration [32]. With a longitudinally polarized lepton beam, and a transversely polarized target, the double spin asymmetry from SIDIS has an azimuthal angular dependence of $\cos(\phi_h - \phi_S)$ that allows for the determination of the g_{1T} TMD as was done in [44]. With a longitudinally polarized target, the single target spin asymmetry with an azimuthal angular dependence of $\sin(2\phi_h)$ is sensitive to h_{1L}^\perp , while the double spin asymmetry allows for the determination of the helicity TMD, g_1 .

In recent years a great deal of understanding of transverse spin effects, final state interactions, and the spin orbit structure of partonic-hadronic interactions has been gained from model calculations of the TMDs and fragmentation functions. In particular the final state interactions in TSSAs through the Siverson function has been studied in spectator models and the light-cone wave function approach [38, 39, 40, 47, 48, 49, 50, 51] as well as the bag model [52] and the NJL jet model [56]. The Collins function has been calculated in [53, 54, 55] while studies of the universality of T-odd fragmentation functions have been carried out in [57, 58, 59]. The Boer-Mulders function has been calculated in [60, 40, 61, 49, 51] and the spin orbit effects of the pretzelosity function have been

studied in both light-cone constituent quarks models [62, 63, 64, 65], while model predictions of azimuthal and transverse spin asymmetries have been predicted in [66, 49, 67].

The first model dependent extractions of the transversity distribution have been carried out [68] by combining SIDIS [28, 27, 69, 70] data with e^+e^- data [25] on the Collins function. Within the uncertainties, the Soffer bound is respected. In addition, the extraction of the Sivers function [71, 72, 73, 74, 75] has been performed by combining SIDIS data from the HERMES [28] on the proton and COMPASS data [30] on the deuteron. Complementing the data from the HERMES [28, 27], COMPASS [70], and BELLE [25] experiments, the recent results from the Jefferson Lab Hall A experiment E06-010 [32] on the neutron (with polarized ^3He) will facilitate a flavor decomposition of the transversity distribution function, h_1 [10, 76] and the Sivers distribution function f_{1T}^\perp [31] in the overlapping kinematic regime. However a model-independent determination of these leading twist functions requires data in a wider kinematic range with high precision in *four dimensions* of $(Q^2, x, z, \mathbf{P}_T)$.

1.2.4 Overview of SIDIS program with SoLID

The 12-GeV energy upgrade at CEBAF together with the newly proposed SoLID opens a great new window to perform precision studies of the transverse spin and transverse-momentum-dependent structure in the valence quark region for both the proton and the neutron. The experimental program on TMDs is one of the main thrusts of the 12-GeV physics program at Jefferson Lab.

Currently, there are three A rated SoLID experiments (E12-10-006 [77], E12-11-007 [78], and E12-11-108 [79]) on TMD physics with two involving a transversely (longitudinally) polarized ^3He (neutron) target, and one employing a transversely polarized NH_3 (proton) target. To extract TMDs with precisions from single and double spin asymmetry measurements, the detection system should have the capability to handle large luminosities, a full azimuthal angular coverage, good kinematic coverage in terms of Q^2, x, z, \mathbf{P}_T for SIDIS, and good particle identification for electrons and charged pions. Further, the influence due to the residual magnetic field of the spectrometer magnet needs to be negligible for polarized targets. SoLID is such a device that has been proposed and designed for these newly approved SIDIS experiments.

These new SIDIS experiments employ a superconducting solenoid magnet, a detector system consisting of forward-angle detectors and large-angle detectors, and a high-pressure polarized ^3He target or a polarized NH_3 target positioned upstream of the magnet. The polarized ^3He target is based on the technique of spin-exchange optical pumping of hybrid Rb-K alkali atoms. Such a target was used successfully in the recently completed SSA experiment [32, 44] with a 6-GeV electron beam at JLab and an in-beam polarization of 55-60% was achieved. For the polarized proton experiment E12-11-108, an upgraded version of the JLab/UVa/SLAC polarized NH_3 target will be used. The main upgrade will involve using a new magnet to replace the aging Helmholtz-coil magnet and to have fast spin-flip capability with the Adiabatic Fast Passage (AFP) technique. Preliminary design study has been carried out for such a magnet with a vertical opening angle of $\pm 25^\circ$ to satisfy the requirement of the experiment. The target is based on the principle of dynamic nuclear polarization (DNP) by using microwave pumping to reach high proton polarizations [80, 81]. The CLEO-II magnet with new end caps and modification of the yolks has been identified as the magnet of the choice for SoLID based on both the requirements of the experiments and the availability of the magnet. Six layers of GEM detectors will be placed inside the coils as tracking detectors. A combination of an electromagnetic calorimeter, gas Čerenkov counters, a layer of Multi-gap Resistive Plate Chamber (MRPC) and a thin layer of scintillator will be used for particle identification in the forward-angle region. As only electrons will be identified in the large-angle region, a shashlyk-type [82, 83] electromagnetic calorimeter will be sufficient to provide the pion

rejection. More details about SoLID experimental setup, kinematic coverage, particle identification, and other important considerations for SIDIS can be found in Section 2.2 and 2.3.

1.2.5 Beam Time and Projections

E12-10-006 Experiment E12-10-006 was approved 90 days of total beam time with $15 \mu\text{A}$, 11/8.8 GeV electron beams on a 40-cm long, 10 amgs transversely polarized ^3He target. 69 days is for beam on the polarized ^3He target, and 10 days for a dedicated study of the $x - z$ factorization with Hydrogen and Deuterium gas using a reference target cell. Additional 3.0 days is requested with a longitudinal target polarization to study the systematics of potential A_{UL} contamination, where U stands for an unpolarized beam and L for a longitudinally polarized target. A total overhead time of 8 days is requested. This overhead time will be shared among activities such as unpolarized target runs, target spin flip and target polarization measurements, as has been done in the past during other Hall A polarized ^3He target experiments. Although beam polarization is not required for the proposed SSA measurements, polarized beam with polarization of 85% or higher will be used for for parasitic measurements of A_{LT} , which can be used to access, g_{1T} as demonstrated in [44].

Projected data from E12-10-006 are binned into 4-dimensional (x, P_h, z, Q^2) bins. For a typical z and Q^2 bin ($0.40 < z < 0.45$, $2 \text{ GeV}^2 < Q^2 < 3 \text{ GeV}^2$), data projections for Sivers asymmetry measurements, left panel for π^+ and right panel for π^- , are shown in Fig. 2 as examples. Also shown are results from the 6-GeV experiment E06-010 [32], and predictions of Sivers asymmetries from Anselmino *et al.* [84] with model uncertainties. For complete projections which consist of 1400 data points, we refer to the proposal [77].

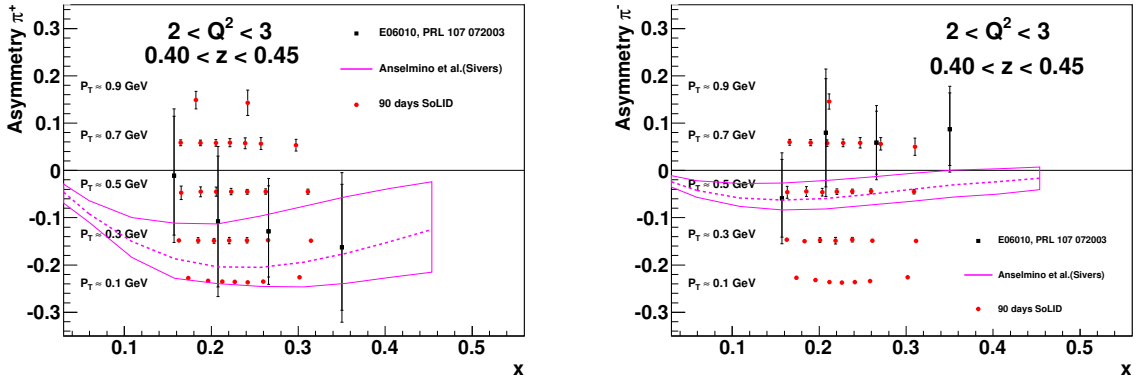


Figure 2: The left panel shows the projected Sivers asymmetry measurement for π^+ for a typical z and Q^2 bin ($0.40 < z < 0.45$, $2 \text{ GeV}^2 < Q^2 < 3 \text{ GeV}^2$) as a function of x with different ranges of the hadron transverse momentum labeled. The right panel shows the projection for the corresponding π^- Sivers asymmetry measurement. Also shown are the results from the 6-GeV experiment E06-010 [32].

E12-11-007 Experiment E12-11-007 was approved 35 days of total beam time with $15 \mu\text{A}$, 11/8.8 GeV electron beams on a 40-cm long, 10 amgs longitudinally polarized ^3He target to match about 50% statistics of experiment E12-10-006. When combined with experiment E12-10-006, this experiment will not require any beam time for calibration data, including reference cell runs and detector calibrations.

A maximum likelihood method [85] was used to extract angular modulations with combined, projected data sets from both E12-11-007 and E12-10-006. Projected data are binned into 4-

dimensional (x, P_h, z, Q^2) bins. For a typical z and Q^2 bin ($0.40 < z < 0.45$, $2 \text{ GeV}^2 < Q^2 < 3 \text{ GeV}^2$, one of the total 48 $z - Q^2$ bins), data projections are shown in Fig. 3 as examples. For complete projections, we refer to the proposal [78].

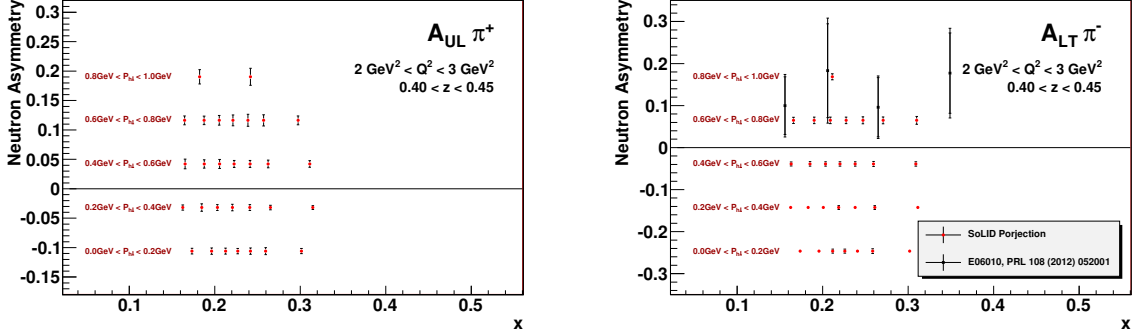


Figure 3: The left panel shows the projection for a typical z and Q^2 bin ($0.40 < z < 0.45$, $2 \text{ GeV}^2 < Q^2 < 3 \text{ GeV}^2$, one of the total 48 $z - Q^2$ bins) for the π^+ single target spin asymmetry $A_{UL}^{\sin(2\Phi_h)}$ measurement as a function of x with different ranges of the hadron transverse momentum labeled. The right panel shows the projection for the corresponding $z - Q^2$ bin for the π^- double spin asymmetry $A_{LT}^{\cos(\Phi_h - \Phi_S)}$ measurement. Also shown are the results from the 6-GeV experiment E06-010 [44].

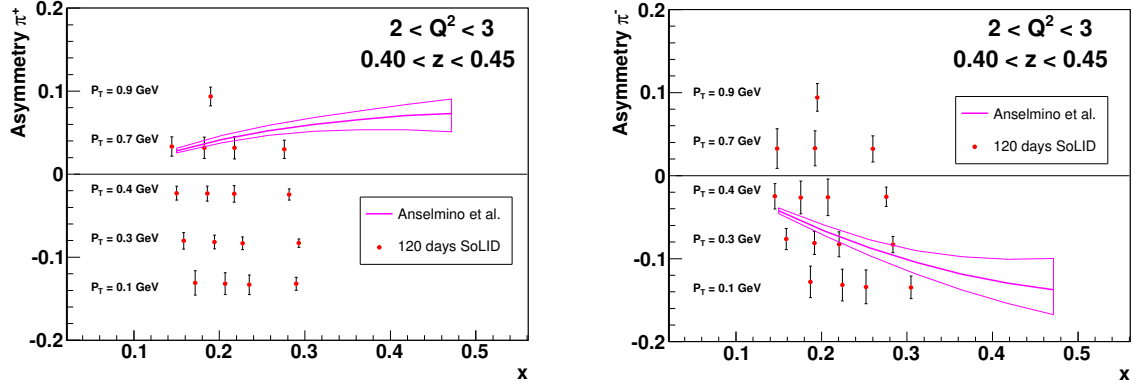


Figure 4: The left panel shows the projection for a typical z and Q^2 bin ($0.40 < z < 0.45$, $2 \text{ GeV}^2 < Q^2 < 3 \text{ GeV}^2$) for the π^+ Collins asymmetry measurement as a function of x with different ranges of the hadron transverse momentum labeled. The right panel shows the projection for the corresponding $z - Q^2$ bin for the π^- measurement. Also shown are predictions of Collins asymmetries from Anselmino *et al.* [84] with model uncertainties.

E12-11-108 Experiment E12-11-108 was approved 94 days of total beam time with 100 nA, 11/8.8 GeV electron beams on a 3-cm long, polarized NH_3 target. The 8.8 GeV beam energy will provide precision data on the radiative corrections along with the increased Q^2 coverage. 90 days are for beam on a transversely polarized NH_3 target including 7.5 days for dilution measurements, optics, and detector calibrations. Also 4 days are requested with a longitudinal target polarization to study the systematics of potential A_{UL} contamination. Although beam polarization is not required for the proposed SSA measurements, a longitudinally polarized beam will be used for a parasitic

measurement of the A_{LT} , which can be used to access g_{1T} . In addition, there will be an overhead time of 26 days for regular target annealing which does not need an electron beam.

Projected data from E12-11-108 are binned into 4-dimensional (x, P_h, z, Q^2) bins. For a typical z and Q^2 bin ($0.40 < z < 0.45, 2 \text{ GeV}^2 < Q^2 < 3 \text{ GeV}^2$), data projections for Collins asymmetry measurements, left panel for π^+ and right panel for π^- , are shown in Fig. 4 as examples. Also shown are predictions of Collins asymmetries from Anselmino *et al.* [84] with model uncertainties. For complete projections of E12-11-108, we refer to the proposal [79].

The combination of these three experiments will allow for accessing important information about TMDs from proton and neutron, and the flavor separation of the TMDs (transversity, Sivers, pretzelosity, and g_{1T}) for u and d quark. A good example based on a study by A. Prokudin to demonstrate the impact of this program is shown in Fig. 5 in which the projected Sivers function for the d quark is shown in one-dimension of x with the other dimensions integrated out with the assumptions that one knows the k_T dependence, the Q^2 evolution of the TMD, and the transverse momentum dependent fragmentation function. The expected improvement in the knowledge of the d-quark Sivers function is enormous: from the grey error band based on the current knowledge to the dark band from the SoLID program, and the access to the valence quark region, which has been essentially unexplored as of now. In fact the proposed SoLID SIDIS program will allow for studies of the k_T dependence, and the Q^2 evolution of the TMDs also. Furthermore, the SoLID SIDIS program will provide precise information on the tensor charge of the nucleon, an important property of the nucleon like spin or magnetic moment, and is determined by the valence quarks inside the nucleon. The flavor separation of the nucleon tensor charge from proton and neutron will determine the tensor charge of the u and the d quark to an accuracy of 10% and allows for benchmark tests of lattice QCD predictions. The high impact of these data on the extraction of the tensor charge of the u and d quark is shown in Fig. 6.

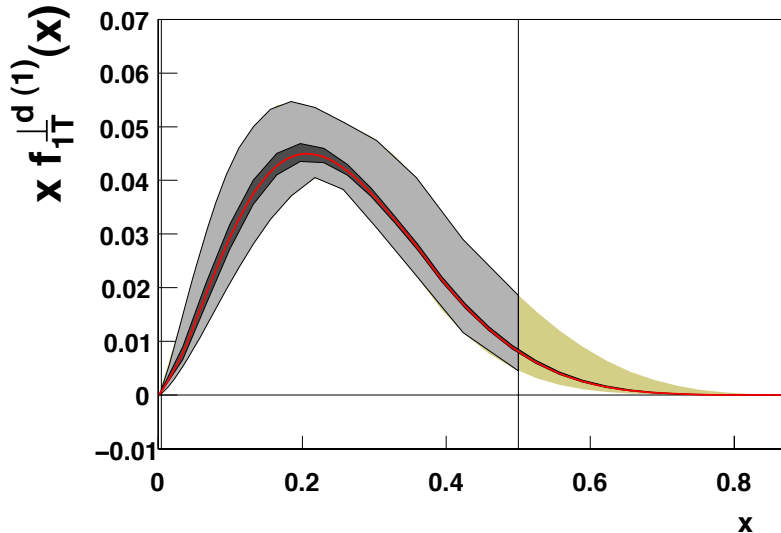


Figure 5: The impact on the d-quark Sivers function by the SIDIS program using SoLID. The impact is shown by comparing the grey band to the black band (see text).

References

- [1] European Muon, J. Ashman *et al.*, Phys. Lett. **B206**, 364 (1988).
- [2] B. W. Filippone and X.-D. Ji, Adv. Nucl. Phys. **26**, 1 (2001), hep-ph/0101224.
- [3] S. E. Kuhn, J. P. Chen, and E. Leader, Prog. Part. Nucl. Phys. **63**, 1 (2009), 0812.3535.
- [4] X. Artru and M. Mekhfi, Z. Phys. **C45**, 669 (1990).
- [5] P. J. Mulders and R. D. Tangerman, Nucl. Phys. **B461**, 197 (1996), hep-ph/9510301.
- [6] D. Boer and P. J. Mulders, Phys. Rev. **D57**, 5780 (1998), hep-ph/9711485.
- [7] X.-d. Ji, J.-P. Ma, and F. Yuan, Phys. Lett. **B597**, 299 (2004), hep-ph/0405085.
- [8] K. Hidaka, E. Monsay, and D. W. Sivers, Phys. Rev. **D19**, 1503 (1979).
- [9] J. P. Ralston and D. E. Soper, Nucl. Phys. **B152**, 109 (1979).
- [10] R. L. Jaffe and X.-D. Ji, Phys. Rev. Lett. **67**, 552 (1991).
- [11] V. Barone, Phys. Lett. **B409**, 499 (1997), hep-ph/9703343.
- [12] C. Bourrely, J. Soffer, and O. V. Teryaev, Phys. Lett. **B420**, 375 (1998), hep-ph/9710224.
- [13] J. Soffer, Phys. Rev. Lett. **74**, 1292 (1995), hep-ph/9409254.
- [14] W. Vogelsang, Phys. Rev. **D57**, 1886 (1998), hep-ph/9706511.
- [15] G. R. Goldstein, R. L. Jaffe, and X.-D. Ji, Phys. Rev. **D52**, 5006 (1995), hep-ph/9501297.
- [16] J. Ralston, private communications.
- [17] QCDSF, M. Gockeler *et al.*, Phys. Lett. **B627**, 113 (2005), hep-lat/0507001.
- [18] H.-X. He and X.-D. Ji, Phys. Rev. **D52**, 2960 (1995), hep-ph/9412235.
- [19] B. Q. Ma, I. Schmidt, and J. Soffer, Phys. Lett. **B441**, 461 (1998).
- [20] L. P. Gamberg and G. R. Goldstein, Phys. Rev. Lett. **87**, 242001 (2001), hep-ph/0107176.
- [21] I. C. Cloet, W. Bentz, and A. W. Thomas, Phys. Lett. **B659**, 214 (2008), 0708.3246.
- [22] M. Wakamatsu, Phys. Lett. **B653**, 398 (2007), 0705.2917.
- [23] B. Pasquini, M. Pincetti, and S. Boffi, Phys. Rev. **D72**, 094029 (2005), hep-ph/0510376.
- [24] J. C. Collins, Nucl. Phys. **B396**, 161 (1993), hep-ph/9208213.
- [25] Belle, K. Abe *et al.*, Phys. Rev. Lett. **96**, 232002 (2006), hep-ex/0507063.
- [26] HERMES, A. Airapetian *et al.*, (2010), hep-ex/1006.4221.
- [27] HERMES, A. Airapetian *et al.*, Phys. Rev. Lett. **103**, 152002 (2009), 0906.3918.
- [28] HERMES, A. Airapetian *et al.*, Phys. Rev. Lett. **94**, 012002 (2005), hep-ex/0408013.

- [29] COMPASS, M. G. Alekseev *et al.*, (2010), 1005.5609.
- [30] COMPASS, V. Y. Alexakhin *et al.*, Phys. Rev. Lett. **94**, 202002 (2005), hep-ex/0503002.
- [31] D. W. Sivers, Phys. Rev. **D41**, 83 (1990).
- [32] X. Qian *et al.*, Phys. Rev. Lett. **107**, 072003 (2011).
- [33] G. L. Kane, J. Pumplin, and W. Repko, Phys. Rev. Lett. **41**, 1689 (1978).
- [34] M. Anselmino, M. Boglione, and F. Murgia, Phys. Lett. **B362**, 164 (1995), hep-ph/9503290.
- [35] J. C. Collins, Phys. Lett. **B536**, 43 (2002), hep-ph/0204004.
- [36] A. V. Belitsky, X. Ji, and F. Yuan, Nucl. Phys. **B656**, 165 (2003), hep-ph/0208038.
- [37] D. Boer, P. J. Mulders, and F. Pijlman, Nucl. Phys. **B667**, 201 (2003), hep-ph/0303034.
- [38] S. J. Brodsky, D. S. Hwang, and I. Schmidt, Phys. Lett. **B530**, 99 (2002), hep-ph/0201296.
- [39] X.-d. Ji and F. Yuan, Phys. Lett. **B543**, 66 (2002), hep-ph/0206057.
- [40] L. P. Gamberg, G. R. Goldstein, and K. A. Oganessyan, Phys. Rev. **D67**, 071504 (2003), hep-ph/0301018.
- [41] M. Burkardt, Phys. Rev. **D69**, 057501 (2004), hep-ph/0311013.
- [42] M. Burkardt, Phys. Rev. **D72**, 094020 (2005), hep-ph/0505189.
- [43] S. J. Brodsky and S. Gardner, Phys. Lett. **B643**, 22 (2006), hep-ph/0608219.
- [44] J. Huang *et al.*, Phys. Rev. Lett. **108**, 052001 (2012).
- [45] T.-C. Meng, J.-C. Pan, Q.-b. Xie, and W. Zhu, Phys. Rev. **D40**, 769 (1989).
- [46] M. Anselmino, M. Boglione, and F. Murgia, Phys. Rev. **D60**, 054027 (1999), hep-ph/9901442.
- [47] A. Bacchetta, A. Schaefer, and J.-J. Yang, Phys. Lett. **B578**, 109 (2004), hep-ph/0309246.
- [48] Z. Lu and B.-Q. Ma, Nucl. Phys. **A741**, 200 (2004), hep-ph/0406171.
- [49] L. P. Gamberg, G. R. Goldstein, and M. Schlegel, (2007), 0708.2580.
- [50] A. Bacchetta, F. Conti, and M. Radici, Phys. Rev. **D78**, 074010 (2008), 0807.0323.
- [51] B. Pasquini and F. Yuan, Phys. Rev. D **81**, 114013 (2010).
- [52] F. Yuan, Phys. Lett. **B575**, 45 (2003), hep-ph/0308157.
- [53] D. Amrath, A. Bacchetta, and A. Metz, Phys. Rev. **D71**, 114018 (2005), hep-ph/0504124.
- [54] A. Bacchetta, L. P. Gamberg, G. R. Goldstein, and A. Mukherjee, Phys. Lett. **B659**, 234 (2008), arXiv:0707.3372 [hep-ph].
- [55] H. H. Matevosyan, A. W. Thomas, W. Bentz, Phys. Rev. D **86**, 034025 (2012), arXiv:1205.5813 [hep-ph].

- [56] A. Kotzinian, H. H. Matevosyan and A. W. Thomas, arXiv:1403.5562 [hep-ph].
- [57] A. Metz, Phys. Lett. **B549**, 139 (2002).
- [58] J. C. Collins and A. Metz, Phys. Rev. Lett. **93**, 252001 (2004), hep-ph/0408249.
- [59] L. P. Gamberg, A. Mukherjee, and P. J. Mulders, Phys. Rev. **D77**, 114026 (2008), 0803.2632.
- [60] G. R. Goldstein and L. Gamberg, (2002), Transversity and meson photoproduction Proceedings of ICHEP 2002; North Holland Amsterdam, p. 452 (2003), hep-ph/0209085, Published in Amsterdam ICHEP 452-454.
- [61] Z. Lu and B.-Q. Ma, Phys. Rev. **D70**, 094044 (2004), hep-ph/0411043.
- [62] H. Avakian *et al.*, Phys. Rev. D **78**, 114024 (2008).
- [63] J. She, J. Zhu, and B.-Q. Ma, Phys. Rev. D **79**, 054008 (2009).
- [64] B. Pasquini, S. Cazzaniga, and F. Yuan, Phys. Rev. D **78**, 034025 (2008).
- [65] S. Boffi, A. V. Efremov, B. Pasquini, and P. Schweitzer, Phys. Rev. **D79**, 094012 (2009), 0903.1271.
- [66] V. Barone, Z. Lu, and B.-Q. Ma, Phys. Lett. **B632**, 277 (2006), hep-ph/0512145.
- [67] V. Barone, A. Prokudin, and B.-Q. Ma, Phys. Rev. **D78**, 045022 (2008), 0804.3024.
- [68] M. Anselmino *et al.*, Phys. Rev. **D75**, 054032 (2007), hep-ph/0701006.
- [69] COMPASS, E. S. Ageev *et al.*, Nucl. Phys. **B765**, 31 (2007), hep-ex/0610068.
- [70] COMPASS, M. Alekseev *et al.*, Phys. Lett. **B673**, 127 (2009), 0802.2160.
- [71] M. Anselmino *et al.*, Eur. Phys. J. **A39**, 89 (2009), 0805.2677.
- [72] M. Anselmino *et al.*, Phys. Rev. **D72**, 094007 (2005), hep-ph/0507181.
- [73] M. Anselmino *et al.*, (2005), hep-ph/0511017.
- [74] M. Anselmino *et al.*, Phys. Rev. **D71**, 074006 (2005), hep-ph/0501196.
- [75] J. C. Collins *et al.*, Phys. Rev. **D73**, 014021 (2006), hep-ph/0509076.
- [76] V. Barone, A. Drago, and P. G. Ratcliffe, Phys. Rept. **359**, 1 (2002), hep-ph/0104283.
- [77] Jefferson Lab Experiment E12-10-006, Spokespersons: Chen, Gao (contact), Jiang, Peng, and Qian.
- [78] Jefferson Lab Experiment E12-10-006, Spokespersons: Chen, Huang (contact), Qiang, and Yan.
- [79] Jefferson Lab Experiment E12-11-108, Spokespersons: Allada, Chen, Gao (contact), Li, and Mezziani.
- [80] D. Crabb *et al.*, Phys. Rev. Letts. **64**, 2627 (2008).
- [81] C. Keith *et al.*, Nucl. Inst. Meth. **A501**, 327 (2003).

- [82] G. S. Atoian *et al.*, Nucl. Inst. Meth. **A531**, 467 (2004).
- [83] G. S. Atoian *et al.*, Nucl. Inst. Meth. **A584**, 291 (2008).
- [84] M. Anselmino and A. Prokudin, private communications.
- [85] J. Huang and Y. Qiang, *Maximum likelihood estimation of asymmetry and angular modulation for transversity (2010)*, URL <http://www.jlab.org/jinhuang/Transversity/MLE.pdf>.

1.3 PVDIS Program with SoLID

1.3.1 Motivation for PVDIS

The unique opportunities for experiments on parity-violation at Jlab with the 12 GeV upgrade were recognized in the NSAC long-range planning exercises. The experiment was approved by the PAC 35. Quoting the PAC 35 report, “the PAC believes the mission of this and future experiments using SoLID are sufficiently important that the Laboratory should make every effort to assist in securing the necessary funding.”

We reiterate here the physics topics that become accessible with the advent of a longitudinally polarized 11 GeV electron beam via measurements of the parity-violating asymmetry A_{PV} in deep inelastic scattering (DIS) in the kinematic region of large Bjorken $x = Q^2/2M\nu$. A_{PV} is defined to be:

$$A_{PV} = \frac{\sigma_R - \sigma_L}{\sigma_R + \sigma_L} \quad (1)$$

where $\sigma_R(\sigma_L)$ is the cross-section for incident right-(left-) handed electrons.

The primary motivation of PVDIS is to search for new interactions beyond the Standard Model (SM). PVDIS is unique in that it is sensitive to fundamental axial-hadronic currents but does not have large radiative corrections that involve soft hadronic physics and are impossible to make reliably.

We propose to obtain data over a broad kinematic range, with $x > 0.2$, $2 < Q^2 < 10$. With a deuterium target, the asymmetry is approximately independent of kinematics and insensitive to the structure function. However, it is possible that the following physics could be observed in our data:

1. Charge Symmetry violation (CSV) at the quark level.
2. Higher-twist effects in the parity-violating asymmetry. Significant higher-twist effects are observed in DIS cross sections, but in PVDIS large higher-twist contributions can only be due to quark-quark correlations.

If these effects are large, they will constitute an important discovery. If they are small, our test of the SM will be quite reliable.

It has been suggested that there is additional CSV in heavier nuclei. By obtaining data with a lead target, we could test this hypothesis. Such an effect would have profound implications for our understanding of the EMC effect.

By switching the target to hydrogen, we can also measure the d/u ratio in the proton, without requiring any nuclear corrections.

1.3.2 Review of the Theory

The general expression for A_{PV} for $Q^2 \ll M_Z^2$ is[1]

$$A^{PV} = - \left(\frac{G_F Q^2}{4\sqrt{2}\pi\alpha} \right) \left[g_A^e Y_1 \frac{F_1^{\gamma Z}}{F_1^\gamma} + \frac{g_V^e}{2} Y_3 \frac{F_3^{\gamma Z}}{F_1^\gamma} \right] = - \left(\frac{G_F Q^2}{4\sqrt{2}\pi\alpha} \right) (Y_1 a_1 + Y_3 a_3). \quad (2)$$

Here the F_i^γ are the electromagnetic structure functions and the $F_i^{\gamma Z}$ are structure functions for the parity-violating interference term. The Y_i are functions of the kinematic variable $y = \nu/E$ and the ratios of structure functions $R^j(x, Q^2)$:

$$Y_1(x, y, Q^2) = \frac{1 + (1-y)^2 - y^2(1-r^2/(1+R^{\gamma Z})) - 2xyM/E}{1 + (1-y)^2 - y^2(1-r^2/(1+R^\gamma)) - 2xyM/E} \left(\frac{1+R^{\gamma Z}}{1+R^\gamma} \right) \quad (3)$$

$$Y_3(x, y, Q^2) = \frac{1 - (1-y)^2}{1 + (1-y)^2 - y^2(1-r^2/(1+R^\gamma)) - 2xyM/E} \left(\frac{r^2}{1+R^\gamma} \right) \quad (4)$$

The above expressions are quite general.

In order to account for possible violations of the Standard Model, it is essential to express the parity-violating part of the electron-hadron interaction in terms of general phenomenological four-fermion contact interactions. couplings C_{ij}

$$\mathcal{L}^{PV} = \frac{G_F}{\sqrt{2}} [\bar{e}\gamma^\mu\gamma_5 e (C_{1u}\bar{u}\gamma_\mu u + C_{1d}\bar{d}\gamma_\mu d) + \bar{e}\gamma^\mu e (C_{2u}\bar{u}\gamma_\mu\gamma_5 u + C_{2d}\bar{d}\gamma_\mu\gamma_5 d)]$$

with additional terms as required for the heavy quarks. Here C_{1j} (C_{2j}) gives the vector (axial-vector) coupling to the j^{th} quark. For the Standard Model:

$$C_{1u} = g_A^e g_V^u \approx -\frac{1}{2} + \frac{4}{3} \sin^2 \theta_W \approx -0.19 \quad (5)$$

$$C_{1d} = g_A^e g_V^d \approx \frac{1}{2} - \frac{2}{3} \sin^2 \theta_W \approx 0.34 \quad (6)$$

$$C_{2u} = g_V^e g_A^u \approx -\frac{1}{2} + 2 \sin^2 \theta_W \approx -0.030 \quad (7)$$

$$C_{2d} = g_V^e g_A^d \approx \frac{1}{2} - 2 \sin^2 \theta_W \approx 0.025 \quad (8)$$

The numerical values include electroweak radiative corrections. The key point is that the C_{1i} are about an order of magnitude larger than the C_{2i} , which makes the a_1 term dominant. Recently, the JLab PVDIS collaboration published in the journal Nature[2] the result that the C_{2i} 's are indeed nonzero. The results are shown in Figure 7.

As recently pointed out by Mantry, et al., [3] for the deuteron where $I = 0$, $Y_1 = 1$ and

$$a_1^D(x) = g_A^e \frac{F_1^{D\gamma Z}}{F_1^{D\gamma}} = a_1^D(x) = \frac{6}{5} (2C_{1u} - C_{1d}) \left(1 + \frac{2s^+}{u^+ + d^+} \right)$$

The only corrections to these formulae are physics beyond the Standard Model, CSV and quark-quark correlations, which form the motivation for the experiment, and known corrections including strange quarks and target mass corrections.

For the a_3 term, we use the quark-parton model (QPM), which describes the structure functions in terms of parton distribution functions (PDF's) functions $f_i(x)$ ($\bar{f}_i(x)$), which are the probabilities

that the i^{th} quark (antiquark) carries a fraction x of the nucleon momentum. With the definitions $f_i^\pm = f_i \pm \bar{f}_i$, $y = \nu/E$, the structure functions are given by

$$F_1^\gamma = \frac{1}{2} \sum_i e_i^2 (f_i(x) + \bar{f}_i(x))$$

$$F_1^{\gamma Z} = \sum_i e_i g_V^i (f_i(x) + \bar{f}_i(x))$$

$$F_3^{\gamma Z} = 2 \sum_i e_i g_A^i (f_i(x) - \bar{f}_i(x)),$$

where e_i is the electromagnetic charge of the i^{th} quark. Then

$$a_3^D(x) = \frac{g_V^e}{2} \frac{F_3^{\gamma Z}}{F_1^\gamma} = 2 \frac{\sum_i C_{2i} e_i f_i^-(x)}{\sum_i e_i^2 f_i^+(x)} = \frac{6}{5} (2C_{2u} - C_{2d}) \left(\frac{u^+ - d^-}{u^+ + d^+} \right) + \dots$$

Contributions due to higher twist to this term can be obtained from neutrino scattering. The contribution of R^γ to A_{PV} is given in the Y_3 factor.

The key is that since $(2C_{2u} - C_{2d})$ is small, there is less sensitivity to the hadronic physics, whereas $(u^+ - d^-)(u^+ + d^+) \sim 1$ so that we are sensitive to new physics contributions to the C_{2i} .

The main goal of the experiment is to place a narrow error band on the C_{2i} plots of Figures 8 and 7. An example of new physics that can contribute to the C_{2i} but not to the C_{1i} that have been precisely measured by Qweak and atomic parity violation in Cs, is a leptophobic Z' [4] as illustrated in Fig. 9. At the LHC, such a particle would be swamped by background. The proposed data will also improve the mass limits for generic models for composite for quarks and leptons[5] as shown in Figure 10.

1.3.3 Charge Symmetry Violation

The subtle violation of fundamental symmetries in hadronic systems can often provide important insights into the dynamics at work in those systems. The famous Nolen-Schiffer anomaly has played a significant role in nuclear structure for decades. When it comes to hadron structure charge symmetry violation is of great interest because of its link to the role of di-quarks in non-perturbative parton distribution functions [6, 7, 8].

The NuTeV experiment published a discrepancy with the Standard Model [9] with a significance of about three sigma. The result stirred a lot of controversy, resulting in a serious re-evaluation of the work. Additional corrections, including changes in the Cabibbo angle, strange sea, and improved radiative corrections, have recently been made, but have changed the result very little.

One possible explanation of the NuTeV result is charge symmetry violation (CSV) in the PDF's. This was overlooked in the NuTeV analysis, even though estimates which suggested how important it could be had existed in the literature for almost a decade [7, 8]. Various authors [10, 11, 12] have also presented the case that this is a reasonable explanation.

Our experiment is also sensitive to CSV. If the x -dependence of the CSV falls slower than the PDF's as suggested by the curves in Figure 11 our asymmetry should display a clear x -dependence. Moreover, these results will provide an important test of the CSV explanation for NuTeV.

Another interesting possible contribution to the NuTeV anomaly is the isovector EMC effect [13], which occurs for heavy nuclei. Measuring PVDIS in a target such as Pb would be able to demonstrate this effect.

1.3.4 Higher Twist

A recent paper has examined the contribution of higher twist (HT) effects to the dominant $Y_1 a_1$ term in A_{PV} . [3] The correction can be parameterized as a fractional contribution $R_1(HT)$ by

$$Y_1 a_1 \approx Y_1 a_1 (1 + R_1(HT) + \dots)$$

where the \dots refer to other corrections including CSV. It turns out that the only contribution comes from the operator

$$\mathcal{O}_{ud}^{\mu\nu} = \frac{1}{2} [\bar{u}(x) \gamma^\mu u(x) d(0) \gamma^\nu d(0) + (u \leftrightarrow d)]$$

which arises only from quark-quark correlations, or in other words, di-quarks in the nucleon. Higher twist contributions involving gluons cancel in the ratio. The special feature of A_{PV} is that it is the only practical experiment that can isolate higher twist due to four quarks.

The result is

$$R_1(HT) = -\frac{4}{5} \frac{[(9 - 20 \sin^2 \theta_W) F_1^{\gamma;4q} - 5 F_1^{\gamma Z;4q}]}{(1 - \frac{20}{9} \sin^2 \theta_W) [u_p(x) + d_p(x)]}$$

where $F_1^{\gamma;4q}$ and $F_1^{\gamma Z;4q}$ are the four-quark higher twist contributions to the structure functions.

1.3.5 Data Sample and analysis

The observation of CSV is possible with our apparatus only if the effect varies with x . An x -independent CSV effect would be indistinguishable from a change in the C_{1q} 's. It is quite natural, however, to expect that the x -dependence is similar to that shown in Figure 11, and we will make that assumption in our further discussion. From observations of higher-twist contributions to DIS cross sections, it is also natural to assume that Q^2 -dependent effects will also increase with increasing x .

If indeed either higher twist effects or CSV are clearly seen, the experiment will be a success. If they are absent, we plan to untangle the effects of hadronic and electroweak physics by fitting the asymmetries to a function of the form

$$A_{PV}^D = A_{PV}^{EW} \left(1 + \beta_{HT} \frac{1}{(1-x)^3 Q^2} + \beta_{CSV} x^2 \right) \quad (9)$$

Since the size of the hadronic effects is small, the sensitivity to the exact form is not important. The resulting statistical errors on the fit parameters are:

$$\delta A_{PV}^{EW} / A_{PV}^{EW} = 0.3\%; \quad \delta \beta_{HT} = 0.0026; \quad \delta \beta_{CSV} = 0.017$$

With this method, we use the full statistical power of the data set. However, the result has some sensitivity to the exact form of the chosen fitting functions. Under the scenario where the hadronic effects are small, these errors are negligible as long as we assume that CSV and higher twist effects depend strongly on x , as expected. The one-sigma band for the CSV term is plotted in Figure 11.

If the pattern of higher twist effects is the same for A_{PV} as it is for the cross sections, then at $x = 0.6$ the asymmetries at the different Q^2 values will differ by 15%. In that scenario, the rapid x -dependence of the higher-twist coefficients for the cross section would imply that higher twist effects would still be negligible at $x = 0.4$. With a comparable x -dependence, a Q^2 -dependent effect as small as $\sim 3\%$ of the effect seen in cross-section measurements would be easily identifiable given our statistical precision.

Measuring d/u at high x Hydrogen is another useful target. Since it is not isoscalar, the structure functions do not cancel in the expression for $a(x)$. In particular,

$$a(x) \approx \frac{3}{4} \left[\frac{6C_{1u}u(x) - 3C_{1d}d(x)}{u(x) + \frac{1}{4}d(x)} \right] \sim \left[\frac{u(x) + 0.912d(x)}{u(x) + 0.25d(x)} \right]$$

and we see that $a(x)$ is sensitive to the ratio d/u . The determination of this for the proton is a topic of considerable interest at large values of x [14, 15, 16, 17]. The ratio is difficult to determine from cross section data because at large x complicated nuclear physics effects become important for deuterium targets. Alternative methods include comparing ^3He and tritium or detecting the recoil proton from deuteron. Projected errors for all three approaches are shown in Fig. 13.

1.3.6 Beam Time Request

For the deuterium data, we have based our sensitivity on 180 days of production running at $50 \mu\text{A}$, with 1/3 of the data at 6.6 GeV and the rest at 11 GeV. Approximately 27 additional days, run at various currents, will be required for checkout and calibrations. An additional 18 days will be required at 4.4 GeV and $50 \mu\text{A}$ for radiative correction measurements. The total beam request at all energies for the deuterium measurement is 225 days, with about 25 of those days run mostly at reduced beam currents.

For the hydrogen measurement, 90 days are needed for production data at 11 GeV, about 9 days are required at 4.4 GeV to control radiative corrections and another 14 days will be required for calibration. The running time requested for hydrogen totals to 113 days. We have been approved for 180 days total. The plan is to first take half the deuterium data. If nothing exciting appears, we will switch to hydrogen.

In the future, we would also anticipate requesting an additional comparable run for a heavy nucleus such as Pb.

References

- [1] T. Hobbs and W. Melnitchouk, Phys. Rev. D **77**, 114023 (2008) [arXiv:0801.4791 [hep-ph]].
- [2] D. Wang *et al.* [PVDIS Collaboration], Nature **506**, no. 7486, 67 (2014).
- [3] S. Mantry, M. J. Ramsey-Musolf and G. F. Sacco, Phys. Rev. C **82**, 065205 (2010) [arXiv:1004.3307 [hep-ph]].
- [4] M. R. Buckley and M. J. Ramsey-Musolf, Phys. Lett. B **712**, 261 (2012) [arXiv:1203.1102 [hep-ph]].
- [5] E. Eichten, K. D. Lane and M. E. Peskin, Phys. Rev. Lett. **50**, 811 (1983).
- [6] F. E. Close and A. W. Thomas, Phys. Lett. B **212**, 227 (1988).
- [7] E. Sather, Phys. Lett. B **274**, 433 (1992).
- [8] E. N. Rodionov, A. W. Thomas and J. T. Londergan, Mod. Phys. Lett. A **9**, 1799 (1994).
- [9] G. P. Zeller *et al.* [NuTeV Collaboration], Phys. Rev. Lett. **88**, 091802 (2002) [Erratum-ibid. **90** 239902 (2003)].

- [10] J. T. Londergan and A. W. Thomas, *Phys. Lett. B* **558** 132 (2003).
- [11] J. T. Londergan and A. W. Thomas, *J. Phys. G* **31** 1151 (2005).
- [12] M. Gluck, P. Jimenez-Delgado and E. Reya, *Phys. Rev. Lett.* **95** 022002 (2005).
- [13] I. C. Cloet, W. Bentz and A. W. Thomas, *Phys. Rev. Lett.* **102**, 252301 (2009) [arXiv:0901.3559 [nucl-th]].
- [14] W. Melnitchouk, I. R. Afnan, F. Bissey and A. W. Thomas, *Phys. Rev. Lett.* **84** 5455 (2000).
- [15] W. Melnitchouk and A. W. Thomas, *Phys. Lett. B* **377** 11 (1996).
- [16] S. I. Alekhin, *Phys. Rev. D* **63** 094022 (2001).
- [17] S. Kuhlmann *et al.*, *Phys. Lett. B* 476 297 (2000).

1.4 J/Ψ Program

1.4.1 Motivation

One of the fundamental goals of modern nuclear physics is to understand hadrons and nuclei starting with the basic ingredients of QCD namely quarks and gluons and their interactions. While significant progress has been made in exploring the theory in its perturbative region much remains to be understood in the strong region, particularly where gluonic exchanges dominate. Strong gluonic field configurations and interactions are responsible for most of the mass of nucleons and nuclei. Fundamental approaches such as lattice QCD, effective field theories or dual string theories (that would match QCD) could in principle shed light on confinement of hadrons and perhaps make predictions of novel phenomena of strong interactions.

We plan to explore this strong interaction using a particular system that emphasizes the multi-gluon exchange between two color neutral particles which do not share a common valence quark, namely nucleons/nuclei and charmonia. It has long been argued that the force acting between nucleon/nucleus and J/Ψ is an attractive force, which has negligible mesonic ($D\bar{D}$) or multi-mesonic ($\rho\pi$) exchange contribution at low energies [1]. Since the nucleon/nucleus and J/Ψ are color neutral, this force is dubbed as color Van der Waals force in analogy with the atomic-molecular physics case. This situation is unique in nuclear physics where a force exchanged between nucleons or hadrons is purely gluonic especially at low energy. A direct consequence of such an attractive force is the possible existence of a nuclear bound quarkonium state which was proposed more than 20 years ago by Brodsky, Schmidt and de Teramond [2] but has yet to be observed. A calculation using the operator product expansion (OPE) [3] to describe the low energy interaction of quarkonium with nuclei, in the limit where the mass of the charm quark is infinite, found that the J/Ψ binds in nuclear matter with about 10 MeV but the authors caution about possible large corrections due to confinement effects.

Due to the lack of experimental data, a timid but sustained theoretical activity on the subject followed over the past twenty years. For example, Kaidalov and Volkovitsky [4] argued that S-wave quarkonia can be found in nuclei with $A \geq 10$ and with binding energy of few MeV, while de Teramond et al. [5] in an update to his original paper with Brodsky [2] estimated a binding energy of 2 MeV in ^{12}C and 10 MeV in ^{208}Pb , while Shevchenko [6] pointed in a later work that the interaction of charmonium-nucleon is so small that the potential depth for nuclear bound state may only be possible for nuclei with $A > 200$. Applying QCD sum rules Hayashigaki [7] finds a 4

to 7 MeV binding of the J/Ψ in nuclear matter. Yokokawa, Sasaki, Hatsuda and Hayashigaki [8] performed a first lattice study in the quenched approximation of low energy charmonium-hadron interaction to determine the scattering length. But more recently Kawanai and Sasaki [9] calculated the charmonium-nucleon potential from the equal-time Bethe-Salpeter amplitude through the effective Schrödinger equation and found that the charmonium-nucleon potential is weakly attractive at short distances and exponentially screened at large distances. Finally, Tsushima, Lu, Krein and Thomas [10, 11] have recently explored the J/Ψ -nuclear bound states and found that the attractive potential that originate from the D and D^* meson loops in the J/Ψ in nuclear medium should produce bound states.

Many of the J/Ψ photoproduction experiments that have been performed at high photon energies and low t or in the case of electroproduction at large center of mass energy s and low t (see Refs. [12, 13, 14, 15, 16, 17, 18, 19]) are usually considered as a diffractive production. Experiments in the threshold region are few and were performed soon after the discovery of the J/Ψ particle more than 35 years ago [20, 21, 22, 23]. In particular, the measurements of Cornell [21] and SLAC [23] show large discrepancies at photon energy around 10 GeV.

It is fair to say that not much is known in the region where the energy of the photon is just above 8.2 GeV and where t is about 2 GeV, namely the threshold region. With Jefferson Lab at 12 GeV, we enter a new kinematic domain where the electro/photo-production of charmed hadrons near threshold becomes possible. It is precisely a region well suited for the investigation of the QCD Van der Waals interaction, since as we approach the threshold and due to the conformal scale anomaly of the low energy J/Ψ -nucleon interaction [24, 25] the non-perturbative part of the interaction vanishes more slowly than the perturbative part. In his paper of 1998 [25], Kharzeev considered explicitly the possible enhancement of the threshold cross section due to this conformal scale anomaly which corresponds to a diagram where the coupling of the quarkonium to the nucleon occurs through triangle gluonic lines (see Fig. 14). As shown in Fig. 15, the scattering amplitude in the threshold region is also dominated by its real part in contrast to the case of high energy.

Later Brodsky, Chudakov, Hoyer and Laget [26] discussed the photoproduction of charm near threshold and invoked the two-gluon exchange mechanism in the production. These authors also considered the possible enhancement of the cross section at threshold due to a strong interaction beyond two-gluon exchanges as shown in Fig. 16. Whereas Sibirtsev, Krewald and Thomas [27] attributed the mechanism of the J/Ψ photoproduction at low energies and large t to a mechanism different from pomeron or two-gluon exchange. They considered the possibility of the exchange of an axial vector trajectory that couples with the axial form factor of the nucleon in this case also enhancing the cross section at threshold.

At first, the charmonium production near the threshold region would not seem to lend itself to calculations using pQCD similar to the case of deep inelastic scattering at large Q^2 . However, a closer look reveals a new scale at play, namely the mass of heavy quarks, which when compared to Λ_{QCD} enables a perturbative approach to evaluate the scattering amplitude of the process. This fact was used a while ago to derive charm photoproduction sum rules in a way similar to deep inelastic scattering [28, 29, 30].

In the reaction $\gamma^* + N \rightarrow J/\Psi + N$, the production mechanism at threshold can be viewed in a way similar to the J/Ψ elastic scattering off a nucleon at small relative velocity. The coupling of the soft gluonic fields to the nucleon, at low Q^2 is determined by the low-energy theorem in QCD based on the anomaly in the trace of the energy-momentum tensor. The J/Ψ -nucleon scattering amplitude is proportional to the nucleon matrix element of the following gluon operator [31]:

$$\langle N | \frac{1}{2} \vec{E}^a \cdot \vec{E}^a | N \rangle = \frac{4\pi^2}{b} \langle N | \theta_\mu^\mu | N \rangle + 2\pi\alpha_s \langle N | \theta_G^{00} | N \rangle, \quad (10)$$

where \vec{E}^a represents the chromo-electric field, $\theta_G^{\mu\nu}$ is the energy-momentum tensor of the gluon field, θ_μ^μ is the anomalous trace of the full energy-momentum tensor in QCD in the chiral limit, b is the coefficient in the QCD beta function with three light (massless in the chiral limit) quarks and α_s is the QCD coupling.

It is argued [31] that this matrix element is bound by

$$\langle N | \frac{1}{2} \vec{E}^a \cdot \vec{E}^a | N \rangle \geq \frac{4\pi^2}{b} 2m_N^2 \quad (11)$$

In a measurement of electroproduction close to the threshold region, and unlike at high energy, the real part of the scattering amplitude contribution dominates compared to the imaginary part even though the allowed exchanges are purely gluonic. This contribution probes the matrix element represented by $\langle N | \theta_\mu^\mu | N \rangle = 2m_N^2$. Hence, in a threshold measurement we probe the conformal anomaly contribution to the low energy $J/\Psi - N$ interaction comparable to a Higgs-like coupling¹. Furthermore, the determination of an upper limit of the strength of this interaction will help determine whether or not a nucleon- J/Ψ bound state due to the Van der Waals color forces would exist.

1.4.2 Program Overview

The high luminosity and large solid angle offered by the Jefferson Lab 12 GeV energy upgrade combined with the SoLID detector in Hall A is a unique tool to start an investigation program of the J/Ψ -nucleon interaction.

In a first phase, the measurement of the cross section of electroproduction of J/Ψ on a nucleon near threshold will take place. These measurements at threshold have not been revisited since the 70s. The precision and energy range close to threshold of the proposed measurement will best probe the possible enhancement of the cross section due to the contribution of the conformal anomaly in the threshold region. Threshold enhancements due to on-shell rescattering or quasi-bound states around threshold have been observed in several processes such as $e^+e^- \rightarrow p\bar{p}, \Lambda\bar{\Lambda}, \Sigma^0\bar{\Sigma}_0, \Lambda\bar{\Sigma}_0$ [32] as well as in the J/Ψ radiative decays, e.g. $J/\Psi \rightarrow p\bar{p}\gamma$ [33]. The experiment E12-12-006 aims at observing such enhancement in the J/Ψ -proton system and offers the capability to explore the region below threshold if there are hints of an enhancement of the cross section just above threshold. Furthermore, the proposed cross section measurement could also shed light on the existence of predicted super-heavy N^* with hidden charm with a mass around 4.3 GeV [34].

In a second phase we shall explore the interference of the Bethe-Heitler amplitude with that of the J/Ψ electroproduction to attempt a determination of the relative contribution of the real and the imaginary part of the scattering amplitude. Moreover, a study of the angular distribution of the J/Ψ decay can reveal whether the J/Ψ was originally produced from an octet or singlet state.

Finally, studies of J/ψ production and propagation in the nuclear medium is the natural extension of the proposed measurements on a nucleon. The study of multi-gluon QCD Van der Waals forces in nuclei is believed to shed new light on their possible role in J/ψ -nuclear bound states [2, 3, 4, 5, 2, 6, 7, 8, 9]. Another related challenge is the in-medium properties of charmonia as well as the possible restoration of the chiral symmetry in the nuclear medium, which is closely connected to the modifications of masses and widths of mesons when embedded in the nuclear environment [10]. For these studies, it is important to find the appropriate kinematical conditions to produce J/ψ near rest, or with small momentum relative to the nucleus. Therefore, measurements near threshold and even sub-threshold look promising [35].

¹The coupling of the contact term is sensitive to the entire mass of nucleon, and as such is similar to the Higgs coupling.

At JLab Hall C, a photoproduction experiment (E03-008) was performed in the *subthreshold* regime using the CEBAF at 6 GeV. Unfortunately no signal was observed after one week of beam on a ^{12}C target [35]. This experiment allowed to set a limit on the cross section, which was found to be consistent with the quasi-free production. The experiment used a bremsstrahlung beam produced on a copper radiator by the 6 GeV incident electron beam. The pair of spectrometers (HMS and SOS) of Hall C were used to detect the pair of leptons resulting from the decay of the J/Ψ . More recently, the proposal "A-dependence of J/Ψ photoproduction near threshold" [36] for the 12 GeV upgrade of Hall C was considered by the PAC32 and conditionally approved. The authors proposed the use of bremsstrahlung photon beam created in a radiator to look at the photoproduction near threshold in a series of nuclei. The physics goal was to measure the photoproduction cross section on hydrogen and then investigate the A dependence of the propagation of the J/Ψ in the nuclear medium. In this proposal, only the J/Ψ is detected through the detection of the decay leptonic pair.

The experiment E12-12-006 as the first phase of the program, will utilize the SoLID spectrometer to measure the cross section of the full exclusive electroproduction of J/Ψ near threshold ($4.05 \text{ GeV} < W < 4.45 \text{ GeV}$ and $|t - t_{min}| < 2.5 \text{ GeV}^2$) to study QCD in the non-perturbative regime with luminosity $10^{37} \text{ N cm}^{-2} \text{ s}^{-1}$.

For the proposed measurement, we argue that electroproduction rather than photoproduction is the preferred way to perform this experiment at threshold for reasons listed below:

- The virtual photon energy and momentum are well defined by detecting the scattered electron in this rapidly varying kinematic region.
- In contrast to the photon measurements, the radiation background created in the Hall is significantly reduced allowing for the experiment to run for a good period of time without the limitation due to the radiation budget of the Hall.
- The achievable virtual photon flux using CEBAF 12 GeV with a luminosity up to $10^{37} \text{ N cm}^{-2} \text{ s}^{-1}$ is critical in this region of rapidly falling cross sections.
- Full exclusivity is required by detecting the scattered electron, the J/Ψ decay leptonic pair and with/without proton to clean up any background contamination in this low cross section production process on hydrogen.

1.4.3 Beam Time and Projection

The experiment E12-12-006 was approved by Jefferson Lab PAC39 with total 60 PAC days. Among them, 50 days will be used for production run with $3 \mu\text{A}$, and 11 GeV electron beam on a 15 cm long liquid hydrogen target. The other 10 days will be shared among activities, such as detector calibration, data taking with Al dummy target, and special low luminosity running for understanding the trigger efficiency and normalization for the cross section measurement.

Our projections for the total cross sections are then plotted against the effective photon energy in Fig. 17. Together, we have also plotted the world data of J/Ψ photoproduction. The fit of 2-gluon exchange only model and (2+3)-gluon exchange model are plotted as well with dotted and solid lines, respectively. It is clear that the proposed measurements will significantly advance our knowledge of electroproduction of J/Ψ near the threshold region.

References

- [1] S. J. Brodsky and G. A. Miller. Is J/Ψ - nucleon scattering dominated by the gluonic van der Waals interaction? *Phys. Lett.*, **B412**:125–130, 1997.

- [2] S. J. Brodsky, I. A. Schmidt, and G. F. de Teramond. Nuclear bound quarkonium. *Phys. Rev. Lett.*, **64**:1011, 1990.
- [3] M. E. Luke, A. V. Manohar, and M. J. Savage. A QCD Calculation of the interaction of quarkonium with nuclei. *Phys. Lett.*, **B288**:355–359, 1992.
- [4] A. B. Kaidalov and P. E. Volkovitsky. Heavy quarkonia interactions with nucleons and nuclei. *Phys. Rev. Lett.*, **69**:3155–3156, 1992.
- [5] G. F. de Teramond, R. Espinoza, and M. Ortega-Rodriguez. Proton proton spin correlations at charm threshold and quarkonium bound to nuclei. *Phys. Rev.*, **D58**:034012, 1998.
- [6] V. I. Shevchenko. Nonperturbative effects in the nonrelativistic hadron scattering. *Phys. Lett.*, **B392**:457–462, 1997.
- [7] A. Hayashigaki. J/Ψ nucleon scattering length and in-medium mass shift of J/Ψ in QCD sum rule analysis. *Prog. Theor. Phys.*, **101**:923–935, 1999.
- [8] K. Yokokawa, S. Sasaki, T. Hatsuda, and A. Hayashigaki. First lattice study of low-energy charmonium-hadron interaction. *Phys. Rev.*, **D74**:034504, 2006.
- [9] T. Kawanai and S. Sasaki. Charmonium-nucleon potential from lattice QCD. *Phys. Rev.*, **D82**:091501, 2010.
- [10] K. Tsushima, D. H. Lu, G. Krein, and A. W. Thomas. J/Ψ -nuclear bound states. *Phys. Rev.*, **C83**:065208, 2011.
- [11] K. Tsushima, D. H. Lu, G. Krein, and A. W. Thomas. J/Ψ mass shift and J/Ψ -nuclear bound state. *AIP Conf. Proc.*, **1354**:39–44, 2011.
- [12] M. Binkeley et al. J/Ψ Photoproduction from 60 to 300 GeV/c. *Phys. Rev. Lett.*, **48**:73, 1982.
- [13] B. H. Denby et al. Inelastic and Elastic Photoproduction of J/Ψ (3097). *Phys. Rev. Lett.*, **52**:795, 1984.
- [14] M. D. Sokoloff et al. An Experimental Study of the a -Dependence of J/Ψ Photoproduction. *Phys. Rev. Lett.*, **57**:3003, 1986.
- [15] R. Barate et al. Measurement of J/Ψ and Ψ' real photoproduction on ${}^6\text{Li}$ at a mean energy of 90 GeV. *Z. Phys.*, **C33**:505, 1987.
- [16] P. L. Frabetti et al. A Measurement of elastic J/Ψ photoproduction cross-section at fermilab E687. *Phys. Lett.*, **B316**:197, 1993.
- [17] S. Aid et al. Elastic and inelastic photoproduction of J/Ψ mesons at HERA. *Nucl. Phys.*, **B472**:3, 1996.
- [18] J. Breitweg et al. Measurement of inelastic J/Ψ photoproduction at HERA. *Z. Phys.*, **C76**:599, 1997.
- [19] S. Aid et al. Photoproduction of J/Ψ Mesons in ep Collisions at HERA. *Nucl. Phys.*, **B472**:2, 1996.
- [20] U. Camerini et al. Photoproduction of the Ψ Particles. *Phys. Rev. Lett.*, **35**:483, 1975.

- [21] B. Gittelmann et al. Photoproduction of the Ψ (3100) Meson at 11-GeV. *Phys. Rev. Lett.*, **35**:1616, 1975.
- [22] B. Knapp et al. Photoproduction of Narrow Resonances. *Phys. Rev. Lett.*, **34**:1040, 1975.
- [23] R. L. Anderson. Excess Muons and New Results in Ψ Photoproduction. SLAC-PUB-1471.
- [24] D. Kharzeev. Quarkonium interactions in QCD. 1995. nucl-th/9601029.
- [25] D. Kharzeev, H. Satz, A. Syamtomov, and G. Zinovjev. J/Ψ photoproduction and the gluon structure of the nucleon. *Eur. Phys. J.*, **C9**:459–462, 1999. 8 pages, latex, 4 figures Report-no: BI-TP 98/36.
- [26] S. J. Brodsky, E. Chudakov, P. Hoyer, and J.M. Laget. Photoproduction of charm near threshold. *Phys. Lett.*, **B498**:23–28, 2001.
- [27] A. Sibirtsev, S. Krewald, and A. W. Thomas. Systematic analysis of charmonium photoproduction. *J. Phys.*, **G30**:1427–1444, 2004.
- [28] M. A. Shifman, A. I. Vainshtein, and V. I. Zakharov. Photoproduction of Charmed Particles and Asymptotically Free Field Theories. *Phys. Lett.*, **B65**:255, 1976.
- [29] V. A. Novikov, M. A. Shifman, A. I. Vainshtein, and V. I. Zakharov. Charm Photoproduction and Quantum Chromodynamics. *Nucl. Phys.*, **B136**:125, 1978.
- [30] . A. Shifman, A. I. Vainshtein, and V. I. Zakharov. Remarks on Charm Electroproduction in QCD. *Nucl. Phys.*, **B136**:157, 1978.
- [31] A. Sibirtsev and M. B. Voloshin. The Interaction of slow J/Ψ and Ψ' with nucleons. *Phys. Rev.*, **D71**:076005, 2005.
- [32] Rinaldo Baldini Baldini, Simone Pacetti, and Adriano Zallo. Point-like Baryons? 2008.
- [33] M. Ablikim et al. Spin-Parity Analysis of $p\bar{p}$ Mass Threshold Structure in J/ψ and ψ' Radiative Decays. *Phys.Rev.Lett.*, 108:112003, 2012. 5 pages, 3 figures, submitted to Phys. Rev. Lett.
- [34] J. J. Wu, R. Molina, E. Oset, and B. S. Zou. Prediction of narrow n^* and λ^* resonances with hidden charm above 4 gev. *Phys. Rev. Lett.*, **105**:232001, 2010.
- [35] P. Bosted, J. Dunne, C. A. Lee, P. Jannackar, M. Strikman, et al. Search for Sub-threshold Photoproduction of J/Ψ Mesons. *Phys. Rev.*, **C79**:015209, 2009.
- [36] Contact Person: E. Chudakov, PAC32 PR12-07-106 The A-dependence of J/Ψ Photoproduction near Threshold.
- [37] Contact Person: P. Souder, PAC34 <http://hallaweb.jlab.org/collab/PAC/PAC34/PR-09-012-pvdis.pdf>.
- [38] Contact Person: H. Gao, PAC34 <http://hallaweb.jlab.org/collab/PAC/PAC34/PR-09-014-transversity.pdf>.
- [39] Contact Person: J. Huang, PAC37 [http://www.jlab.org/exp_prog/PACpage/PAC37/proposals/Proposals/New Proposals/PR-11-007.pdf](http://www.jlab.org/exp_prog/PACpage/PAC37/proposals/Proposals/New%20Proposals/PR-11-007.pdf).

- [40] Contact Person: H. Gao, PAC38 http://wwwold.jlab.org/exp_prog/proposals/11/PR12-11-108.pdf.
- [41] X. Qian et al. Study of the $A(e, e'\pi^+)$ Reaction on ^1H , ^2H , ^{12}C , ^{27}Al , ^{63}Cu and ^{197}Au . *Phys. Rev.*, **C81**:055209, 2010.
- [42] S. J. Brodsky et al. Photoproduction of charm near threshold. *Phys. Lett.*, **B498**:23, 2001.
- [43] K. Schilling and G. Wolf. How to analyze vector meson production in inelastic lepton scattering. *Nucl. Phys.*, **B61**:381, 1973.
- [44] R. Fiore et al. Exclusive J/Ψ electroproduction in a dual model. *Phys. Rev.*, **D80**:116001, 2009.
- [45] C. Adloff et al. Elastic Electroproduction of ρ Mesons at HERA. *Eur. Phys. J.*, **C13**:371, 2000.
- [4] L. W. Whitlow. Ph. D. thesis, Stanford University, SLAC-Report-357 (1990).
- [5] Developed by J. W. Lightbody and J. S. O'Connell in 1988.
- [6] D. E. Wiser. Ph. D. thesis, Univ. of Wisconsin (1977).
- [49] X. Qian. *Measurement of Single Target-Spin Asymmetry in Semi-Inclusive $n^\uparrow(e, e'\pi^\pm)$ Reaction on a Transversely Polarized ^3He Target*. PhD thesis.
- [50] T. Abe. GRAPE dilepton (Version1.1): A Generator for dilepton production in ep collisions. *Computer Physics Communications*, **136**:126, 2001.
- [51] PYTHIA. <http://projects.hepforge.org/pythia6/>, 2006.
- [52] Y. Kubota et al. Superfish-a Computer Program for Evaluation of RF Cavities with Cylindrical Symmetry. *Nucl. Instr. and Meth.*, **A320**, 1992.
- [53] Poisson Superfish, http://laacg1.lanl.gov/laacg/services/download_sfp.html.
- [54] G. Atoian et al. An improved Shashlyk Calorimeter. *Nucl. Instr. and Meth.*, **A584**(3):291, 2008.
- [55] W. Anderson et al. Design, Construction, Operation and Performance of a Hadron Blind Detector for the PHENIX Experiment. arXiv:1103.4277 [physics.ins-det].
- [56] B. Azmoun et al. Collection of Photoelectrons and Operating Parameters of CsI Photocathode GEM Detectors. *IEEE Trans. Nucl. Sci.*, **56-3**:1544, 2009.
- [57] C. Lu and K. T. McDonald. Properties of reflective and semitransparent CsI photocathodes. *Nucl. Instr. and Meth.*, **A343**:135, 1994.
- [58] Y. Wang et al. A prototype of a high rating MRPC. *Chinese Phys.*, **C33**:374, 2009.

1 – JLab 12

2 – Anselmino et al., Nucl.Phys.Proc.Suppl. (2009)

3 – Cloet, Bentz and Thomas, Phys.Lett.B (2008)

4 – Wakamatsu, Phys.Lett.B (2007)

5 – Gockeler et al., Phys.Lett.B (2005)

6 – He and Ji, Phys. Rev. D (1995)

$$\delta u = 0.54^{+0.09}_{-0.22}, \delta d = -0.23^{+0.09}_{-0.16}$$

$$\delta q = \int_0^1 dx (h_1^q(x) - \bar{h}_1^{\bar{q}}(x))$$

JLab 12 Proton and He³ targets

$$\delta u = 0.54^{+0.02}_{-0.02}, \delta d = -0.23^{+0.01}_{-0.01}$$

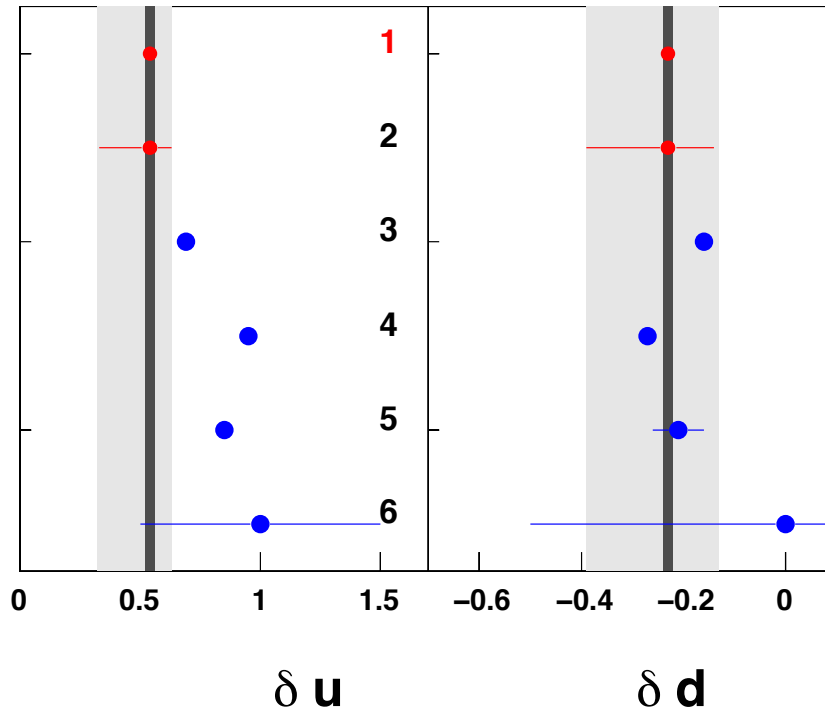


Figure 6: The impact of the projected SoLID measurement of the tensor charge for the u and d quark together with current knowledge from models and lattice QCD calculations.

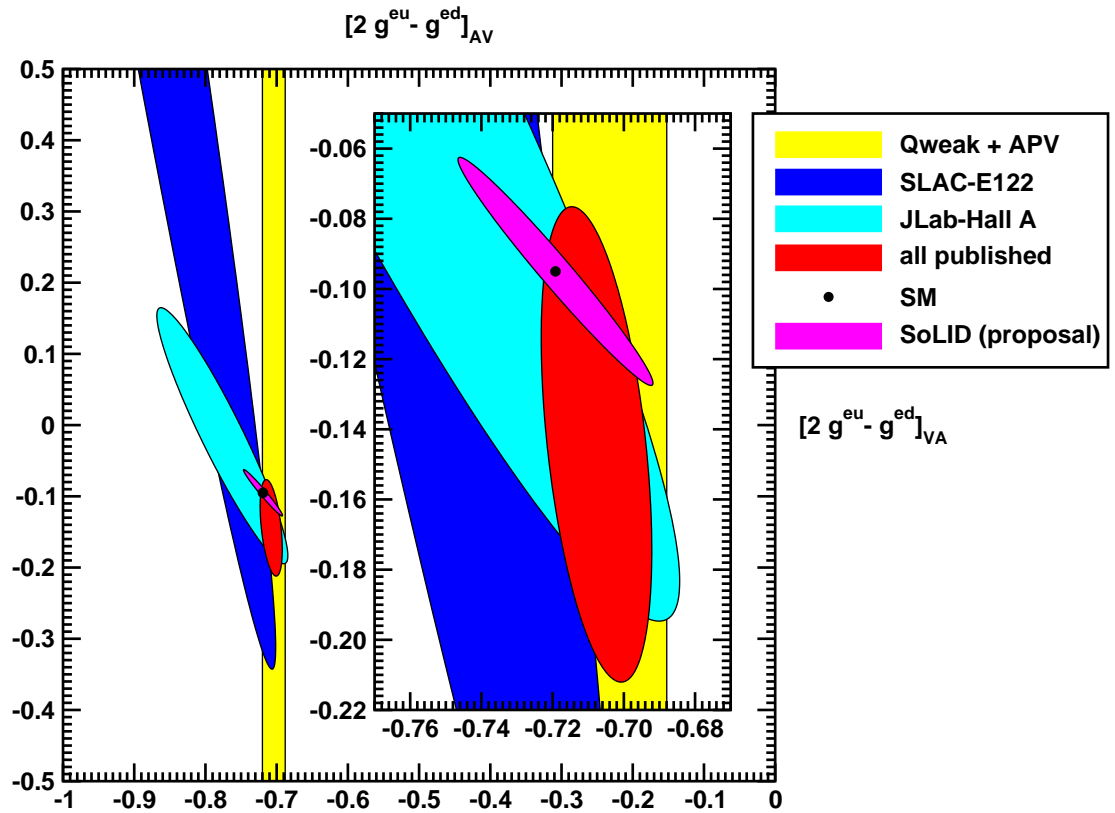


Figure 7: Results from the JLab PVDIS collaboration together with the projected results from the SoLID PVDIS experiment.

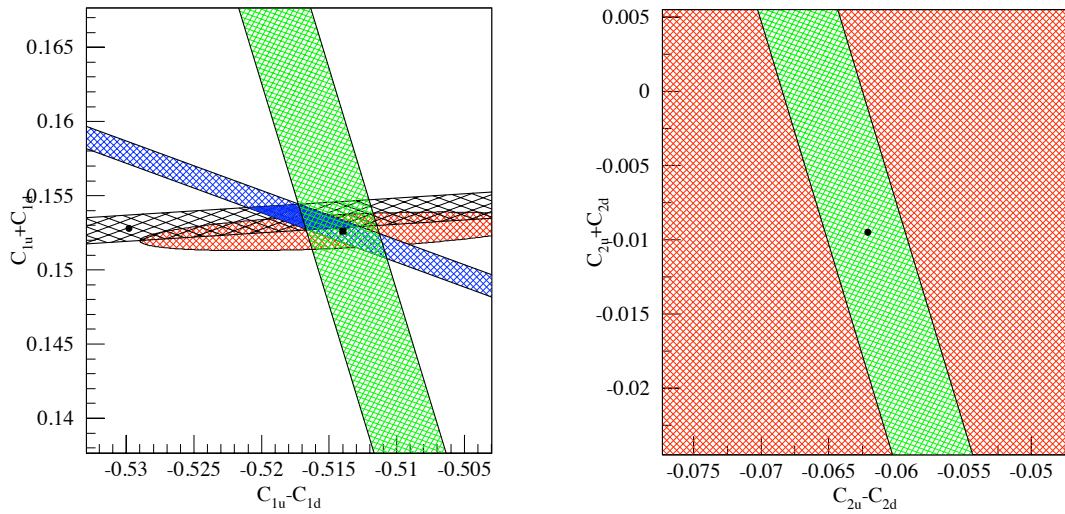


Figure 8: Green band: limits projected for this experiment. The blue band is the Qweak experiment and the black is the Cs APV.

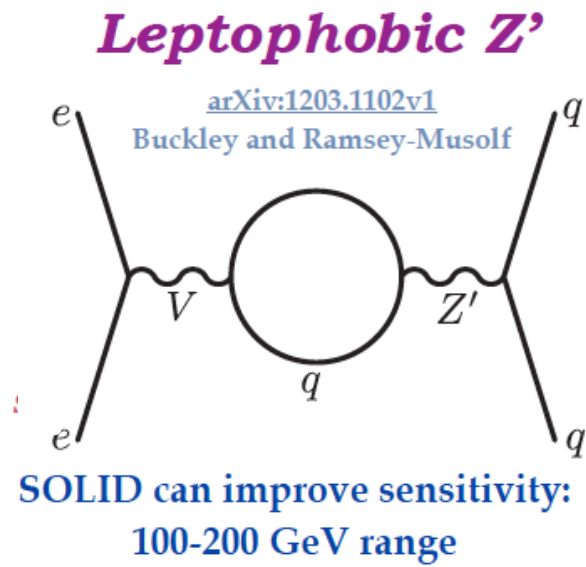


Figure 9: Diagram of a leptophobic Z' that can contribute to the C_{2i} and few other observables.

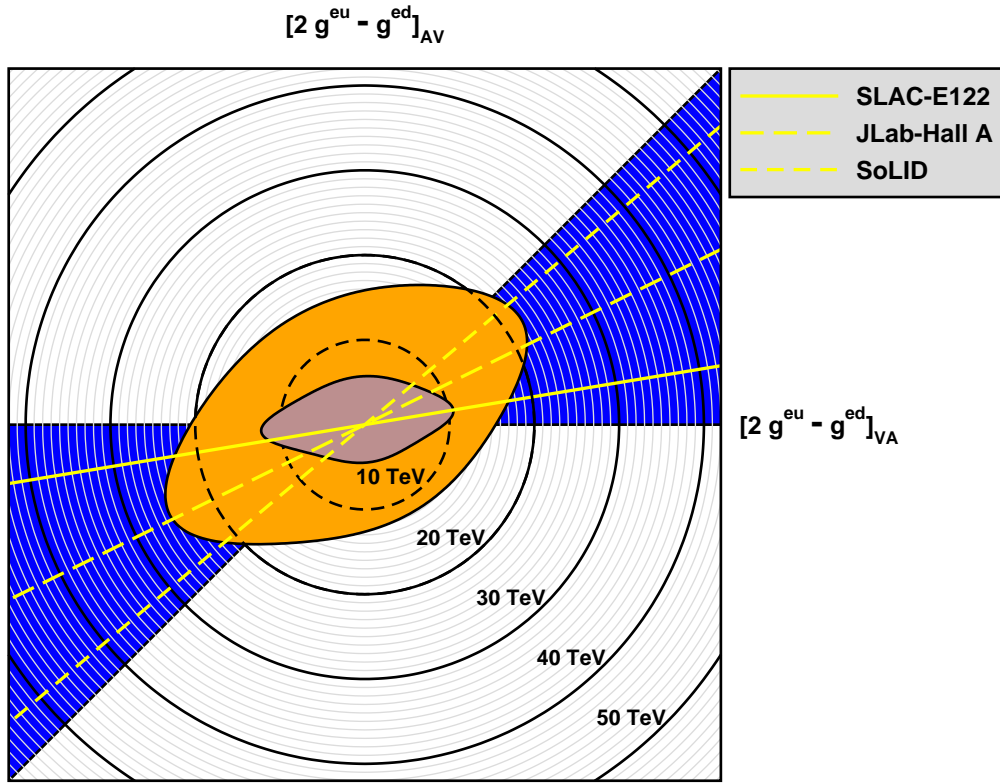


Figure 10: Polar plot for limits on composite models. The gray ellipse includes the published results from the PVDIS and Qweak collaborations. The orange ellipse gives the projected limits with the full Qweak statistics and the SoLID data.

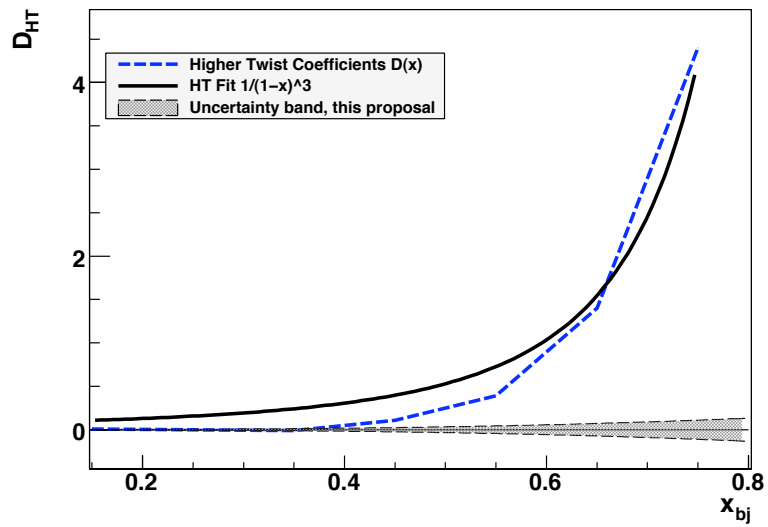


Figure 11: Possible contribution to A_{PV} due to CSV

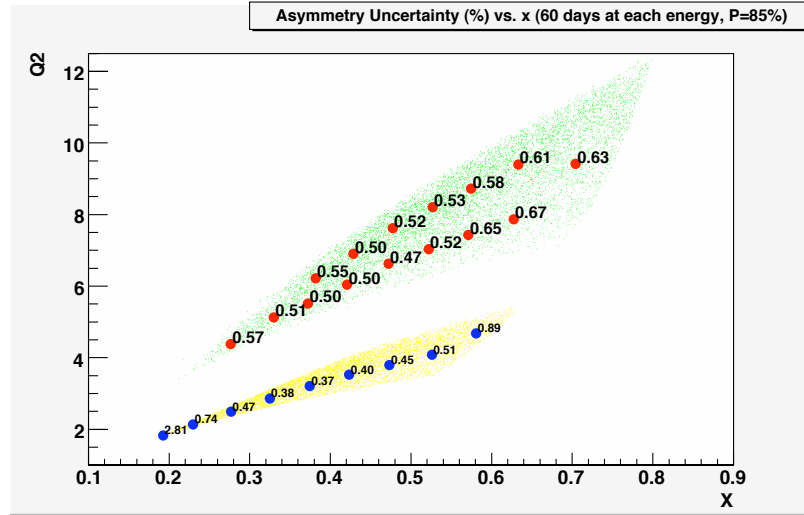


Figure 12: Anticipated statistical precision for Solid

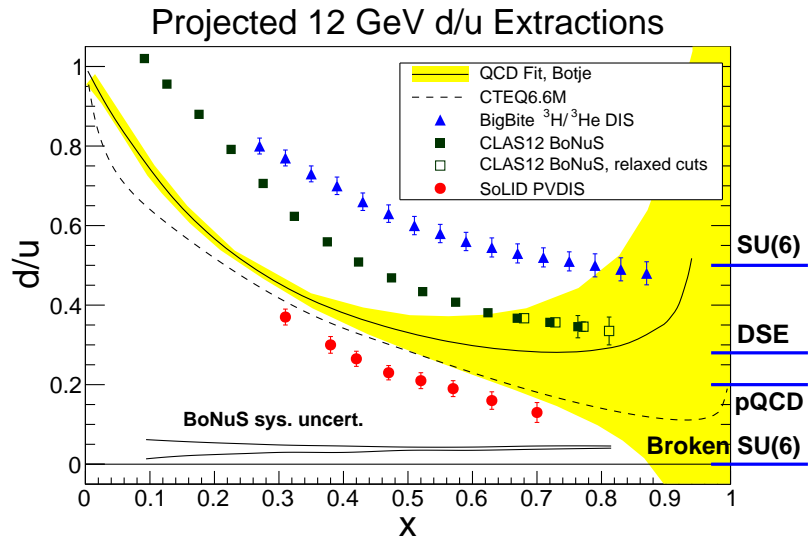


Figure 13: Anticipated precision for d/u measurement with Solid as well as other proposed experiments.

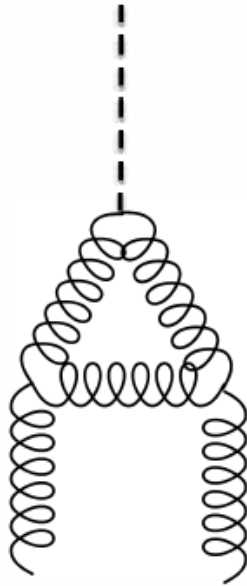


Figure 14: Anomaly diagram which dominate the cross section interaction at threshold.

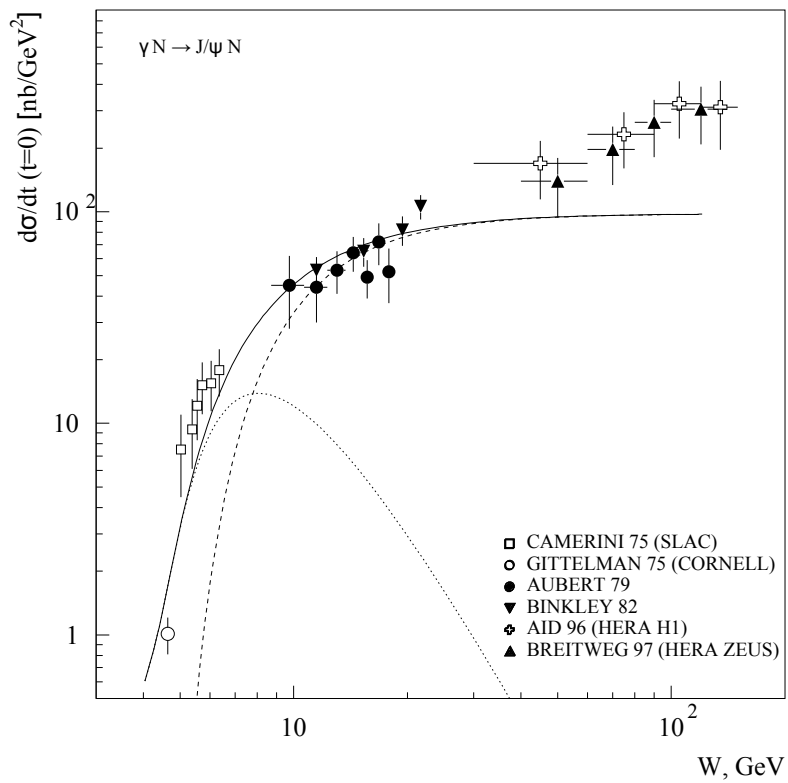


Figure 15: Forward J/Ψ photoproduction data compared to the results of [25] with (solid line) and without (dashed line) the real part of the amplitude.

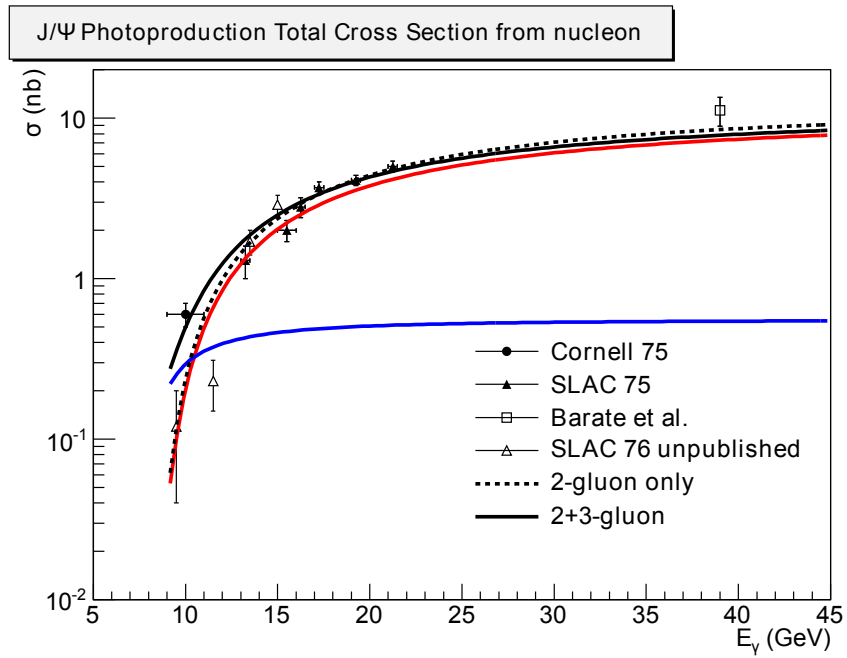


Figure 16: The 2-gluon model is shown as dotted black line. The (2+3)-gluon model is shown as solid black line. Furthermore, the 2-gluon contribution and 3-gluon contribution in the (2+3)-gluon model are shown as red and blue lines as well. Data are from “Cornell 75” [21], “SLAC 75” [20], “SLAC 76” [23] and “Barate et al.” [15].

J/Ψ Photoproduction Total Cross Section from nucleon

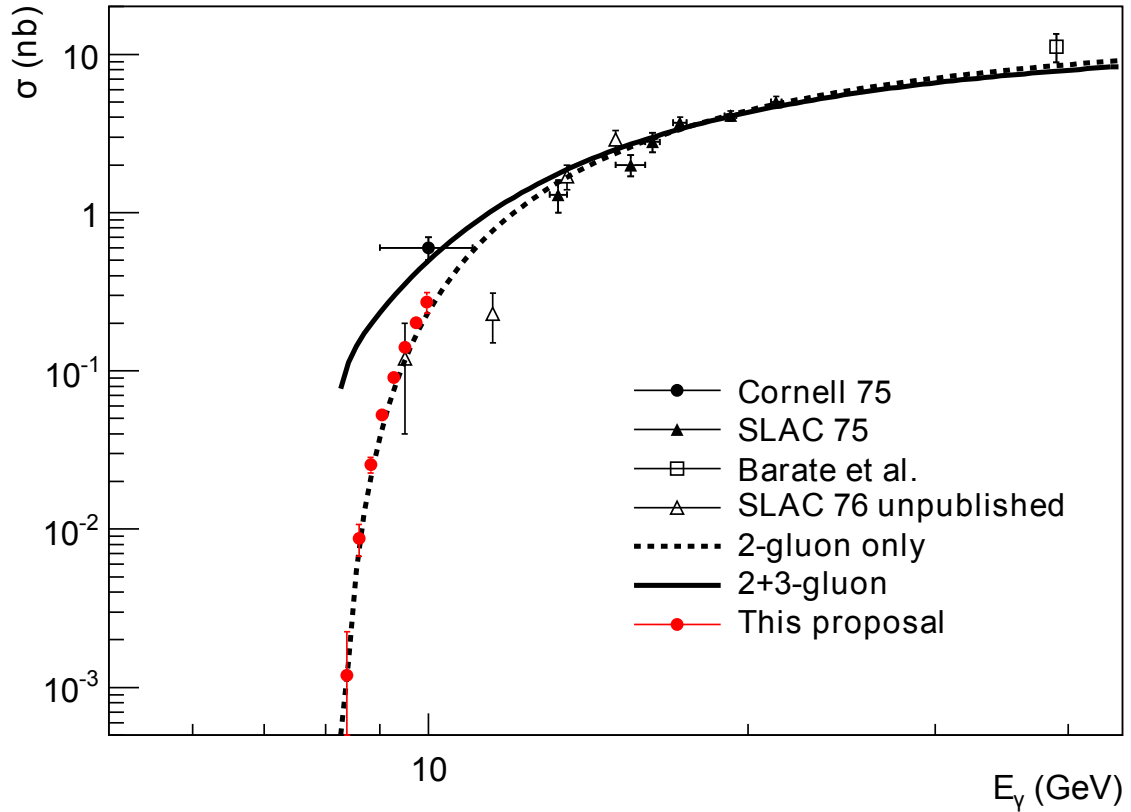


Figure 17: Projected uncertainties on total J/Ψ photoproduction cross section. Our projections are based on the 2-gluon exchange model. The central point of our projections are positioned at 1.2 times of the predicted total cross section of the 2-gluon exchange model in order to differentiate our projections from SLAC76 [23] points. The electroproduction data is plotted against effective photon energy.

2 Technical Requirements and Experimental Setup

2.1 Summary of Requirements

The minimum requirements of the base equipment for SoLID are summarized below and also listed in Table 1,

- Magnet: Out diameter is 3 meters (to fit in Hall A), inner diameter is 1 meter and length is greater than 3 meters. Field strength is greater than 1.35 Tesla and integrated BDL is 5 Tesla-meters. Acceptance in azimuthal angle (ϕ) is 2π , in polar angle (θ) is 8° to 24° for the SIDIS configuration and 22° to 35° for the PVDIS configuration. Momentum range is 1-7 GeV, and momentum resolution (combined with 100-micron tracking resolution) is 2%. Fringe field at the front end after endcap (shielding) is less than 5 Gauss (for polarized target operation).
- GEM Tracking Chambers: Six planes for SIDIS and five for PVDIS. Total area is 37 m^2 , total number of channels 165K. Tracking efficiency is greater than 90%. Radial position resolution reaches 0.1 mm. Works in high rate environment.
- EM Calorimeter: Shashlyk sampling (lead-scintillator/fiber) calorimeter. Total 1800 modules of shower (18 radiation length) and 1800 pre-shower (2 radiation length), with an area of 100 cm^2 for each module. In front of them are 300 pieces of scintillator pedal detectors (SPDs) with thickness of 5 mm. Energy resolution is $10\%/\sqrt{E}$. Reaches 50 : 1 π suppression with electron efficiency better than 90%. Reaches 5 : 1 photon suppression. Radiation hard (gain decreasing less than 20% after 400 KRad). Combined EC and Cherenkov for PVDIS trigger rate to be below 600 KHz (20 KHz/sector).
- Light Gas Cherenkov: 2-meter long of 1-atm CO_2 gas for SIDIS and 1-meter long with 1-atm $\text{C}_4\text{F}_8\text{O}$ (65%) mix with N_2 (35%) for PVDIS. Contains 60 mirrors and 270 PMTs. The total area is 20 m^2 . Provides the number of photo-electrons larger than 10 and the electron efficiency greater than 90%. π suppression is greater than 500 for momentum less than 4 GeV (SIDIS) or less than 3.2 GeV (PVDIS). Works in moderate field up to 200 Gauss (< 100 Gauss after Mu-metal shielding). Combined EC and Cherenkov for PVDIS trigger rate to be below 600 kHz (20 KHz/sector).
- Heavy Gas Cherenkov: 1-meter long 1.5-atm $\text{C}_4\text{F}_8\text{O}$ gas, with 30 mirrors and 480 PMTs. Total area is 20 m^2 (active 8.5 m^2) and the number of photo-electrons is greater than 10. With an efficiency for π better than 90%, Kaon suppression is greater than 10:1. Works in moderate field up to 200 Gauss (< 100 Gauss after Mu-metal shielding)
- MRPC: 50 super-modules, each of which contains 3 MRPC modules. There are totally 1650 strips and 3300 readout channels, covering an area of 10 m^2 . Timing resolution is better than 100 ps. Kaon suppression is about 20:1 for momentum from 2.5 to 7 GeV and Photon suppression is as good as 10:1. Works at a high rate up to 10 KHz/cm^2 .
- DAQ: 282 FADC sampling at 250 MHz. 32 high-speed pipeline VME switched Series (VXS) system. 30 GEM Scalable-read-out system (SRS). Can handle trigger rate of 100 KHz for SIDIS with event size of 2.6 KBytes and trigger rate of 600 KHz (20 KHz per sector) for PVDIS with event size of 48 KBytes
- Baffles: Eleven planes of lead blocks, 30 sectors in each plane, thickness of 9 cm, with azimuthal angle opening for each block to be more than 4° out of 12° ($360^\circ/30$). One

additional lead block with thickness of 5 cm is placed in front of the pre-shower at the small radius region ($110 \text{ cm} < r < 200 \text{ cm}$). The design is optimized to block low energy particle, photon and hadron background to an acceptable level (total trigger rate below 600 kHz for PVDIS configuration).

These requirements are resulted from the summary of the detector requirements of all approved experimental programs as in Table. 2. The key parameters of the approved programs are in Table 3. The experimental setup of SoLID-PVDIS, SoLID-SIDIS, and SoLID- J/ψ are shown in the next a few subsections, as in Fig. 24, Fig. 18, and Fig 26, respectively.

Table 1: Summary of Minimum Requirements of SolID Base Equipment. Items listed in brackets are particularly for SolID-PVDIS requirements.

Equipment	dimension/description	description	performance, eff	performance, rej	conditions
Magnet	OD 3m, ID 1m, L > 3m	B > 1.35 T, BDL > 5 T-m	2 π , 8 to 24° (22 to 35°)	P: 1-7 GeV, Res 2%	Fringe field < 5 G
GEMs	6 planes (5 planes)	Total 37 m ² , Chan 165K	Track Eff > 90%	Posi res 100 μ m	high rate
EM Calorimeter	1800 \times 100 cm ²	18 RL + 2 RL + 5 mm SPD	E res 10%, eff > 90%	50:1 π , 5:1 γ	rad hard
Light Cherenkov	2m CO2 (1m C4F8O/N2)	60 mirr, 270 PMTs, 20 m ²	γ -e > 10, Eff > 90%	π 500:1 < 4.5/3.2 GeV	100 G field
Heavy Cherenkov	1m 1.5 atm C4F8O	30 mirr, 480 PMTs, 20 m ²	γ -e > 10, Eff > 90%	K 10:1 2.5-7 GeV	100 G field
MRPC	50 \times 3 modules, 10 m ²	1650 strips, 3300 chan.	Time res < 100 ps	K 20:1 < 2.5 GeV, γ 10:1	high rate
DAQ	282 FADC @ 250 MHz	32 pipeline VXS, 30 SRS	Trig 100 KHz \times 2.6 KB	Trig 30 \times 20 KHz \times 48 KB	high noise
Lead Baffle	11 \times 30 blocks, 9 cm	5 cm, r 110-200 cm	area open ϕ > 4° / 12°	reduce background	

Table 2: Detector Summary for Approved Experiments

Experiments	PVDIS	SIDIS- ^3He	SIDIS-Proton	J/ψ
Target Length	LH ₂ /LD ₂ 40 cm	^3He 40 cm	NH ₃ 3 cm	LH ₂ 15 cm
Target Polarization	N/A	$\sim 60\%$	$\sim 70\%$	N/A
Target Spin Flip	N/A	≤ 20 mins	≤ 4 hours	N/A
GEM Tracking Chambers	5 chambers	6 chambers	6 chambers	6 chambers
E&M Calorimeter	Forward angle	Forward + Large angle	Forward + Large angle	Forward + Large angle
Light Gas Čerenkov	1 m long	2 m long	2 m long	2 m long
Baffles	Yes	N/A	N/A	N/A
Heavy Gas Čerenkov	N/A	1 m long	1 m long	N/A
MRPC (TOF)	N/A	100 ps resolution	100 ps resolution	100 ps resolution
Beam Polarimetry	0.4% determination	$< 3\%$	$< 3\%$	N/A
Target Polarimetry	N/A	$\sim 3\%$	$\sim 3\%$	N/A
DAQ	Single trigger	Coincidence trigger	Coincidence trigger	Coincidence trigger

Table 3: Summary of Key Parameters for Approved Programs

Experiments	PVDIS	SIDIS- ³ He	SIDIS-Proton	J/ψ
Reaction channel	$p(\bar{e}, e')X$	$(e, e'\pi^\pm)$	$(e, e'\pi^\pm)$	$e + p \rightarrow e' + J/\Psi(e^-, e^+) + p$
Approved number of days	169	125	120	60
Target	LH ₂ /LD ₂	³ He	NH ₃	LH ₂
Unpolarized luminosity (cm ⁻² s ⁻¹)	$0.5 \times 10^{39} / 1.3 \times 10^{39}$	$\sim 10^{37}$	$\sim 10^{36}$	$\sim 10^{37}$
Momentum coverage (GeV/c)	2.3-5.0	0.8-7.0	0.8-7.0	0.6-7.0
Momentum resolution	$\sim 2\%$	$\sim 2\%$	$\sim 2\%$	$\sim 2\%$
Polar angle coverage (degrees)	22-35	8-24	8-24	8-24
Polar angle resolution	1 mr	0.6 mr	0.6 mr	0.6 mr
Azimuthal angle resolution	-	5 mr	5 mr	5 mr
Trigger type	Single e^-	Coincidence $e^- + \pi^\pm$	Coincidence $e^- + \pi^\pm$	Triple coincidence $e^- e^- e^+$
Expected DAQ rates	~ 20 kHz $\times 30$	< 100 kHz	< 100 kHz	< 10 kHz
Backgrounds	Negative pions, photons	$(e, \pi^- \pi^\pm)$ $(e, e' K^\pm)$	$(e, \pi^- \pi^\pm)$ $(e, e' K^\pm)$	B-H process Random coincidence
Major requirements	Radiation hardness 0.4% Polarimetry π^- contamination Q^2 calibration	Radiation hardness Detector resolution Kaon contamination DAQ	Shielding of <i>sheet-of-flame</i> Target spin flip Kaon contamination	Radiation hardness Detector resolution

2.2 SoLID-³He-SIDIS Experiments

The E12-10-006 [2] (E12-11-007 [3]) is designed to measure the single/double spin asymmetries through the semi-inclusive deep-inelastic scattering (SIDIS) ($e, e'\pi^\pm$) with the SoLID spectrometer and the transversely (longitudinally) polarized ³He target. The layout of the experiment is shown in Fig. 18 and Fig. 19. The entire detector system consists of two parts: the forward-angle detectors and the large-angle detectors.

At forward angle, there are five layers of GEM detectors inside the coils to provide the forward-angle tracking, and the first three of them are shared with the large-angle detectors. A 2.04 m long light gas Čerenkov counter is installed after the GEM detectors to discriminate the scattered electrons from the produced pions. A 90 cm long heavy gas Čerenkov counter right after the light gas Čerenkov counter can separate kaons and protons from the pions at momenta larger than 2.5 GeV/c. One layer of Multi-gap Resistive Plate Chamber (MRPC) is placed after the heavy gas Čerenkov counter to provide timing information and particle identification of hadrons at low momentum (< 2.5 GeV/c), as well as to suppress photon background. A “Shashlyk”-type forward-angle Electromagnetic calorimeter (FAEC) will be used for electron/pion separation. One layer of scintillator pad detector (SPD) is placed in front of the FAEC to reject photons and reduce the calorimeter-based trigger rates. The polar angular coverage for the forward-angle detectors ranges from 8° to 14.8° and the momentum coverage extends from 0.8 GeV/c to 7.0 GeV/c. A combination of the FAEC, the gas Čerenkov counter, and the MRPC will be used for electron and pion identifications.

To cover the large electron scattering angles, there are four layers of GEM detectors placed inside the coils, with the last three layers shared with the forward angle detectors. Following a layer of SPD, another “Shashlyk”-type large-angle Electromagnetic calorimeter (LAEC) will be placed inside the coils to detect electrons and hadrons. A low energy background absorber locates between the fifth and the sixth GEMs, and another absorber is placed close to the beam line near the light gas Čerenkov counter. These absorbers will be used to protect the forward detectors from low energy background. The large-angle detectors are mainly used for electron detection in a momentum range of 3.5-6.0 GeV/c where the expected π^-/e ratio smaller than 1.5. The polar angle coverage ranges from 15.7° to 24° for the momentum range.

The standard Hall A polarized ³He target will be used in its transverse mode. A higher than 60% target polarization with a faster than 20 minutes target spin flip is expected at the full polarized luminosity of 10^{36} N cm⁻² s⁻¹, which is corresponding to the unpolarized luminosity of 10^{37} N cm⁻² s⁻¹. The target polarization is expected to be limited by the magnetic field gradient in the target region, which is dominated by the leakage field from the SoLID magnet. Therefore, the design of the magnet yokes is important to achieve the required target polarization. As shown in Fig. 18 and Fig. 19, the target will be located about 80 cm upstream of the front yoke. Target collimators will be placed close to the end caps of the 40 cm long target in order to reduce backgrounds generated from both endcaps. The expected kinematic coverage includes: i) $0.05 < x < 0.6$ which comprises the majority of the valence quark region; ii) $0.3 < z < 0.7$ in which the leading order $x-z$ factorization is expected to hold; iii) maximum pion transverse momentum P_T up to 1 GeV/c, where the TMD framework is valid; and iv) $1 \text{ GeV}^2 < Q^2 < 8 \text{ GeV}^2$ with about 2 GeV^2 coverage in ΔQ^2 at fixed x . These kinematic coverages can be achieved by combining data with incident electron energies of 11 and 8.8 GeV.

In order to achieve the proposed precision in asymmetries, the negative pion contamination in the electron sample needs to be controlled to below 1%. At forward angle, it is achieved by a combination of the FAEC and the light gas Čerenkov detector. At large angle, the LAEC alone will be enough to provide the required pion rejection, since the expected pion to electron ratio is small. Furthermore, the coincidence detection of electron and leading pion in the SIDIS kinematics would

SoLID CLEO SIDIS

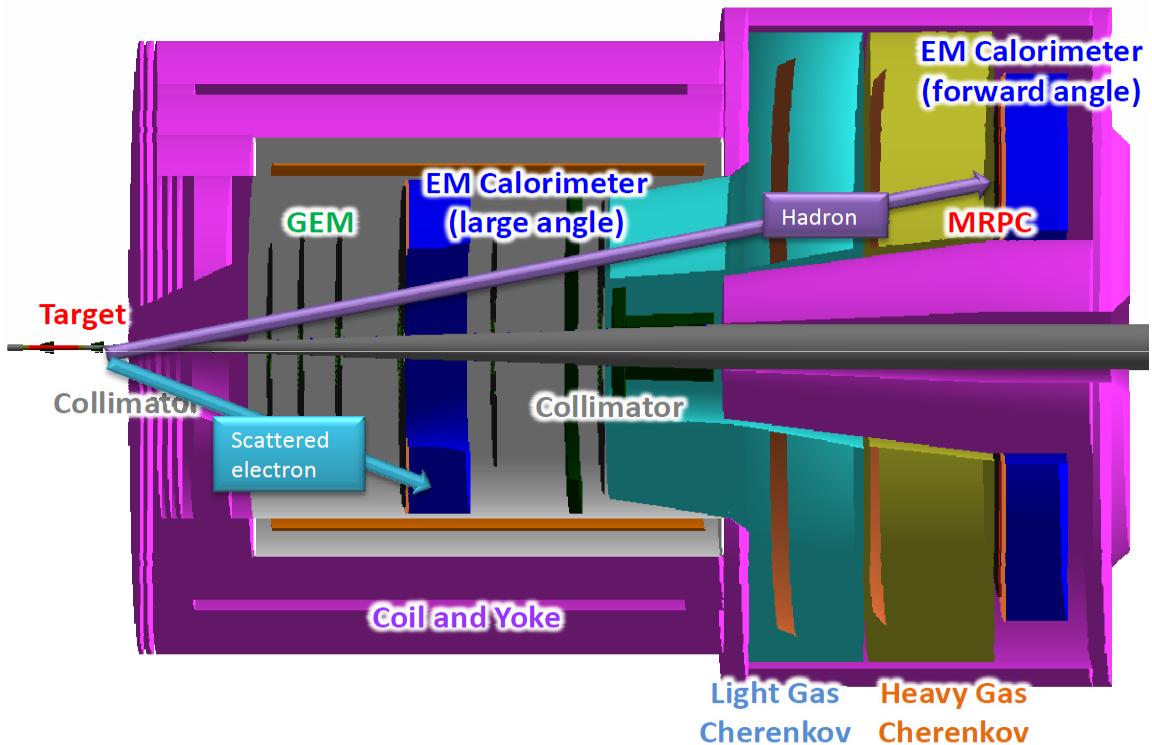


Figure 18: The experimental layout of the SoLID SIDIS based on the CLEO magnet. The scattered electrons are detected by both forward-angle and large-angle detectors. The leading pions are detected by the forward-angle detector only. The polarized ${}^3\text{He}$ (or NH_3) target will be placed upstream in front of the spectrometer entrance.

further reduce the pion contamination in the electron sample.

The particle identification of the leading pion (forward angle detector only) will be achieved by a combination of time-of-flight (TOF) from the MRPC and the heavy gas Čerenkov detector. The electron, kaon, and proton contaminations in the pion samples are all required to be kept below the 1% level. The electron rejection will be achieved by the combination of the FAEC and the light gas Čerenkov counter. With the expected 100ps TOF resolution from the MRPC, a separation of 3 standard deviations (6 standard deviations from peak to peak) between pions and protons can be achieved for momenta up to $4\text{ GeV}/c$. Pions with momenta higher than $2.5\text{ GeV}/c$ will trigger the heavy gas Čerenkov detector, while the momentum threshold for kaons to trigger the same detector is $7.6\text{ GeV}/c$. Therefore, the heavy gas Čerenkov detector would provide additional rejection of protons when the pion momenta are larger than $2.5\text{ GeV}/c$. For pions with momenta below $2.5\text{ GeV}/c$, the TOF would provide a separation better than 2 standard deviations (4 standard deviations from peak to peak) between pions and kaons. Since the kaon to pion ratio is expected to be about 0.1, a combination of the TOF and the heavy gas Čerenkov detector would easily satisfy the requirement of below 1% kaons contamination.

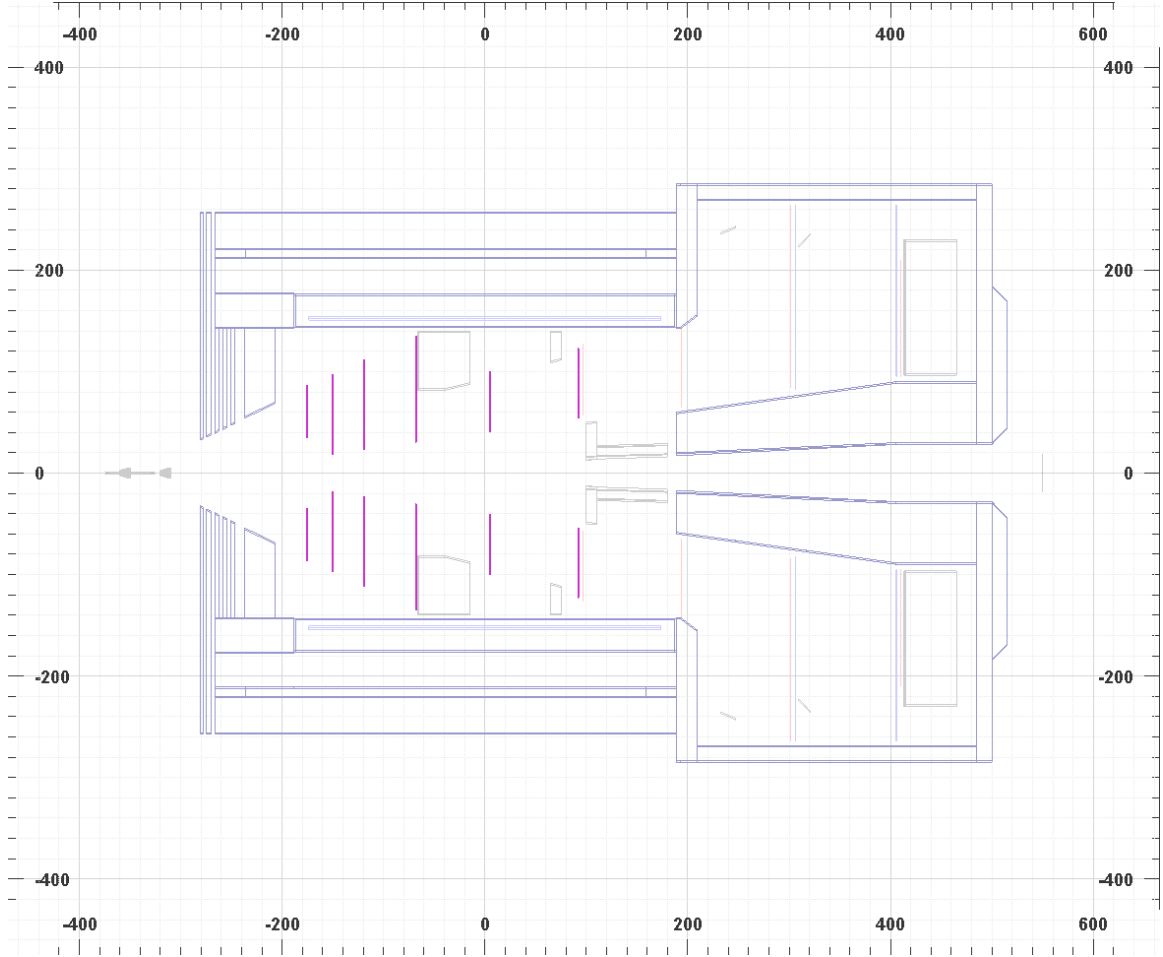


Figure 19: A 2D representation of the experimental layout of SoLID SIDIS ^3He .

The extraction of various TMD asymmetries relies on the ϕ_S and ϕ_h angular dependence of the measured single/double spin azimuthal asymmetries in each kinematic bin of the 4-D (x , Q^2 , z , and P_T) phase space. Since the kinematics of interests are in the deep-inelastic-scattering (DIS) region, the requirements on the resolution of the reconstructed kinematic variables are modest. For example, a better than a few percent momentum resolution, a better than 1 mr polar angular resolution, a better than 10 mr azimuthal angular resolution, and a 1-2 cm reconstructed vertex resolution would satisfy the needs of these experiments. Fig. 20 shows the expected momentum and angular resolution for different polar angles and momentum ranges. The position resolution of the GEM chambers is assumed to be $100\mu\text{m}$, and the angle between the u/v readout strips is assumed to be 10° . Furthermore, the effects of multiple scattering due to the finite thickness of the GEM chambers and the air in the SoLID spectrometer are taken into account. The average momentum resolution, the average polar angular resolution, and the average azimuthal angular resolutions are about 2%, 0.6 mr, and 5 mr, respectively. These expected resolutions will satisfy our requirements.

With similar reaction channels, E12-10-006 [2], E12-11-007 [3], and E12-11-108 [4] (see next section) will share the same design of the DAQ system. The required overall luminosity of E12-10-006 and E12-11-007 is $10^{37} \text{ N/cm}^2\text{s}^{-1}$, which is an order of magnitude higher than that of E12-11-108. The goal of the SIDIS DAQ is to satisfy the requirement of $\sim 100 \text{ kHz}$ single electron-like

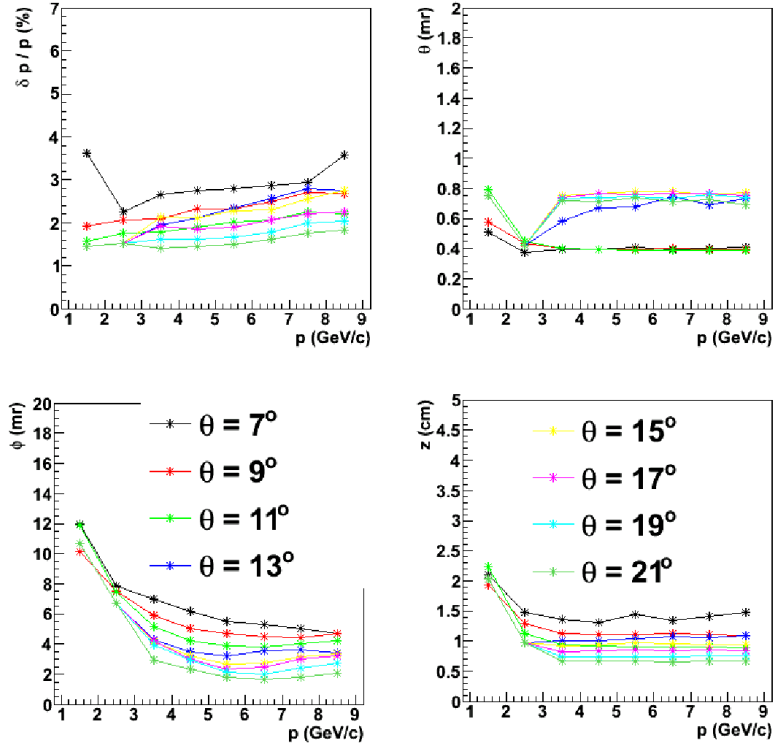


Figure 20: The expected momentum, angular and interaction vertex resolution for SoLID. The position resolution of the GEM chambers is assumed to be $100 \mu\text{m}$. The angle between u/v readout strip is assumed to be 10 degrees.

(background particles which are misidentified as electrons) trigger rate.

The SIDIS process requires the detection of both the scattered electron and the leading pion. Therefore, a single electron trigger or a coincidence trigger of electron and hadron would satisfy this need. The electron trigger at the large-angle detectors will be provided by the LAEC at an energy threshold of about 3 GeV. Such a trigger would be sensitive to both high energy electrons and high energy photons (mostly from the π^0 decay). With the SPD and the MRPC being incorporated into the trigger, the electron-like triggers can be significantly suppressed.

The electron trigger at the forward angle detector will be formed by a coincidence between the gas Čerenkov detector, the FAEC, the SPD and the MRPC. Considering the kinematic information of the scattered electrons from the DIS process (e.g. $Q^2 > 1 \text{ GeV}^2$), a position dependent energy threshold with a low limit at 0.8 GeV in FAEC could significantly reduce the trigger rate. A 400 suppression factor from the FAEC and the gas Čerenkov detector was included in calculating the pion rate.

The charged hadron trigger at the forward angle will be formed with a coincidence between the FAEC and the MRPC. The coincidence trigger is given by overlapping the electron trigger and the hadron trigger within a 30 ns window. If the SIDIS DAQ design can not satisfy the requirement of ~ 100 kHz trigger rate, the coincidence trigger could retain more SIDIS events. Therefore, it is important to include the coincidence trigger in the baseline design of the SIDIS DAQ system. A more detailed discussion of the SIDIS trigger rates is given in Section 12.

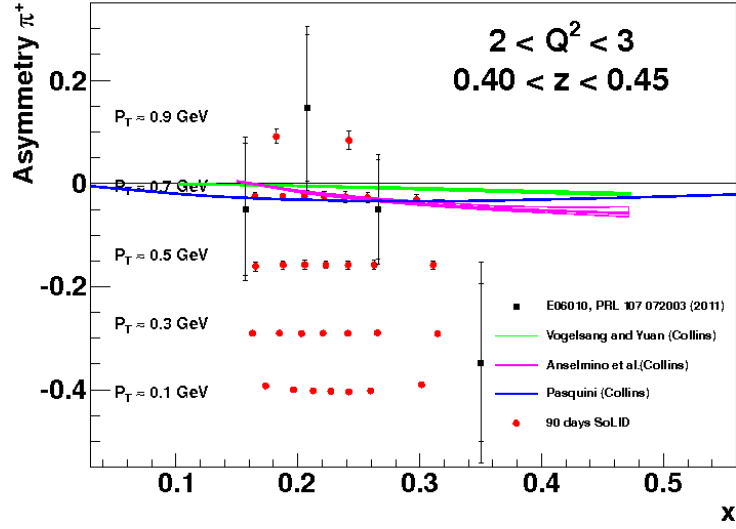


Figure 21: 12 GeV Projections with SoLID. π^+ Collins/pretzelosity asymmetries at $0.45 > z > 0.4$, $3 > Q^2 > 2$. 6 GeV results [9] are shown together with calculations from Ref. [5, 7, 8].

The projections combine both 11 GeV data and 8.8 GeV data. The projected results for π^+ Collins and pretzelosity asymmetries at one typical kinematic bin, $0.45 > z > 0.4$, $3 > Q^2 > 2$, are shown in Fig. 21 together with theoretical predictions of Collins asymmetries from Anselmino *et al.* [5], Vogelsang and Yuan [7] and predictions of Collins asymmetries from Pasquini [8]. The 6 GeV results [9] are shown as black squares. The x -axis is x_{bj} . The y -axis shows the scale of the asymmetry. Each line of red points represents a particular P_T bin whose central value is labeled in the plot.

2.3 SoLID-proton-SIDIS Experiment

The E12-11-108 [3] is designed to measure the single/double spin asymmetries through the semi-inclusive deep-inelastic scattering (SIDIS) ($e, e'\pi^\pm$) with the SoLID spectrometer and a transversely polarized proton target. The overall luminosity in this case is smaller compared to that of using the polarized ^3He target.

An improved version of JLab/UVa/SLAC polarized NH_3 target (shown in Fig. 22) will be used. The main upgrade is to replace the aging Helmholtz-coil magnet with a new magnet and to have a fast spin-flip capability with the AFP technique to minimize the systematic uncertainty in the single spin asymmetry measurement. In order to satisfy the requirements of phase space coverage, the new design will further allow both transverse and longitudinal direction to have a nominal forward opening of more than $\pm 25^\circ$, while maintaining the same maximum field (5 Tesla) and a uniform field region in the center. The target polarization is required to be higher than 70% with the spin flip every few hours.

Due to the large magnetic field in the transverse direction, this experiment suffers from a different kind of background compared to the low field polarized ^3He experiment, known as *sheet-of-flame*. The main feature of such a background is that a very high rate of charged particles with momentum range between 1-2 GeV will be localized in a very narrow region of the acceptance.

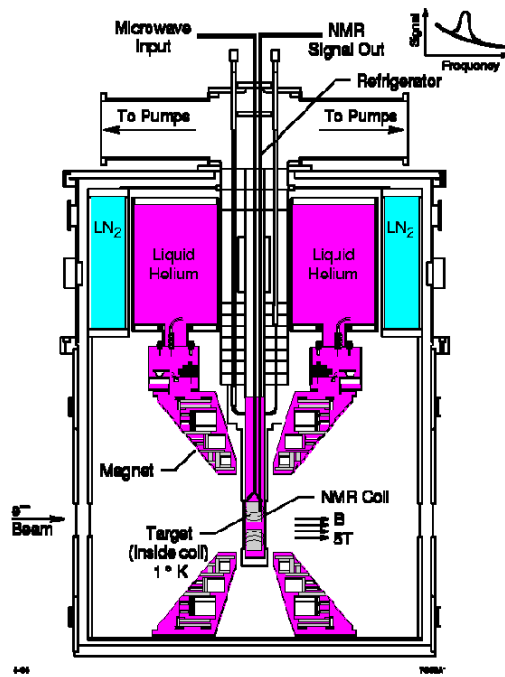


Figure 22: Polarized target system.

Fig 23 shows this background on all six GEM planes in the SoLID. The GEM chambers in regions outside of the *sheet-of-flame* location see a background rate of less than 1.0 KHz/mm² on, whereas the regions inside have much higher rates. In order to handle this background and avoid damage to the apparatus, detector sectors in the direct line-of-sight of this *sheet of flame* will be removed or turned off during the proton experiment.

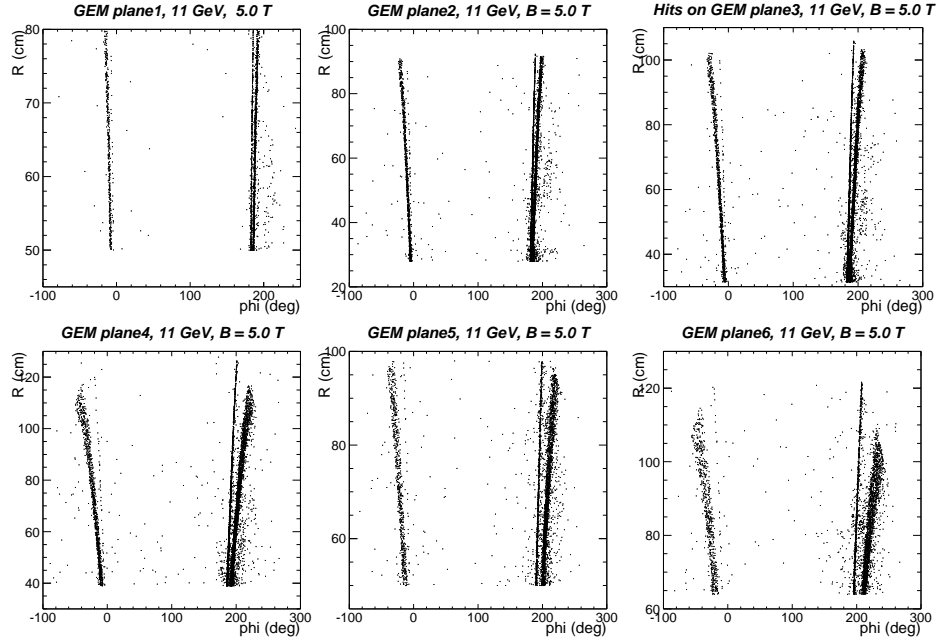


Figure 23: GEANT3 simulation results of background with NH_3 target field ON. The x -axis is the azimuthal angle in lab frame. The y -axis is the radius of GEM chambers (1-6). Narrow regions of high rate (compared to rest of the acceptance) are clearly seen as a function of azimuthal angle ϕ .

2.4 SoLID-PVDIS Experiment

The E12-10-007 [1] is designed to measure the parity violating asymmetries (A_{PV}) through the inclusive deep-inelastic scattering (DIS) $p(\vec{e}, e')X$ with the SoLID spectrometer. The layout of the experiment is shown in Fig. 24 and Fig. 25. In order to eliminate high energy ($\sim \text{GeV}$) photons, a lead baffle will be placed downstream of the target to block direct lines of sight to the detector system. The detector system consists of four layers of GEM chambers for particle tracking, a 107 cm long light Gas Čerenkov counter for electron/pion separation, and a “shashlyk”-type electromagnetic calorimeter system for the trigger and additional electron/pion separation. The GEM chambers will be divided into two groups, with one group placed in front of the Gas Čerenkov counter and the other group behind it. Such configuration will maximize the detector resolution, leading to about 2% momentum and 1 mrad polar angle resolutions. The entire detector system will be divided into 30 independent sectors in the azimuthal angle.

The polar angle and momentum coverages of the detector system are from 22° to 35° on an extended (40 cm) target and from 1.5 GeV/c to 5 GeV/c, respectively. These coverages transform into kinematic coverages of $0.2 < x < 0.8$ and $2 (\text{GeV}/c)^2 < Q^2 < 12 (\text{GeV}/c)^2$. The overall luminosity is required to be larger than $5 \times 10^{38} \text{ N cm}^{-2} \text{ s}^{-1}$ in order to reach about 0.5% relative statistical uncertainties on the parity violating asymmetries A_{PV} in each of the kinematic bin (see Fig. 12). Such a high luminosity places specific requirements on the radiation hardness of the detector system.

SoLID CLEO PVDIS

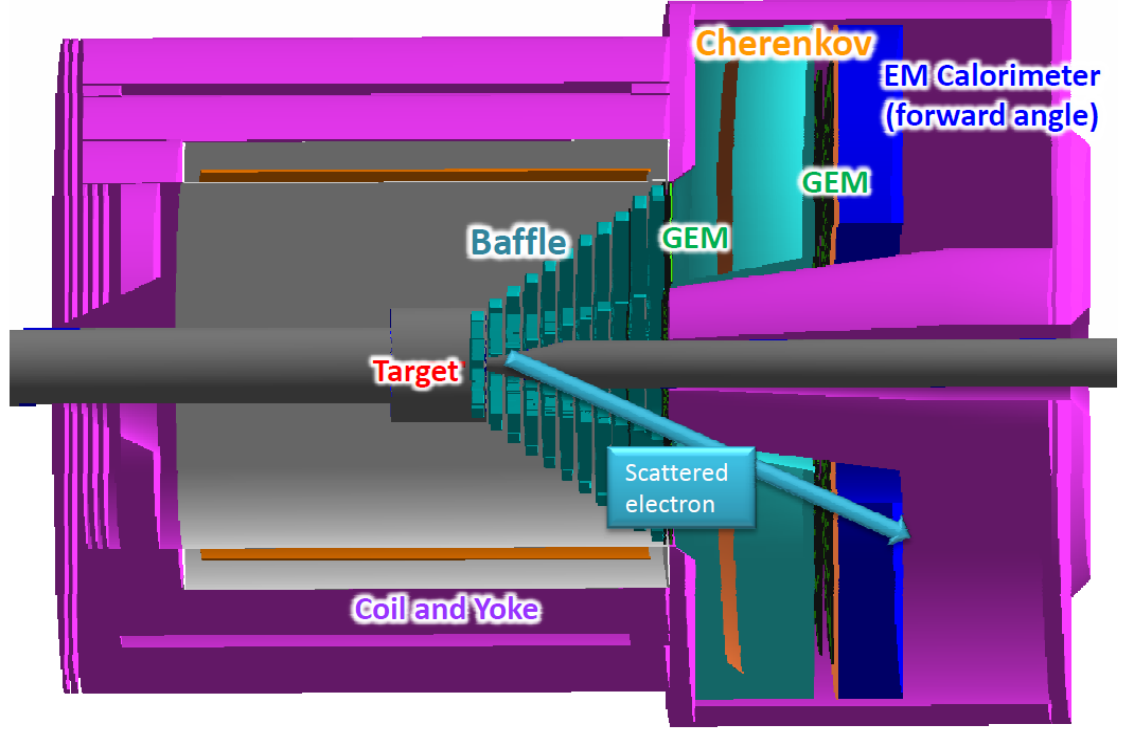


Figure 24: The experimental layout of SoLID PVDIS based on the CLEO magnet. The arrow shows a scattered electron.

To leading order, the physics asymmetry A_{PV}^{phys} is related to the measured asymmetry $A_{PV}^{measured}$ as:

$$A_{PV}^{phys} \sim \frac{1}{Q^2 \cdot P_{beam}} \cdot \frac{A_{PV}^{measured} - f \cdot A_{PV}^{\pi^-}}{1 - f}. \quad (12)$$

where P_{beam} is the polarization of the electron beam, f and $A_{PV}^{\pi^-}$ are the pion contamination and the parity violating asymmetry of pions, respectively. The proposed high precision measurement of A_{PV} (about 0.5% in each kinematic bin) requires high accuracy. The uncertainty of the electron beam polarization is required to be smaller than 0.4%. Since A_{PV} for produced pions is expected to be similar to that of scattered electrons, the contamination of negative pions in the electron sample needs to be determined to about a 10^{-3} level. Furthermore, the uncertainty in Q^2 also requires to be controlled to below 0.1% using a precise and comprehensive optics calibration program.

Since only the scattered electrons are detected in this experiment, each sector of the detector system can employ an independent DAQ system. Thus the requirement on the DAQ system for this experiment is modest. The average trigger rate for each sector is estimated to be less than 20 kHz, leading to a total trigger rate to be less than 600 kHz.

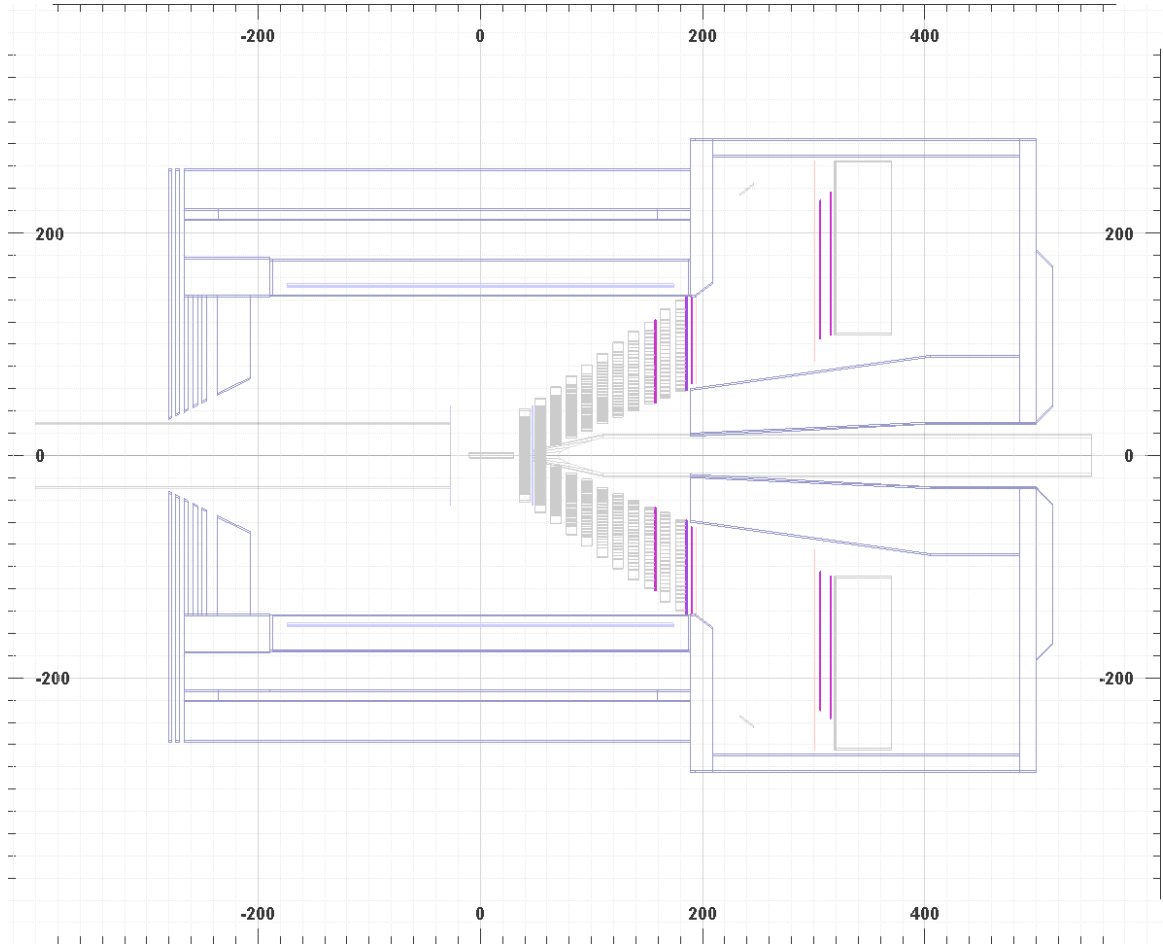


Figure 25: A 2D representation of the experimental layout of SoLID PVDIS.

2.5 SoLID- J/ψ Experiment

The E12-12-006 experiment [16] is designed to measure the cross section of J/Ψ electroproduction near threshold. The reaction of interest is $e + p \rightarrow e' + J/\Psi(e^-, e^+) + p$ where J/Ψ is detected through its decay in a lepton pair (e^+, e^-) with 5.94% branching ratio. Primary detection channels include a 4-fold coincidence, which consists of a detection of the scattered electron, the recoil proton, and the leptonic pair (e^+e^-) from the J/Ψ decay, and a 3-fold coincidence, which is similar to the 4-fold coincidence but without the proton detection. In the 3-fold coincidence channel, the full kinematics of the recoil proton can be reconstructed through energy and momentum conservation. Since the recoil proton is not detected, the total number of events and the kinematic coverage are greatly enhanced compared to the 4-fold coincidence channel. Possible background in the 3-fold coincidence channel can be investigated fully with the 4-fold coincidence channel which offers a better signal to noise ratio. Because the electrons, positrons, as well as protons are required to be detected in coincidence, the configuration of SoLID will be similar to that of SoLID-SIDIS. Fig. 26 and Fig. 27 illustrates the layout of the experiment and the particle detection scheme of the 4-fold coincidence. The scattered electron and the recoil proton will be detected by the forward angle detector, while the electron-positron pair from J/Ψ decay will be mostly detected by the large-angle detector. Compared to the SoLID-SIDIS setup, the polarized target will be replaced by the

SoLID CLEO J/ψ

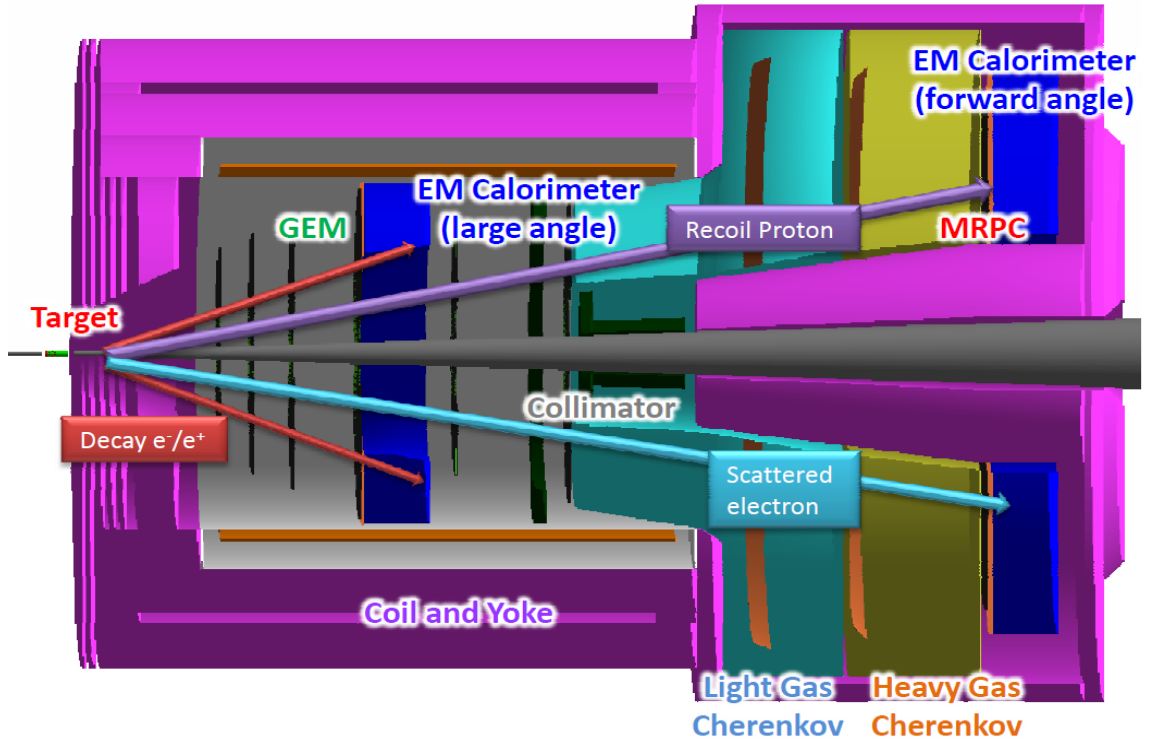


Figure 26: The experimental layout for the SoLID- J/ψ . The sub-detectors are labeled and the four final state particles are illustrated with arrows. The scattered electron and recoil proton are detected by the forward angle detector. The electron-positron pair from J/ψ decay is primarily detected by the large-angle detector.

standard Hall A 15 cm liquid Hydrogen target, but its position will be located about 30 - 40 cm more downstream relative to the target center of the SoLID-SIDIS setup to improve the acceptance.

The approved beam time for this experiment is 60 PAC days at an unpolarized luminosity of 10^{37} $\text{N cm}^{-2} \text{s}^{-1}$. The kinematic coverage will be $4.05 \text{ GeV} < W < 4.45 \text{ GeV}$ and $|t - t_{min}| < 2.5 \text{ GeV}^2$. Depending on the cross section model, the expected physics counts with 50 days production data for 4-fold (3-fold) coincidence range from $\sim 0.7\text{k}$ (2.1k) to $\sim 2.9\text{k}$ (8.1k) at the proposed luminosity. Since this measurement is limited by statistics due to the rare nature of the J/ψ production near threshold process, a higher luminosity ($> 10^{37} \text{ N cm}^{-2} \text{ s}^{-1}$) is strongly desired.

The primary trigger is a triple coincidence of scattered electron, J/ψ decay electron, and J/ψ decay positron. With a 100 ns coincidence window, the trigger rate would be dominated by the random coincidence events with a rate of about 3 kHz, which is far below the required ~ 100 kHz trigger rate of SoLID-SIDIS. Therefore, the main requirement of SoLID- J/ψ is the capability of forming hardware coincidence trigger.

Since we are interested in the exclusive electroproduction of J/ψ , the resolution of the SoLID spectrometer is important in rejecting different backgrounds. The resolution of the SoLID spec-

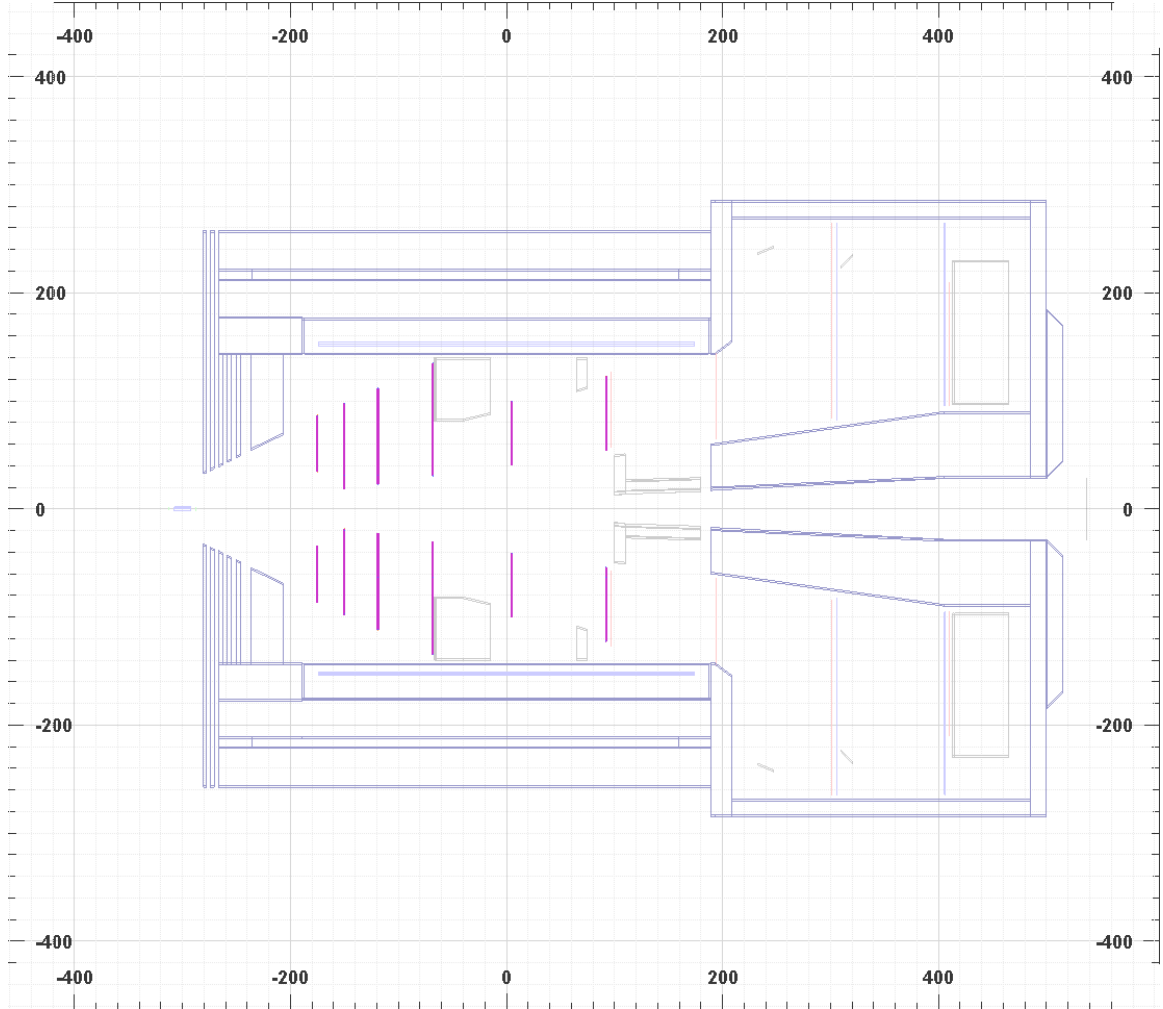


Figure 27: A 2D representation of the experimental layout of SoLID J/ψ .

trometer has been studied extensively by the SoLID-SIDIS collaboration [1]. Fig. 20 shows the expected momentum and angular resolution for different polar angles and momentum ranges. The average momentum resolution, the average polar angular resolution, and the average azimuthal angular resolution are about 2%, 0.6 mr, and 5 mr, respectively. These expected resolution would satisfy the requirement of this experiment.

The particle identification of the recoil proton for the 4-fold coincidence relies on the time-of-flight (TOF) from the MRPC. The highest momentum of the recoil proton is about 3 GeV/c. With the designed 100 ps resolution in TOF, protons can be separated from kaons at 2 standard deviations (4 standard deviations from peak to peak). In addition, protons can be separated from pions at 6 standard deviations (12 standard deviations from peak to peak). The requirement on the exclusive kinematics in the off-line data analysis would further strengthen the particle identification of protons.

There are two major types of backgrounds. The main physics background originates from the Bethe-Heitler (B-H) process. At the proposed kinematics, the B-H background is expected to be

smaller than the physics J/ψ events by 1-2 order of magnitude in average ². The cross section associated with the B-H background can be directly measured by choosing the invariant mass of the electron-positron pair to be away from the J/ψ peak. The other major background is the random coincidence of a J/ψ (normally photo-produced) and a scattered electron. The random coincidence background is expected to be 1-2 orders of magnitude smaller than the physics events with the proposed setup. In addition, the random coincidence backgrounds can also be directly measured/subtracted through the commonly used off-window method. The projected results are shown in Fig. 17.

References

- [1] E12-10-007 “Precision Measurement of Parity-violation in Deep Inelastic Scattering Over a Broad Kinematic Range” Contact person: P. Souder.
- [2] E12-10-006, “Target Single Spin Asymmetry in Semi-Inclusive Deep-Inelastic ($e, e'\pi^\pm$) on a Transversely Polarized ^3He Target at 8.8 and 11 GeV”, Spokesperson: J.-P. Chen, H. Gao (contact), X. Jiang, J.-C. Peng, and X. Qian.
- [3] E12-11-007, “Asymmetries in Semi-Inclusive Deep-Inelastic ($e, e'\pi^\pm$) Reactions on a Longitudinally Polarized ^3He Target at 8.8 and 11 GeV”, Spokesperson: J.-P. Chen, J. Huang (contact), Y. Qiang, and W.-B. Yan.
- [4] E12-11-108 “Target Single Spin Asymmetry in Semi-Inclusive Deep-Inelastic ($e, e'\pi^\pm$) on a Transversely Polarized Proton Target”, Spokespersons: K. Allada, J.-P. Chen, H. Gao (contact), Z.-E. Meziani, and X.-M. Li.
- [5] M. Anselmino and A. Prokudin, *private communications*. Predictions are based on the extractions of Ref. [6].
- [6] M. Anselmino *et al.*, proceedings of the XVI International Workshop on Deep Inelastic Scattering and Related Subjects, DIS 2008, London, U.K. 2009. e-Print: arXiv:0807.0173.
- [7] W. Vogelsang and F. Yuan, *private communications*.
- [8] B. Pasquini, *private communication*.
S. Boffi, A. V. Efremov, B. Pasquini and P. Schweitzer, Phys. Rev. **D79**, 094012 (2009) arXiv:0903.1271.
- [9] X. Qian *et al.* (JLab Hall A Collaboration) Phys. Rev. Lett. **107**, 072003 (2011).
- [10] J. Huang *et al.* (JLab Hall A Collaboration) Phys. Rev. Lett. **108**, 052001 (2012).
- [11] X. Qian, Modern Phys. Lett. **A27**, 1230021 (2012).
- [12] Y. Zhang *et al.* Chinese Physics **C36**, 610 (2012).
- [13] L. W. Whitlow, SLAC-Report-357 (1990).
- [14] J. W. Lightbody and J. S. O’Connell, Computers in Physics 2, 57 (1988).

²Due to the rapid decrease of the cross section near threshold for the physics J/ψ events, the B-H background becomes comparable at low W.

- [15] D. E. Wiser, Ph. D. thesis, Univ. of Wisconsin (1977).
- [16] E12-12-006, “Near-Threshold Electroproduction of J/ψ with a 11 GeV Beam”, Spokespersons: K. Hafidi, Z.-E. Meziani (contact), X. Qian, N. Sparveris, and Z.-W. Zhao.

3 Simulation

Development of the SoLID spectrometer requires the detailed evaluation of different solenoidal fields, optics from those fields, backgrounds from multiple sources, possible detector and baffle geometries, detector responses, and tracking. Overall, a figure-of-merit must be calculated for different configurations for quantitative comparison. It is also necessary that such simulations be done in a coherent fashion and validated as well as possible. Because details of the design have not been finalized, it must also be flexible enough to be quickly adapted to different configurations.

Initial simulations for SoLID were done using a combination of GEANT3 and COMGEANT. However, these are FORTRAN based and GEANT3 is no longer actively maintained. The decision was made to offer a modern design based on Geant4 [3] to handle particle propagation and interactions. This is a well-supported framework and offers a variety of physics packages, such as simulation of low-energy electromagnetic backgrounds. However, the detector geometries, how magnetic field maps are specified, input parameters, and output formats must all be developed on top of this framework. Furthermore, software for post-processing, such as tracking, also must be developed separately and integrate into the analysis flow efficiently. Because this is being done with a new simulation package, it is necessary to also compare and reconcile the output between GEANT3 and Geant4.

To accomplish all these goals, we have adopted a simulation suite, GEMC, which was successfully developed and employed for similar CLAS12 simulations [4]. It utilizes Geant4 and includes facilities for external event generators, output to a compact style similar to that utilized by JLab data acquisition systems, and a flexible framework to specify arbitrary detector geometries. A framework for specifying sensitive detectors, processing particle hits, and generating output is also included. The geometry and sensitive detector types are read in at run type allowing for easy modification of designs. Advanced visualization abilities are available, which provides a useful debugging tool.

As described in Sec. 4, magnetic field maps for GEMC can be produced using the Poisson Superfish package [5] developed at LANL or TOSCA [6]. The POISSON package allows for the calculation of azimuthally symmetric magnetic fields (relevant for the solenoidal spectrometer). Because both the optics and the fields in the detector regions are relevant, accurate optimization of the iron yoke is important. More detailed field maps produced by TOSCA can be used for more advanced stages of design should it become necessary.

3.1 Framework

The overall framework design is based on a modular philosophy which is general enough to allow many different software components to interact with each other. This needs to encompass ideas such as external event generators, ROOT analysis scripts, raw hit digitization, and tracking analysis. A schematic is given in Fig. 28. Detailed discussions of the individual components follow in later subsections and Sec. 13.

GEMC and generally Geant4 provide the predominant simulation component in modeling secondary physics processes (such as multiple scattering) and propagation through a magnetic field. Physics generators provide information on the initial particle type, position, and momentum to the simulation for each event and are described in Sec. 3.2. These can take more than one form and we allow for general text file input and internal generators within GEMC. Magnetic field maps are described over a grid using text files. GEMC allows for various coordinate systems to be used in the grids and handles all interpolation and lookup.

Geometries and detectors are described externally in a SQL database. The specific detector response-types are assigned within the SQL database tables, but the details of how events are pro-

cessed and sent to output are hard-coded within GEMC. To avoid the need for active development in GEMC to tailor our needs to that simulation, GEMC is built as a library and linked to a version developed specifically within the SoLID collaboration. This gives access to all of the functionality within GEMC, but allows us to modify and add components as we need them without interference to the CLAS development.

Output from GEMC is through EVIO, which is a binary format developed at Jefferson Lab. Libraries are available to provide decoding. These files can be converted to ROOT files through available tools or used by higher level analysis packages, such as the detector digitization.

Presently, a library exists to do the digitization for GEMs, Sec. 3.3, (other detector systems are planned for the future) which produces a standard ROOT file with tree objects and operates within the Hall A analyzer framework. This provides generic C++ class objects for representing detectors and useful parameter database tools. These can be read by the Hall A tree-search code (or potentially any other tracking code base) to do tracking simulations. A more detailed discussion of that component of software can be found in Sec. 13

3.2 Generators

Beyond the physics included in Geant4, several generators have been implemented to study specific processes. The interface between the generator and GEMC is the LUND format (or an extension of it), which is a text-based file containing event-by-event information of the initial particle configuration. These generators allow for an extended target and randomly sampled position to simulate a fast-rastering system. The generators implemented presently are

- Deep inelastic scattering cross sections from the CTEQ6 parton distribution fits [9].
- Charged and neutral pion production based on empirical fits to SLAC data [12] using the Weizsäcker-Williams approximation.
- Elastic scattering from protons and neutrons based on dipole parameterizations.

Additional generators are planned, which includes extending the present generators to include initial radiative and multiple-scattering effects. Additionally, self-analyzing hyperon decay processes are a potential systematic and must be evaluated as well. Background rates for processes included in Geant4 can be evaluated by simulating sufficient numbers of individual electrons passing through the target.

3.3 GEM Digitization

GEM digitization is a crucial aspect in evaluating hit tracking under realistic conditions. The method implemented is based on an approach by the Super-BigBite collaboration, which take the individual ionization events in the GEM drift region, and produces a charge signal across several readout strips based on a realistic model with parameters tuned to real data.

A track passing through a GEM in Geant4 will record energy deposition events caused by ionization which are then amplified through the GEM foils, resulting in a detectable signal over several readout strips, Fig. 29. Within the simulation, the individual ionization events are written into the output and are post-processed through an independent library built upon the Hall A analyzer analysis software [1]. The digitization and track reconstruction can then be developed within a single framework similar to what could be used for analysis of real data.

A full description of the digitization process can be found in Ref [10]. To summarize, from the individual ionization hits, an average number of hole/electron pairs are determined by sampling a

Poisson distribution based on the ionization energy W , such that $n_{\text{ion}} = \Delta E/W$. The physical spread of the resulting charge cloud is described by a simple diffusion model assuming a constant drift velocity, where the Gaussian width of the cloud is given by

$$\sigma_s(t) = \sqrt{2Dt} \quad (13)$$

where D is the diffusion constant and t is the time from ionization. Variation in the amplification of the GEM signal is described by a Furry distribution

$$f_{\text{Furry}} = \frac{1}{\bar{n}} \exp\left(-\frac{n}{\bar{n}}\right) \quad (14)$$

where \bar{n} is the average number of ionization pairs. The previous formalism provides a realistic (unnormalized) charge distribution over an area which can then be associated with a set of GEM readout strips.

The final component of the digitization is to reproduce the time-shaping of the electronics components. For this application, we have assumed the use of APV25 electronics developed at CERN (see Sec. 12.5). The time-dependent digitized signal $S(t)$ is produced by convoluting the charge signal with the form

$$S(t) = A \frac{t}{T_p} \exp(-t/T_p) \quad (15)$$

which provides a good parameterization of real data, Fig. 30. The parameters are chosen to represent real data and the time constant T_p is roughly 50 ns, providing a full-width half-max of about 100 ns.

The advantage to using such a shaping signal, is that three samples can be used to deconvolute the longer, shaped signal to suppress out-of-time background hits. Assuming the form given in Eq. 15, the signal in time sample k is given by

$$s_k = w_1 v_k + w_2 v_{k-1} + w_3 v_{k-2} \quad (16)$$

where weights w_i are proportional to

$$w_1 \sim e^x/x, w_2 \sim 2/x, w_3 \sim e^{-x}/x. \quad (17)$$

3.4 Future Plans

At present, the simulation software used for the calorimeter and portions the software for the Cerenkov systems have been developed by their individual groups. To facilitate a full evaluation of systems, in particular how subsystems interact such as for particle identification simulations and data acquisition needs, a fully merged software package must be developed. Important in merging these is being able to provide flexibility for the subsystems to be developed, but in a clean and unified way.

In particular, one challenge will be for simulating the calorimeter responses in a detailed, but computationally fast way for general simulations. While being able to study full showers are important in optimizing the calorimeter configuration, producing these event-by-event is time consuming. Allowing for optional, energy and angle-dependent, multi-block parameterizations would be very useful for other types of simulations. Similar methods could be applied to optical photon responses in the Cerenkov.

It is anticipated that digitization will be handed in a method integrated with the GEM digitization within the Hall A analyzer framework. This is handled as a separate step from event simulation as these steps are typically very time consuming. Much of the framework and infrastructure is already in place for this and requires only the details to be implemented for each subsystem.

Other practical improvements in the simulation framework would also be desirable, such as integrating the event generators into the software itself, removing the need to keep intermediate event files. Similarly, implementing a direct-to-ROOT tree output would be very useful. Also useful for optimization and configuration debugging and reproducibility would be some facility to track the simulation configuration and tie it directly to the output. As the hardware design is still undergoing optimization, many different configurations over long periods of time are being evaluated. Being able to identify the geometry and detector configuration, version of source, and simulation options for any output helps ensure accuracy and can save enormous amounts of time.

3.5 Background and Radiation damage estimates

The simulation and background calculation software for SoLID is using the two simulation packages with independent code base (Geant4 and FLUKA [13] [14]). This allows independent cross checks both in geometry and in physics modelling. At the same time the two codes each provide unique capabilities expanding the overall reach. FLUKA provides useful tools that simplify the study of radiation damage and estimates but the physics processes present in the simulation lack of direct electro-nuclear dissociation and fragmentation models. Such electro-nuclear reactions are dominant in the neutron production from the Liq.D target at high energies (see figure 36). If one just considers the neutron photo-production, both codes (GEANT4 and FLUKA) have really good agreement with experimental cross section, as shown in figure 34 and 35. A full simulation and tests are underway in order to construct a better and common target background generator for both simulation packages (see figure 36). To have a first idea of the tolerance of different material to radiation damage, see figure 31. As a weighting factor to estimate the effect of radiation damage on electronics I used, in parallel to the calculation of full Dose estimates, the Displacement damage in silicon, on-line compilation curves by A. Vasilescu (INPE Bucharest) and G. Lindstroem (University of Hamburg). This curves assume that the damage effects by energetic particles in the bulk of any material can be described as being proportional to the so called Non Ionizing Energy Loss and normalize the damage in Silicon to the one caused by a 1 MeV neutron (more details can be found here [16]).

3.5.1 Radiation damage to GEM electronics

A simulation in order to test the radiation level on the GEM foils has been done. Comparison to estimated radiation level of the CMS experiment, which shares the part of the electronics most susceptible to radiation damage for the GEM chambers detectors, permitted us to establish a radiation limit flux for our expected running time. Already with our first conceptual design of the shielding we are able to reach tolerable radiation levels also in the first layer of the GEM chambers (the one that is supposed to sustain the higher radiation fluxes). This result is show in figure 37

3.5.2 Power deposited

A detailed study of the power deposited in the SoLID spectrometer has been done in order to detect areas of possible activation. In these areas, in order to define possible activations, the FLUKA simulation has been used as a tool, and particle fluxes were provided by GEANT4 for areas where was the particle fluxes estimated by FLUKA were known to be incorrect. FLUKA in fact provides many good tools for activation and radiation estimates, but lacks in direct electro-nuclear dissociation-fragmentation models and has limitations in producing more complex geometry, like the Baffle design for the PVDIS experiment in SoLID. In the following study of activation, GEANT4 has been used as a common input for an estimate of the background radiation in areas where direct electro-nuclear dissociation-fragmentation models are important.

Power in 1st baffle (due to Mollers), (Cooling, activation) The first baffle, due to his proximity to the Deuterium target in the PVDIS configuration for SoLID, has a power deposition of $\sim 8W$ for a beam current of $50\mu A$ and an energy of $6.6GeV$. The high production of neutrons from the Deuterium target can be an ulterior source for activation in the baffle. For this reason an investigation of the possible activation has been done. In this study has been considered at the same time the radiation coming from the target and from the baffle itself that “self-irradiate” different parts of its structure. These results (see show the Dose equivalent radiation spatial distribution for 3 different cooling times. This study (see figure 38) shows, for example, that, in order to survey the area in proximity of the first baffle, one should wait around 1 day of cooling, in order to reach level of radiation tolerable. The Residual nuclei activated in the Lead baffle are shown for the same cooling time in the bottom plots of figure 38.

Power in exit hole in magnet (elastics) (Cooling, activation) Another spot for possible activation will be the part close to the exit hole of the magnet. Further investigation will need to be done, after a final design of the magnet will be reached, but it is expected to be less important than the activation on the first baffle, due to the not proximity to the target and to the less intense and less localize radiation. This situation has been investigated and compared to the PVDIS design, because it is the one with the expected higher activation of all the configuration with SoLID, with the proximity of the lead baffles to the target (see this section at page 58). This has been done in order to compare power deposition to have a first idea of possible activation areas. The levels of power deposited in the exit hole of the magnet are at least lower by one order of magnitude respect to the expected in the first baffle, as shown in figure 40a and 40b. The integrated value (using the cylindrical symmetry) over the higher area of power deposition in the exit hole of the magnet has a maximum of $\sim 0.9W$ per cm in the z direction over the full internal section of the exit hole with $r_{xy} < 40cm$ (color scale of $\sim 3E - 04$ in figure 40a). This compares to a full power deposition on the first baffle of $\sim 20W$, running in the same conditions. A power deposition estimate for the beam-line downstream is shown in figure 40b. As one can see in 41c, is considerably smaller the impact of the configurations like SIDIS to the activation in this area.

Power in the entrance surface of the magnet (Cooling, activation) (external target configurations) With configuration like SIDIS that have the target positioned outside the magnet, there is a consistent power deposition in the front part of the magnet. Some simulation has been done in order to estimate the possible activation in this area. The results of these studies are presented in figure 41 and show the areas of power deposition in the magnet and in the front surface of the magnet. As expected the areas of possible activation is the area more exposed to the target radiation and the collimator positioned in front of the nose-cone of the magnet.

Heat load in magnet cryostat The power deposited from Neutron radiation on magnet cryostat has been studied and it is expected to be less than $1W$. The energy distribution of the Neutrons irradiating the magnet cryostat is shown in figure 39.

3.5.3 Estimates for radiation damage in the Hall

A study has been done in order to address possible radiation damage areas with the current SoLID design with no further shielding in place. This work has been done in order to address and pinpoint areas that will need to be further investigated when a final design for the magnet and electronics will be reached.

Radiation damage to electronics in Hall The results of the different simulations run suggest that the design of a shielding structure to minimize the radiation in the Hall seems not to be a priority. With the current different layouts of the multiple configuration possible with the SoLID spectrometer. In this study the magnet has been placed in a dome structure of concrete that mimics the presence of the Hall (It is important to consider that the SoLID spectrometer will not be placed in an open environment, but in an Hall full of equipments, with relative reflectivity that could cause an enhancement of the radiation present in the Hall). Different features of these results are in common with the different configurations for SoLID:

- The radiation damage estimated with the simulation is, as expected, consistently lower in the area outside the SoLID spectrometer respect to the one inside the magnet.
- In the downstream part of the Hall, the predominant part of the radiation that escape the magnet is present in the last part of the beam-line, enhancing the choice of keeping in the upstream section of the Hall the existing left and right arm spectrometers existing in Hall-A.
- The configurations that have the target area external to the solenoid have also an high radiation area in the proximity of the target

The configuration that gives the higher radiation estimates in this simulation study, is the PVDIS configuration with Deuterium target. The radiation damage estimate in this configuration is investigated in detail in the next section.

Radiation from beam pipe The main source of radiation leaking from the magnet to the Hall is from the beam pipe downstream. In order to quantify the leaking with the different layouts with SoLID, different simulation have been carried out. The one that presents the biggest impact on possible damage to electronics is the PVDIS configuration with 40cm Liquid Deuterium target, but the localization of the leakage (close to the beam-line, see figures 42 ,43 and 44), and the low level of radiation present, suggest that a shielding construction is not needed. A further factor of 10 reduction, if needed, can probably be reached placing shielding material on the hot areas, around the beam-line, if this area, will be used during the experiment, reaching levels of radiation compatible also to commercial electronics.

Radiation with external targets Some of the configuration with the SoLID spectrometer, position their target in the proximity of the entrance of the magnet. Simulations have been done in order to evaluate possible high radiation areas for electronics. An example for the possible areas of high radiation with these layouts for the experiments is shown in figure 45 (SIDIS configuration with 3He target).

References

- [1] ROOT/C++ Analyzer for Hall A <http://hallaweb.jlab.org/podd/index.html>.
- [2] Fluka. <http://www.fluka.org>.
- [3] Geant4. <http://geant4.cern.ch/>.
- [4] Gemc. <https://gemc.jlab.org/>.

- [5] Poisson superfish. http://laacg1.lanl.gov/laacg/services/download_sf.phtml.
- [6] Tosca. <http://www.chilton-computing.org.uk/inf/eng/electromagnetics/p001.htm>.
- [7] Hall A. Hall a c++ analyzer. <http://hallaweb.jlab.org/podd/>.
- [8] C. Altunbas *et al.* *Nucl. Inst. Meth*, A490:177, 2002.
- [9] J.Huston H.L. Lai P. Nadolsky W.K. Tung J. Pumplin, D.R. Stump. *JHEP*, 0207:12, 2002.
- [10] G.M. Urciuli M. Capogni, E. Cisbani. Note on gem digitiation modeling. <http://www.iss.infn.it/cisbani/atmp/gemc/code/>.
- [11] R. Mankel. *Rept. Prog. Phys*, 67:553, 2004.
- [12] D.E. Wiser. PhD thesis, University of Wisconsin-Madison, 1977.
- [13] *The FLUKA code: Description and benchmarking* G. Battistoni, S. Muraro, P.R. Sala, F. Cerutti, A. Ferrari, S. Roesler, A. Fasso', J. Ranft, Proceedings of the Hadronic Shower Simulation Workshop 2006, Fermilab 6–8 September 2006, M.Albrow, R. Raja eds., AIP Conference Proceeding 896, 31-49, (2007)
- [14] *FLUKA: a multi-particle transport code* A. Ferrari, P.R. Sala, A. Fasso', and J. Ranft, CERN-2005-10 (2005), INFN/TC_05/11, SLAC-R-773
- [15] *Photodisintegration of deuterium and big bang nucleosynthesis* K.Y.Hare and others, *Phys. Rev. D* 68, 072001 (2003)
- [16] *Displacement damage in silicon, on-line compilation* A. Vasilescu and G. Lindstroem available at http://hepweb03.phys.sinica.edu.tw/opto/Irradiation/Documents/NIEL_scaling/gunnar.htm

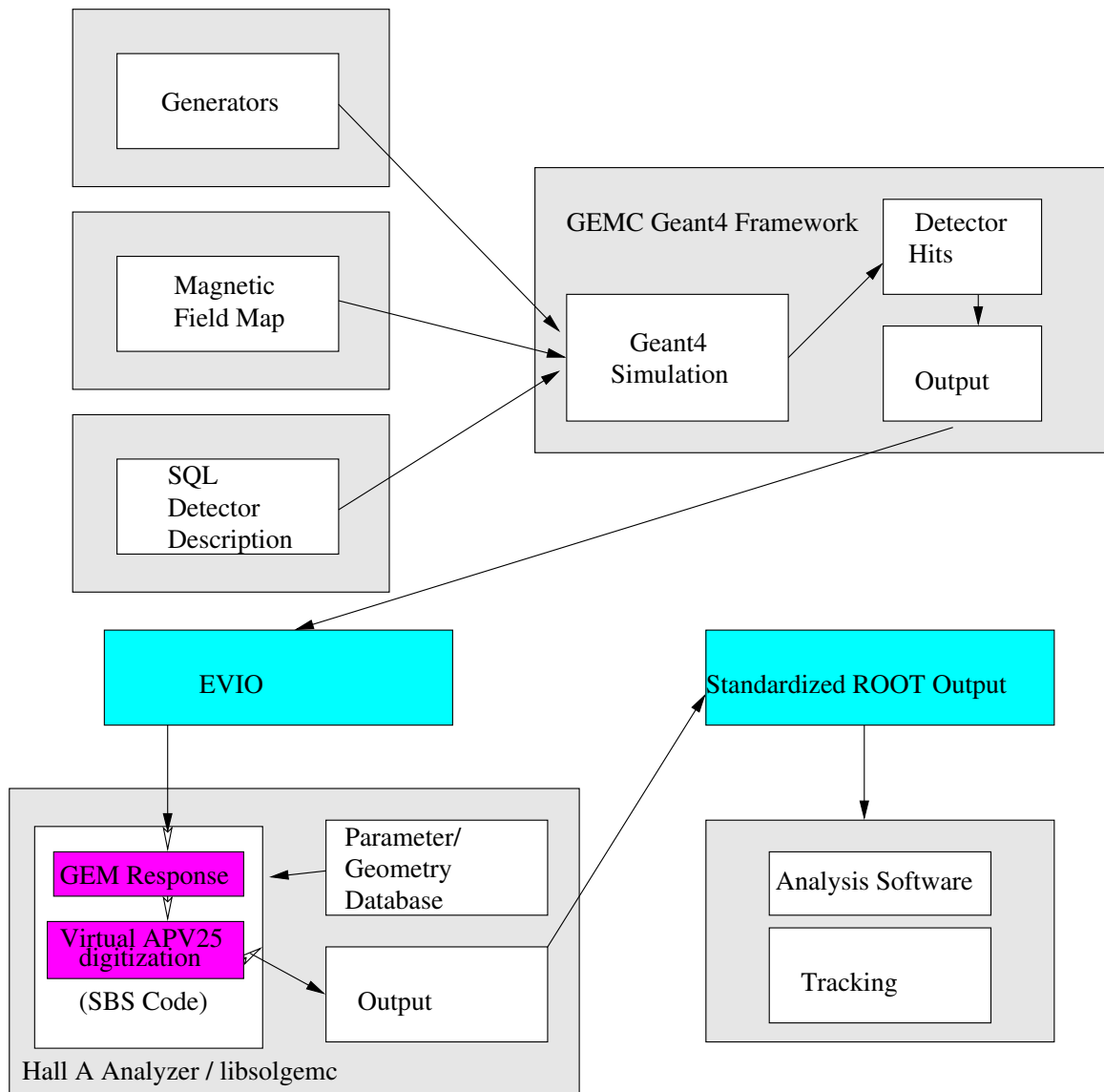


Figure 28: Schematic of the simulation and software framework.

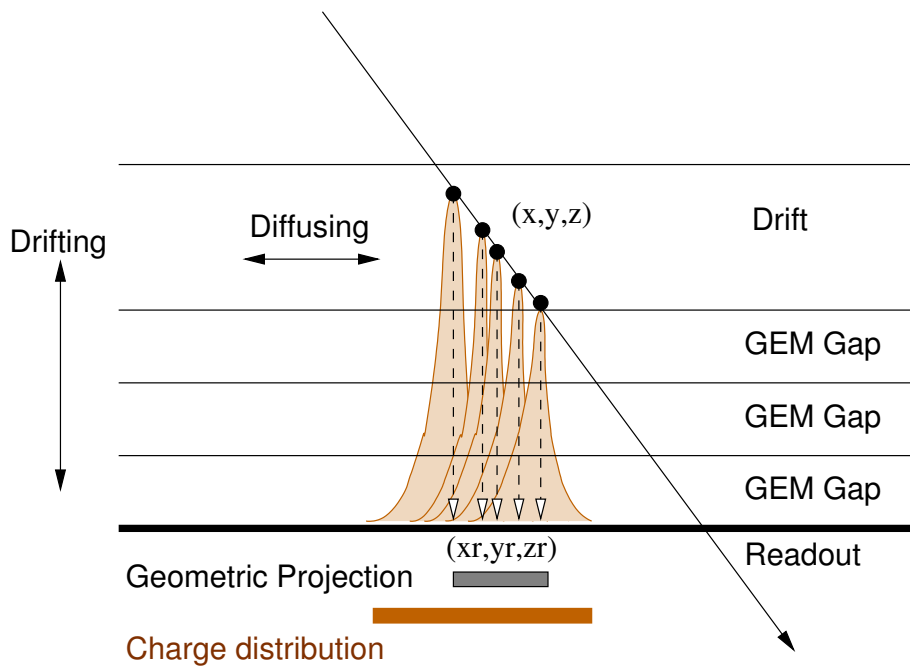


Figure 29: Diagram of the concept behind GEMs using electron avalanching and detection through a set of readout strips.

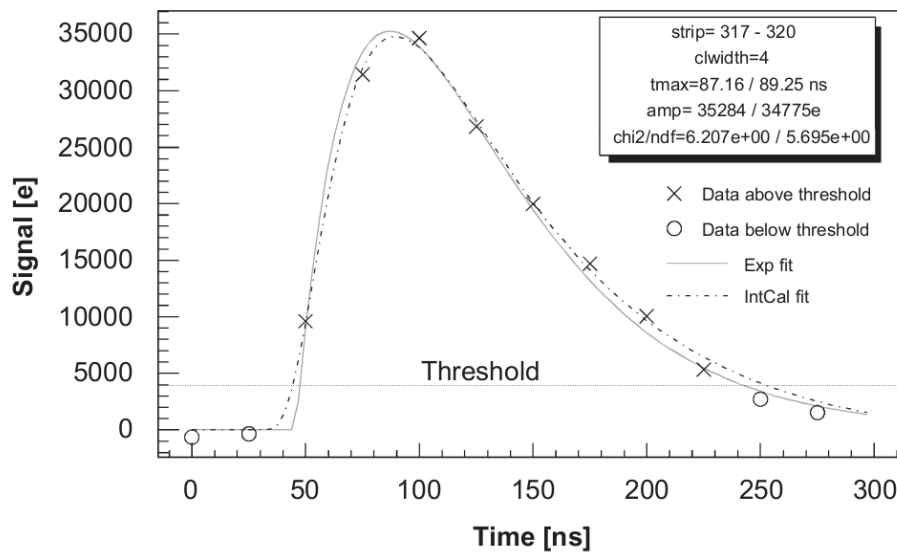
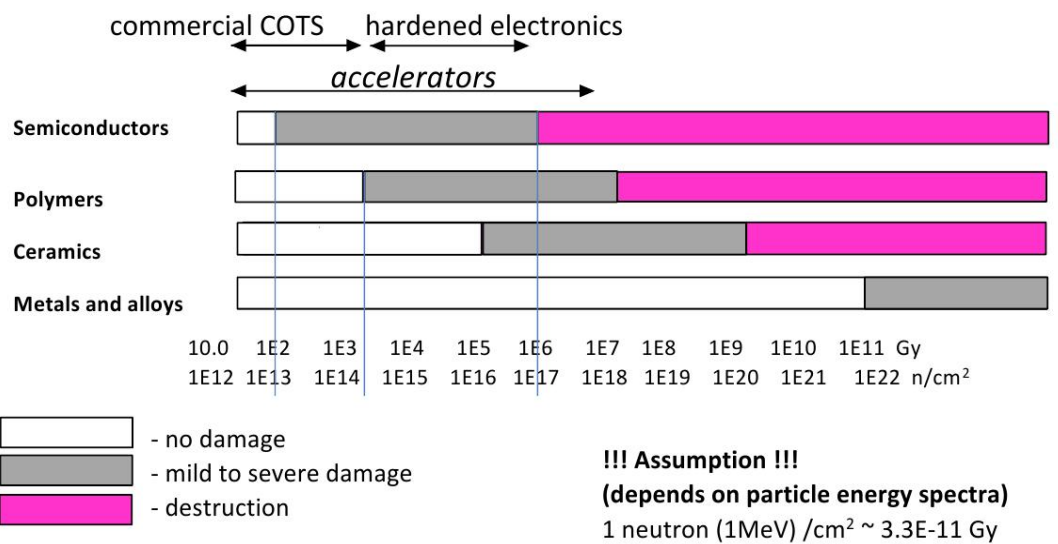


Figure 30: Representation of the signal vs. time response for an APV25 module.



© Lockheed Martin

Figure 31: Estimate of the tolerance of different material to different level of radiation exposure given in Gy and $\frac{\text{neutron}(1\text{MeV})}{\text{cm}^2}$. This is just a first order approximation and a detailed analysis of each equipment is needed in order to establish the correct radiation tolerance of each detector/material

Displacement damage in Silicon for neutrons, protons, pions and electrons

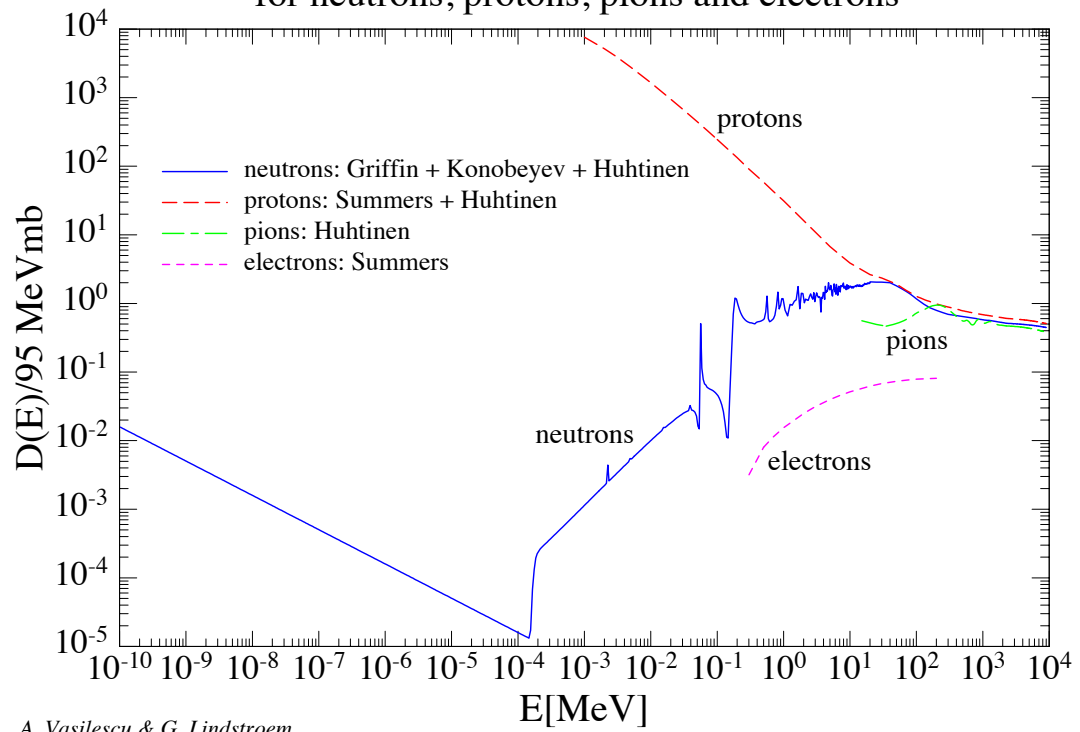


Figure 32: Not Ionizing Energy Loss curves to 1MeV equivalent damage in Silicon for electrons, pions, neutrons and protons

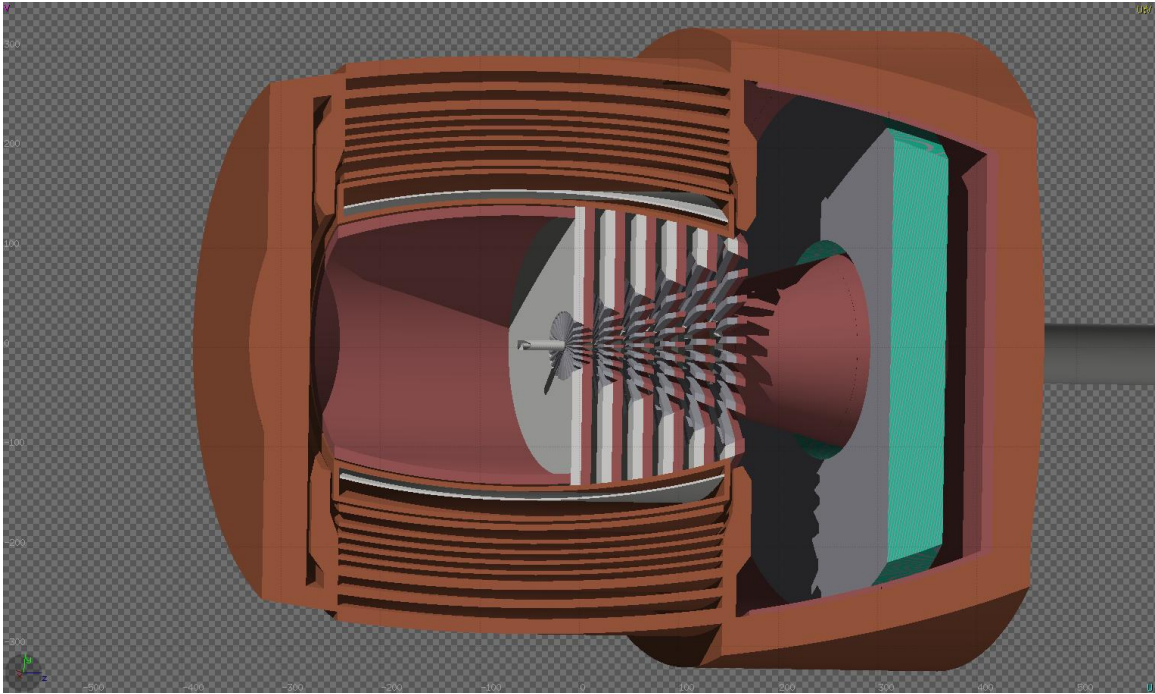


Figure 33: FLUKA simulation for the PVDIS experiment with SoLID. A first conceptual design for the neutron shielding is shown in

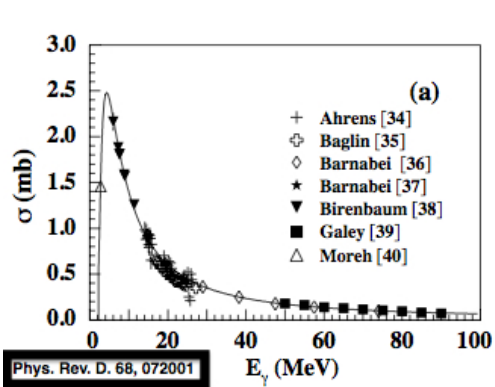


Figure 34: Neutron cross section for photo-production [15]

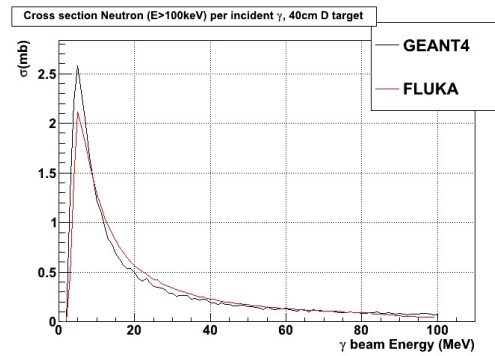


Figure 35: Test for Neutron cross section for photo-production with FLUKA and GEANT4

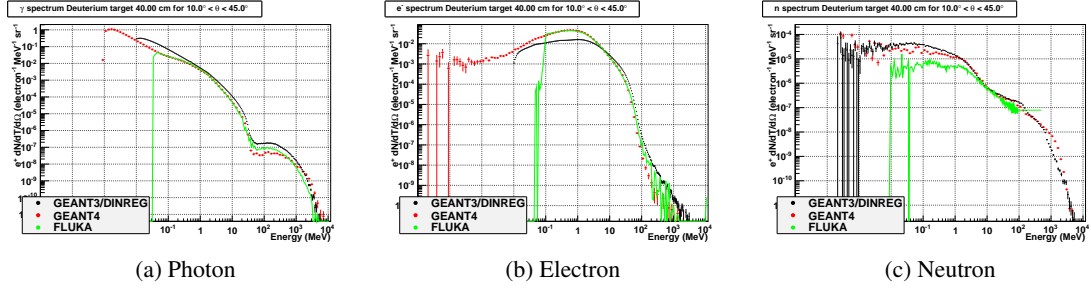


Figure 36: Background comparison produced from GEANT3(DINREG), GEANT4 and FLUKA with 40cm of Liquid Deuterium. Here is plotted the $\frac{d^2 N}{dT d\Omega}$ per incoming electron in the angle range of $10^\circ < \theta < 45^\circ$ for γ (a), e^- (b) and n (c)

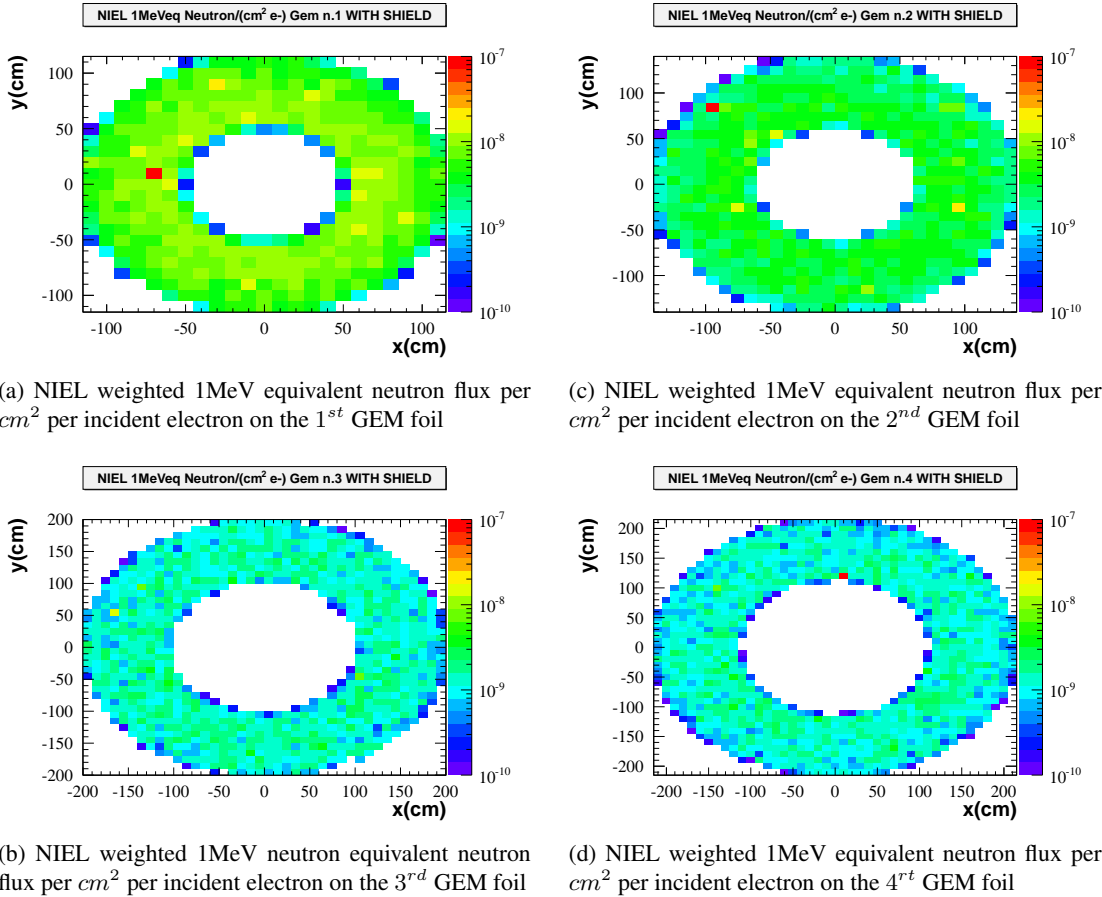


Figure 37: The CMS experiment dose rates are expected to be of the order of $10 \text{ MRad}(SiO_2)$ ($5 \times 10^{13} \frac{n}{cm^2}$). This translate for us, assuming 2000 hours of beam at $100\mu A$, in a flux of $\sim 1.1 \times 10^{-8} \frac{1MeVeqn}{e^-cm^2}$. This put us on the same level of radiation that the APV25 chip was built to tolerate

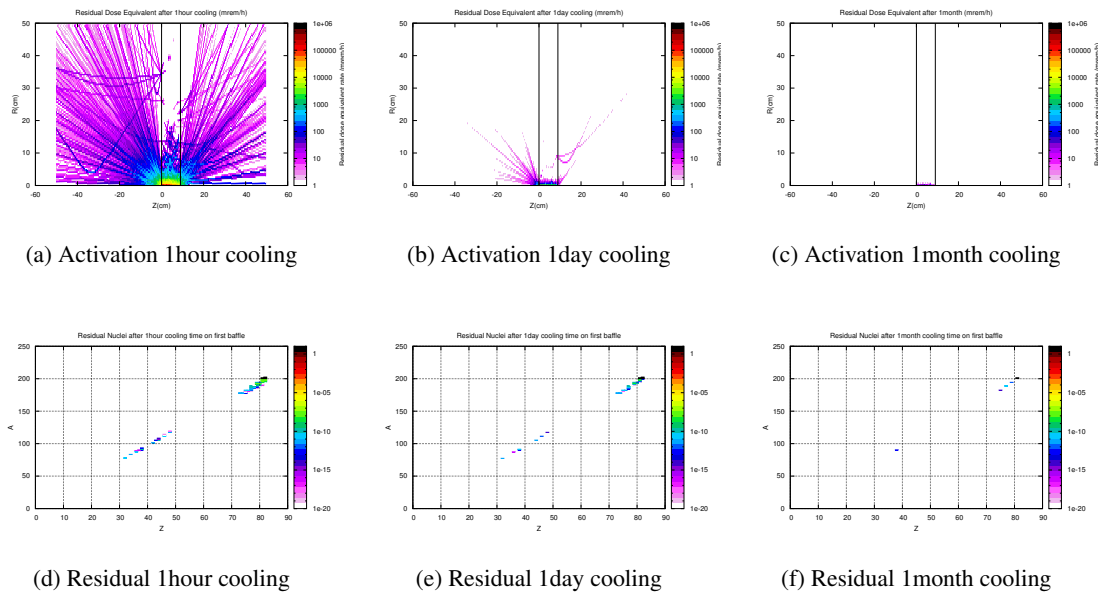


Figure 38: First Baffle: Activation study for 3 different Cooling times, after an assumed exposure to the beam of 3 separate full weeks interleaved by a down time of 4 days. (38a, 38b,38c) The dose is expressed in $mrem/h$ and here is shown their spatial distribution. (38d, 38e,38f) The Residual decaying Nuclei are shown as a function of Z,A.

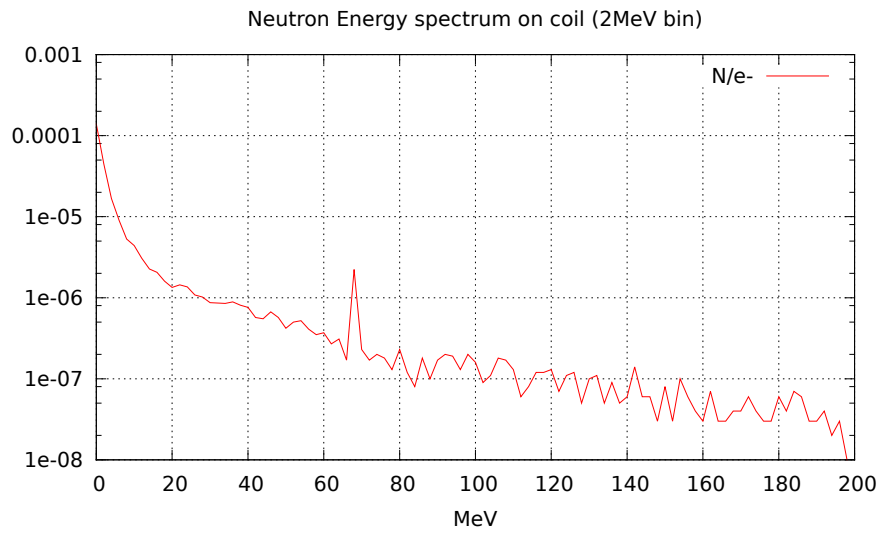
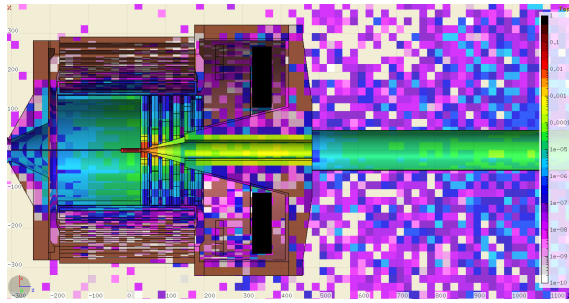
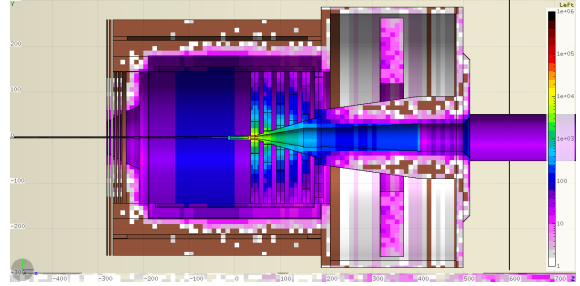


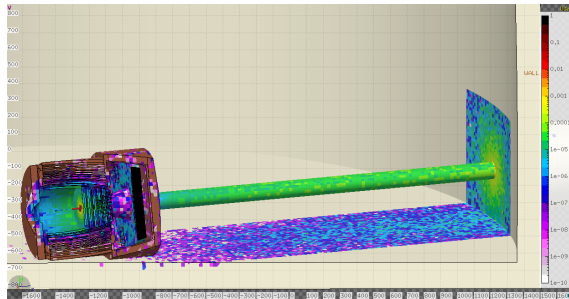
Figure 39: Neutron energy spectrum per electron on the magnet cryostat



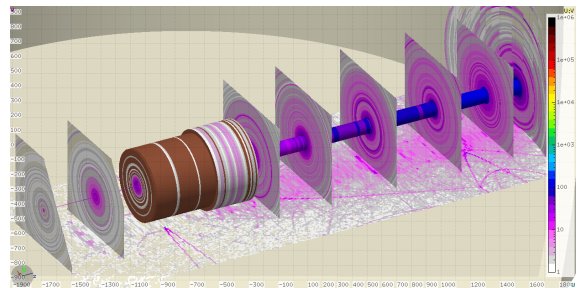
(a) Energy deposited (W) per cm^3 for PVDIS configuration and Liquid Deuterium target



(c) Dose equivalent (mrem) per hour after 1 hour from beam exposure for PVDIS configuration and Liquid Deuterium target

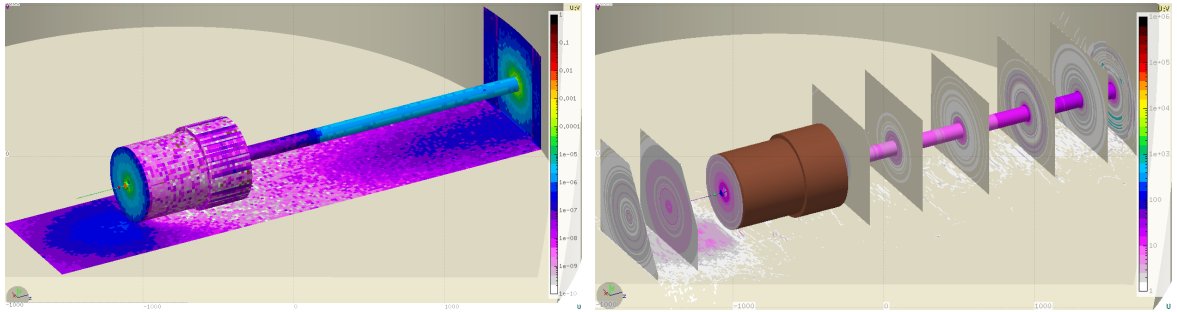


(b) Energy deposited (W) per cm^3 for PVDIS configuration and Liquid Deuterium target (Hall view)

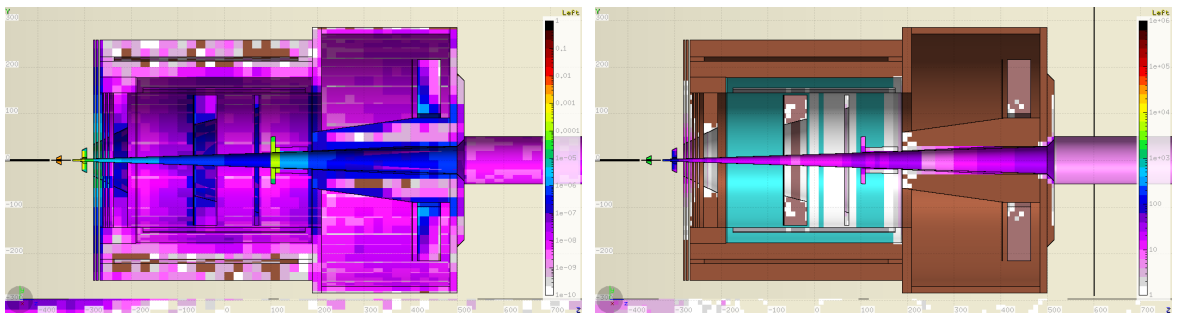


(d) Dose equivalent (mrem) per hour after 1 hour from beam exposure for PVDIS configuration and Liquid Deuterium target (Hall view)

Figure 40: Energy deposited (W) per cm^3 (40a and 40b) considering running condition with Liquid Deuterium target and electron beam current of $100\mu A$. The spectrum is averaged in blocks of size of $20cm \times 20cm \times 20cm$ in order to boost statistics, since this simulation with the complex SoLID design is very high demanding in CPU time. One can see how the power deposited in the first baffle region is considerably higher respect to the one expected in the exit hole of the magnet. In order to obtain the integrated power deposition for the expected beam time for the PVDIS configuration (2000h), multiply the values of the plots by $7.2E+06$. Activation dose equivalent (mrem) rate per hour (40c and 40d) expected with the same configuration after 1 hour from beam exposure ($100\mu A$ for a month). This study has been done in order to simulate condition in the Hall during running time. For a more accurate description of the activation expected in the baffle area, see figure 38



(a) Energy deposited (W) per cm^3 considering SIDIS running (b) Dose equivalent (mrem) per hour after 1 hour from beam condition with 3He target and electron beam current of $15\mu A$ exposure for SIDIS configuration and 3He target (Hall view) (Hall view)



(c) Energy deposited (W) per cm^3 considering SIDIS running (d) Dose equivalent (mrem) per hour after 1 hour from beam condition with 3He target and electron beam current of $15\mu A$ exposure for SIDIS configuration and 3He target (Inside the magnet) (Inside the magnet)

Figure 41: Energy deposited (W) per cm^3 (41a 41c) considering running condition with 3He target and electron beam current of $15\mu A$. In order to obtain the integrated power deposition for the expected beam time for the SIDIS configuration (3000h), multiply the values of the plots by $1.08E+07$. The main part of the energy is deposited, as expected, in the target area and in the collimator positioned in front of the nose-cone part of the magnet. The energy deposited in the exit hole of the magnet is considerably lower than with the PVDIS configuration. Activation dose equivalent (mrem) rate per hour (41b and 41d) expected with the same configuration after 1 hour from beam exposure ($15\mu A$ for a month). This study has been done in order to simulate condition in the Hall during running time.

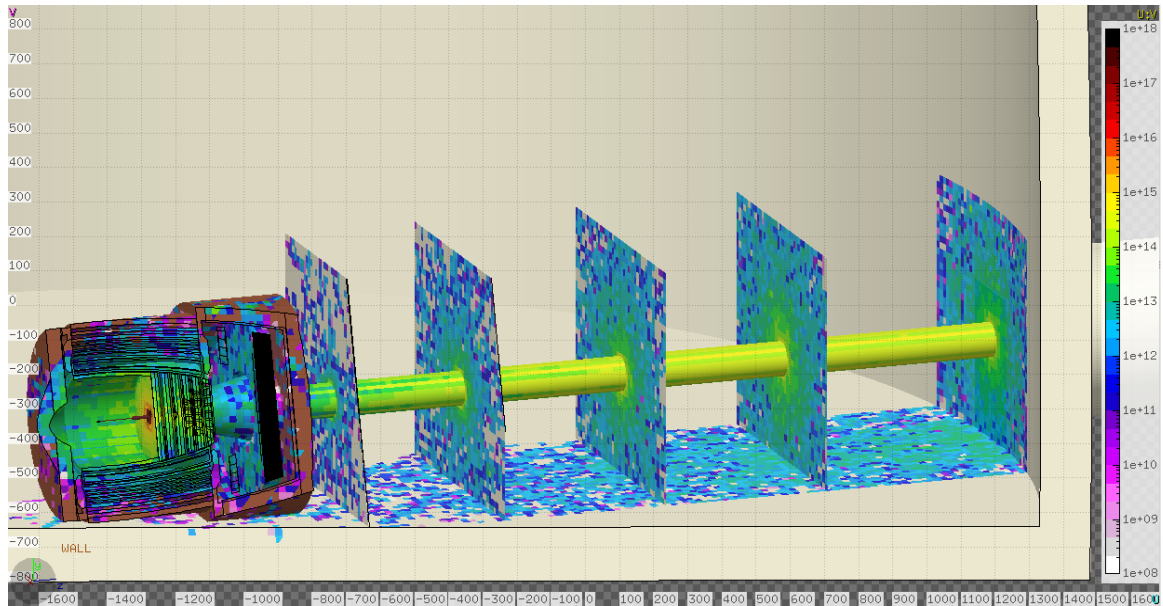


Figure 42: Estimate of radiation damage in the Hall with the SoLID spectrometer and the PVDIS configuration. The leading part of radiation present in the Hall for the SoLID spectrometer is leaking through the downstream part of the beam-line assembly. In this plot is shown the 1MeV Neutron equivalent flux per cm^2 on the volumes surfaces estimated for 2000h of continuous running with a beam current of $100\mu A$ (This is the expected beam-time with the PVDIS configuration). In order to better show the behavior of the radiation leaking, different plane of observation have been inserted (at a distance from the target of $\Delta z = 6m$, $\Delta z = 10m$, $\Delta z = 15m$, $\Delta z = 20m$). The level of radiation leaking increases as one moves farther from the target, reaching a maximum $\leq 10^{15} \frac{N_{1MeV}}{cm^2}$. These levels of radiation is on the “mild to severe” damage range for commercial semiconductors (as one can see comparing them with Estimate of the tolerance of different material plots 31). This area is not expected to carry any delicate equipment. On the upstream section of the beam-line, the level of radiation leaking is tolerable to also commercial equipment (not rad-hard). A comparable plot of this one, with a projection plane on the zy axis, is show in figure 43

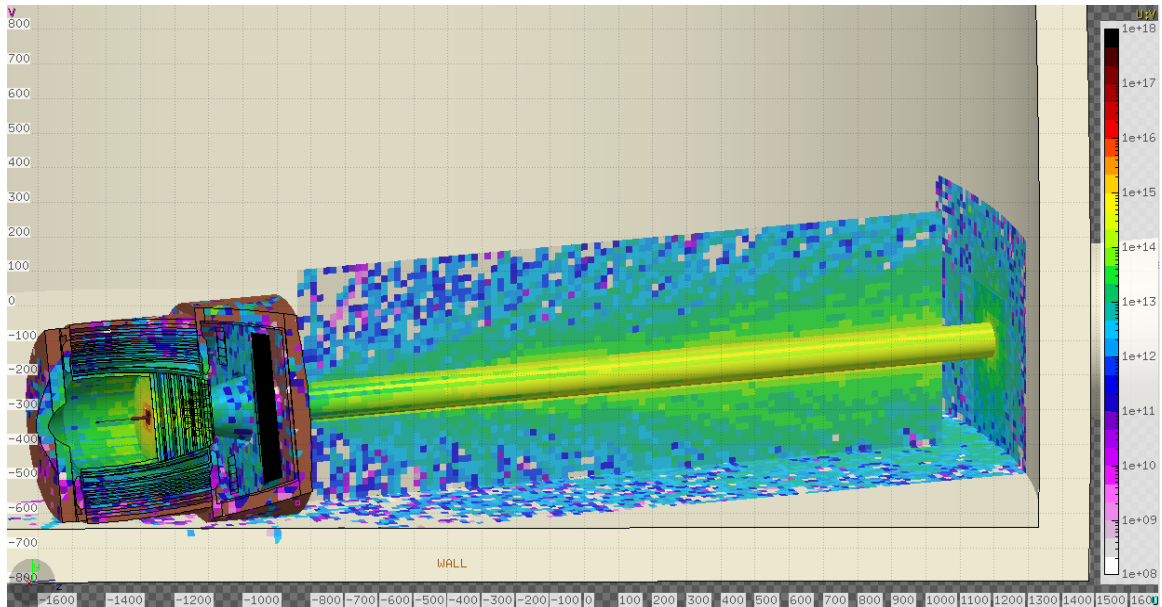


Figure 43: Estimate of radiation damage in the Hall with the SoLID spectrometer and the PVDIS configuration. A projection plane parallel to the beam-line is shown here to show full zy dependence of the 1MeV equivalent Neutron flux. For a full explanation see the caption of figure 42

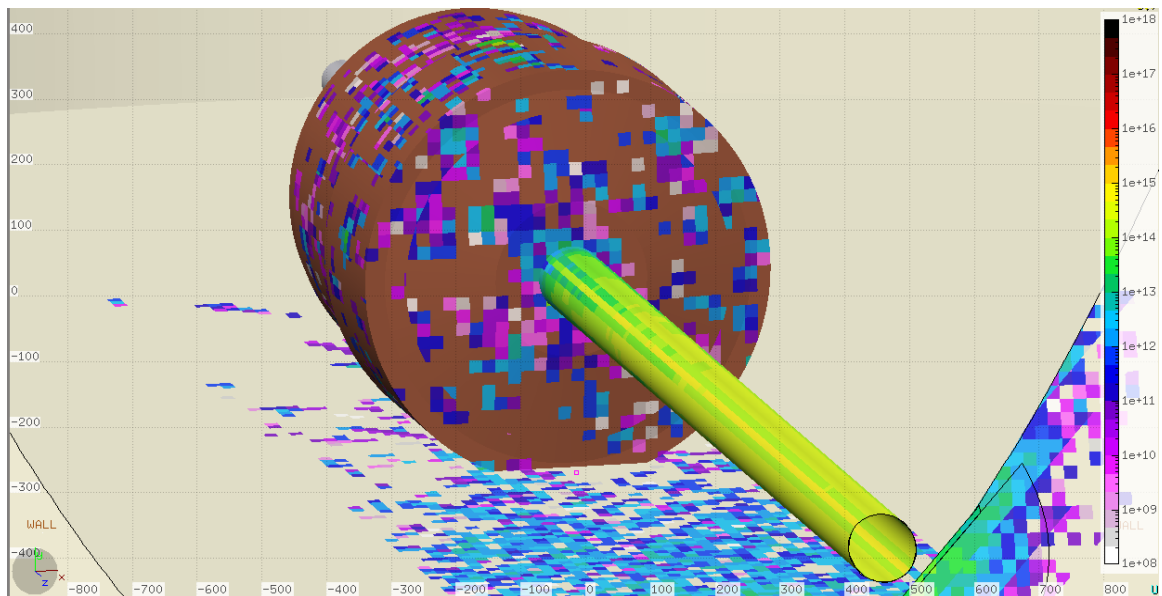


Figure 44: Estimate of radiation damage in the Hall with the SoLID spectrometer and the PVDIS configuration. View of the back part of the SoLID spectrometer. The predominant part of the leaking radiation is supposed to pass through the downstream beam-line.

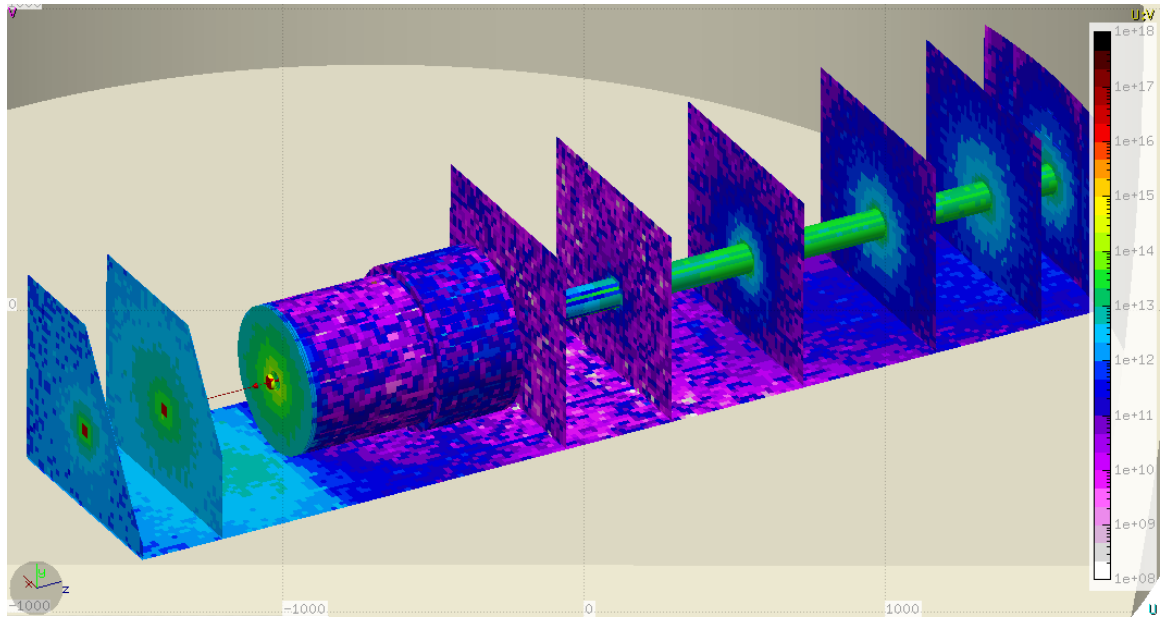


Figure 45: Estimate of radiation damage in the Hall with the SoLID spectrometer and the SIDIS ^3He configuration. The leading part of radiation present in the Hall for the SoLID spectrometer is originating from the target area and the closer surface of the magnet. In this plot is shown the 1MeV Neutron equivalent flux per cm^2 on the volumes surfaces estimated for 3000h of continuous running with a beam current of $15\mu\text{A}$ (This is the expected beam-time with the SIDIS configuration). In order to better show the behavior of the radiation leaking, different planes of observation have been inserted (at a distance from the center of the Cryostat of the magnet of $\Delta z = -10\text{m}$, $\Delta z = -6\text{m}$, $\Delta z = 6\text{m}$, $\Delta z = 10\text{m}$, $\Delta z = 15\text{m}$, $\Delta z = 20\text{m}$, $\Delta z = 24\text{m}$). The level of radiation leaking increases as one moves farther from the target, reaching a maximum $< 10^{14} \frac{\text{N}_{1\text{MeV}}}{\text{cm}^2}$. These levels of radiation is on the “mild to severe” damage range for commercial semiconductors (as one can see comparing them with Estimate of the tolerance of different material plots 31). This area is not expected to carry any delicate equipment.

4 Magnet

4.1 Requirements

The SoLID spectrometer is designed to have large acceptance in polar angle, azimuthal angle, and momentum acceptance, and also operate at high luminosity. A solenoid magnet is a natural choice in this case. The magnetic field is symmetric around the beamline, confining the copious low energy charged background particles to the beam pipe region. The detectors are placed symmetrically around the beamline, both within the solenoid and in the end cap region. The approved experiments all have some requirements on the magnet. They are summarized below:

- The PVDIS experiment requires polar angle coverage for the center of the target from 22° to 35° . Its hydrogen and deuterium targets can operate in the magnetic field. To operate the detectors at the design luminosity of $10^{39}/\text{cm}^2/\text{s}$, a set of baffles is required to block unwanted photons and hadrons originating in the target. The magnetic field must then be strong enough to spiral the several GeV DIS electrons through the gaps in the baffles and also provide sufficient curvature in the tracks so that their momentum can be reconstructed. Both requirements can be met with a field integral along the flight path on order of 2.5 T-m.

- Both SIDIS proton and neutron experiments need polar angle coverage from 8° to 24° . The ^3He and NH_3 targets must be located just upstream of the solenoid where the fringe fields before additional shielding are on the order of 5 G. The NH_3 targets require a uniform 5 T field and the ^3He targets require uniform fields on the order of a 25 Gauss. There are two sets of detectors. The forward detectors, located in the end cap, cover particles with angles below 15° . This requires the solenoid to be on the order of 3-4 m long. The large angle detectors are located near the center of the magnet, requiring a diameter on the order of 3 m. The field integral needs to be on the order of 5 T-m in order to provide sufficient momentum resolution from the GEM tracking system.

- The J/ψ experiment must detect the electron-positron pair from the J/Ψ decay as well as the scattered electron. With a liquid hydrogen target placed upstream of the magnet, the configuration for the SIDIS experiment meets the requirements.

Overall, the ideal SoLID solenoid needs to have an outer radius < 3 m to fit in the experimental hall, an inner radius > 1 m, a length of 3–4 m, and a field integral on the order of 5 T-m.

4.2 SoLID magnet

We have chosen the CLEO II magnet for the SoLID spectrometer. It is a solenoidal magnet with a uniform axial central field of 1.5 T, a large inner space with a clear bore diameter of 2.9 m and a coil of 3.1 m diameter. With a coil length of 3.5 m, its magnetic field uniformity is $\pm 0.2\%$. It was built in the 1980s by Oxford in England and installed for CLEO II in 1989 [2, 3].

The coil is made of $5 \times 16 \text{ mm}^2$ aluminum stabilized superconductor and run at 3266 A with an average current density of 1.2MA/m. The large conductor size provides simpler construction and ease of protection. A 3.8 m long cryostat encloses the coil and cools it with a thermosyphon system. The return yoke has 3 layers with 36 cm thickness each and is octagonally divided. There are 2 collars 60 cm thick supporting not only the return yokes, but also the coil with 4 rods. The magnet has good stability, low cryogenic heat load, passive cooling, and passive protection. This gave it the flexibility to be frequently de-energized for maintenance and accelerator studies. It has been kept in good condition since stopping beam, but is still locked in the Cornell Electron Storage Ring (CESR). To use the CLEO magnet for SoLID, we will reuse the coil and cryogenic system, but the downstream collar and return yoke will be modified to allow the PVDIS acceptance up to 35° . New endcap and front pieces will be fabricated.

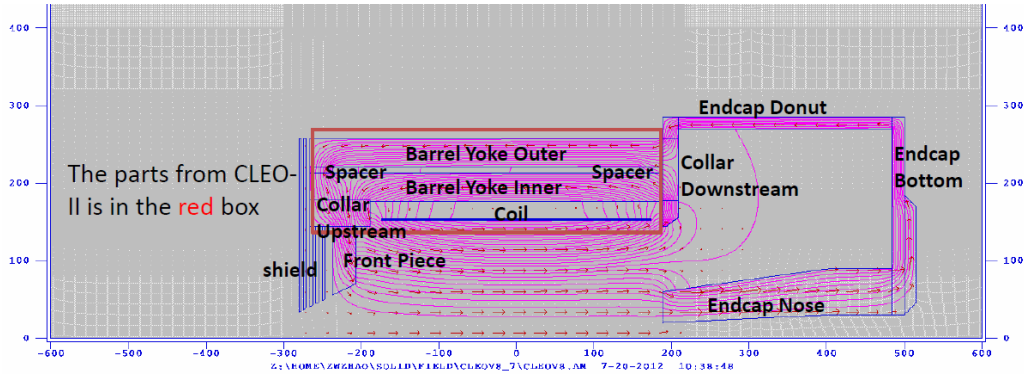


Figure 46: Design of the CLEO II magnet yoke for SoLID.

The design of the yoke for SoLID with the CLEO II magnet is shown in Figure 46. There are two layers of barrel flux return and an upstream collar which are kept from the original CLEO-II magnet. The simulation has shown that the original third layer of barrel flux return is not needed for SoLID and the field in the rest of two layers is well below saturation. The downstream collar is either modified or a new part. All other parts including the endcap, the front piece and the target shielding need to be built.

The B field for the CLEO II magnet with the SoLID yoke is shown in Figure 47. The strongest field is within the solenoid and drops sharply in the endcap and upstream opening. The magnetic field was calculated using the 2D Poisson Superfish program.

The B_z and B_r fields along the beamline are shown in Figure 48. The B_z field at the center is about 1.4 T, dropping to 0.8 T at the exit of the coil.

The axial force for the 3 section of coils and all parts of yoke are shown in Figure 49. There are two strong forces compressing the coil. These forces can be balanced so that the net force on the coil is small. It can be adjusted by moving the location of the front piece, where the force varies by 3–5 t/cm.

4.3 Planned modifications

The CLEO magnet will require some modifications to its design for use in the SoLID experiments. Much of the CLEO magnet will be reused in its original condition. However, SoLID will not use the outermost muon ring. It will use the inner two rings, each consisting of 8 slabs of iron to make up the 8-sided ring. Each of these slabs will have to be shortened to allow the proper position of the endcap. The original upstream coil collar will be reused. Spacers between the slabs will also be reused. The downstream coil collar will be modified if an economical way of reducing its thickness can be found without wasting a majority of its unwanted material. If a solution is not found then a new downstream coil collar will be created. Additional pieces of iron will need to be fabricated to allow for the proper mating of the endcap with the barrel yoke. The existing outer and inner shower counters that mount inside of the coil collars do not appear to be reusable as the upstream coil cup that will reside inside the upstream coil collar. All supporting structure for the magnet barrel yoke and detector endcap will be new fabrications. Please refer to the study in Ref. [1].

The endcap, which consists of the outer cylindrical ring, the backplate, and endcap nose, will all be made from new material. The endcap is designed to be part of the magnetic flux return yoke and house the downstream forward angle detector package. The endcap will be split vertically into

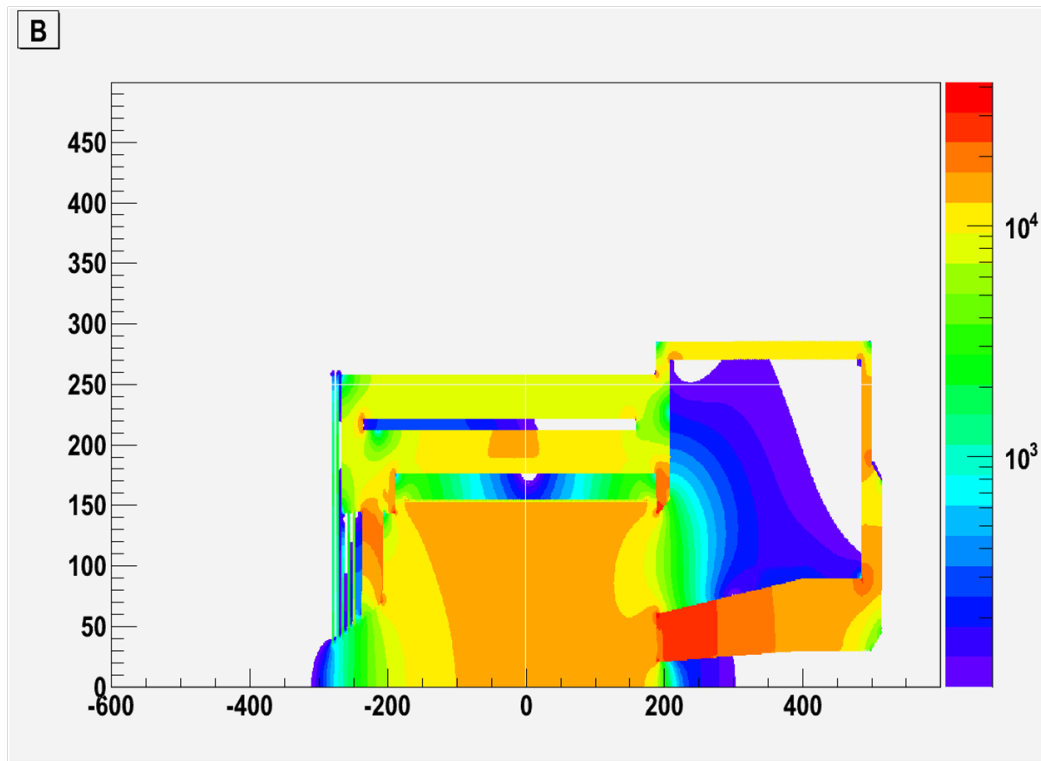


Figure 47: SoLID CLEO magnet field $B > 100G$.

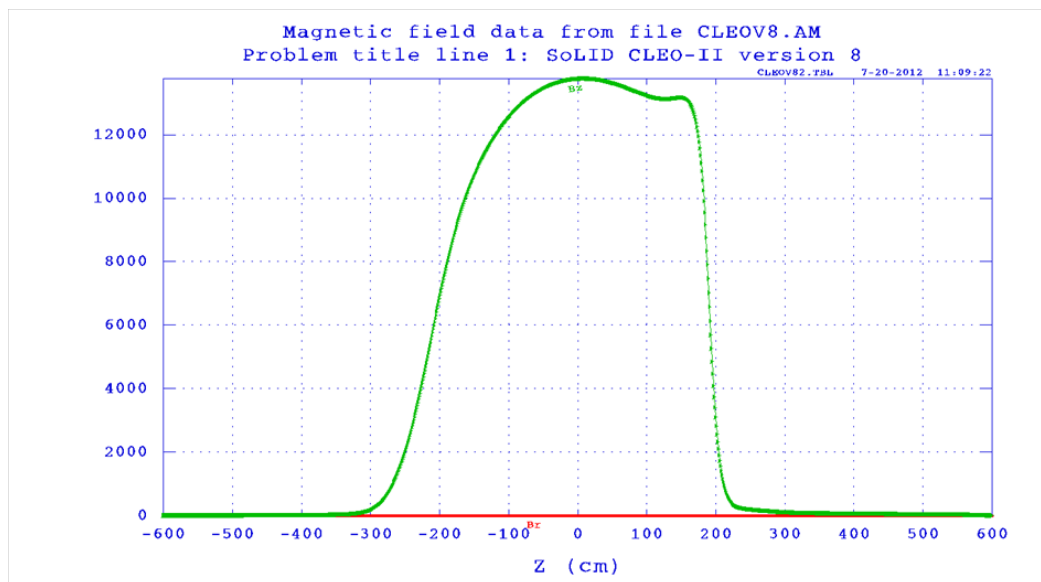


Figure 48: SoLID CLEO magnet field along beamline.

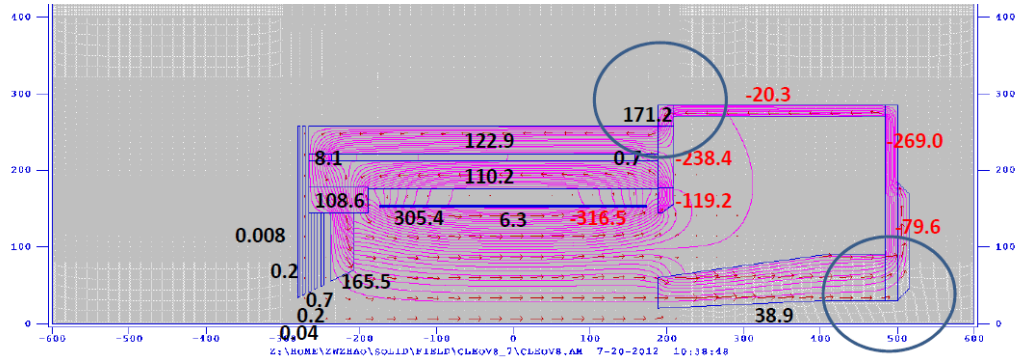


Figure 49: SoLID CLEO axial force in metric t. The two circles show where the force changes direction.

halves and capable of separation to allow for access to the detector package, see 50. The endcap nose with a secondary backing plate will be a cast two piece design to allow for separation. Each section of the nose will bolt to the main backplate which consists of a two piece round disk. The two halves of the cylindrical outer ring will bolt to the corresponding backplate. The structural support and motion mechanism for the endcap will be discussed in 15.

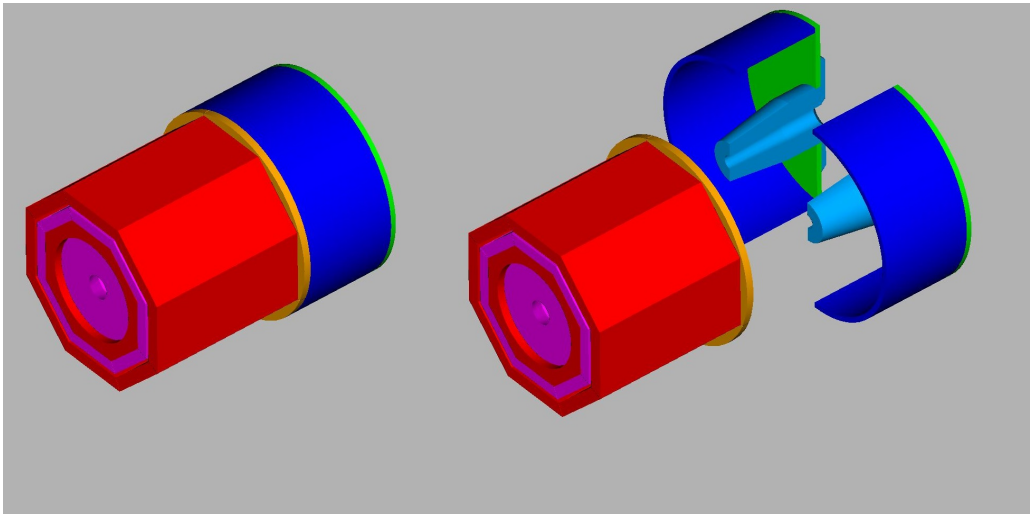


Figure 50: The endcap will be split vertically and also have the capability of separating in the lateral direction

References

- [1] Study of modifying CLEO II magnet for SoLID, E.Chudakov (https://userweb.jlab.org/~gen/jlab12gev/cleo_mag/)
- [2] Y. Kubota *et al.*, Nucl. Inst. and Meth., **A320** 66 (1992)
- [3] D. M. Coffman *et al.*, IEEE Transactions on Nuclear Science, **37** 1172 (1990)

5 Targets

There are five approved SoLID experiments. Two semi-inclusive DIS experiments (E12-10-006 and E12-11-007) use a polarized ^3He target with the achieved performance. One SIDIS experiment (E12-11-108) uses a transversely polarized proton (NH_3) target. The parity-violating DIS experiment (E12-10-007) uses a 40-cm cryogenic liquid deuterium (hydrogen) target system. The J/Psi experiment uses the standard cryogenic liquid hydrogen target. The following subsections will describe the polarized ^3He target, the polarized proton (NH_3) target and the PVDIS cryotargets,

5.1 Polarized ^3He Target

The polarized ^3He target is based on the technique of spin-exchange optical pumping of hybrid Rb-K alkali atoms. Such a target was used successfully in the recently completed SIDIS experiment [1] with a 6-GeV electron beam at JLab. Three sets of Helmholtz coils provide a 25 Gauss holding field for any direction, supporting polarization in transverse (for E12-10-006) or longitudinal (for E12-11-007) direction. Target cells were 40-cm long with density of about 10 amg (10 atm at 0°). The luminosity was about 10^{36} nuclei/s/cm with a beam current of $15 \mu\text{A}$. An in-beam polarization of up to 60% was achieved. Both achieved luminosity and figure-of-merit are the world-best so far. Two kinds of polarimetry, NMR and EPR (paramagnetic-Resonance), were used to measure the polarization of the target. The precision for each method was about 5% (relative) and the methods agreed well within uncertainties. It is expected to be able to reach 3% with the planned improvements.

Frequent target polarization direction reversal is needed to minimize target-spin-correlated systematic uncertainties. The fast target spin reversal was achieved in a few seconds for the 6 GeV SIDIS experiment by using RF AFP technique. The frequency of the spin reversal was kept to 20 minutes to minimize the polarization loss due to AFP. The additional polarization loss due to frequent spin reversal was kept at $< 10\%$ (relative). The above quoted maximum in-beam polarization achieved for the 6 GeV experiment (up to 60%) included the loss due to spin reversal. A new method using field rotation for spin reversal was tested and a nearly no polarization-loss result was achieved and will result in an improved performance. It will allow to have more frequent (a few minutes instead of 20 minutes) spin reversal to help further improve the target-spin-correlated systematics.

The upstream endcap plate will keep the magnetic field and its gradients under control in the target region. In this design, the absolute magnetic field strength in the target region is about a few Gauss with field gradients 50 mG/cm. Correction coils around the target will further reduce field gradients to the desired level of 30 mG/cm.

A collimator, similar to the one used in 6 GeV experiment, will be placed next to the target cell window to minimize the target cell contribution to the total events.

In addition to the polarized ^3He target, the current target system has a multi-foil ^{12}C target for spectrometer optics study, a BeO target for beam tuning and a reference target cell system, which allows to have different target gases, hydrogen, deuterium, ^3He and nitrogen, be used to measure unpolarized cross sections, for calibration and dilution study.

Upgrades are planned for other polarized ^3He experiments before the SoLID experiments. These upgrades are not required for the SoLID experiments but will benefit them.

5.2 Transversely Polarized Proton Target for SoLID

The SoLID collaboration proposes to measure single spin asymmetries in the semi-inclusive, deep-inelastic ($e, e'\pi^\pm$) reaction using a transversely polarized proton target. The target to be used is the dynamically polarized ammonia target that has been used at SLAC and at Jefferson on numerous

occasions [2]. Its last use was in 2012 for the g2p/Gep experiments, which took place in Hall A [3]. Proton luminosities of $10^{35} \text{ cm}^{-2}\text{s}^{-1}$ have been achieved with this target, in conjunction with electron beam currents up to 100 nA. In order to meet requirements of the SoLID measurements however, a new superconducting magnet must be procured, as discussed below.

Dynamic nuclear polarization (DNP) has been used to polarize solid targets for nuclear and particle experiments for more than four decades. To realize DNP, a paramagnetic species is implanted into the target material, either by dissolving a stable radical into the material (if the latter is liquid at room temperature), or by producing radicals directly within the material using ionizing radiation. The unpaired electrons are highly polarized by cooling the sample to a low temperature and exposing it to a high magnetic field. For example, at the 1 K and 5 T operating conditions of the JLab target, the electron polarization is -99.8%. Off-center microwave saturation of the radicals Electron Spin Resonance (ESR) frequency is used to transfer this polarization to nearby nuclear spins, with one or more mechanisms, such as the solid effect, thermal mixing or the cross effect, being responsible for the polarization transfer. Spin diffusion then transports the nuclear polarization throughout the bulk of the sample. The polarization may be positive or negative, depending upon whether the microwave frequency is below or above the ESR frequency. In well-designed systems, proton polarizations exceeding 95% [4] and deuteron polarizations approaching 90% [5] have been achieved.

Frozen ammonia (NH_3) has been the target material of choice for electron beam experiments at Jefferson Lab. Proton polarizations in excess of 90% are routinely achieved in ammonia, and it has a relatively high ratio of polarizable-to-nonpolarizable nucleons (17.6%). Additionally, ammonia displays a very high resistance to radiation damage, and simply warming the material to about 100 K for a few minutes can largely repair the damage that does occur. Prior to the experiment, paramagnetic radicals (chiefly NH_2) are created within the ammonia by irradiating the material (under liquid argon) with an electron beam. For convenience, this irradiation is typically done off site, and the material is then stored under liquid nitrogen until required for the experiment. The JLab target system, as utilized in Hall A, is shown in Fig 51. It consists of a 5 T split-coil superconducting magnet, a ^4He evaporation refrigerator with a cooling power of about 1 W at 1 K, and a target insert containing two samples of frozen ammonia along with additional targets for background and dilution studies. These reside in a purpose-built, evacuated scattering chamber with thin windows around its perimeter for beam entrance and exit. Equipment outside the chamber includes a large set of vacuum pumps for the evaporation refrigerator, microwave electronics for polarizing the target sample, and a NMR system for measuring its polarization. Liquid helium is provided to the target from a nearby 500 L dewar.

Before its use in the g2p/Gep experiments, numerous upgrades were made to the polarized target in order to improve its performance, reliability, and safety:

- An entirely new refrigerator was constructed at JLab according to the safety regulations dictated by 10 CFR 851;
- The quench-relief piping system for the superconducting magnet was upgraded to replace leaking rubber seals with copper gaskets, and also made compliant to 10 CFR 851;
- The pumping system and controls were overhauled;
- A more robust sample insert and motion mechanism were constructed to address problems that were encountered in previous experiments;
- A new rotary vacuum seal was implemented that significantly reduces the time required to rotate the magnet between its longitudinal and transverse orientations. With the new seal,

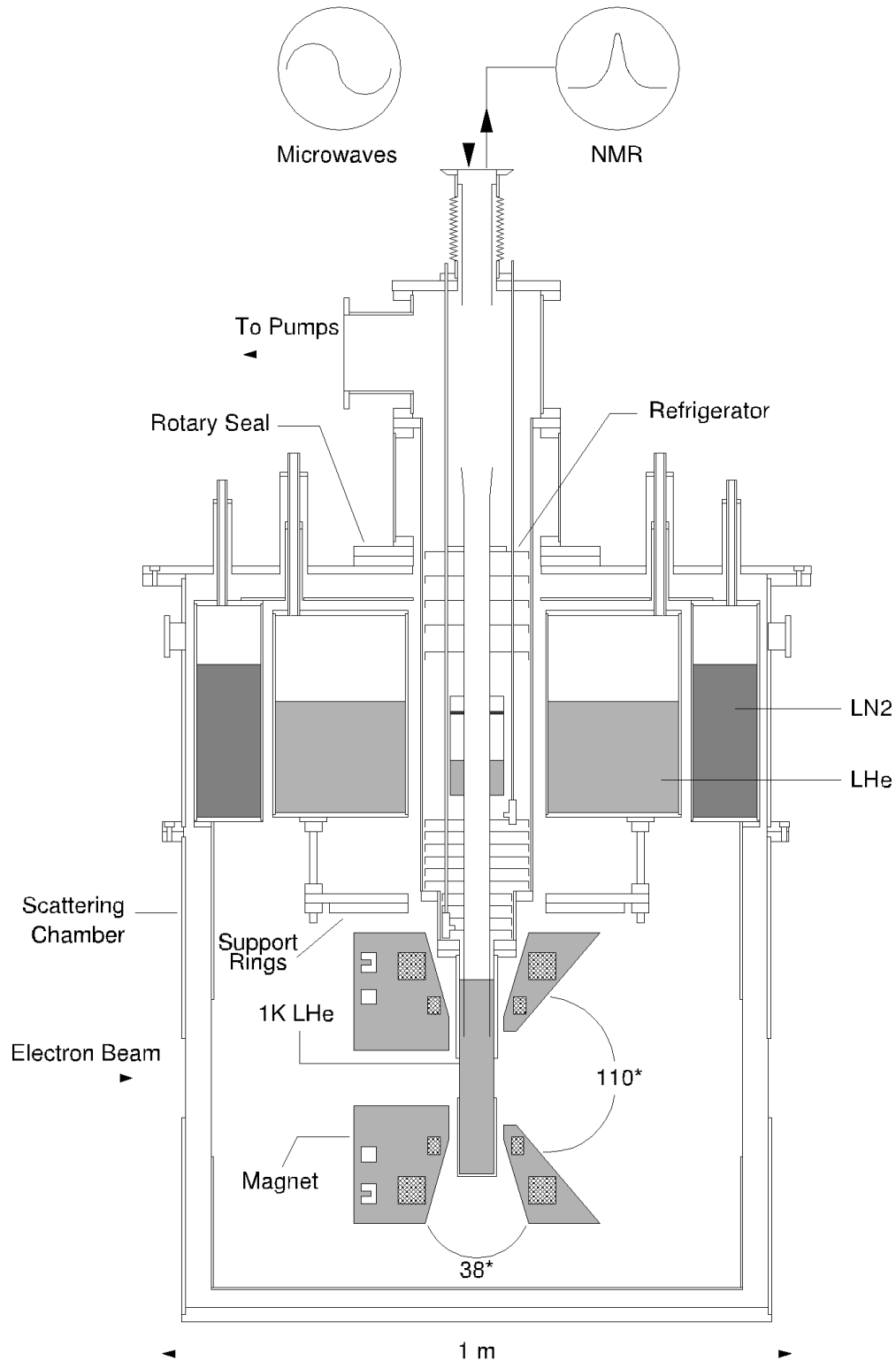


Figure 51: The dynamically polarized target, as utilized in Hall A. The cryostat can rotate 90° about the vertical axis, thus providing either longitudinal or transverse polarization with respect to the electron beam. The longitudinal orientation is shown.

there is no longer a need to disconnect the refrigerator pumping line, nor remove and replace the sample insert;

- The 5 T magnet suffered irreparable damage during the final systems tests, and was replaced with a similar magnet removed from the Hall B polarized target [6].

It should be noted that both the original and Hall B magnets were primarily designed to provide longitudinal polarization, while still permitting limited use for transverse polarization. As such, each magnet possesses an opening angle of $110^\circ (\pm 55^\circ)$ in the direction parallel to the magnetic field, compared to only $\pm 17^\circ$ perpendicular to it (see Fig. 51). Because the SoLID proposal requests transverse polarization with an opening angle $\pm 25^\circ$ or greater, a new magnet will be necessary.

Oxford Instruments (manufacturer of both the Hall B and original magnet) has performed a detailed feasibility study and concludes that they can build a 5 T split-coil magnet with both a $\pm 25^\circ$ split angle and the homogeneity required for DNP [7]. The SoLID collaboration and JLab Target Group will work alongside the eventual vendor to ensure the magnet can be easily incorporated into the existing JLab cryostat. This will greatly reduce the time and cost required to field a transversely polarized target for SoLID.

5.3 Cryogenic Target for PVDIS (SOLID)

The proposed target consists of 40 cm liquid hydrogen/deuterium cell. This cell will be filled with either hydrogen or deuterium as needed. The heat load on this target will be much more modest than the Qweak target that was employed from 2010 to 2012 at JLAB. A conceptual design of the target is shown in the figure. The current concept allows for remote placement of a single cryogenic cell and a dummy cell with several solid targets necessary for calibrations. Such a target has the following basic elements:

1. Heat exchanger (HX)
2. Insulating vacuum chamber (IVC)
3. Target stack
 - (a) Cell
 - (b) Dummy target
 - (c) Solid targets
4. Recirculating pump
5. Cryostat
6. Temperature stabilizing heater
7. Positioning system
8. Gas handling system and gas storage
9. Instrumentation
10. Depolarizer

All components in the system must comply with 10 CFR 851 with regard to pressure, electrical, and fire safety. The majority of these components will remain outside the high magnetic field of the solenoid. The cell and connecting piping together with the rest of the target stack are necessarily placed in the magnetic field of the solenoid. Selection of materials for these components shall consider this.

The insulating vacuum chamber will consist of two main sections. One section will be inside the bore of the solenoid and a section similar to the IVC for the standard Hall A cryogenic target will be upstream of the magnet. This later section will contain the motion system, heat exchanger, etc. The section in the magnet will only contain the target stack and connecting piping. Materials for the chamber section inside the solenoid must be compatible with the magnetic field inside the solenoid. The exit of the chamber will be compatible with the acceptance of the detector.

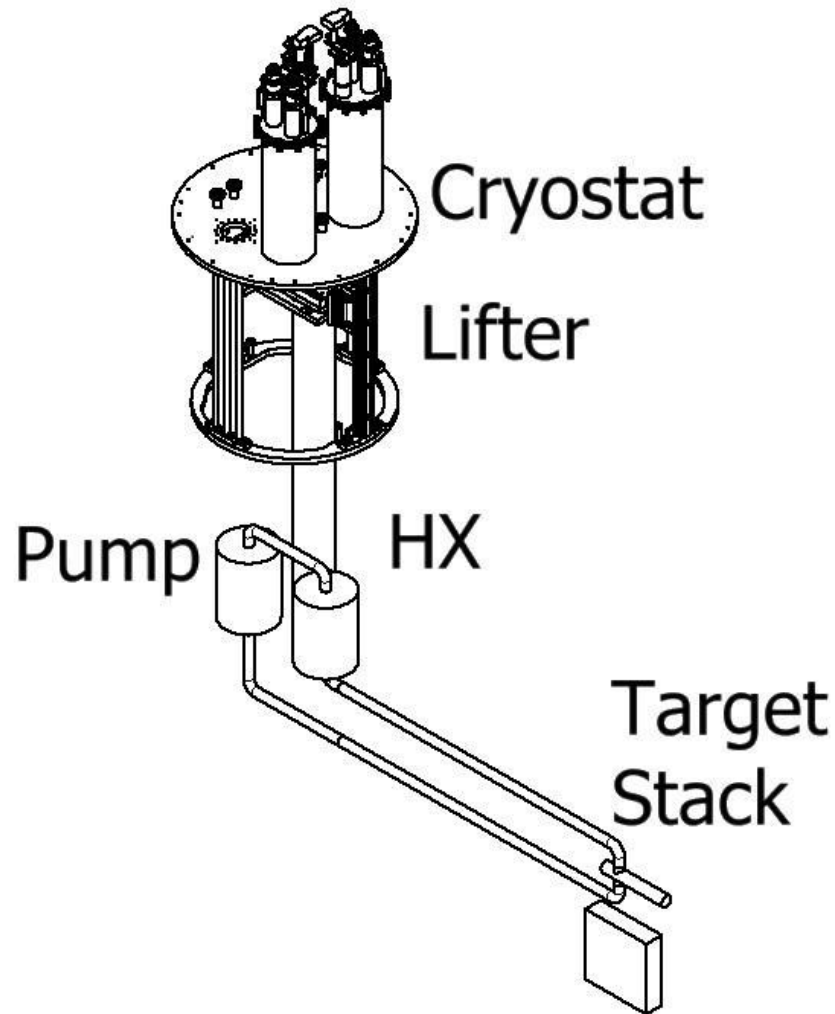
Careful attention must be given to the design of the cell. While the requirements of this target regarding density fluctuations are much less stringent than those imposed on either the Qweak or G0 targets, it is of some concern. Analysis of the cell design using computational fluid dynamics (CFD) will be employed to ensure an acceptable cell design. Based on experience with previous targets at JLAB, noise associated with density fluctuations is not expected to be significant compared to counting statistics. To reduce the background from Al-e- asymmetries, the sections of the cell upon which the beam impinges will be thin. Thicknesses of 120 μm are commonly available and are adequate for the needs of the experiment. The remainder of the cell will be designed to optimize boiling performance, detector acceptance, and pressure safety. High strength aluminum alloys such as AL-7075 and AL-2219 (used on welded components) shall be used on critical parts of the cell. Through extensive experience it has been shown that cell and cell block assemblies are much more reliable when welds and mechanical joints such as conflat (CF) are employed. This avoids the issues with solder and other sealing techniques. This approach also accelerates the design and prototyping phase and simplifies testing and assembly.

To avoid interference between the exiting particles at maximum scattering angle of 35° and the upper and lower target components, the cell and dummy target must be separated by a minimum of 28 cm plus half the width of the cell and dummy target. Similarly the dummy and the solid targets (positioned at $Z = 0$) will require 14 cm of separation plus half the width of the dummy target and first solid target frame. A total stack height of more than 70 cm is expected. The motion system must accommodate this height and allow for some alignment adjustments. The standard Hall A cryogenic target has over 70 cm of travel, thus a similar mechanism will be suitable.

Dummy and solid targets can be selected and installed as needed. The thickness of the dummy target will be chosen to match the radiation length of the liquid cell. Solid targets required for optics studies, background measurements and alignment checks will also be installed.

The cryogenic liquid hydrogen and deuterium target must accommodate a beam current of 50 μA on a 40 cm long cell. The estimated beam heat load for this is $\sim 800\text{W}$. The pump, heater overhead, transfer line and other losses require an additional estimated $\sim 250\text{W}$. During the Qweak experiment, more than 3 kW of power at 20K was dissipated by the heat exchanger. This design made use of both 15K and 4K refrigerant from the End Station Refrigerator (ESR) and the Central Helium Liquefier (CHL). A careful study of the target heat load and ESR/CHL refrigerators will be necessary to design the heat exchanger. However, it is expected that the heat exchanger will not need to dissipate more than 1500 W which includes a comfortable operating margin. Operationally, only $\sim 1\text{kW}$ of refrigeration will be required by one or more refrigerator.

The hydrogen and deuterium target fluids may become slightly polarized in the magnetic field of the solenoid. This would result in an asymmetry unrelated to the physics of interest. This effect can be mitigated in the case of deuterium with an RF-depolarizer. In the case of hydrogen, pure para-hydrogen would reduce this effect. A catalyst (such as an iron oxide bed) would enhance the



para to ortho fraction.

References

- [1] X. Qian *et al.*, Phys. Rev. Lett. 107, (2012) 072003. J. Huang *et al.*, Phys. Rev. Lett. 108 (2012) 052001.
- [2] T.D. Averett, *et al.*, Nucl. Instr. and Meth. A 427 (1999) 440.
- [3] J. Maxwell *et al.*, to be submitted to Nucl. Instr. and Meth. A.
- [4] D.G. Crabb, C.B. Higley, A.D. Krisch, R.S. Raymond, T. Roser, and J.A. Stewart, Phys. Rev. Lett. 64, (1990) 2627.
- [5] C.D. Keith, *et al.*, Nucl. Instr. and Meth. A 684 (2012) 27.
- [6] C.D. Keith, *et al.*, Nucl. Instr. and Meth. A 501 (2003) 327.

[7] Design Report rfq 14231, Oxford Instruments Nanotechnology Tools Ltd.

6 Baffles

In order for the detectors in the PVDIS experiment to operate at the design luminosity, a set of baffles is required that passes a reasonable fraction of the DIS electrons while blocking as much of the background as possible. The baffles provide curved channels through which only the spiraling high energy negative particles can pass. Most line-of sight photons and positively charged hadrons are blocked.

The design of the baffles requires careful optimization since there are many sources of background and the different detectors respond differently to the different backgrounds. The dominant background in the GEM's is soft photons, especially those between 1 and 2 MeV. The GEM's are relatively inefficient for lower energy photons. Sources of these photons include beam bremsstrahlung, forward radiation from wide-angle 30-100 MeV Møller electrons generated in the target, and photons from showers in the baffles induced by neutral pions. The light gas Cerenkov is sensitive to pair production from photons above 20 MeV or so which can come from neutral pions produced in the target to bremsstrahlung from the wide-angle Møller electrons. The ECal is sensitive the positive hadron punch-through and high energy photons from neutral pion decay.

To design the baffles for a specific magnetic field and detector configuration, ray-tracing of simulated DIS electrons is performed for the desired momentum range. For a uniform solenoidal field, high momentum electrons have a trajectory in $\phi - z$ space that is linear and the $\theta - z$ trajectory is independent of the field. The design process takes simulated electrons in a realistic field and exploits this approximate behavior to define pathways for ranges of electron momenta. This allows for a relatively simple design process involving an extended target where one considers radial rings of restricted scattering angle and places blocking material to only allow these trajectories.

In Fig. 52, the trajectories for two specified momenta cutoffs are shown by solid black and red lines. If one places material which follows the profile by the solid black and dotted lines, the acceptance is optimized to allow particles between the two momenta while disfavoring particles outside that range. The number of sectors to be used for this experiment is driven by the azimuthal angle ϕ traversed by the number of particles, which for these kinematics is on the order of 12° , hence 30 sectors.

To block line-of-sight photons, there must be sufficient material to block line particles that have a constant trajectory in ϕ . Due to the fact that the target is extended, the simple model does not completely hold, allowing some fraction to leak through.

The present design is shown in Fig. 53. The number of baffles has been increased from the original proposal design to prevent pion punch-through. The acceptance of DIS electrons for this design is shown in Fig. 54. The photons that leak through this design are blocked by 2.5 degree wide (in phi angle) lead strips in front of the calorimeter. This causes very small loss of DIS electrons which are bent away from the line-of-sight area when they reach the calorimeter. Further baffle design should be able to improve the overall performance. The PVDIS asymmetry uncertainty for 11 GeV beam with this baffle is shown in Fig. 55.

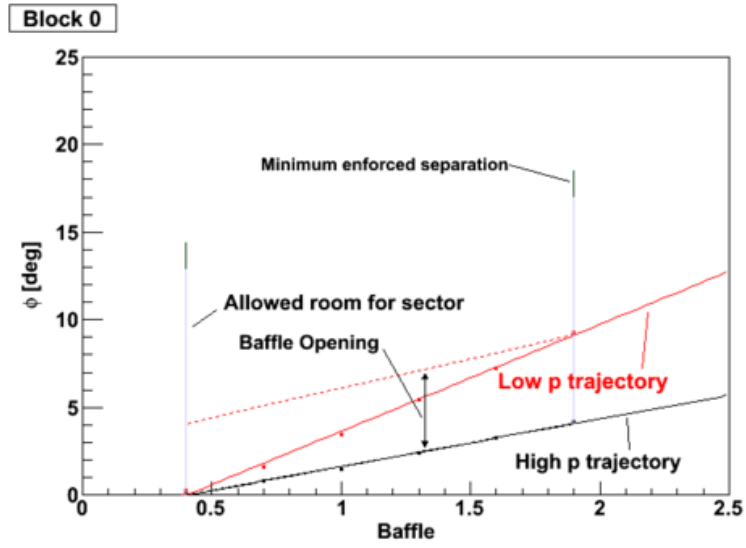


Figure 52: Raytraced electron trajectories used in baffle width design.

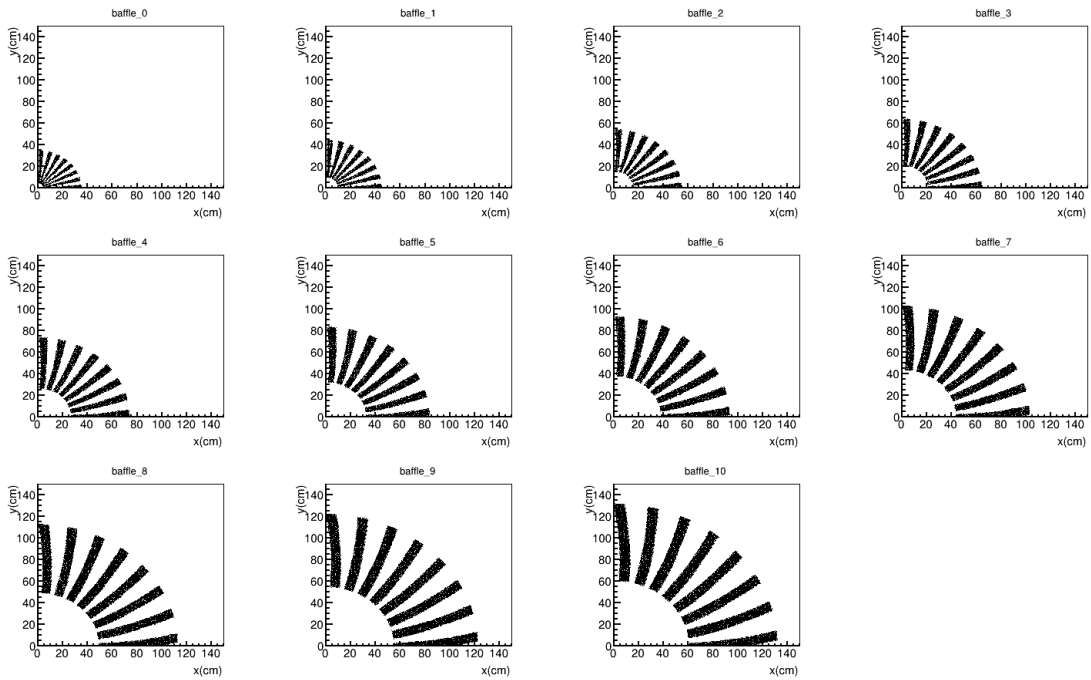


Figure 53: Baffle profiles

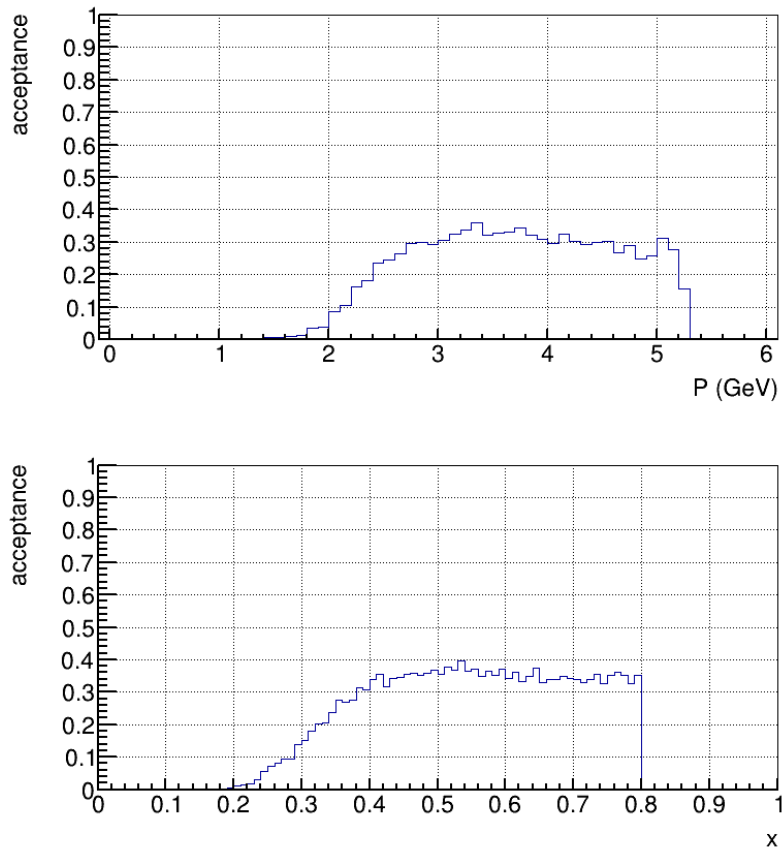


Figure 54: DIS electron propagation efficiencies

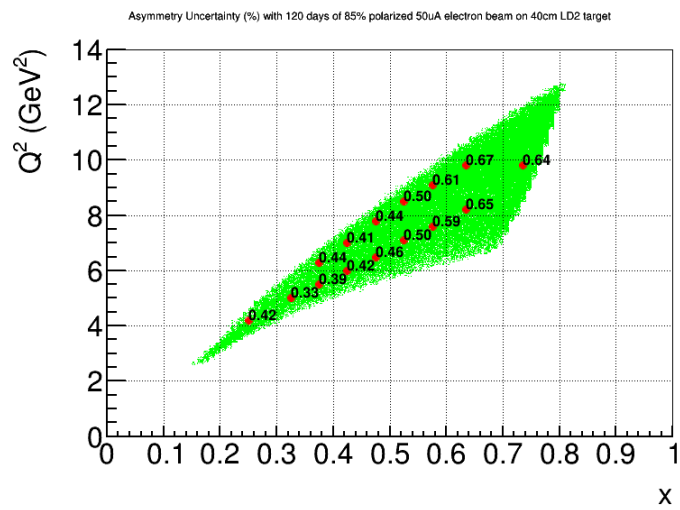


Figure 55: Anticipated statistical precision for SoLID with the current baffle.

7 GEM Tracker

The SoLID spectrometer requires high resolution track reconstruction under high rate conditions over a large area. A cost effective solution for such requirements is provided by the Gas Electron Multiplier (GEM) technology invented by F. Sauli [1] in 1997. The GEM is based on gas avalanche multiplication within small holes (on a scale of $100\ \mu\text{m}$), etched in a Kapton foil with a thin layer of copper on both sides. The avalanche is confined in the hole resulting in fast (about 10 ns rise time) signals. Several GEM foils (amplification stages) can be cascaded to achieve high gain and stability in operation. The relatively small transparency of GEM foils reduces the occurrence of secondary avalanches in cascaded GEM chambers. All these properties result in very high rate capabilities of up to 100 MHz per cm^2 and an excellent position resolution of $70\ \mu\text{m}$. Fig. 57 illustrates the principle of operation of a triple (three foil) GEM chamber. Triple GEM chambers were successfully used in the COMPASS experiment at CERN [2].

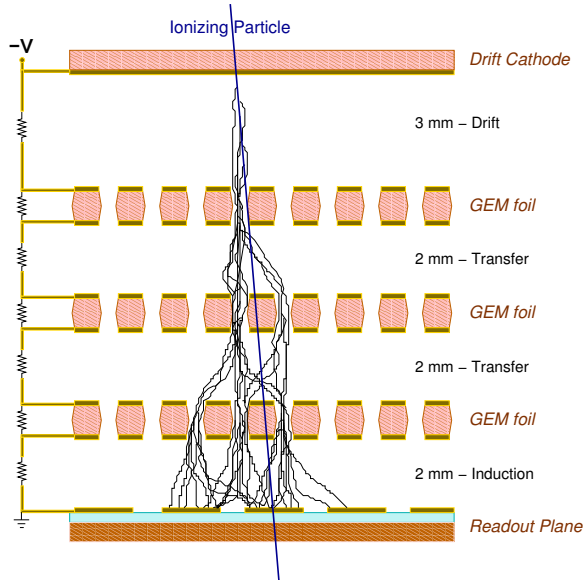


Figure 56: Principle of triple GEM operation.

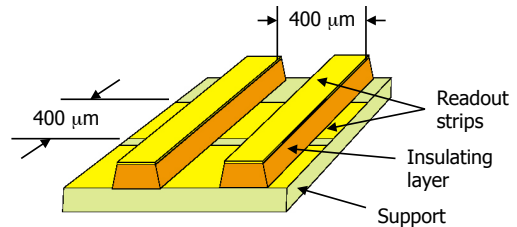


Figure 57: 3D view of the readout board.

For the PVDIS configuration of SoLID, detector locations 1, 2, 3, 4, and 5 will be instrumented with GEM chambers. Table 4 summarizes the parameters of the SoLID PVDIS GEM chambers. At each detector location there will be 30 trapezoidal GEM chamber modules, one for each sector defined by the baffles. The GEM modules will have an angular width of 12° with the readout stripes parallel to the two edges of the sector, so that the stripes from the two readout layers are at a 12° stereo angle. The readout pitch for locations 1, 2 and 3 will be 0.4 mm while the pitch for locations 4 and 5 will be 0.6 mm. Figure 58 shows the GEM module arrangement for one of the detector locations of the PVDIS configuration. Figures 59 and 60 show the details of the GEM module edges and mounting at the inner and outer radii of the SoLID detector wheel.

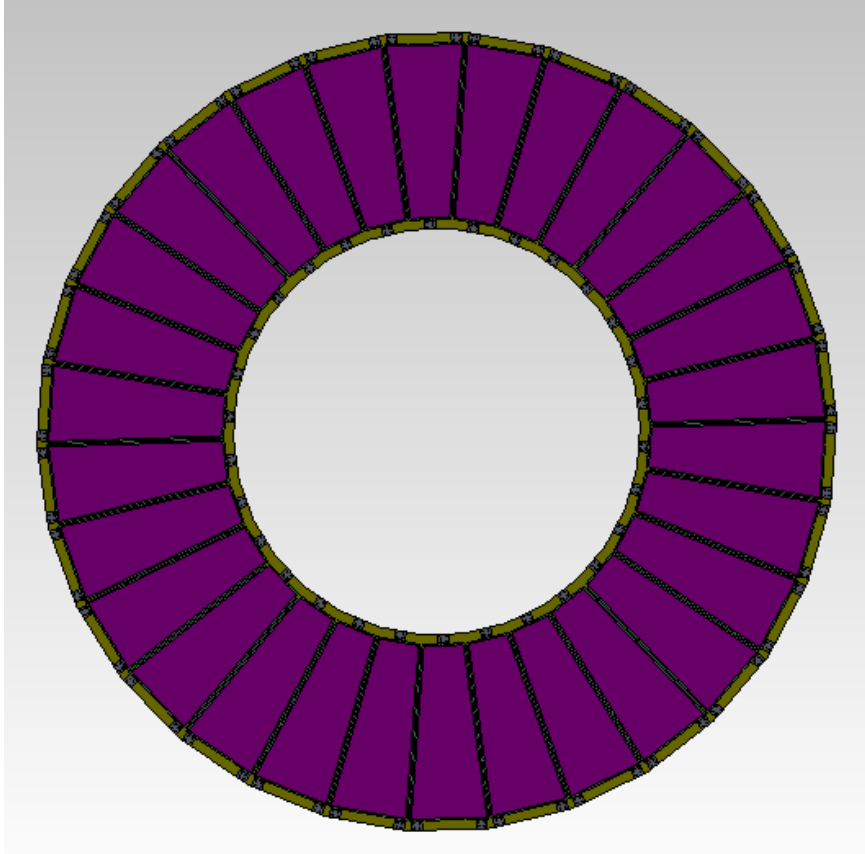


Figure 58: The GEM module arrangement at one of the detector locations of the SoLID PVDIS configuration

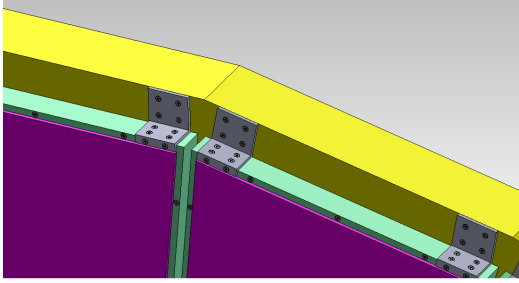


Figure 59: GEM module mounting at the outer edge of a GEM ring in the PVDIS configuration.

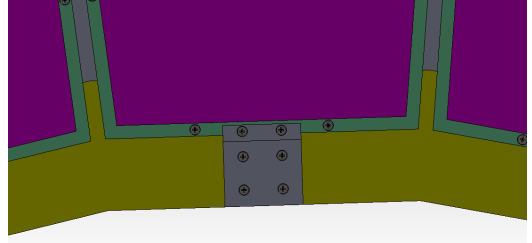


Figure 60: GEM module mounting at the inner edge.

Location	Z (cm)	R_{min} (cm)	R_{max} (cm)	Surface (m ²)	# chan
1	157.5	51	118	3.6	24 k
2	185.5	62	136	4.6	30 k
3	190	65	140	4.8	36 k
4	306	111	221	11.5	35 k
5	315	115	228	12.2	38 k
Total				≈ 36.6	≈ 164 k

Table 4: The locations, sizes and number of readout channels of GEM detectors for the SoLID PVDIS configuration

The SIDIS configuration of SoLID calls for detector locations 1, 2, 3, 4, 5, and 6 instrumented with GEM modules. Table 5 summarizes the parameters of the SIDIS GEM chambers. While the number of detector stations is higher in the SIDIS configuration, the inner and outer radii of the detector wheels are significantly smaller compared to the PVDIS configuration. Furthermore, since there are no baffles in the SIDIS configuration, the active detection area has to cover the entire surface area of each detector wheel. In order to meet these requirements, the SIDIS detector configuration will be set up by arranging the GEM modules from the PVDIS configuration in an overlapping two-wheel arrangement at each detector station as indicated in Figure 61. In this arrangement, 20 modules cover the entire active area of each detector station.

Location	Z (cm)	R_{min} (cm)	R_{max} (cm)	Surface (m ²)	# chan
1	-175	36	87	2.0	24 k
2	-150	21	98	2.9	30 k
3	-119	25	112	3.7	33 k
4	-68	32	135	5.4	28 k
5	5	42	100	2.6	20 k
6	92	55	123	3.8	26 k
Total				≈ 20.4	≈ 161 k

Table 5: The locations, sizes and number of readout channels of GEM detectors for the SoLID SIDIS configuration

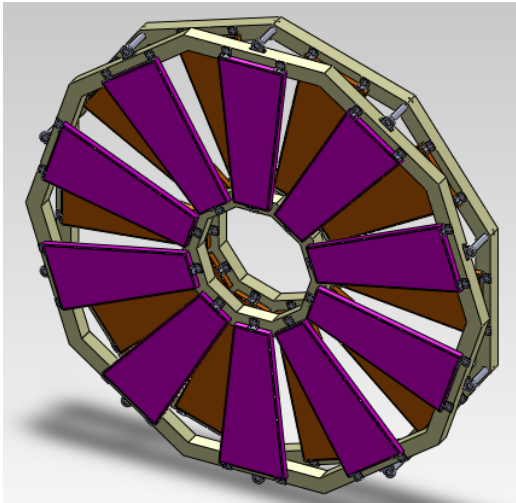


Figure 61: The GEM module arrangement at one of the detector locations of the SoLID SIDIS configuration

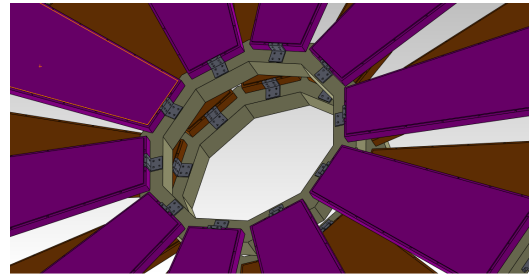


Figure 62: GEM module mounting at the inner edge of the ring in the SIDIS configuration

Figure 63 shows the detailed design for a GEM module of the size proposed for SoLID. The “wings” shown in the frames are to support the frames during chamber assembly; they will be removed once the chamber is completed. The 2D readout plane will be glued on the bottom plate (shown in cyan). This plate, made out of a 3 mm thick honeycomb structure material, also provides

structural rigidity to the GEM chamber. All other frames are made out of Permaglass³ with 8 mm wide sides. The spacers shown within the active area are for keeping the GEM foils from touching each other; these spacers are approximately 300 μm wide and contribute only about 1% reduction to the active area of the chamber. The GEM foils are mounted on the 3 light green frames, while the drift cathode is glued on the red frame. A thin gas window is glued on the orange frame.

Figure 64 shows the concept for the 2D readout frame. Strips for one direction (shown in blue) continue across the readout plane, while the short segments of the strips for the other direction (shown in red) are connected via through holes to readout lines running along the back of the plane. Large area readout planes of similar design have been tested in prototype GEM chambers for KLOE2 at Frascati.

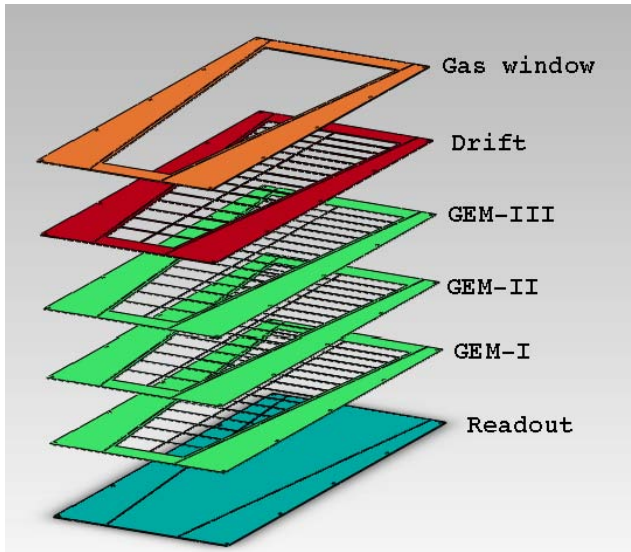


Figure 63: The frame assembly for a GEM module prototype of the size proposed for the largest SoLID GEMs

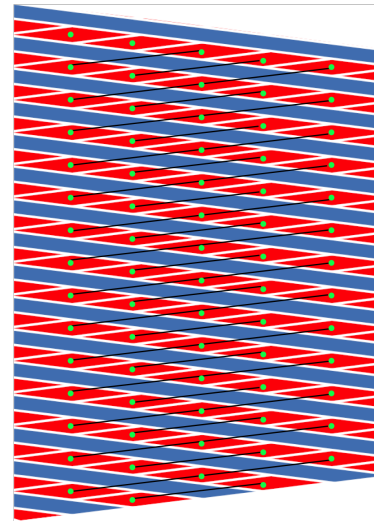


Figure 64: The schematics of the 2D readout plane proposed for SoLID

One challenge we are facing for the GEM trackers of SoLID is the large active area required; the active area of the largest GEM modules needed will be approximately $113 \times (21-44) \text{ cm}^2$. Until recently, the maximum GEM foil area had been limited to $45 \times 50 \text{ cm}^2$. However, over the last few years the Micro Pattern Gas Detector (MPGD) group at CERN, in collaboration with INFN, has perfected two techniques to produce large area GEM foils: single mask GEM etching and GEM splicing [3, 4]. The single mask technique allows for the fabrication of foils as large as $100 \times 200 \text{ cm}^2$. The splicing technique allows for two such foils to be combined with only a 3 mm wide dead zone between the two foils. Recently several large prototype GEM chambers were constructed and tested at CERN using the large area GEM foils fabricated using the new techniques [5]. These new prototype chambers, constructed under the CMS upgrade GEM project, have trapezoidal shapes with an active areas of $99 \times (25-45.5) \text{ cm}^2$; these dimensions are close to the dimensions of the largest GEM chamber modules planned for SoLID.

Furthermore, there have been significant advances in the GEM chamber readout systems in the recent years. The RD-51 collaboration funded Scalable Readout System (SRS) project at CERN has already developed and tested a low cost APV-25 based readout. The APV25-S1 analog readout

³Permaglass is a glass fiber material with randomly oriented fibers that can be machined with very high precision.

chip [6] is currently in use for the COMPASS GEM trackers and the CMS silicon strip detectors. A mid-size prototype system consisting of 15,000 channels was successfully tested and was shown to work very well. The SRS group is continuing the development and is also working with a commercial vendor to fabricate the SRS modules. The cost of the APV-25 based SRS readout is expected to be approximately \$ 3 per channel.

7.1 GEM tracker R&D

Research and development towards the SoLID GEM tracker is currently being conducted in the United States at the University of Virginia (UVa) and in China at five institutions: China Institute of Atomic Energy (CIAE), Lanzhou University (LZU), Tsinghua University (THU), the University of Science and Technology of China (USTC) and the Institute of Modern Physics (IMP). According to the current plan, the UVa group, which has an ongoing large area GEM module production program, will do the initial designs and prototyping of the SoLID GEM chambers, while the Chinese institutions get their large area GEM production programs set up. At the same time CIAE has been working with CERN and Chinese manufacturers to develop large area GEM foil production capabilities in China.

7.1.1 GEM chamber R&D program in UVa

The Istituto Nazionale di Fisica Nucleare (INFN)-Roma group and the University of Virginia group are currently leading an aggressive R&D program to develop large area GEM chambers for the Hall A Super Bigbite apparatus (SBS). The active area of large tracking chambers of SBS will be $50 \times 200 \text{ cm}^2$. These large GEM trackers will be assembled by combining $40 \times 50 \text{ cm}^2$ and $50 \times 50 \text{ cm}^2$ “chamber modules” with narrow edges. The UVa group has already constructed several $40 \times 50 \text{ cm}^2$ and $50 \times 50 \text{ cm}^2$ GEM chamber modules. The expertise gained with these GEM modules will be applied to the design of GEM modules for SoLID.

The UVa group operates a well-equipped GEM R&D facility that includes the following:

- **UVa Detector development lab:** This $10 \times 10 \text{ m}^2$, well-equipped nuclear physics detector lab has been used for the development, construction and testing of many large detector systems. The detector lab consists of two $3 \times 3 \text{ m}^2$ level 1,000 clean rooms located within a $4 \times 10 \text{ m}^2$ semi-clean area. So far seven large area GEM chambers have been successfully constructed in this clean room. The specialized GEM construction equipment in the lab includes large area GEM foil stretchers, GEM foil testing high-voltage boxes, a large volume ultra-sonic cleaner for GEM frame cleaning, a Keithley 6485 picoammeter for GEM foil testing, and a GEM foil storage dry N_2 box.
- **GEM readout systems based on APV25-S1 electronics:** The UVa group has two APV25 based readout systems: a 10,000 channel SRS system from CERN and a 3,500 channel system developed by the INFN group. Both systems are fully operational and are used for testing prototype GEM chambers.
- **Wiener-Iseg multi-channel high voltage system** The UVa detector group owns a brand new Wiener-Iseg multi-channel high voltage system that is especially suited to provide high voltage to sensitive tracking chambers. This system currently has 24 channels and can be expanded to 160 channels.

The $50 \times 50 \text{ cm}^2$ GEM chambers built at UVa are currently being tested with radioactive sources and cosmic rays. Figures 65 and 66 show results obtained from these test data. Figures 65 is the

absolute efficiency measured at several locations using electrons from a beta source, as a function of the high voltage. An efficiency of $\approx 97\%$ is achieved. Figure 66 is the ratio of cluster charge for x and y hits.

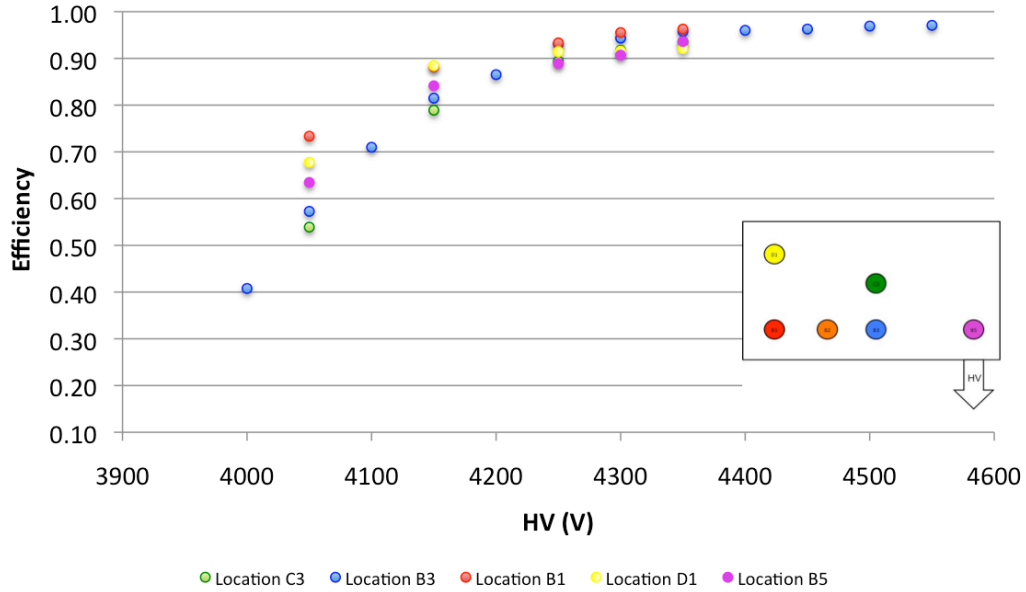


Figure 65: Efficiency of the $40 \times 50 \text{ cm}^2$ GEM chamber

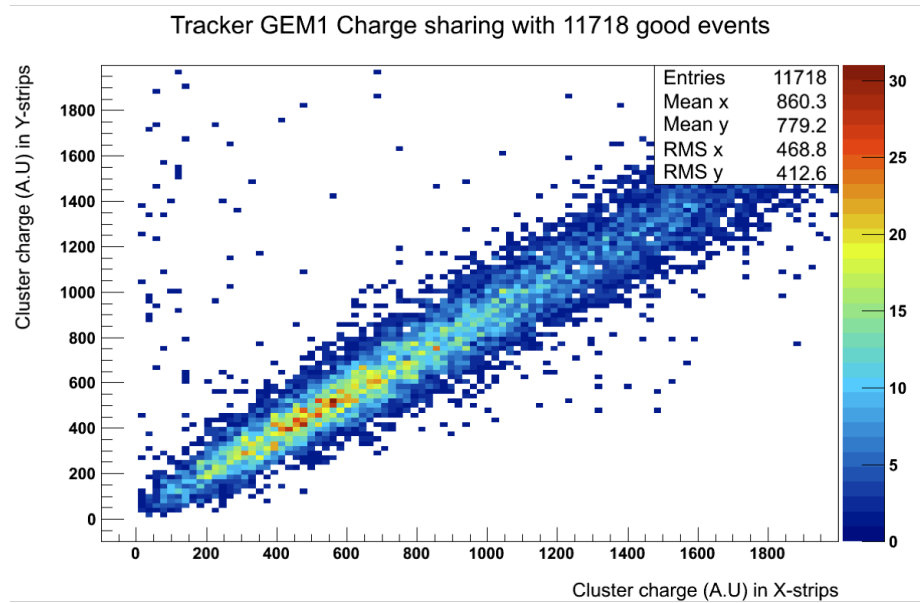


Figure 66: The charge division between x and y stripes for the $40 \times 50 \text{ cm}^2$ GEM chamber.

The UVa group recently completed the fabrication of a large prototype GEM module with di-

mensions of $100 \times (21-38)$ cm², approaching the proposed size of the largest SoLID GEM sectors (Figure 67). This prototype was constructed under the Electron Ion Collider (EIC) detector R&D program. This chamber is the largest GEM chamber ever built with a 2-D readout. Its readout consists of stripes from the two readout layers at a 12° stereo angle. The chamber is currently prepared for a beam test at Fermilab scheduled for October 2013. The development and testing of this large prototype is used to gain expertise and understand the mechanical, electrical and electronic properties of very large area GEM chambers.

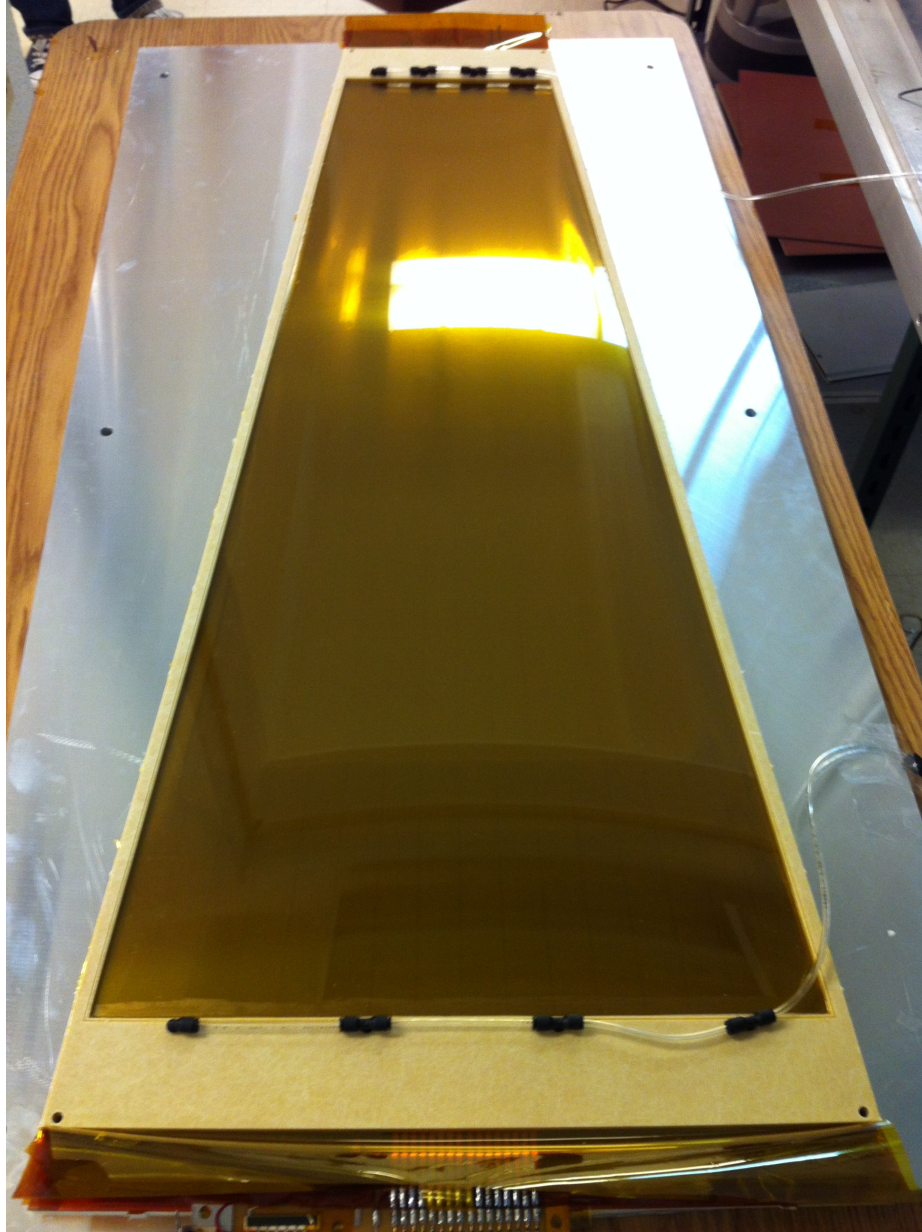


Figure 67: The 100 cm x (21 - 38) cm prototype GEM chamber at UVa being prepared for a beam test.

7.1.2 GEM chamber R&D programs in China

The five institutions of the Chinese collaboration for SoLID GEM detectors all have worked on gas detectors for many years, including R&D work on MWPC, MRPC, GEM, Micromegas, THGEM, and TPC, and applications of these detectors. These institutions have well-equipped GEM R&D facilities that include:

- Clean rooms for GEM detector assembling
- Front-end readout electronics based on APV25-S1 (developed by the INFN group)
- Multi-channel HV power supply systems and DAQ systems

CIAE, which has over 20 years of experience in nuclear pore foil production and Kapton etching, just signed a license agreement for manufacturing and commercialization of GEM foils and GEM based products with CERN, and received technical assistance from CERN. The base material of GEM foil is ultrathin, non-adhesive copper on a polyimide substrate, which can be purchased from CERN and other vendors. Several printed circuit board (PCB) technologies are applied during the manufacture of GEM foil. Recently, CIAE has started working on:

- Production of photo-masks, a component for the manufacturing of PCBs which is transferred onto a light-sensitive chemical resist covering the surface of copper layer in the production of GEMs.
- Lamination and exposure of dry film photoresist: Using a hot roll lamination (HRL) machine, both sides of the GEM substrate are laminated simultaneously by photoresist. The exposure system consists of an exposure unit, vacuum exposure frame, light source cooling, and an exposure control unit. This treatment transfers the photo-mask pattern onto the photoresist, forming an exact copy.
- Copper etching.
- Polyimide film etching.
- Final cleaning and chrome coating.

Figure 68 shows the film etching device at CIAE. In the beginning of 2013, a physicist from CIAE completed a training in GEM foil manufacturing at CERN.

LZU has been building a Micromegas+AFTER chip system for fast neutron (14 MeV) imaging in the past few years. The experience gained from this R&D work is useful to their GEM project. For instance, several designs of neutron converters with different parameters were tried in a simulation based on MCNP4 and GEANT4 (for both Micromegas and GEM), and different conversion efficiencies were compared. Other studies based on Garfield to improve the spatial and time resolution (as shown in Figure 69) were also performed and were proved to be helpful for the experimental study. The first version of the detector frame was designed and manufactured. 4 sets of GEM foils with the standard frame were purchased from CERN. Currently, a PhD student and a staff member are working together on the APV25-VME system. In the summer of 2013, an engineer visited JLab to gain experience about the SoLID DAQ.

THU has experience with GEM detectors by developing the electronics, such as a GEM-based TPC readout, a 16-channel CSA and shaping amplifier for GEM. Recently, a planar GEM tracking detector prototype was assembled for a spatial resolution test. In this test, THU used the event rate



Figure 68: Film etching device at China Institute of Atomic Energy

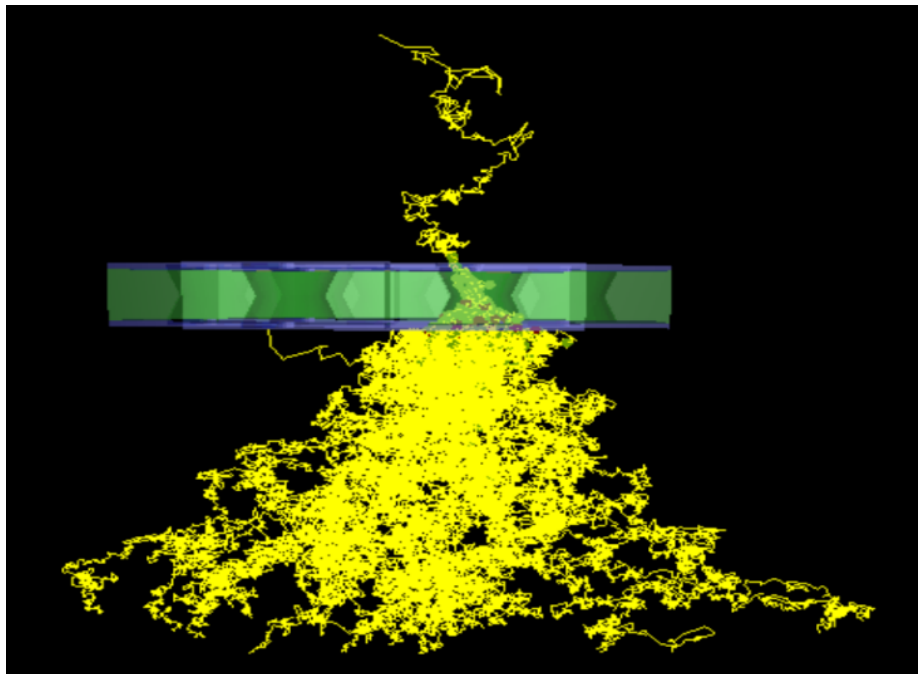


Figure 69: Avalanche process of an electron in a hole of GEM

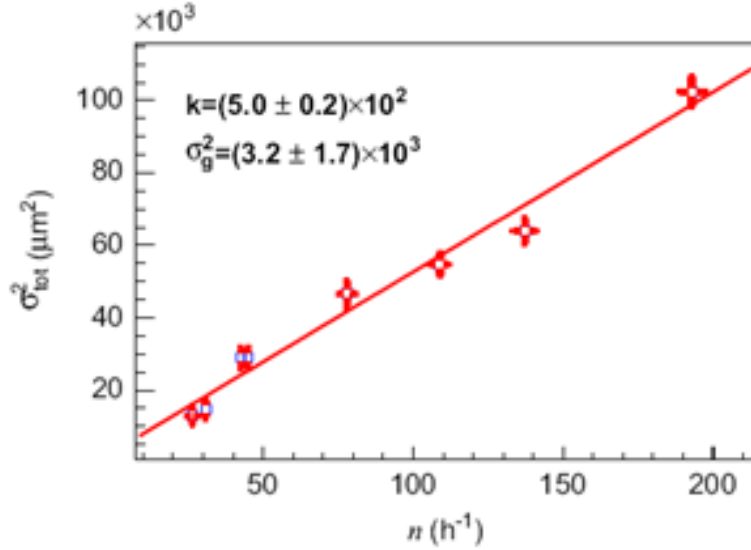


Figure 70: Linear fit of σ_{tot}^2 versus n

to substitute for the square of the slit width to overcome the magnified uncertainty of the spatial resolution which arises from the uncertainty of the slit width. The test demonstrated that the total position variance of the incident particles exhibits a linear dependence on the event rate or square of the slit width. The next step was to extend the measurement to zero slit width which is not directly achievable, and it was practically implemented by a linear fit to data points on the $\sigma_{tot}^2 - n$ plane. Figure 70 shows the linear fitting of σ_{tot}^2 versus n and the spatial resolution of the prototype is $56 \pm 14 \mu\text{m}$. Currently, THU is focusing on the inter-foil and inter-strip distance effects of the GEM detector. An APV based DAQ system will be built in the near future.

USTC started the GEM R&D work in 2000. After working on the 3D electric field simulation of GEM, USTC carried out a detailed gain performance test for the $10 \times 10 \text{ cm}^2$ triple GEM detector, then made a GEM X-ray imaging prototype. Both Center-of-Gravity (COG) and delay-line readout methods were used on this imaging prototype and a very good spatial resolution ($\sim 80 \mu\text{m}$) was obtained. Currently, USTC is focusing on the R&D of the large area GEM detector. Due to the fact that large area GEMs built by the glue technology have some disadvantages (e.g. very long assembling period; parts of GEM detector are not replaceable; dead regions in the effective area; aging problems of the glue and so on), USTC decided to use the NS2 (No Stretch, No Stress) technology for the construction of a $30 \times 30 \text{ cm}^2$ GEM detector. NS2, which was developed at CERN recently, is a totally new technology especially used for large area GEM detectors. The idea of NS2 is to use screws and a stable main frame to achieve self-stretching of the GEM foils. The advantages of NS2 are:

- The whole construction process involves mainly tightening the screws, so it is easy and fast and we can assemble a detector in half a day.
- Because all the GEM foils are self-stretched, the detector does not need support frames. There is no glue aging problem or dead area inside the detector.
- All the screws can be loosened and tightened again, so that any part of the detector is replaceable. This also means that the cost of the project can be greatly reduced.

USTC just finished the design of the new $30 \times 30 \text{ cm}^2$ NS2 GEM and purchased six $30 \times 30 \text{ cm}^2$ GEM foils from CERN. The HV dividers and screws are ready. The frames, drift electrode and readout PCB are in manufacturing. The readout electronics and instruments are ready. Figure 71 shows a model of the $30 \text{ cm} \times 30 \text{ cm}$ NS2 GEM detector (without readout PCB). This detector has been assembled and tested in Summer 2013.

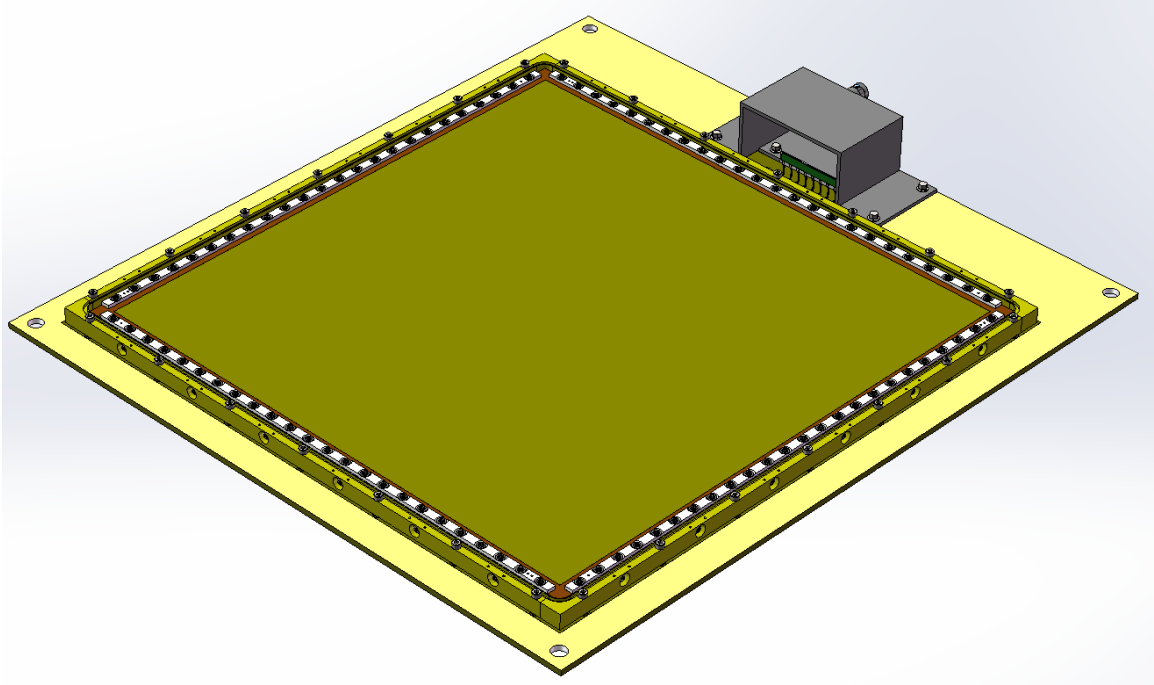


Figure 71: Design of the $30 \times 30 \text{ cm}^2$ NS2 GEM detector

References

- [1] F. Sauli, Nucl. Inst. and Meth. **A 386**, 531 (1997).
- [2] B. Ketzer *et al.*, Nucl. Phys. B (Proc. Suppl.) **125**, 368 (2003).
- [3] M. Villa, *et al.*, Nucl. Inst. and Meth. **A 628** 182 (2011).
- [4] M. alfonsi *et al.*, Nucl. Inst. and Meth. **A 617**, 151 (2010).
- [5] D. Abbaneo *et al.*, Nucl. Inst. and Meth. **A** (2010).
<http://dx.doi.org/10.1016/j.nima.2012.10.058>
- [6] M.J. French *et al.*, Nucl. Instr. and Meth. **A 466** 359 (2001).
- [7] F.Sauli, RD51-NOTE-2012-007 REVISED 21.09.2012.
- [8] D. Abbaneo *et al.*, RD51-NOTE-2012-012 16.11.2012.
- [9] William Whyte, “Cleanroom Technology: Fundamentals of Design, Testing and Operation” (2001) ISBN 978-0-470-74806-0

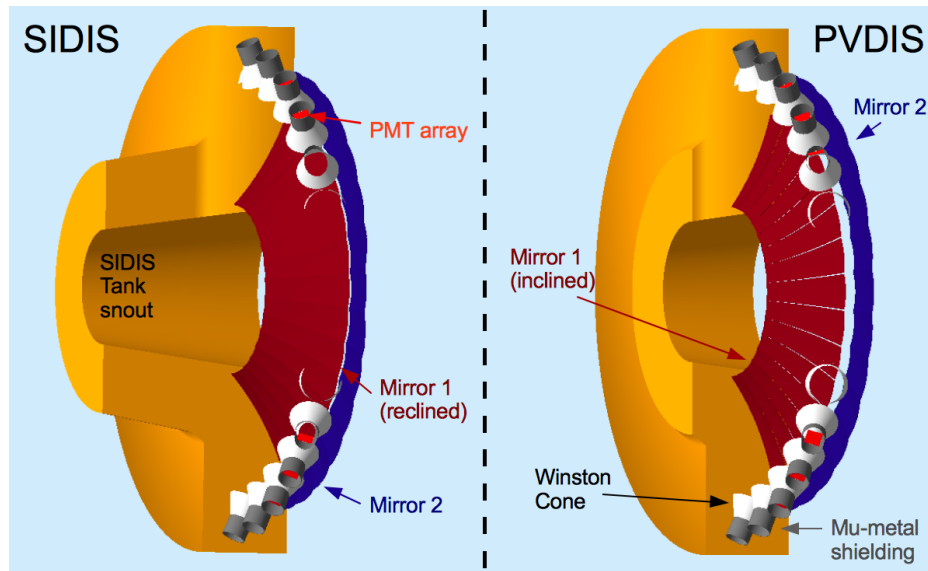
- [10] P. Walker, V. Weber, *et al.*, Journal of Photographic Science, **18** 150 (1970).
- [11] J. M. Shaw, J. D. Gelorme, *et al.*, IBM Journal of Research and Development. **41** 81 (1997)
ISSN: 0018-8646
- [12] Rensheng Wang, Yan Huang, Zhigang Xiao *et al.*, Nucl. Inst. and Meth. **A701** 54 (2013)

8 Light Gas Čerenkov

8.1 Design

The light gas Čerenkov detector for SoLID is divided into 30 identical sectors to match the 30 sector symmetry of the PVDIS baffle system. Many elements of the light gas Čerenkov remain identical between the PVDIS and SIDIS / J/Ψ experimental configurations, but some elements are adjusted or added / removed. Beyond the criteria dictated by the experimental physics requirements, the design of the Čerenkov detector was optimized with the goal of reducing the costs of construction and maintenance over the detector's lifetime including the switch over between experiments. The specifications of the tank and each major element per sector for each configuration are described below:

Figure 72: A side by side cross-section comparison of the light gas Čerenkov detector for both the SIDIS and PVDIS configuration with all major components labeled.



8.1.1 Tank and Čerenkov Gas

The main body of the tank remains identical between PVDIS and SIDIS configurations, and has a length roughly 105 cm with an inner radius of 71 to 85 cm, and an outer radius of 265 cm. With the PVDIS baffles removed for SIDIS, an additional tank 'snout' is attached upstream of the main tank inside the additional space evacuated by the baffle system. This tank snout adds an additional 107 cm of length to the tank with an inner radius of 58 to 71 cm, and an outer radius of 127 to 144 cm. In both configurations, the windows will be constructed from polyvinyl fluoride (PVF or Tedlar) at a thickness of 0.05 mm and 0.1 mm for the entrance and exit windows respectively. PVF provides a strong and gas-tight seal at minimal density (1.45 g/cm^3). SIDIS will use a standard CO_2 gas radiator (refractive index 1.0004), where PVDIS will use a mixture of 65% $\text{C}_4\text{F}_8\text{O}$ and 35% N_2 (refractive index 1.001) to increase Čerenkov radiation due to a shorter path length through the Čerenkov gas without the tank snout. Both configurations will use the Čerenkov gas at near standard atmospheric pressure.

8.1.2 Mirrors

Each sector will consist of two spherical mirror segments with dimensions listed in Tab. 6. Radially outward from the beam line, the inner most segment we will refer to as mirror 1 (red in Fig. 72) and the outermost segment as mirror 2 (blue in Fig. 72). In order to accommodate two different incident particle angles between PVDIS (22° to 35° from a central Z-vertex 270 cm away) and SIDIS (8.0° to 15.0° from a vertex 520 cm away), mirror 1 must be adjusted between experiments such that the reflected Čerenkov light in both configurations falls into the PMT detector acceptance. This is achieved by rotating mirror 1 by an angle of approximately 8° inward about the mirror’s inner-most edge (or edge closest to the beam-line). In Fig. 72 we see a cross section of the light gas Čerenkov, sliced along the beam or Z-direction, with the mirrors in both the reclined and inclined positions. Mirror 2 is fixed in position and rotation and non-contributing to the SIDIS configuration; however, mirror 2 is necessary to cover the larger angular range in the PVDIS configuration. The mirrors will be crafted from carbon-fiber-reinforced polymer (CFRP) by Composite Mirror Applications (CMA) [2] with an areal density no larger than 6 kg/m^2 . The surface smoothness and uniformity will achieve a D0 spot size of $<2 \text{ mm}$ and be of similar quality to the mirror blanks CMA manufactured for the RICH detectors at LHCb [3]. Mirror coating will be preformed by our collaborators at Stony Brook, and will consist of high reflectance ($\geq 85\%$ for $\lambda = 200 \text{ nm}$ to 620 nm) aluminum with a protective coating of MgF_2 .

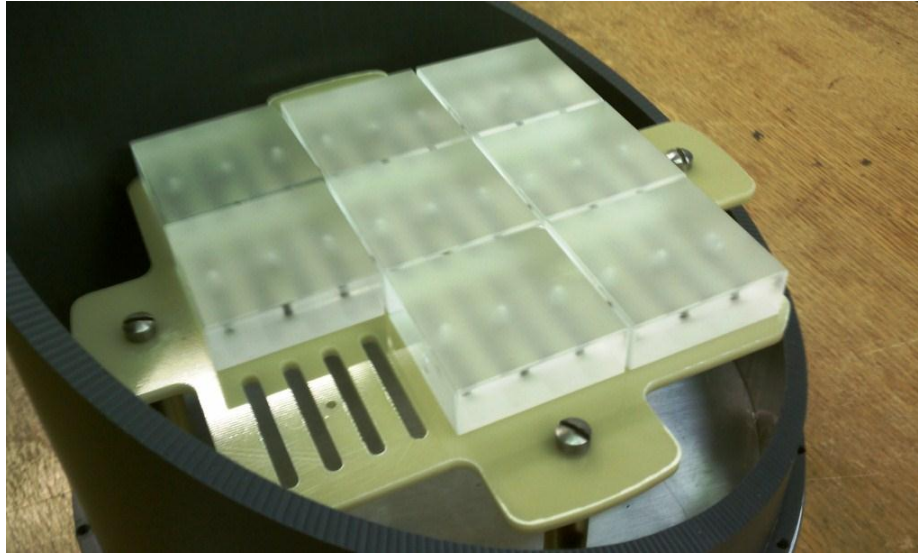
Mirror	inner-edge W (cm)	outer-edge W (cm)	L (cm)	R of curv. (cm)
Mirror 1	16.26	36.03	114.53	277.51
Mirror 2	37.06	45.95	59.26	157.99

Table 6: The dimensions of the two mirror segments in the light gas Čerenkov.

8.1.3 PMTs

The light gas Čerenkov will use Hamamatsu flat panel multianode photomultiplier tube assemblies: H8500C-03 [4]. These PMT assemblies are an 8×8 pixel square array with a total active surface area of $49 \text{ mm} \times 49 \text{ mm}$ with a UV-glass window, Bialkali photocathode material producing an average quantum efficiency around 15%, and a 12-stage dynode structure allowing resolution down to a single photoelectron. A 3×3 array of these PMT assemblies will be mounted in each sector, as shown in the PMT mounting prototype in Fig. 73. The position and orientation of the PMT array will remain fixed between PVDIS and SIDIS configurations. Every pixel in the H8500C-03 will be wired together to produce one signal per PMT; a trigger will then be constructed by requiring two PMT assemblies in the same array to fire in the same time-window, with a minimum photoelectron discrimination. Simulations show a $>90\%$ average electron detection efficiency, integrated over all angles and momenta, when requiring 2 separate PMTs assemblies in an array to each generate 3 or more photoelectrons in either the PVDIS or SIDIS configurations. This trigger configuration would result in 36 possible coincidences per sector consequently reducing the single photoelectron rate due to dark current or other backgrounds by at least a factor of 10. Specific filtering of the PMT signals will be tested while prototyping the PMT array and electronics. Additionally, we plan on improving the resolution of the PMT sum signal through matrix gain balancing of the PMT pixel-array patented by Vladimir Popov to Jefferson Lab.

Figure 73: PMT assembly mounting prototype showing 3×3 array of dummy PMTs inside the space restricted by magnetic shielding.



8.1.4 Magnetic Shielding and Winston Cones

The PMTs will be shielded by a mu-metal cylinder / cone construction that doubles as support for a reflective aluminum inner glass cone to direct light onto the PMT array. The cylinders will measure 30 cm in length with an inner radius of 11.28 cm, the cone will have a height of 30 cm with an inner radius of 7.8 cm at the narrow end and an inner radius of 21 cm at the wide end. The mu-metal shielding will be 0.04 inch thick reinforced by 0.125 inch thick 1008 carbon steel and manufactured by Amuneal Manufacturing Corp [5]. The PMTs are most sensitive to the magnitude of the magnetic field parallel to the photon collection face (transverse direction). We require a reduction of 95 gauss to <50 gauss in the transverse direction, and a reduction of 135 gauss to <50 gauss in the longitudinal direction, to where we expect an output loss <10% as seen in Fig. 74.

8.2 Tank Support

The Čerenkov tank front and back windows will be divided into six radial sections. Between each section will be two thin-rectangular Aluminum support spokes, one to support and frame the upstream side of the tank and another to support and frame the downstream side (see Fig. 75). Both spokes are positioned and aligned to minimize the probability of tracks passing through the support material. Additionally, both spokes are interconnected at the outer radius of the tank, outside of the desired physics acceptance, by a solid arc-shaped plane to increase the rigidity of the frame and add additional support for mounting the focusing cones and PMT assemblies. The space between the upstream and downstream spokes will remain open to maximize Čerenkov light collection. The combined frame itself will be mounted to the back wall of the downstream magnet housing, to support the full weight of the Čerenkov detector. This alleviates placing additional stress on the end-cap nose, which other additional downstream detectors will use to support their weight. Each PMT array will be accessible from the outer radial wall of the tank for alignment or maintenance purposes.

Figure 74: A test of the Hamamatsu H8500C PMT assembly in a magnetic field, courtesy of S. Malace [5]. The green boxes correspond to a magnetic field perpendicular to the PMT collection face. The blue and red markers show the effects of a transverse field on the PMTs.

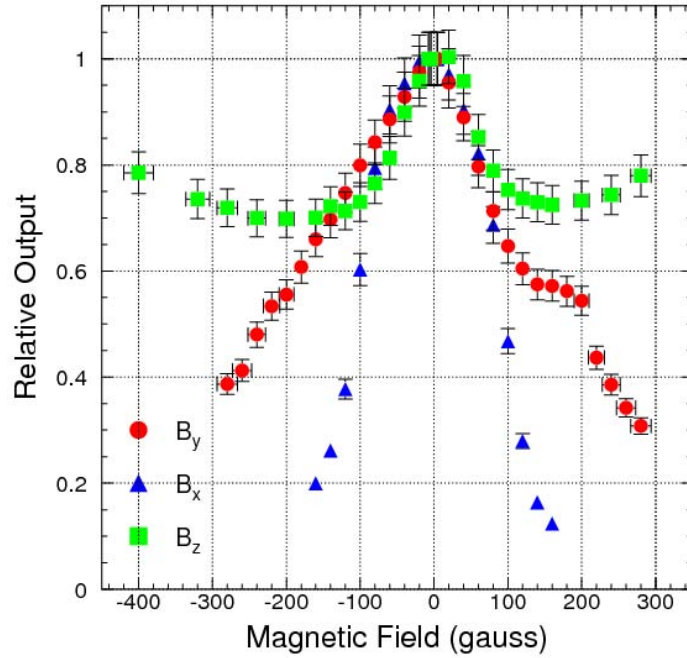
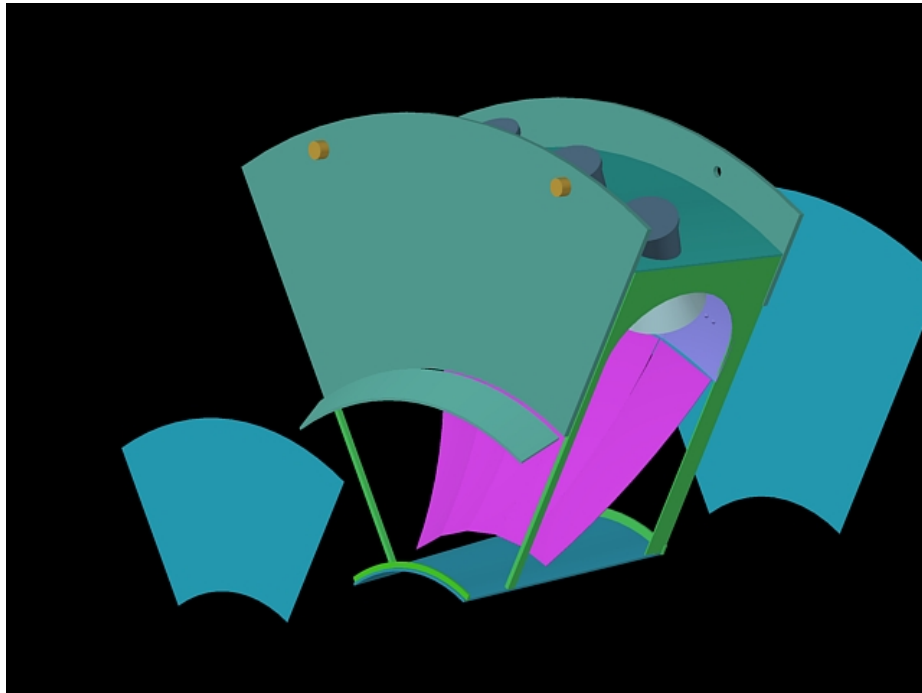


Figure 75: The support frame for one subsection of the light gas Čerenkov. The front and back acceptance windows (blue) are exploded to show the mirrors (pink and purple) and the support frame (green). The mounting points of the tank to the magnet housing are shown in orange.



8.3 Simulations

All simulations were done with a slightly modified version of the GEMC [6] software developed at Jefferson Lab. GEMC uses a GEANT4.95 [7] backend to simulate all particle tracking through and interaction with materials and geometries. All plots shown in the light gas Čerenkov section of this document use the same simulation dataset. Event generation was performed by the eicRate DIS event generation tool authored by Seamus Riordan. The simulations also have the following features:

- Acceptance through the PVDIS baffle system (PVDIS events only).
- Čerenkov radiation process for creation of optical photons.
- Expected Delta-ray and pair creation from e^- and π^- particles interacting with the Čerenkov front window using the standard and low energy EM packages for GEANT4.
- Expanded mirror reflection properties in GEMC to be more inline with the latest functionality from GEANT4.
- PMT photoelectron signal simulation which includes the PMT dead area, quantum-efficiency pixel-by-pixel, and optical properties of the PMT UV-glass window.

8.3.1 Collection Efficiencies

The collection efficiencies for electrons in both the PVDIS and SIDIS configuration can be seen in Figs. 76 and 77. The slight jump in photoelectrons around 32° in the PVDIS figure is a result of the inclined inner mirror, which moderately reduces the number of optical photons produced by reducing the particle's pathlength through the gas before crossing the mirror.

8.3.2 Background Rates

A low energy inclusive background simulation was performed using GEMC by generating an electron beam on target, including all expected materials between the beam entrance to the Čerenkov back window. Secondaries produced anywhere in the SoLID detector and above the Čerenkov radiation momentum threshold while passing through the Čerenkov gas were considered as a possible source of background. If any photoelectrons are produced at the PMTs from optical photons for these events, the resulting rates were calculated and explored with different possible trigger cuts. For the PVDIS configuration, a rate of ≈ 1.9 MHz per sector was determined using a greater than 1 photoelectron sum, or a rate of ≈ 1.6 MHz when requiring at least 1 photoelectron in 2 different PMTs in the same sector. For the SIDIS configuration, the expected background rate is considerably less: A rate per sector of ≈ 0.2 MHz is expected with a trigger cut of greater than 1 photoelectron sum, or a rate of ≈ 0.1 MHz when requiring at least 1 photoelectron in 2 different PMTs.

8.3.3 Pion Rejection

The expected pion rejection is shown in Figs. 78 through 81. All pion signal below the pion Čerenkov radiation threshold (3.2 GeV/c for the PVDIS gas) is produced by knock-ons or (e^+ , e^-) pair creation. The photoelectron signal itself is a poisson distribution convoluted with a gaussian to simulate the PMT 1 photoelectron resolution. The pion-electron photoelectron cut is determined by taking the intersection of the two signal distributions, simultaneously maximizing the electron selection probability while maximizing the pion rejection probability. Additional calculations are

Figure 76: PVDIS configuration: The number of surviving photoelectrons versus theta after losses due to quantum efficiency of the PMTs, PMT dead area, or secondary reflections / absorptions off of the cones or PMT UV-glass window for events in the 5 cm of target most upstream (left) and 5 cm of target most downstream (middle). The right plot shows the corresponding collection efficiency versus theta for all 40 cm of the target Z-vertex.

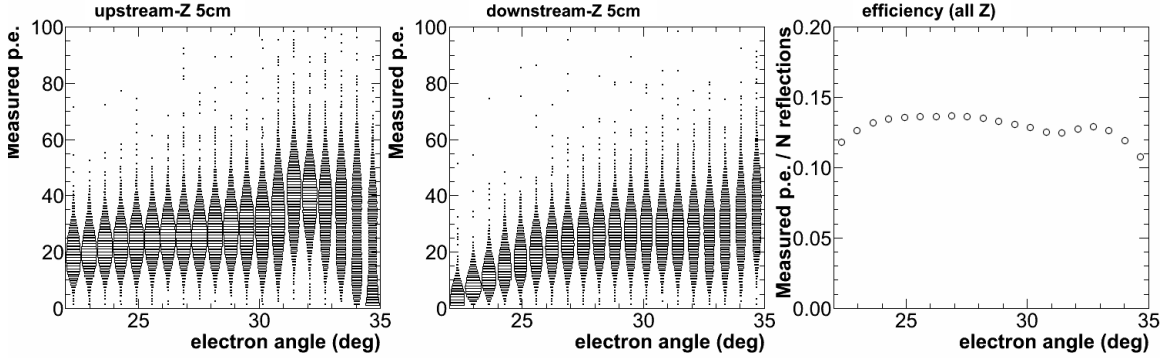
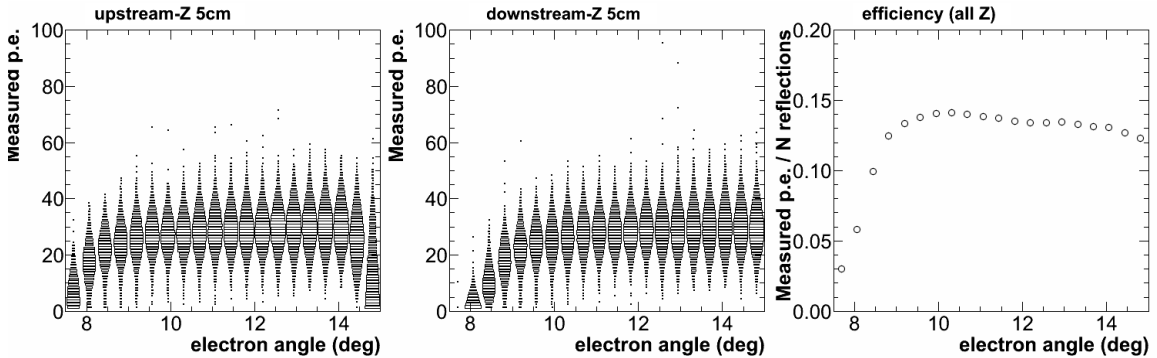


Figure 77: SIDIS configuration: Same as in Fig. 76 but with the SIDIS configuration.



shown in Figs. 78 and 80 with a stricter cut on the pion signal, which consequently reduces the electron efficiency (by 10% for the red points and 20% for the blue points). An example of these photoelectron cuts are shown in table for one bin in momentum in the PVDIS configuration.

References

- [5] S. P. Malace, B. D. Sawatzky and H. Gao, “Studies of single-photoelectron response and of performance in magnetic field of a H8500C-03 photomultiplier tube,” JINST **1309**, P09004 (2013) [arXiv:1306.6277].
- [2] Composite Mirror Applications, Inc. 1638 S. Research Loop, Suite 100 Tucson, Arizona 85710. <http://www.compositemirrors.com>
- [3] LHCb RICH Technical Design Report, The LHCb Collaboration: lhcbrich.web.cern.ch/lhcbrich/richtdr/tdr.pdf
- [4] Hamamatsu flat panel type multianode photomultiplier tube assembly H8500 series specifications are found at http://jp.hamamatsu.com/products/sensor-eta/pd002/pd394/H8500C/index_en.html

Figure 78: PVDIS configuration: The pion rejection factor versus momentum for 3 electron selection efficiencies: The nominal efficiency maximizes the pion rejection while minimizing loss of electrons, the red points correspond to a stricter pion cut with up to 10% additional loss of electrons, and the blue points allow an additional 20% loss of electrons.

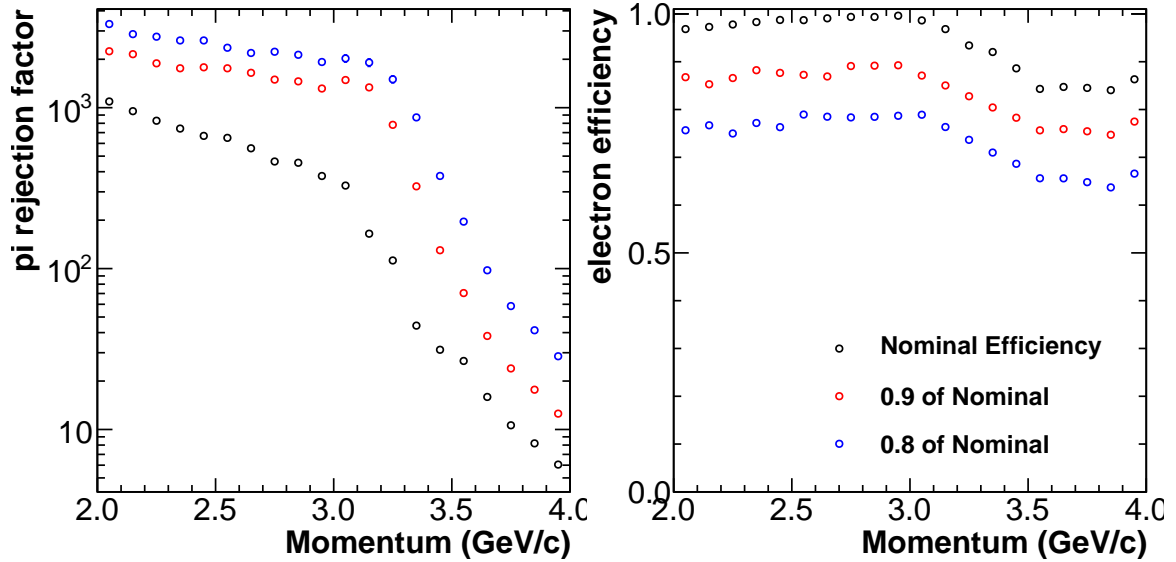
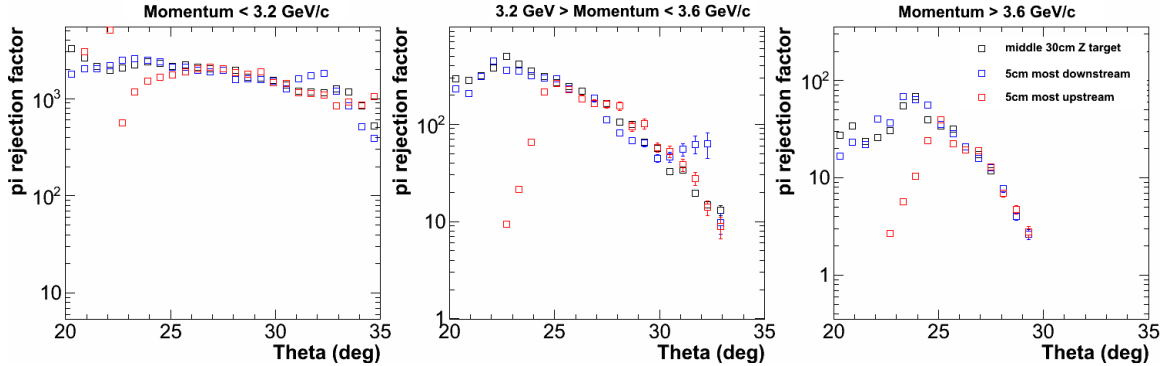


Figure 79: PVDIS configuration: The pion rejection factor versus the electron scattering angle theta over 3 momentum and Z-vertex ranges.



[5] Amuneal Manufacturing Corporation. 4737 Darrah Street Philadelphia, PA 19124, USA. www.amuneal.com

[6] GEMC: a GEant4 Monte Carlo. <https://gemc.jlab.org/>

[7] GEANT4: a toolkit for the simulation of the passage of particles through matter: <http://geant4.cern.ch/>

Figure 80: SIDIS configuration: Same as in Fig. 78 but with the SIDIS configuration.

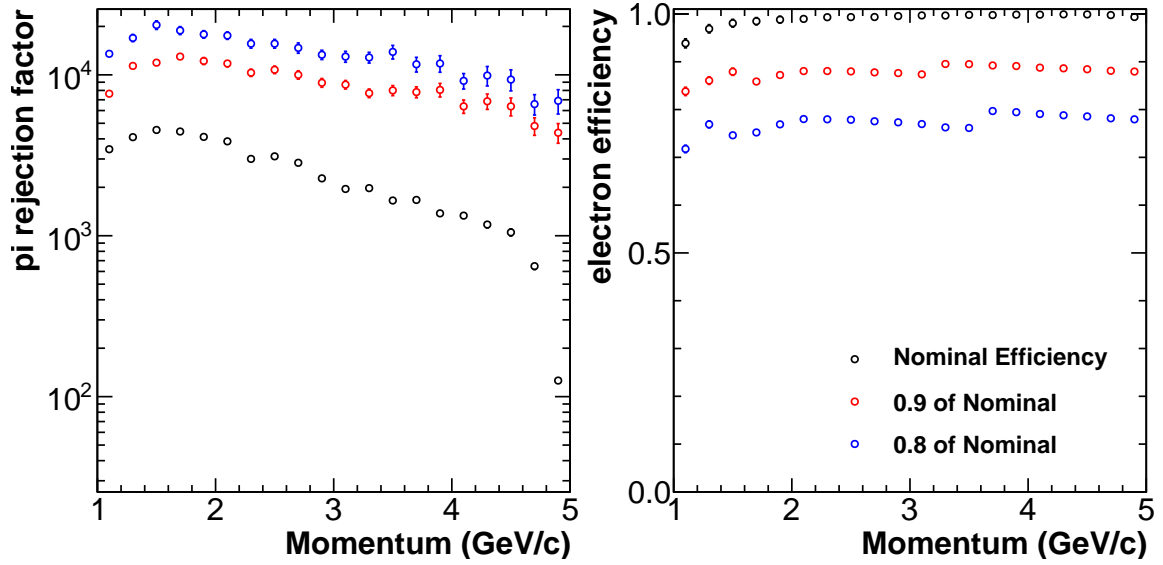


Figure 81: SIDIS configuration: Same as in Fig. 79 but with the SIDIS configuration.

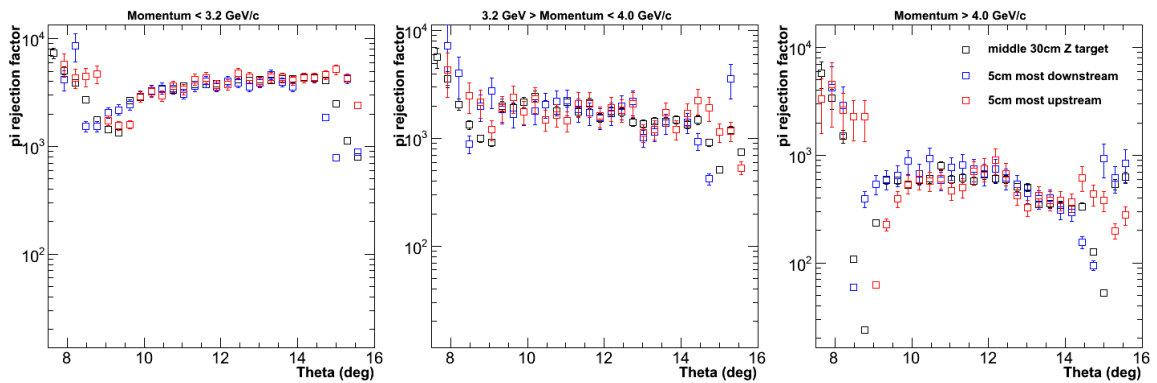
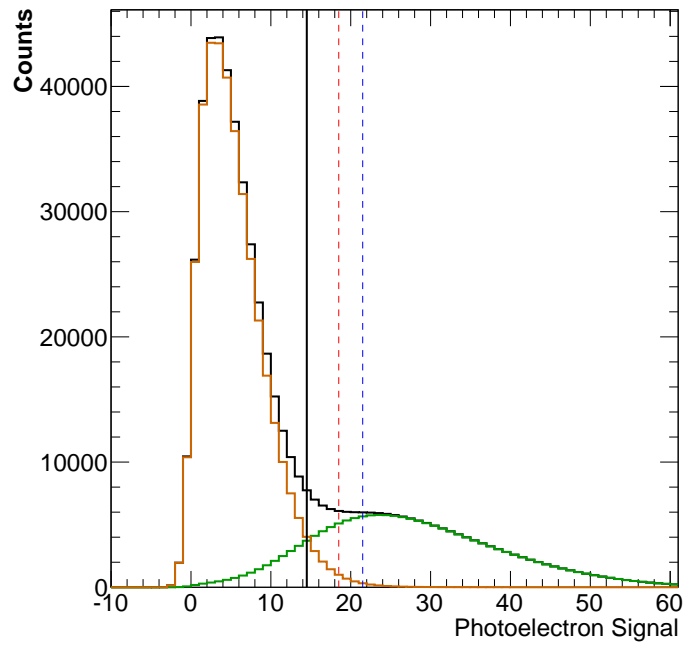


Figure 82: An example of the pion rejection cut made for one arbitrary bin in momentum for the PVDIS configuration. The pion signal is shown in orange and the electron signal is shown in green. The nominal efficiency cut is shown as a solid black line. The 90% and 80% electron efficiency cuts are shown as dashed red and blue lines respectively.



9 Heavy Gas Čerenkov

9.1 Optical System Design

A hadron Čerenkov detector is required to help with the identification of both positive and negative pions. A clear distinction between pion and kaon Čerenkov signals is mostly required in the mid to high momentum range, namely from 2.5 to 7.5 GeV. The C_4F_8O gas at 1.5 atm and a temperature of $20^\circ C$ gives a momentum threshold of 2.2 and 7.5 GeV for pions and kaons, respectively. Due to geometrical acceptance constraints the gas length available for Čerenkov light production is less than 1 m. Stringent requirements on the design are full azimuthal angular coverage and a good detector performance in a magnetic field with strength as high as 200 Gauss. The optical system for the Čerenkov light collection has been optimized using a GEANT4 simulation package taking into account the expected SoLID magnetic field configuration with the CLEO-II magnet. The system consists of a ring of 30 spherical mirrors of 1 m length each and inner and outer widths of 0.2 and 0.4 m, respectively. The mirrors will focus the light onto 30 PMT arrays as shown in Fig.83. The size of each PMT array could be reduced to 8x8 inches (i.e. 16 of 2-inch PMTs per array) by use of straight cones as an additional optical element to mirrors. The PMTs of choice are similar to those used for the light gas Čerenkov namely the multi-anode 2 inch H8500C-03 devices from Hamamatsu: they perform well in relatively high magnetic field, are square shaped, and have good photocathode coverage (89% of total area), making them ideal for tiling.

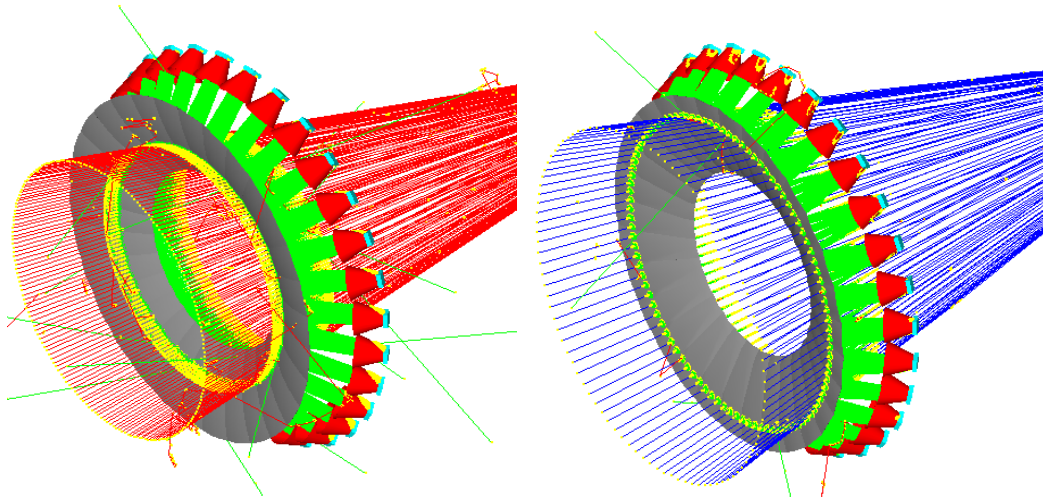


Figure 83: Optical system for the heavy-gas Čerenkov: a ring of 30 spherical mirrors (grey) will focus the Čerenkov photons created by the passage of negative (left panel) and positive (right panel) pions through the C_4F_8O radiator gas onto PMT (cyan) arrays with the aid of straight cones (red).

9.2 Simulation

9.2.1 Photon Electron Yield

Due to the SoLID geometrical acceptance with respect to the target and to the constraints on the photon detector positioning inside the Čerenkov tank, the particles with large polar angle entering the detector will travel a larger gas length compared to those with a low polar angle. Thus, the

optimization was done favoring the low angle kinematics whenever possible and by keeping the number of maximum reflections to 2: one on the mirrors and one possibly on the cones (not all photons need the extra bounce on the cones to be collected by the PMT arrays). As a consequence, the loss of photons through absorption on the reflective surfaces is kept to a minimum.

Our simulation of the expected number of photoelectrons shown in Fig.84, left panel, takes into account realistic parameters for the gas index of refraction, gas transparency, mirror and cone reflectivities and the quantum efficiency of the H8500C-03 PMTs to account for the photon to photoelectron conversion. We scaled down the number of photoelectrons obtained from the GEANT4 simulation by a conservative factor of 0.5 mostly to account for the dead zones on the PMT tiles due to incomplete photocathode coverage. The index of refraction of C_4F_8O has been measured at Syracuse University [1] between 400 and 650 nm, while below 400 nm we used an extrapolation based on a parametrization from HERA/DELPHI of this index[2]. We studied the impact on the expected number of photoelectrons on the large uncertainty in the C_4F_8O refractivity by assuming a refractivity 20% smaller than the nominal value extracted from the Syracuse and HERA/DELPHI measurements. We found that the yield of photoelectrons would still be sufficient, though marginal, at the lowest momentum of 2.5 GeV. The C_4F_8O transmittance has been measured at Jefferson Lab in Hall B with great accuracy in a photon wavelength range of 200 to 500 nm. We used these data in our simulation to account for Čerenkov photon absorption in the gas. For mirror, manufacturing glass could be an option, but we chose the Carbon Fiber Reinforced Polymer (CFRP) option, a more rigid, lighter material as a suitable choice for large size mirrors. We contacted the USA company Composite Mirror Applications (CMA) that manufactured CFRP mirrors for the LHCb program at CERN [3] and we received a favorable response regarding the feasibility of such mirrors for our detector. CMA supplied us with data on CFRP mirror reflectivity as measured on the LHCb mirrors they manufactured. We used these parameters in our simulation to account for the Čerenkov photon absorption on the reflective surface of mirrors and cones.

The photoelectron yield dependence on polar angle and momentum is shown in Fig.84, left panel. For a fixed polar angle the number of photoelectrons increases with increasing momentum as we move away from the pion firing threshold of 2.2 GeV and then saturates. There is also an increase of yield with increasing polar angle due to the detector geometry which allows pions with larger angle to traverse more gas than those with low polar angle.

9.2.2 Pion Detection Efficiency and Kaon Rejection Factor

The expected performance of the detector has been further studied by estimating the pion detection efficiency and kaon rejection factor for a given cut on the number of photoelectrons with no input from other particle identification detectors. Background studies have shown [4] that the expected pion to kaon ratio is 10 to 1. The pion and kaon photoelectron distributions are simulated as convolutions of Poisson and Gauss distributions. The resolution of the PMT enters as the standard deviation of the Gauss distribution while the mean of the Poisson distribution is the output of the GEANT4 simulation shown in Fig.84, left panel. We measured the resolution of H8500C-03 to be 1 photoelectron. We mapped the pion detection efficiency and kaon rejection factor for few kinematics where we expect the smallest number of photoelectrons, namely at 8.0 degrees and momentum between 2.5 and 4.5 GeV and our results are shown in Fig.84, right panel. Assuming that kaons would produce at most 1 photoelectron below the Čerenkov threshold, for a cut on the number of photoelectrons of 3, the pion detection efficiency is 99.0% (99.6%) at 2.7 GeV (3.0 GeV) with the same kaon contamination as small as 0.8%. At 8 degrees and below 2.7 GeV, the pion efficiency starts to drop below 99%. For larger momenta, a cut placed at 4 photoelectrons would result in a pion detection efficiency larger than 99.7% with a kaon contamination below 0.3%. This would

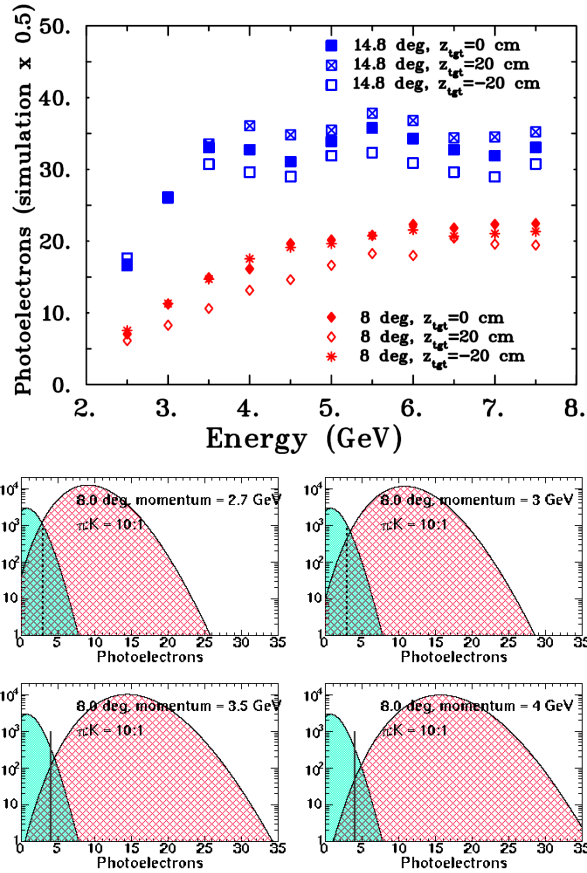


Figure 84: Left: Simulated number of photoelectrons as a function of the pion polar angle and momentum. The results are shown for positive pions. A very similar output is obtained for negative pions. Right: Simulated distributions of pions (red) and kaons (green) at with a polar angle of 8.0 degrees taking into account the photon detector resolution and the expected pion to kaon ratio.

meet the requirements of the approved experiments with SoLID.

9.3 Performance of the PMTs in Magnetic Field

We performed extensive bench tests of the H8500C-03 PMT at Jefferson Lab to map its performance in a magnetic field and assessed its capability of resolving single photoelectron signals[5]. The single photoelectron resolution was measured to be 1 photoelectron or better. The magnetic field test results are summarized in Fig.85. The longitudinal field is perpendicular to the face of the PMT and is labeled as B_z . The transverse field orientations, perpendicular to the sides of the PMT are shown as B_x and B_y . The PMT relative output is reduced by at most 30% when exposed to a longitudinal magnetic field up to 400 Gauss. Our studies of the single photoelectron response in field indicated that these losses happen mostly at the amplification stage on the dynode chain making it possible to compensate for this effect with external amplification. These results are very encouraging as it suggests that the effect of the field component which is hardest to shield, the longitudinal one, could be compensated for by superficial shielding and additional external amplification. The degradation of the PMT output in transverse magnetic field is more pronounced, up to 90% at 180 Gauss but this field component is easier to shield.

We contacted the USA company Amuneal requesting a feasibility study of a magnetic field

shield that would incorporate the cones used for focusing and that would reduce the SoLID field at the PMT location to 20 Gauss in the longitudinal direction and to 0 Gauss in the transverse one. The study showed that a 2-layer shield with a 0.04 inch inner layer of Amumetal and 0.125 inch outer layer of 1008 carbon steel with mylar in between would meet our requirements. Thus the cones would serve a dual purpose: help focus the Čerenkov light onto small size photon detectors and be an integral part of the magnetic field shield. The same reflective coating will be applied to the cones as to the mirrors.

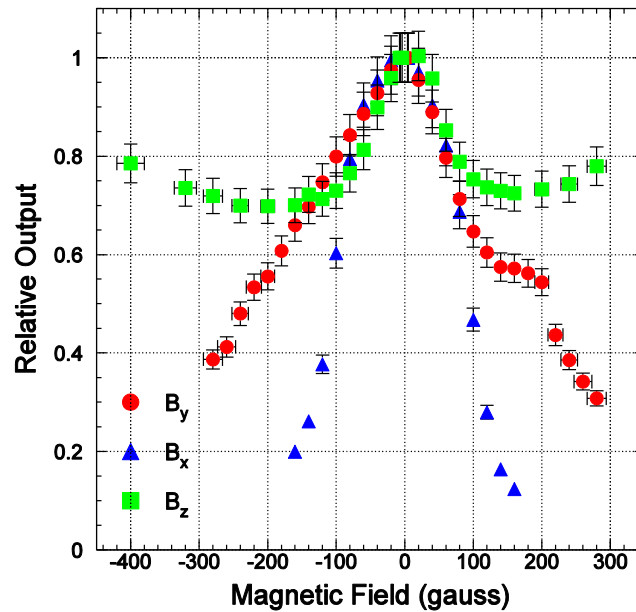


Figure 85: Relative output of the H8500C-03 PMT in magnetic field. The PMT output normalized to the zero magnetic field configuration is shown for a longitudinal field orientation (i.e. perpendicular to the face of the PMT) in squares and for the transverse orientations (i.e. perpendicular to the sides of the PMT) in circles and triangles.

9.4 Support Conceptual Design

A conceptual design of the heavy gas Čerenkov pressure tank is given in Fig.86 (left). The detector is separated into 6 (60 deg) segments to facilitate fabrication and handling. The structure is mostly made of Aluminum. The outer shell parts are formed into an arc, welded and then precision machined. The 30 PMT assemblies, see Fig.86 (right), insert from outside the tank, into tubes arrayed on the outer shell; they seal with an o-ring on a male gland. The Winston cones are mounted inside the outer shell, with the possibility of fine position adjustment (from outside) through the PMT mount tube. The CFRP spherical mirrors are fixed with mounts at each end of the mirror and attached to the tank's outer shell and inner cone, respectively. The detector is positioned, in the magnet pole extension assembly, on large 1.5 inch diameter precision SS rods (they could be shared with the adjacent detectors). The rods are mounted on the magnet extension black plate and insert into the magnet rear pole upon magnet assembly. Each detector segment will slide over them and are held in place (in Z) with shaft collars. The tank's inner cone is secured to the magnet inner cone.

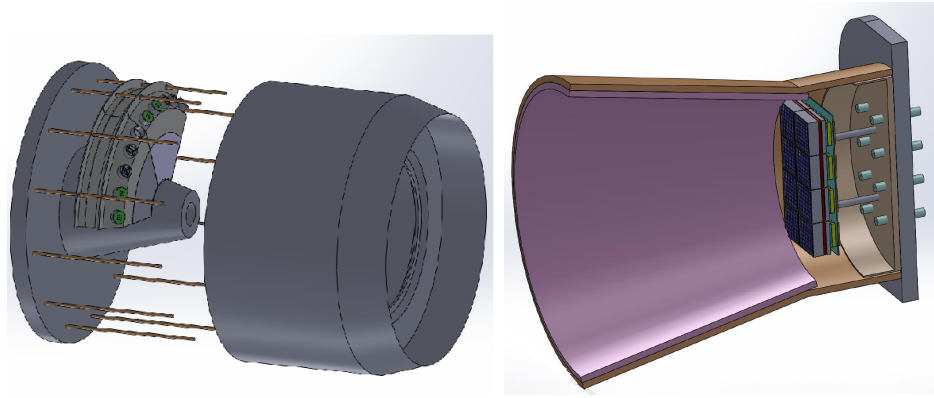


Figure 86: Conceptual design of the heavy gas Čerenkov detector (left) and PMT assembly (right)

References

- [1] M. Artuso *et al.*, Nuclear Instruments and Methods A, 558 373-387 (2006).
- [2] A. Bulla, Ph.D. thesis (1997); E. Foktitis *et al.*, Nuclear Instruments and Methods A 371 255 (1996).
- [3] G.J. Barber *et al.*, Nuclear Instruments and Methods A 593 624-637 (2008).
- [4] JLab approved experiments E-12-09-014 and E-12-10-006
http://www.jlab.org/exp_prog/proposals/09/PR12-09-014.pdf
http://www.jlab.org/exp_prog/proposals/10/PR12-10-006.pdf
- [5] S. P. Malace, B. D. Sawatzky and H. Gao, “Studies of single-photoelectron response and of performance in magnetic field of a H8500C-03 photomultiplier tube,” JINST **1309**, P09004 (2013) [arXiv:1306.6277].

10 Electromagnetic Calorimeter

10.1 Overview

Electromagnetic calorimeters (EC) are used in PVDIS, SIDIS and J/ψ experiments to measure the energy deposition of electrons and hadrons, and to provide particle identification (PID). The SIDIS and J/ψ experiments share similar configurations and will be referred to as the SIDIS configuration hereafter. There are three calorimeters: the PVDIS experiment uses a forward angle calorimeter (FAEC) to detect the scattered electrons; the SIDIS experiments use a forward angle calorimeter (FAEC) and a large angle calorimeter (LAEC), both detect the scattered electrons while FAEC also provide MIP triggers for pions. For electron detection, the dominant background comes from electro- and photo-produced pions. The desired performance is summarized in Table 7 and the EC geometry in Table 8. Please note that the EC geometrical coverage is slightly larger than other detectors because edges of EC are expected to have degraded performance due to shower spreading. The total coverage area of SIDIS FAEC and LAEC is less than that of PVDIS FAEC. The plan is to share modules between the two configurations, thus all modules need to be rearranged when we switch from PVDIS to SIDIS configuration and vice versa.

	Desired performance
π^- rejection	$\gtrsim[50:1]$ for above Cerenkov threshold
e^- efficiency	$\gtrsim 95\%$
Energy resolution	$< 10\%/\sqrt{E}$
Radiation resistance	$\gtrsim 400$ kRad
Position resolution	$\lesssim 1$ cm

Table 7: Overview of the SoLID calorimeter desired performance.

	PVDIS FAEC	SIDIS FAEC	SIDIS LAEC
z (cm)	(320, 380)	(415, 475)	(-65, -5)
Polar angle (degree)	(22,35)	(7.5,14.85)	(16.3, 24)
Azimuthal angle	Full coverage		
Radius (cm)	(110, 265)	(98, 230)	(83, 140)
Coverage area (m ²)	18.3	13.6	4.0

Table 8: Geometrical coverage for the SoLID electromagnetic calorimeters. The z direction is along the electron beam and the origin is at the solenoid center.

Design of the SoLID EC is determined by both the physics goal and the expected running conditions. The design is challenging due to our unique constraints including high radiation background (≈ 400 kRad, as in Table 7), strong magnetic field (1.5 T on SIDIS LAEC), large coverage area, and the budget. These factors prevent the use of many traditional calorimeter technologies, including NaI (Tl), CSI, BGO and lead-glass because of the low radiation resistance; PbWO_4 , LSO and PbF_2 because of their high cost; and lead/scintillator fiber calorimeter because of the high cost and the large amount of light readout required.

Due to the PID requirement, it is necessary to segment the EC longitudinally into a preshower and a shower detector. The following design that meets the experimental requirements was chosen: the shower calorimeter modules are based on the so-called Shashlyk design [1] – a sampling-type design consists of alternating layers of scintillator and lead (as an absorber); the preshower detector is made of a layer of lead as a passive radiator followed by scintillator pads [2, 3]. Details of the design is summarized in Tables 9 and 10.

Type	passive radiator + sensitive layer
passive radiator	$2X_0$, Pb
Sensitive layer	2 cm, plastic scintillator 100 cm ² hexagon tile
Light transportation	WLS fiber embedded in the scintillator

Table 9: SoLID electromagnetic calorimeter, preshower design.

Type		Shashlyk sampling calorimeter
Each layer	Absorber	0.5 mm Pb
	Scintillator	1.5 mm STYRON 637 plastic scintillator
	Gap	Paper, 0.12 mm \times 2 sheets
	Radiation Length	$0.093X_0$
Overall	Radiation length (X_0)	24 cm
	Molire radius	5 cm
	Length	$18 X_0$, 43.4 cm
	Total number of layers	194
	Lateral granularity	100 cm ² hexagon
	Light transportation	WLS fiber, 100 per module, penetrating layers longitudinally

Table 10: SoLID electromagnetic calorimeter, shower design.

The structure of both the preshower and the shower detector are illustrated in Fig. 87. In the experiment, particles incident close to perpendicular to the scintillator-lead layers. Scintillation light is absorbed, re-emitted and transported to the photon detector by wave-length shifting (WLS) optical fibers penetrating through the shower modules longitudinally, along the impact particle direction. The cross sectional area of the shower modules was optimized to be 100 cm² (see Section 10.2.3), with a hexagon shape determined for the convenience of the support structure design. The scintillator tile of preshower modules has the same 100 cm² hexagon shape to match the shower modules, which maximizes PID efficiencies, facilitates the design, and allows fast switch-over between SIDIS and PVDIS. The lead absorber of the preshower can be made of large sheets.

The Institute for High Energy Physics (IHEP) of Russia has extensive experience in the R&D and mass production of Shashlyk type calorimeters. They were consulted and provided inputs to the design of the SoLID EC. Currently they are expected to be the primary manufacturer for the SoLID EC.

Geant4-based simulations are used to study the performance and optimize the design of the key specifications while minimizing the cost. Figure 88 shows the simulated shower of a 3 GeV electron incident on the PVDIS EC. In the following we will present details of the shower and the preshower design, general layout and the support system, light readout, expected radiation dose, PID and trigger performance, and a cost estimate.

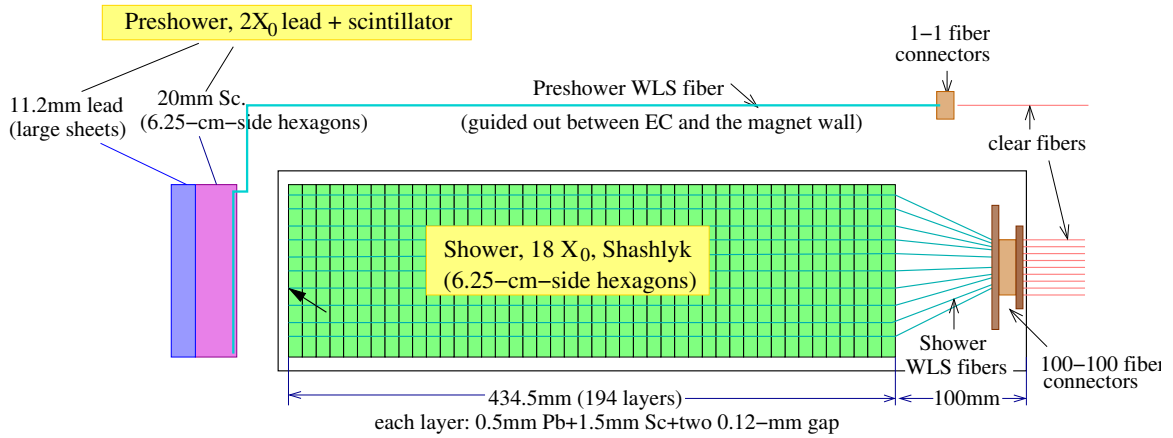


Figure 87: Design diagram of the SoLID electromagnetic calorimeter module. Spacing between the preshower and the shower detectors, and the spacing between the shower module and the 100-100 fiber connectors, need to be kept as small as possible yet still allow safe routing of the WLS fibers and positioning of the support structure.

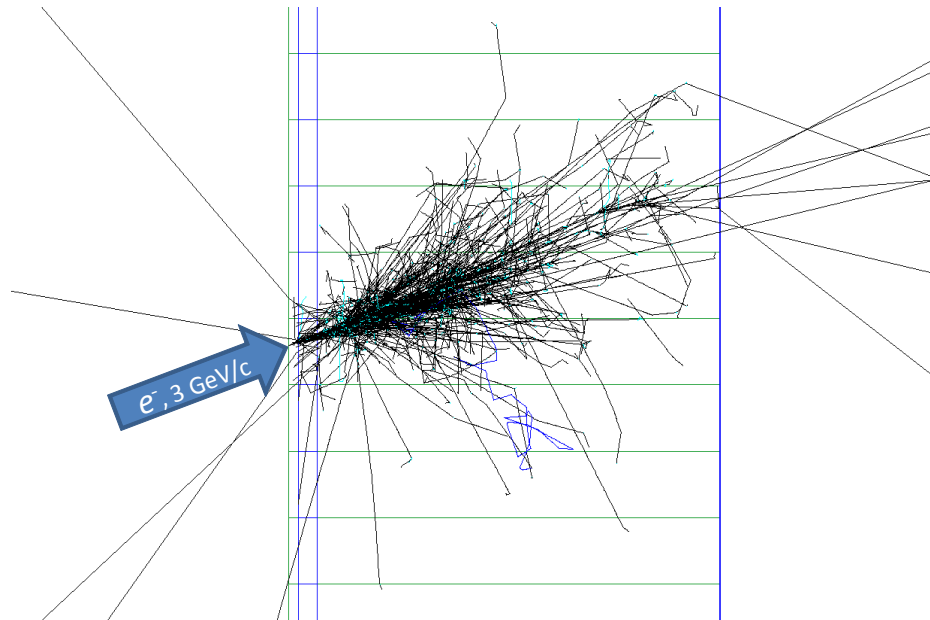


Figure 88: GEANT4 simulation of the shower generated by a 3-GeV electron incident on the PVDIS calorimeter. The black and green tracks are secondary photons and electrons respectively. The green horizontal lines are edges of calorimeter modules. The first two layers of materials are the preshower detector, consisting of $2X_0$ of lead and 2 cm thick of scintillator.

10.2 Shower Detector Design Considerations

10.2.1 Total Length of the Calorimeter

The overall length of calorimeter should be long enough to enclose most of the electromagnetic shower and short enough to maximize the difference in energy deposition between electrons and pions. The fraction of energy leak out for electron showers, averaged inside the acceptance of the SIDIS-Forward calorimeter, was studied for different total lengths of calorimeter. As shown in Fig.89, a total length of 20 radiation lengths was found to be a good balance. Considering the 2-radiation-length thickness of preshower, this leads to a shower detector length of 18 radiation lengths or 43.4 cm.

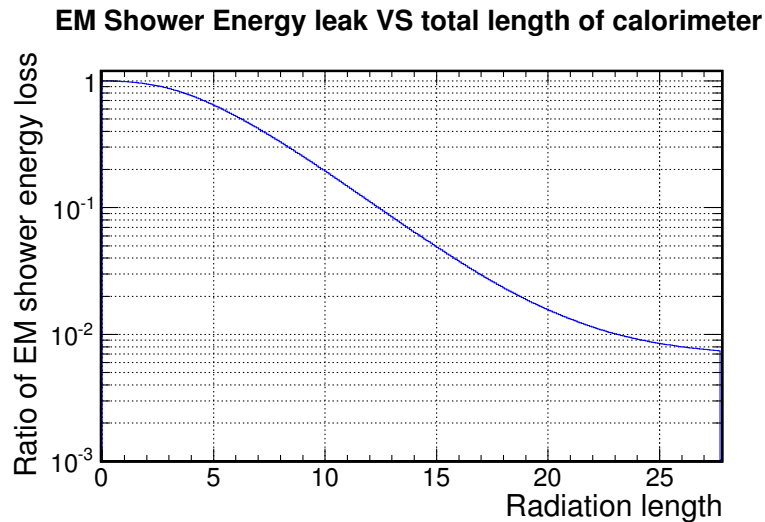


Figure 89: Fractional energy leak for an average SIDIS-Forward electron shower vs. different total length of the calorimeter.

10.2.2 Sampling Ratio of the Shower Detector

Each layer of the shower module consists of a 1.5 mm-thick scintillator plate and a 0.5-mm absorber plate made of lead. The Pb absorber thickness of 0.5 mm or less is favored to provide a fine sampling and therefore better energy resolution. The thickness of the scintillator plate should be thin enough to ensure fine longitudinal sampling, while thick enough to reduce light attenuation on the lateral direction. A thickness of 1.5 mm was chosen following the experience of previous Shashlyk designs used by the KOPIO experiment [1, 4], the PANDA experiment [5], and the COMPASS-II experiment. The COMPASS module is shown in Fig. 90. A gap of 120 μm is kept between each lead and scintillator plates to accommodate a sheet of high-reflectivity paper, which reduces the loss of scintillation light.

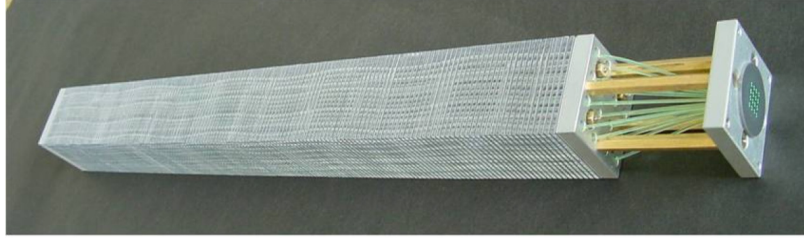


Figure 90: COMPASS-II Shashlyk calorimeter module. This illustrates the basic design of shashlyk modules: each module consists of alternating scintillator and lead (or other absorber material) layers, with WLS fibers penetrating across all layers to guide out the scintillation light signal. Four stainless steel rods are used to fix all layers together and support the whole module.

Figure 91 shows the simulated energy resolution using the chosen configuration of 1.5 mm scintillator and 0.5 mm lead. A resolution of about $4\%/\sqrt{E}$ is achieved.

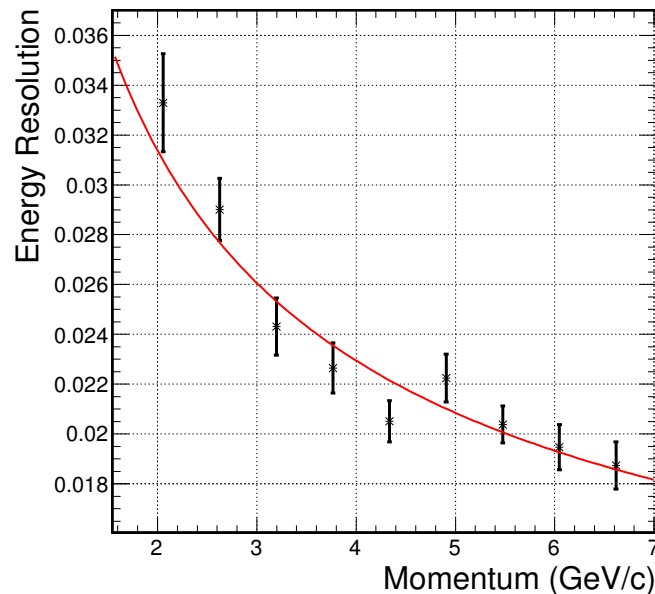


Figure 91: Simulated energy resolution of the SoLID calorimeter using both the Preshower and the Shower. The error bars are statistical error of the simulation. This simulation was performed without background to demonstrate the intrinsic PID performance of the EC. Simulation results including the background will be presented in section 10.7.

10.2.3 Lateral Size of the Calorimeter Module

A smaller lateral size for calorimeter modules leads to a better position and lower background. However, it will also increase the total number of modules and readouts channels, therefore higher overall cost. The study shows that a lateral size of about 100 cm^2 will provide a good balance between position resolution, background and the overall cost as shown in Fig. 92. A hexagon lateral shape is favored by the layout and the support design.

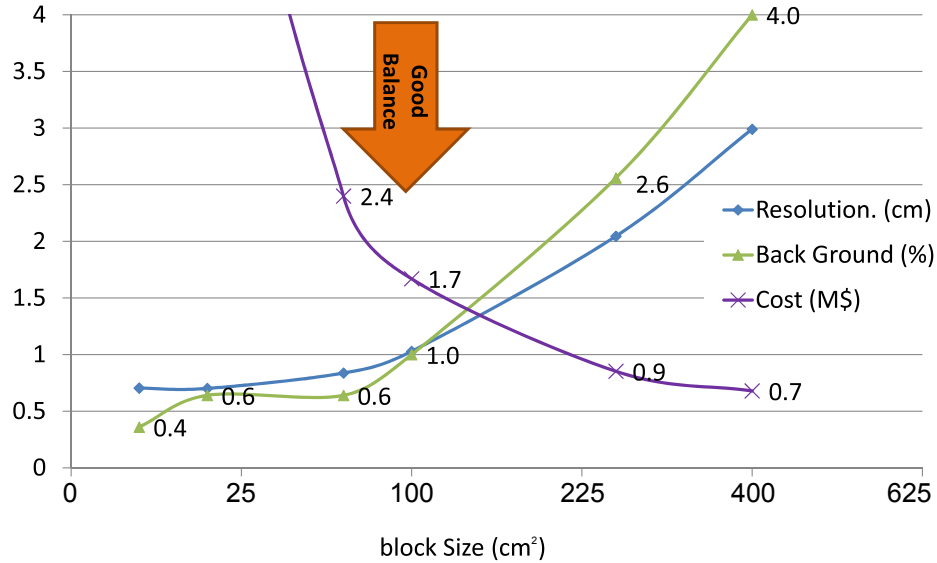


Figure 92: Position resolution and background level from simulation and the cost of the shower detector vs. lateral block size of the module.

10.3 Preshower Detector

Segmenting the EC longitudinally into a preshower and a shower part is essential to reaching the required pion rejection. Two designs were considered for the preshower detector: a full Shashlyk-type design that is optically isolated from the shower detector, and a passive radiator/scintillator pad design as used in the HERMES [2] and LHCb [3] experiments. Comparing to a Shashlyk-type preshower, the passive radiator/scintillator pad design have several advantages including increased radiation hardness, simplicity in construction, and fewer WLS fibers to readout. For a passive radiator of $2X_0$, the impact to overall energy resolution is less than $0.5\%/\sqrt{E}$ for electrons with momentum larger than $2 \text{ GeV}/c$. Therefore, the passive radiator/scintillator pad design was adopted for the preshower detector. Details of the design are as follows:

- The thickness of the preshower radiator was determined by optimizing the overall pion rejection at the desired electron efficiency. As shown in Fig. 93 (top), the preshower-alone pion rejection improves as the radiator thickens up to $3.5X_0$ due to immediate development of the electromagnetic shower. However, the impact to the overall energy resolution degrades with increased thickness of the absorber. A thickness of $2X_0$ for the radiator was found to be an optimal choice for the SoLID application.
- The scintillator and readout design is similar to that of the LHCb experiment [3]: WLS fibers are embedded in one 2 cm-thick scintillator pad to absorb, re-emit and conduct the photons for readouts.

With the above configuration and assuming a response of 100 photoelectrons per MIP (see next paragraph), the relation between pion rejection and electron efficiency for preshower alone can be plotted as a function of scintillator energy cuts, as shown in Fig. 93 (bottom right). One can see a pion rejection of better than 5 : 1 can be achieved at an electron efficiency of $> 94\%$.

Figure 94 shows pictures of the LHCb preshower tile (left) compared to a SoLID preshower prototype made by IHEP (right). Preliminary cosmic tests show that we can achieve up to 50 photoelectrons per MIP by embedding two 1.5-m long, 1-mm diameter Kuraray Y11(200)S WLS fibers

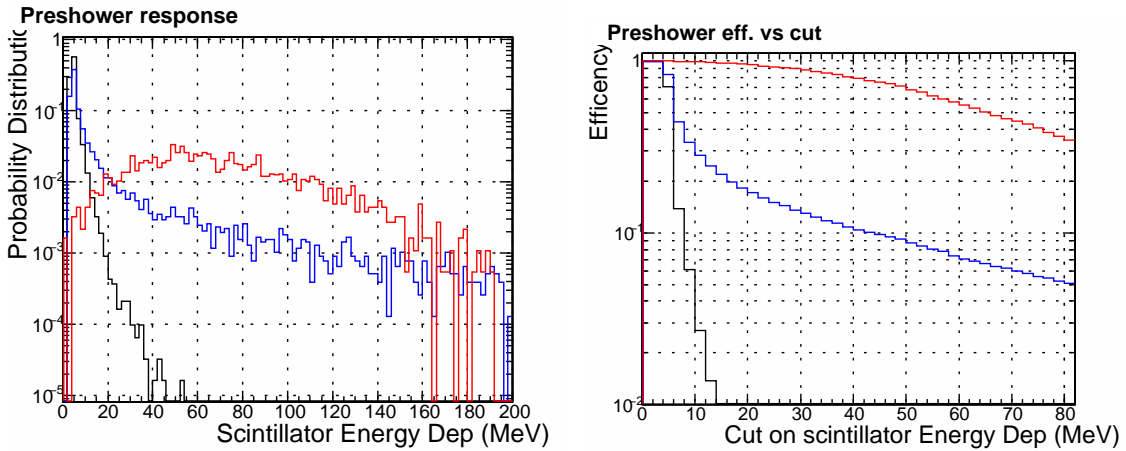
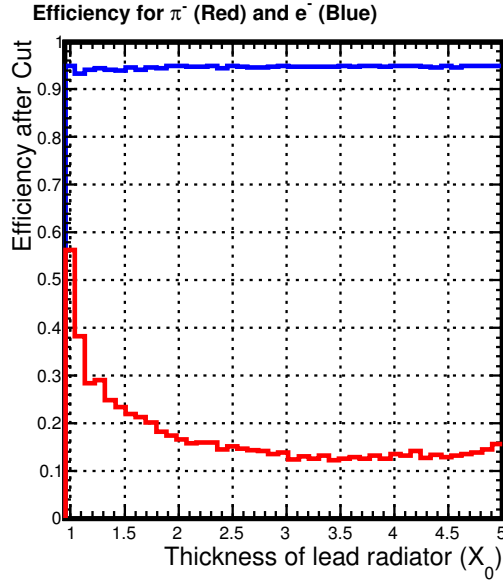


Figure 93: Simulated performance for the preshower detector. Top: $1/(\pi^- \text{ rejection})$ (red curve) at a 95% electron efficiency (blue curve) vs. different thickness of the lead radiator. Bottom: Energy deposition in the scintillator (left) and detector efficiency vs. energy deposition cut (right), for electrons (red), π^- (blue) and μ^- (black), for a preshower consisting of $2X_0$ of lead radiator and 2 cm of scintillator.

in the circular groove on the preshower scintillator. The use of multiple fibers allows minimizing the attenuation due to WLS fiber length. Final number of photoelectrons that reaches the PMT will depend further on loss in the fiber connector and the attenuation in the clear fiber. Current simulation assumes a preshower response of 100 photoelectrons per MIP, and studies about how the number of photoelectrons affects the PID performance is on-going.

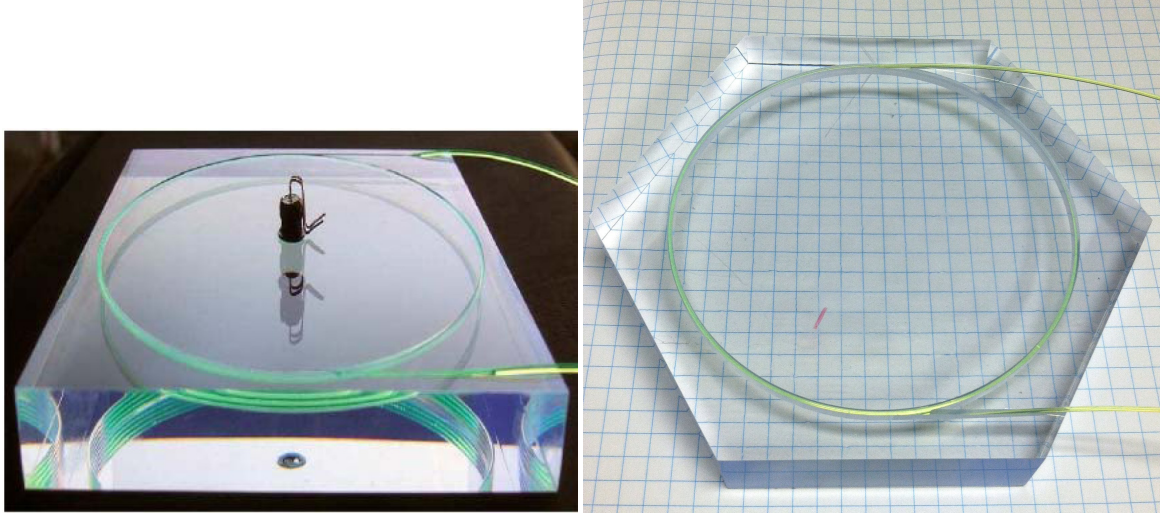


Figure 94: Preshower scintillators. Left: LHCb preshower tile ($12 \times 12 \times 1.5$ cm) [3]. A single WLS fiber is embedded in a circular groove for 3.5 turns. In the middle of the tile is an LED for testing purposes. Right: SoLID preshower prototype made by IHEP. The SoLID prototype has a geometry of 6.25-cm-side hexagon and is 2 cm thick. Shown here are two 1-mm diameter WLS fibers embedded in a 9-cm diameter circular groove, each 2.5 turns.

10.4 Layout and Support

The total area of PVDIS EC is slightly larger than that of SIDIS ECs. The modules will be re-arranged between the two configurations, where modules from PVDIS FAEC will be split and re-arranged into SIDIS FAEC and LAEC. The SIDIS EC layout must preserve the 2-fold rotation symmetry in the spectrometer, and it is convenient to have the same symmetry for the PVDIS configuration as well. The design layout that meets these requirements is shown in Fig.95 for the PVDIS configuration. The forward angle support system is shared by PVDIS and SIDIS FAEC, and the SIDIS LAEC will have a separate support system.

The scintillator tiles of preshower modules will be mounted on a 2-cm thick aluminum plate. For shower modules, the lead and the scintillator layers in each Shashlyk module are held together by four stainless steel rods penetrating longitudinally through the module. These rods are supported by two aluminum plate-like structures, one between preshower and shower, and one 4-cm thick plate behind the Shower. The thickness of the first aluminum plate must be minimized to reduce the impact on the PID and trigger capability. The current design is to have this supporting plate of 1 cm. If thinner thickness is desired, material other than aluminum, such as carbon fiber, will be considered.

10.5 Light Readout

For both preshower and shower, the blue light from scintillators is converted into green light by WLS fibers embedded in or penetrating through the modules. Each preshower module will use 1-2 WLS fibers with 1-mm diameter. The preshower WLS fibers will be routed using the space between preshower and shower to the space between EC and the solenoid wall. Each shower module will use 100 1-mm-diameter WLS fibers arranged along the direction of the particle trajectory, and the fibers will be guided directly towards the back of EC. To avoid light loss over long distances, WLS fibers will be connected immediately to clear fibers using one-to-one connectors for readout by PMTs.

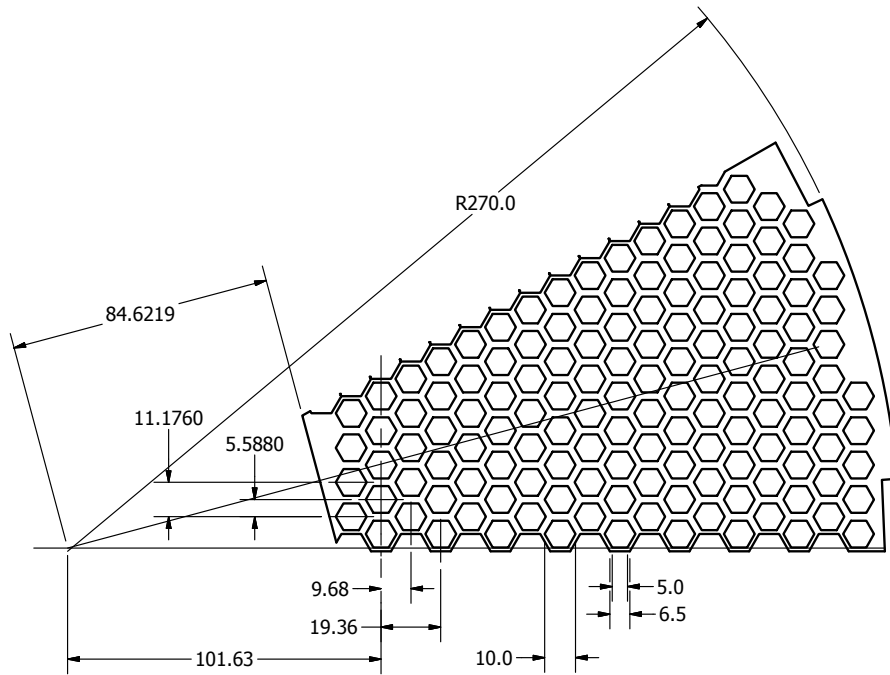


Figure 95: Layout of the hexagon-shaped modules with their support for a 30-degree wedge of the FAEC for the PVDIS configuration. The number of modules is 138 full modules plus 9 half-modules along the horizontal line. If counting 147 modules per 30-degree wedge, the total number of modules needed is 1764. We use 1800 modules for planning purposes at this stage.

We plan to use homemade fiber connectors for both preshower and shower as LHCb did. Prior experience indicates that the light loss of custom connectors to be in the range of 10-20%.

For the preshower it is essential to achieve a high photoelectron yield such that the best PID performance can be reached. We chose the Kuraray Y11(200) fiber because it gives higher light yield, and has been tested to higher radiation dose than Bicron BCF91A and BCF92 fibers. For shower modules, the light yield is expected to be very high, thus the Bicron BCF91a WLS fiber becomes a more economical choice while still satisfying the requirement on radiation hardness. Bicron BCF92 fibers have faster decay time but gives less yield than BCF91A, and is not being considered for SoLID EC.

The magnetic field reaches about 1.5 T behind SIDIS LAEC and a few hundred Gauss behind both PVDIS and SIDIS FAEC. Field-insensitive photon sensors are in general expensive and less radiation-hard compared to PMTs. Therefore, the default design is to use PMTs, one PMT per shower module to read out the 100 fibers. We plan to design custom PMT bases so that preamplifiers with a 2-5 gain can be used, minimizing aging of the PMTs. For preshower modules we plan to use multi-anode PMT (MAPMTs), with all fiber ends (2 or 4) from each module read out by one pixel of the MAPMT. The use of MAPMT allows us to minimize the cost of PMT the PMT and the high voltage power supply. When using MAPMTs, the high background of SoLID experiments constrains us to relatively low gain, in the range of $5E3-2E4$, such that the total anode current is only a fraction of the maximum specification and thus reduce the aging of the MAPMT. At this low gain, pre-amplifiers must be used. We plan to design pre-amplifiers with gain up to 50 and 16-channel MAPMTs. Pre-R&D of MAPMT and its preamplification board is currently underway.

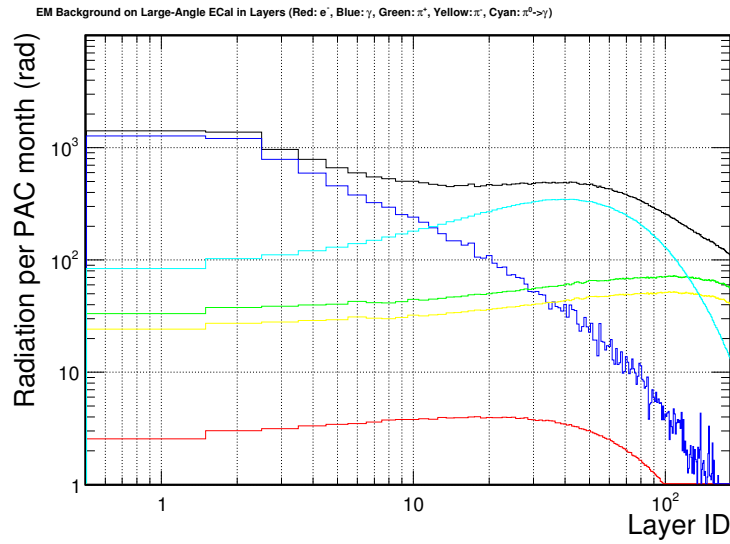
Note that LHCb used 64-ch MAPMTs at a gain of 5E3 combined with a front-end electronic board that provide an intrinsic gain of about 10, and our current design is based on and is consistent with the LHCb readout method.

There are also field insensitive photon sensors that can be used for readout. SiPM has enough gain (10^6) for sampling calorimeters, but its dark rate is prone to neutron background. We are still evaluating the neutron background at the calorimeters and the choice of SiPM as direct readout without the need of fiber connectors and clear fibers.

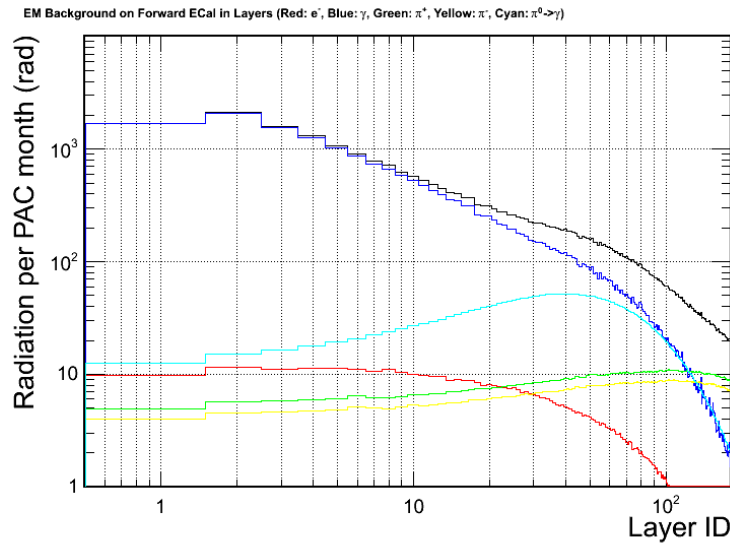
10.6 Radiation Effect

EC for the SoLID spectrometer are designed for high luminosity experiments. The expected luminosity and run time are 169 PAC-days at $10^{39} N \cdot \text{cm}^{-2}\text{s}^{-1}$ in the PVDIS configuration, 245 PAC-days at $10^{37} N \cdot \text{cm}^{-2}\text{s}^{-1}$ for the SIDIS experiments and 60 PAC-days for the J/Ψ experiment. In the current design, the maximum radiation dose on the active material – scintillator and WLS fibers – in the calorimeter is significantly reduced by the use of the $2X_0$ lead plate in the Preshower, and the lead blocks described in section 6 for the PVDIS configuration. Because of the use of lead blocks, the PVDIS configuration has been divided into higher and lower photon flux regions, each consists of thirty 6-degree azimuthal regions.

The radiation dose inside calorimeter was simulated using GEANT4 based simulations considering a wide range of energy and species for the background particles. The dose rates for the active material (scintillators and fibers) are shown in Figs. 96 and 97. The highest radiation region is at the front part of the calorimeter, including the preshower scintillator pad and the front scintillators of the Shashlyk calorimeter modules. The maximum integrated radiation level for the active material reaches 100 kRad for the PVDIS experiment and 20 kRad in the SIDIS and J/Ψ experiments, which leads to a total radiation dose of less than 200 kRad for all approved experiments. This dose level can be safely handled by the choice of scintillator and WLS fibers.

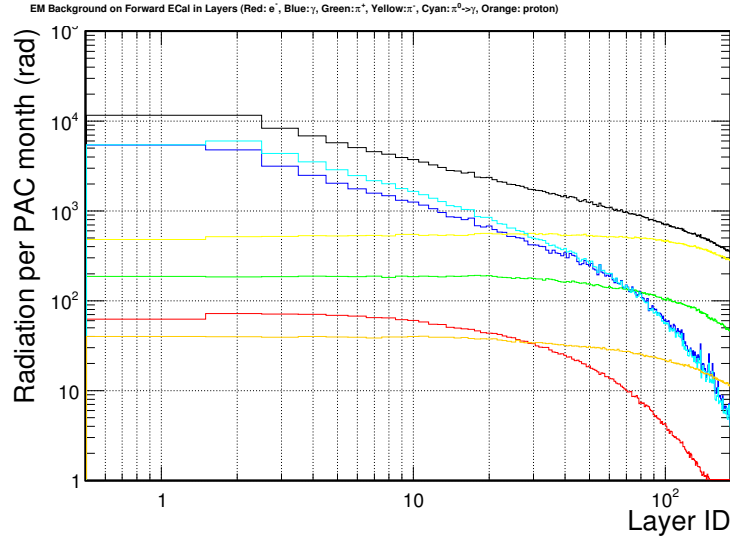


(a) SIDIS large-angle calorimeter

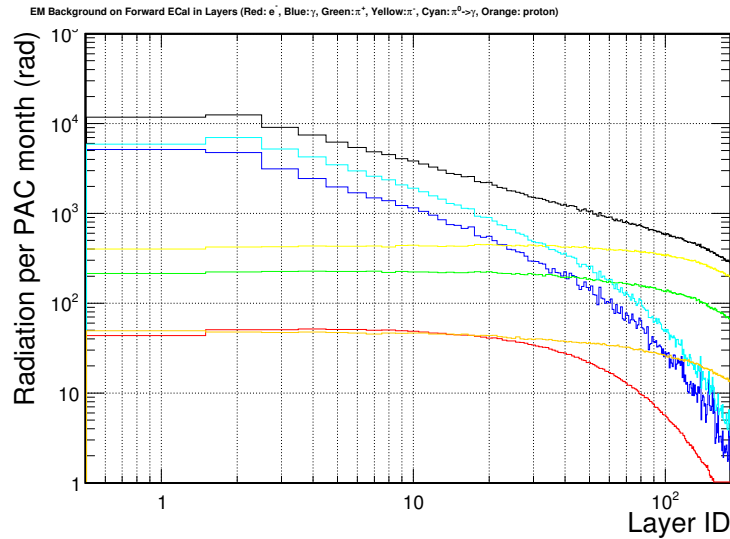


(b) SIDIS forward-angle calorimeter

Figure 96: SIDIS radiation dose rates per PAC month in each layer of the scintillator tiles in the calorimeter. Layer ID 1 is the preshower scintillator. The rest of IDs are assigned for each scintillator layer in the Shashlyk calorimeter in the order of increasing z . The color code stands for different contributions of various particle species at the front surface of the preshower: electrons (red), photons (blue), EM total (magenta), π^+ (green), π^- (yellow). The overall dose is shown by the black curve.



(a) PVDIS calorimeter in higher-photon flux region



(b) PVDIS calorimeter in lower-photon flux region

Figure 97: PVDIS radiation dose rates per PAC month in each layer of the scintillator tiles in the calorimeter. Layer ID 1 is the preshower scintillator. The rest of IDs are assigned for each scintillator layer in the Shashlyk calorimeter in the order of increasing z . The color code stands for different contributions of various particle species at the front surface of the preshower: electrons (red), photons (blue), EM total (magenta), π^+ (green), π^- (yellow), and protons (brown). The overall dose is shown by the black curve.

10.7 Performance

The EC system plays multiple roles in the SoLID spectrometer. Its performance was evaluated in the GEANT4 based simulation and discussed in this section, including PID performance, trigger capability and shower position resolution. A realistic background simulation was setup to evaluate

the calorimeter considering a wide range of species and momenta of the background particles.

10.7.1 Intrinsic electron-pion separation

As a baseline, the PID performance was first evaluated without the background. The primary track is propagated through the SoLID magnetic field in GEANT4, then enters the calorimeter. A local cluster which consists of the central calorimeter module and six neighboring hexagon-shaped modules is formed. With a multidimensional cut of the preshower and shower response within the cluster (see Sec. 10.8), the overall pion rejection averaged over the acceptance of each calorimeter is shown in Fig. 98. A 100 : 1 pion rejection at 95% electron efficiency is achieved for momentum bins of $p > 2$ GeV/ c . For the lowest momentum bin $1 < p < 2$ GeV/ c which is only needed for the SIDIS FAEC, a better than 50 : 1 pion rejection at 90% electron efficiency is obtained.

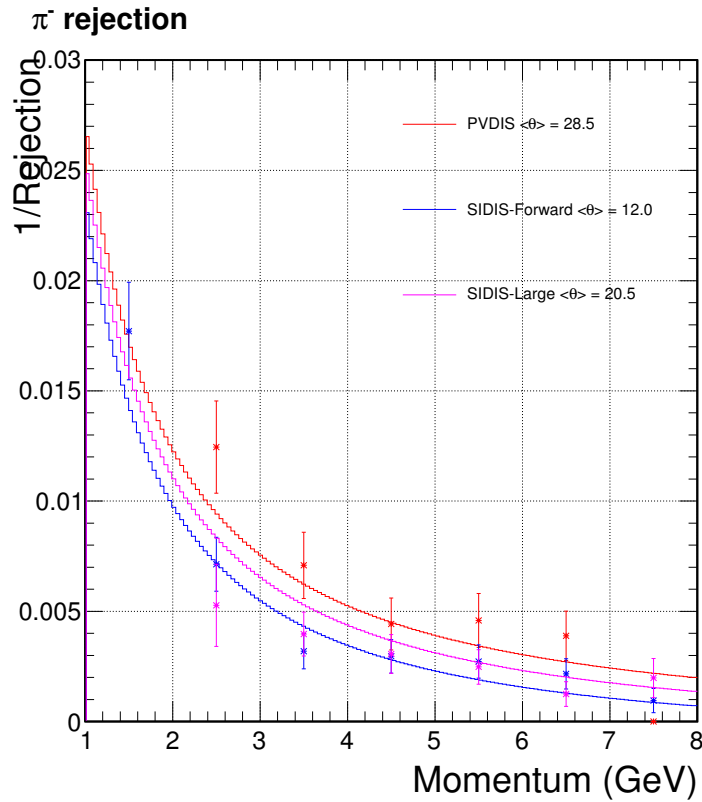


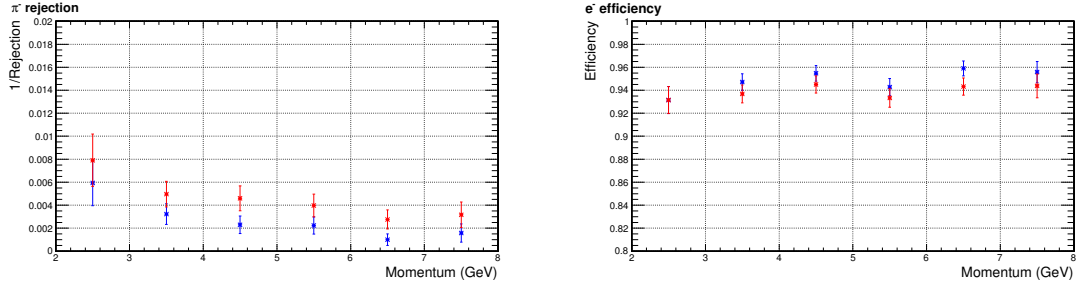
Figure 98: SoLID EC intrinsic (without background) π^- efficiency (1/rejection). From top to bottom: PVDIS with average track polar angle $\langle\theta\rangle = 28.5^\circ$ (red), SIDIS LAEC with $\langle\theta\rangle = 20.5^\circ$ (magenta) and SIDIS FAEC with $\langle\theta\rangle = 12.0^\circ$ (blue). A constant 95% electron detector efficiency is maintained for $p > 2$ GeV/ c . A 90% electron efficiency is maintained for the lowest momentum bin $1 < p < 2$ GeV/ c , which is only required for the SIDIS FAEC. The $\langle\theta\rangle$ value is different for the three calorimeter configurations, which leads to slight differences in the pion rejection curves.

10.7.2 PID performance under realistic background simulation

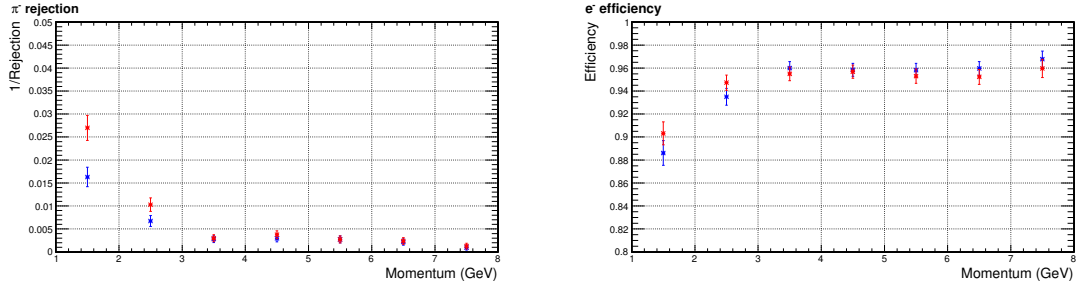
For a large intensity device, background particles and their influence on the calorimeter performance have to be considered. A full background simulation was implemented to study calorimeter performance. The background simulation procedure is as follows:

1. Particles are generated at the target including photons and electrons from the low energy EM processes (based on physics in GEANT4), DIS electrons (based on CTEQ6 PDF), and hadrons (based on Wiser fit);
2. Particles are propagated through a SoLID GEANT4 simulation to the front surface of calorimeter;
3. The EC response is simulated for a wide range of background particles – electrons, photons, pions, and protons – within the momentum range $10 \text{ keV} < p < 11 \text{ GeV}$. A statistical model is used for the correlation between Preshower and Shower responses;
4. The background contribution to each event is produced by combining the background rate at the EC front surface and the EC response described above for a region of interest on the calorimeter, usually defined by a radius-azimuthal angular bin. A conservative 30 ns coincidental window between background particles and the primary event is assumed.
5. The background contribution is embedded into the raw signal from the simulated primary particles (high energy electrons and pions). The background-embedded data are then analyzed as raw ADC signals. The energy response is calibrated and PID and trigger performance are analyzed.

Typically, background rate is the highest in the inner radius region and drops by approximately one order of magnitude in the outer radius region. Figure 99 shows the EC performance for the SIDIS configuration in the inner radius region. For SIDIS experiments, effects from background particles are visible but not significant: for large-angle EC, the pion rejection remains better than 100:1 for all momentum bins; for forward-angle EC, there is no noticeable change in the PID performance other than for the lowest momentum bin $1 < p < 2 \text{ GeV}/c$ where the pion rejection is a half of the no-background case. However, the Cherenkov detector provides high PID performance in the low momentum range and the overall pion rejection is sufficient for the experiment.



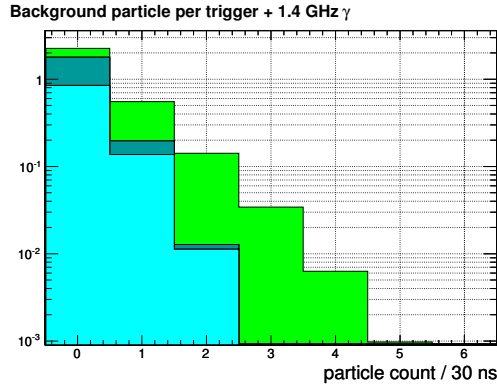
(a) SIDIS large-angle calorimeter



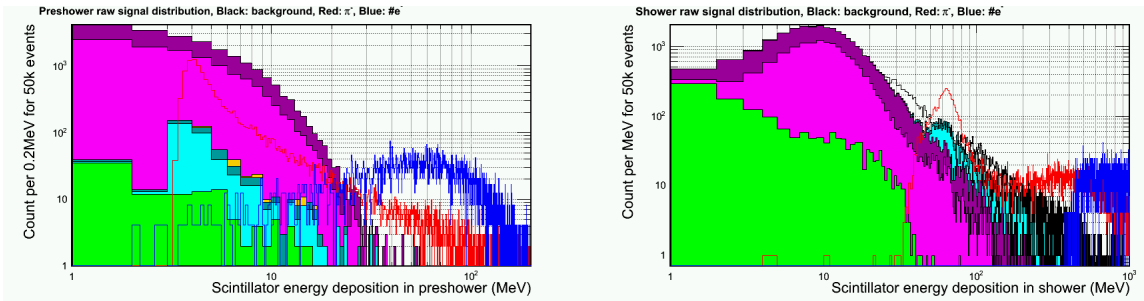
(b) SIDIS forward calorimeter

Figure 99: Calorimeter pion and electron efficiency without (blue) and with (red) the consideration of background particles for the inner radius region (highest background) for the SIDIS configuration.

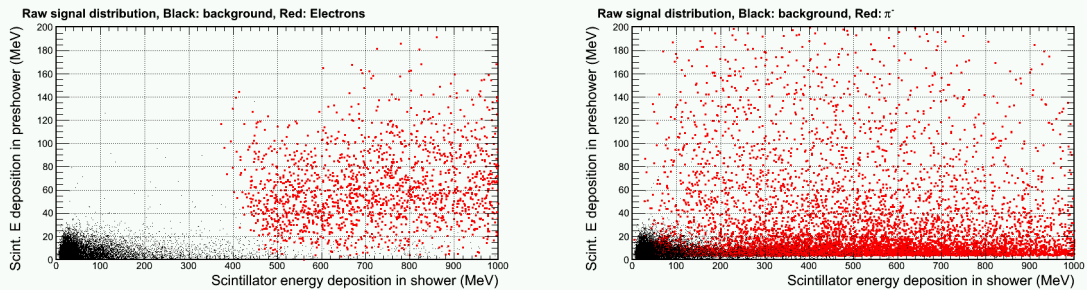
In the PVDIS configuration, the background rate is significantly higher and the performance is affected. The 30-fold structure of the baffle system for the PVDIS experiment causes the background to alternate between high- and low-rate 30 times in the azimuthal direction. Therefore, calorimeter performance is studied for the high- and the low-rate “slices” separately, with each fan-shaped slice covering 6 degrees. Background structure for the inner-radius, high-rate slice is shown in Fig. 100. The PID performance with the background is evaluated for different radius, see Fig. 101. Comparing to the intrinsic performance of Fig. 98, the pion rejection is up to 8 times worse: the pion rejection varies from 25-50 at $p = 2.5$ GeV/ c to 50-100 at $p = 6$ GeV/ c , while keeping the electron efficiency to be in the range (90 – 95)%. Particle identification for the experiment will need to rely on a full-waveform analysis of the EC, combined with information from the Cherenkov detector.



(a) Stacked probability to find the number of background π^- (light blue), π^+ (dark blue) and electrons (green) at the front of the preshower. The photon rate is as high as ~ 1.4 GHz, thus the photon count is off-scale and not shown in this figure.

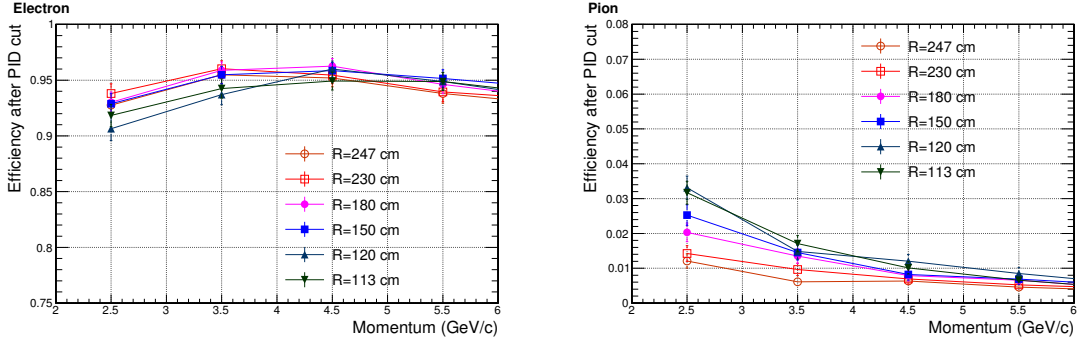


(b) Stacked probability (count per 50k events) vs. Preshower (left) and Shower (right) scintillator energy deposition for incoming background electrons (green), π^- (light blue), π^+ (dark blue), protons (yellow), EM process-originated photons (magenta) and π^0 -originated photons (dark magenta). For comparisons, energy deposition for high energy pion (red) and electrons (blue) are shown as non-filled curves.

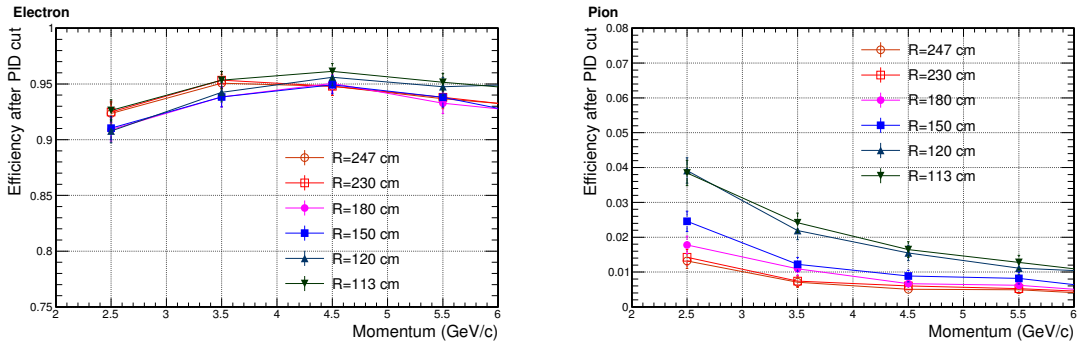


(c) Preshower-shower scintillator energy correlation for background particles (black), compared with high energy electrons (left, red) and pions (right, red)

Figure 100: Background distribution for the PVDIS forward calorimeter at the production luminosity of a liquid deuteron target. Background for the inner radius ($R \sim 1.2$ m) and higher-radiation azimuthal region is shown. The energy deposition originated from background is compatible to that of high energy pions.



(a) lower-radiation azimuthal region



(b) higher-radiation azimuthal region

Figure 101: Calorimeter pion and electron efficiency for the PVDIS experiment, evaluated with the presence of background at eight typical regions on the calorimeter.

10.7.3 Trigger capability

Trigger capability is an important function of the EC. The calorimeter shower energy deposition in all combinations of local 6+1 clusters (central block plus six neighboring hexagon blocks) are first summed after digitization, forming local shower sums. Triggers are then formed by passing the local shower sums through a threshold cut. Electron triggers are formed with a targeted electron threshold, and the efficiency curves for both pions and electrons are studied with the full-background simulation. The following triggering specifications have been studied:

- SIDIS large angle calorimeter: electron triggers of 3 GeV are formed by cutting on local shower sum larger than 2.6 GeV. The trigger turn-on curve is shown in Fig. 102. High electron efficiency is observed for electrons above the threshold. The rejection on few-GeV pion background is high, in the range (20-100):1, which satisfies requirement of the SIDIS experiments.
- SIDIS forward calorimeter: position dependent electron triggers provide high trigger efficiency for electrons of $Q^2 > 1\text{GeV}^2$. The pion rejections with 1 GeV threshold is shown on the left plot of Fig. 103. With higher thresholds, pion rejections are better.
- SIDIS forward calorimeter: MIP triggers allow the calorimeter to trigger on hadrons for the SIDIS measurement. The threshold is determined by MIP peak - two sigma of the Landau

fit of the distribution, which lead to a calibrated local shower sum energy of 220 MeV. The trigger efficiency for pions is high, as shown on the right plot of Fig. 103.

- PVDIS forward calorimeter: electron triggers are formed with radius-dependent trigger thresholds. As shown in Fig. 104, the targeted electron threshold varies from 1.5 GeV at outer radius to 3.8 GeV at inner radius on the calorimeter, which produces high trigger efficiency for DIS electrons with $x > 0.35$. The trigger turn-on curves are evaluated for several regions on the calorimeter as shown in Fig. 104. The efficiency for both electrons and pions are lower for inner radius regions due to the use of high thresholds for background-suppression. Overall the pion rejection at the trigger level is > 2 and varies with the radius.

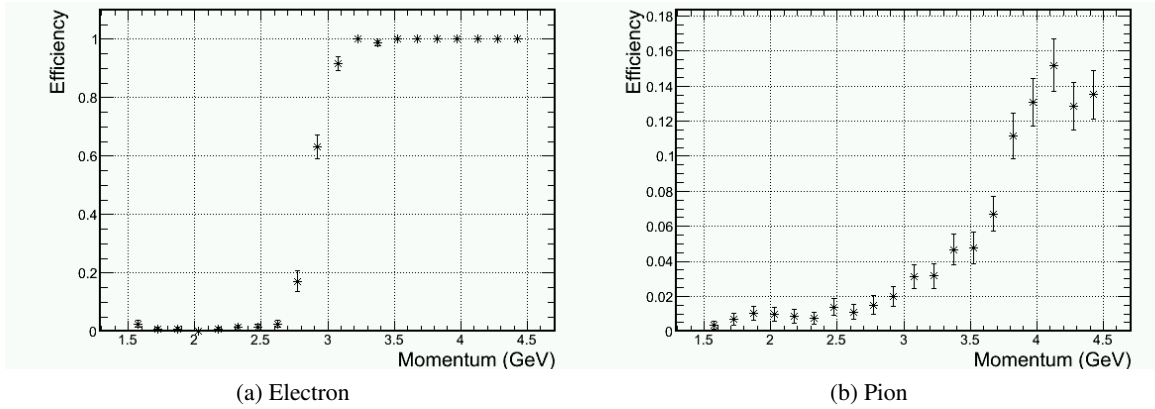


Figure 102: Trigger efficiency for electrons (a) and pions (b) for the SIDIS large angle calorimeter. The target trigger threshold is approximately $P_e = 3 \text{ GeV}/c$. Only the (high-background) inner-radius region is shown here.

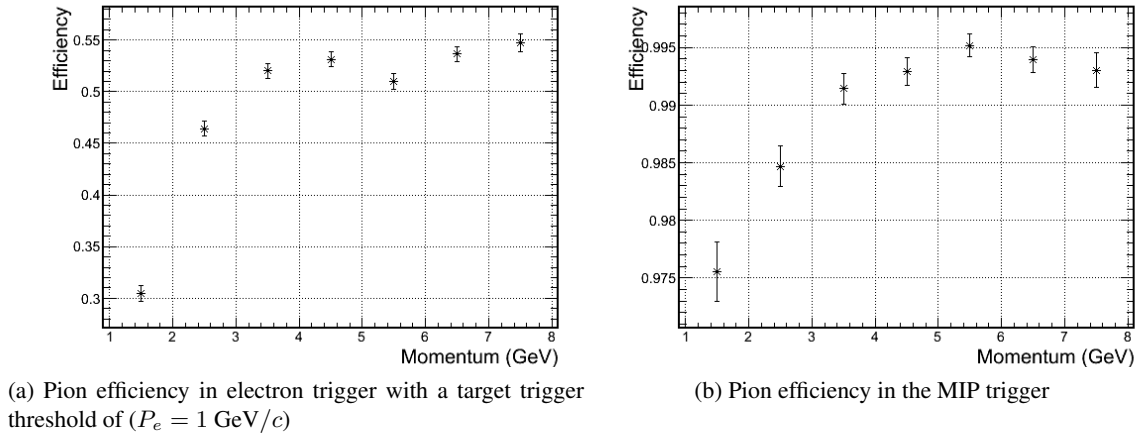
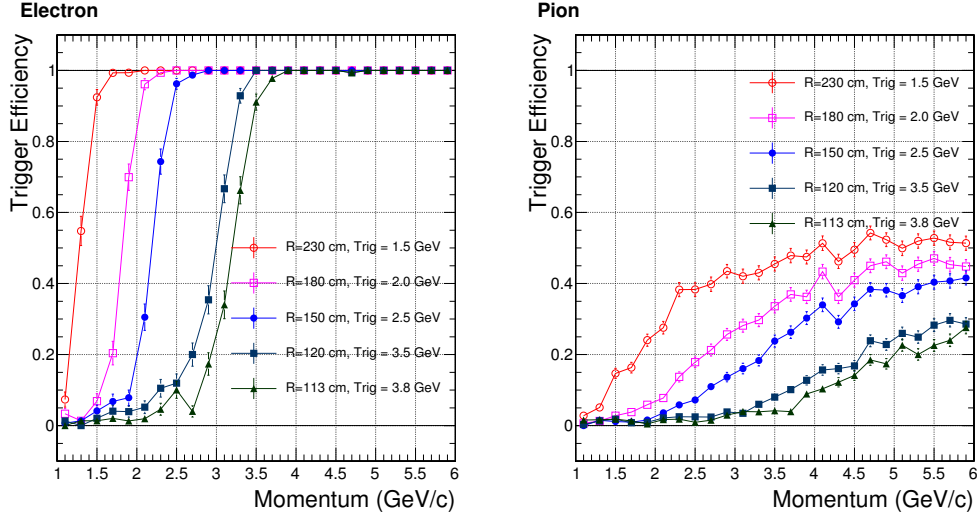
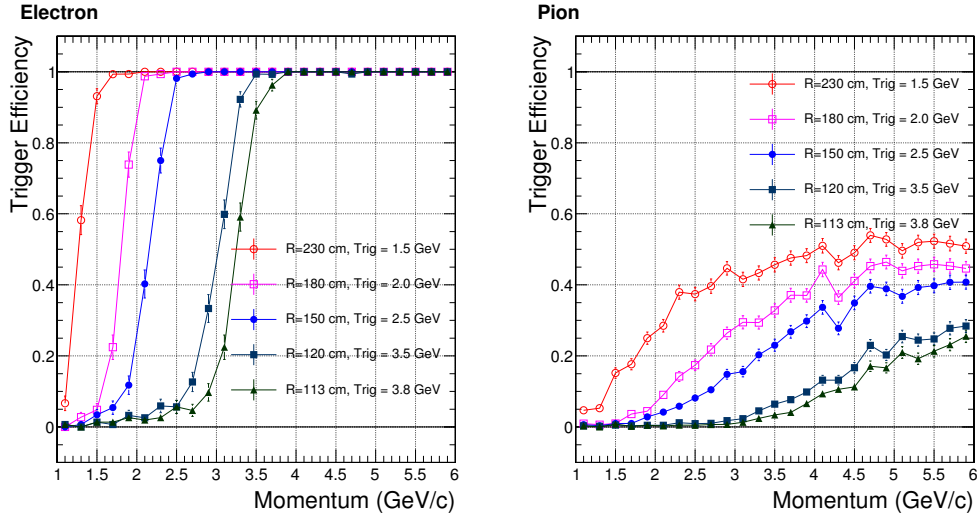


Figure 103: Trigger efficiency for pions in the SIDIS forward calorimeter for electron triggers (a) and MIP triggers (b). Only the (high-background) inner-radius region is shown here.



(a) Higher-radiation azimuthal region



(b) Lower-radiation azimuthal region

Figure 104: Trigger efficiency curves for the PVDIS configuration.

10.7.4 EC trigger rate

The PVDIS experiment will run with a luminosity up to $10^{39} \text{ cm}^{-2} \text{ s}^{-1}$ and thus has high background rates. The trigger of PVDIS will be formed by taking the coincidence between the EC and the gas Cherenkov detector, and care must be taken to ensure the trigger rate is comfortably below the DAQ rate limit. The baffle system is used primarily to reduce the overall rate. To further reduce the rate from high energy photons from neutron pions and low energy backgrounds, fan-shape lead blocks, each covering 2.5 degrees azimuthally, will be placed in front of the EC. As mentioned previously, the EC trigger threshold varies with the radius and is set to preserve DIS electrons with $x > 0.35$. Estimation of the trigger rate is based on the realistic background simulation (described previously in Section 10.7.2). Triggers from low energy backgrounds of $p < 1 \text{ GeV}$ are simulated directly

such that background pileups are properly accounted for. For particles with $p > 1$ GeV, pileups are no longer dominant and triggers from these particles are calculated by combining the various particle rates with the trigger turn-on curve. The latter method greatly reduces the simulation time. Table 11 shows the rates of 11 GeV 50 uA electron beams on 40 cm deuterium for each particle type that enter the whole EC and the resulting trigger rates. These results will be combined with gas Cherenkov trigger rate to obtain the expected DAQ trigger rates.

region	full	high	low
rate entering the EC (kHz)			
e^-	413	148	265
π^-	5.1×10^5	2.7×10^5	2.4×10^5
π^+	2.1×10^5	1.0×10^5	1.2×10^5
$\gamma(\pi^0)$	8.4×10^7	4.2×10^7	4.3×10^7
p	5.5×10^4	2.4×10^4	3.1×10^4
sum	8.5×10^7	4.2×10^7	4.3×10^7
trigger rate for $p > 1$ GeV (kHz)			
e^-	321	80	231
π^-	4.8×10^3	3.4×10^3	1.4×10^3
π^+	0.28×10^3	0.11×10^3	0.17×10^3
$\gamma(\pi^0)$	4	4	0
p	0.18×10^3	0.10×10^3	0.08×10^3
sum	5.6×10^3	3.7×10^3	1.9×10^3
trigger rate for $p < 1$ GeV (kHz)			
sum	$(3.1 \pm 0.7) \times 10^3$	$(1.6 \pm 0.4) \times 10^3$	$(1.5 \pm 0.4) \times 10^3$
Total trigger rate (kHz)			
total	$(8.7 \pm 0.7) \times 10^3$	$(5.3 \pm 0.4) \times 10^3$	$(3.4 \pm 0.4) \times 10^3$

Table 11: PVDIS rates that enter full coverage of the EC, and the resulting trigger rates broken down to $p < 1$ GeV and $p > 1$ GeV particles and the low and the high background regions. Here the low and the high-background regions refer to the two 6-degree azimuthal regions of each sector and the azimuthal variation in the background rate is due to the baffle structure. For particles with momentum $p > 1$ GeV, pileup effects are not significant and the trigger rates are obtained by combining the particle entrance rate with the trigger turn-on curves. For particles with $p < 1$ GeV, pileup effects dominate. This requires a timing simulation which is statistically-limited, and is not possible to be broken down to particle types due to the fact that triggers can be produced by different particles piling up on each other. All rates shown are the sum of 30 sectors, divided by 30 to obtain the per-sector rates.

The SIDIS experiment on ^3He will run with a luminosity up to $3 \times 10^{36} \text{ cm}^{-2}\text{s}^{-1}$ on ^3He target and additional about $3.7 \times 10^{36} \text{ cm}^{-2}\text{s}^{-1}$ on target glass windows. Both FAEC and LAEC will provide the basic electron trigger. FAEC will also provide MIP trigger for hadron detection.

The FAEC trigger threshold varies with the radius and is set to preserve DIS electrons with $Q^2 > 1$. Estimation of the trigger rate is based on the realistic background simulation including target collimators (described previously in Section 10.7.2) and shown in Table 12. Trigger from EC will be combined with Cherenkov, MRPC and SPD to form the final trigger for SIDIS.

region	FAEC	LAEC
rate entering the EC (kHz)		
e^-	93.4	18.7
π^-	5.36×10^3	1.55×10^4
π^+	5.96×10^3	1.66×10^4
$\gamma(\pi^0)$	1.52×10^5	2.43×10^5
$e(\pi^0)$	6.52×10^3	2.04×10^3
p	1.86×10^3	6.16×10^3
electron trigger rate (kHz)		
e^-	74.2	11.68
π^-	500	5.16
π^+	548	5.12
$\gamma(\pi^0)$	896	12.5
$e(\pi^0)$	43	0.14
p	109	2.15
sum	2170	36.75
MIP trigger rate (kHz)		
e^-	93.4	
π^-	5240	
π^+	5800	
$\gamma(\pi^0)$	6760	
$e(\pi^0)$	772	
p	1732	
sum	2×10^4	

Table 12: SIDIS ^3He rates for the full coverage of FAEC plus LAEC. From top to bottom: rates that enter the EC, the resulting electron trigger rate, and the resulting MIP trigger rate.

10.7.5 Shower Position Measurement

Position resolution of the Shower center was studied for different lateral sizes of the calorimeter modules, as shown in Fig. 105. The radial resolution is in general worse than the azimuthal resolution because the tracks are not perpendicular to the radial direction. As can be seen from Fig. 105, with the use of proper algorithm, a position resolution of better than 1 cm is achieved for both directions at the designed lateral granularity of 100 cm^2 .

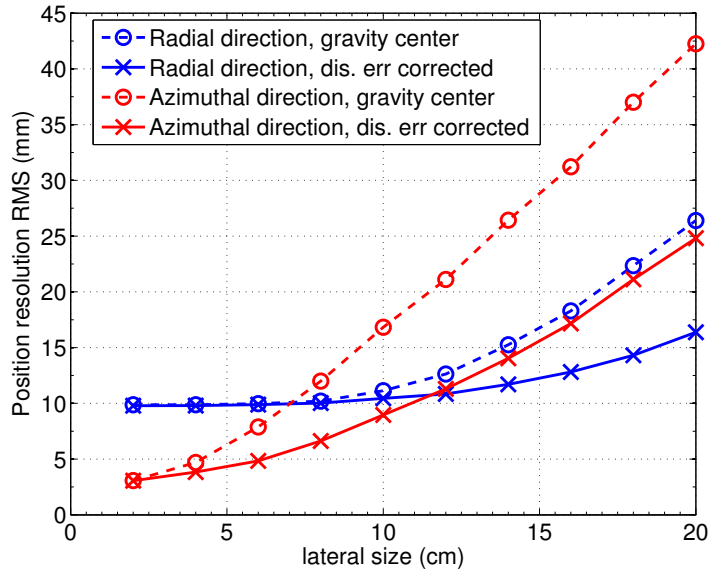
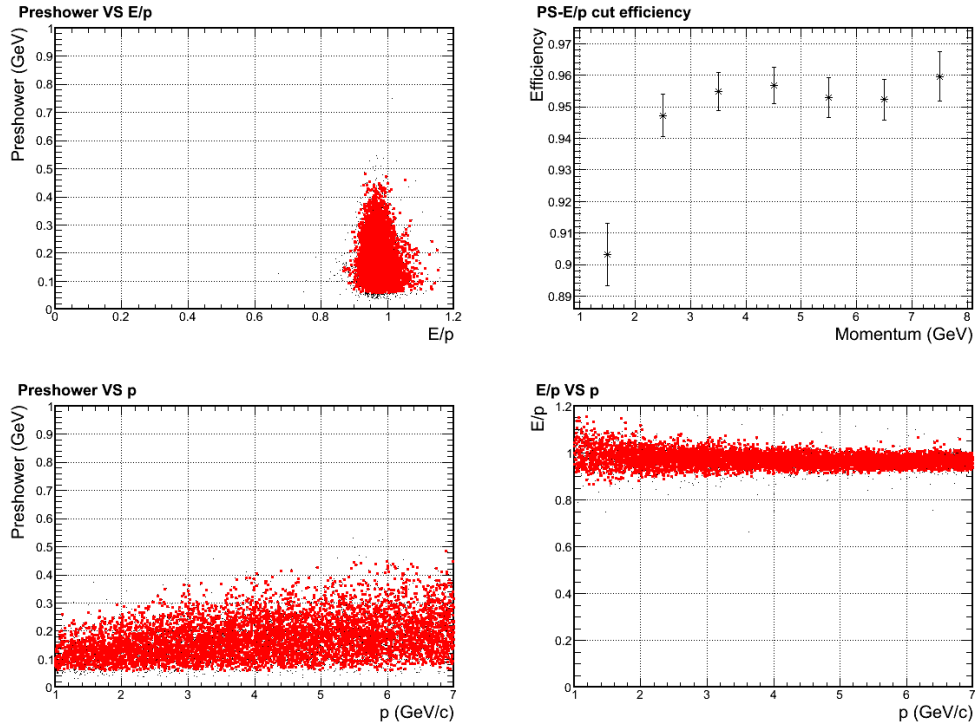


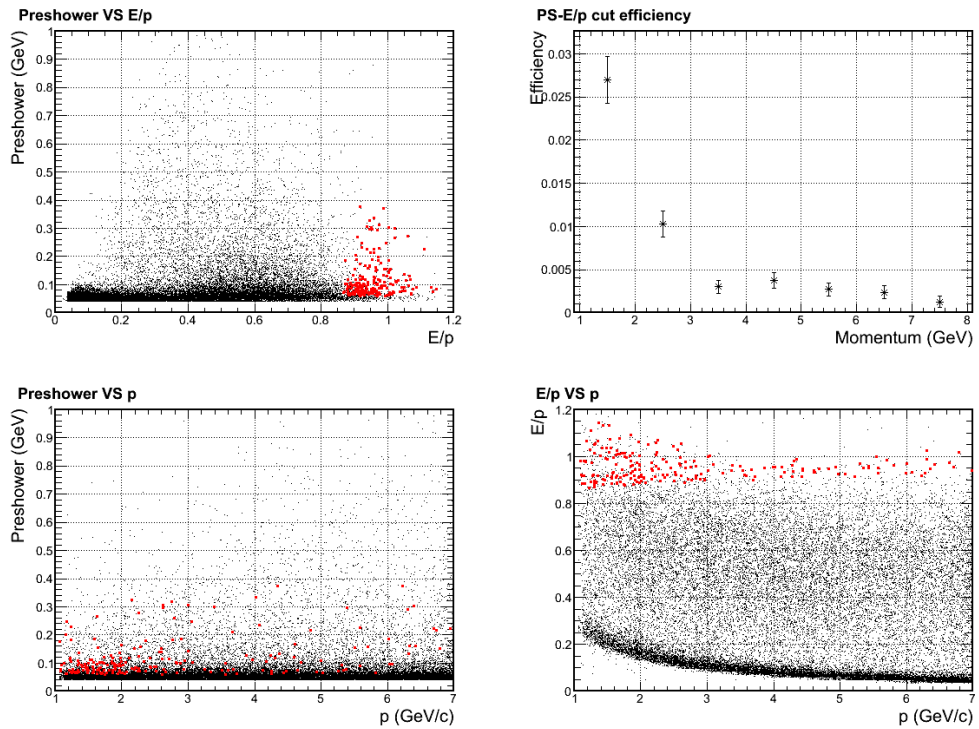
Figure 105: Position resolution for electron showers vs. different lateral size of the calorimeter module. Both azimuthal (red) and radial (blue) resolutions are shown, with the shower center calculated from a simple energy-weighted geometrical center (dashed curves), and those calculated with further corrections using the energy deposition distribution among neighboring modules (solid curves).

10.8 Supplemental Information: PID Selection Cuts

A three dimensional PID cut was used to select the best electron samples with maximal π^- rejection as illustrated in Fig. 106. For each given momentum bin, the cut on E/P and preshower energy roughly follows the contour lines of the ratio of π^- efficiency to e^- efficiency, which is the optimal cut for the π^-/e^- separation. A momentum dependence is then introduced to the cut to maintain a constant 95% electron efficiency for most of the bins. Events passing the cut are highlighted in red in the plots.



(a)



(b)

Figure 106: Illustration of electron sample cuts as highlighted in red dots, in comparison to simulated electron (a) and π^- (b) samples. The SIDIS forward calorimeter in the high background (small radius) region is studied in these plots.

10.9 Scintillator Pad Detector for SIDIS Experiments

The main purpose of the scintillator pad detector (SPD) is to reduce calorimeter-based trigger rates for high-energy charged particles (see Section 10.7.3 for calorimeter trigger capability) by rejecting photons through the coincidence between the SPD and the calorimeter. The SPD consists of fan-shaped scintillator pads arranged perpendicular to the beam direction. Two SPDs will be used: one in the forward direction between the heavy gas Cherenkov detector and the MRPC, and the other in the large-angle direction immediately before the large-angle calorimeter. Photons generated in the scintillator are carried by WLS fibers out of the detector, which are then connected to clear fibers for readout by PMTs. This readout method is similar to that of the preshower.

The performance for the scintillator was studied in the GEANT4 simulation and its parameters are optimized to the following:

- We plan to use 3-5 mm thickness scintillator based on a balance between the number of photons to readout and the radiation length. This results in a radiation length of $\sim 1.3\% \times X_0$ which directly affect the photon conversion rate. Typical responses of the SPD to photons and charged particles are shown in Fig. 107. Approximately 20% of the photon background leave energy in the scintillator due to back splashing from the calorimeter front face. This effect is reduced for low energy photon background, which leads to higher rejection as shown in Fig. 108.
- The trigger threshold was set at two standard deviations below the MIP peak to ensure a high efficiency for charged particles.
- Pile up effects were studied by considering a conservative ADC timing window of 50 ns. The photon rejection therefore depends on the trigger rate per scintillator, and further the scintillator segmentation. The segmentation is chosen to balance the consideration of minimizing the number of readout channels, and reducing pile-ups that affect photon rejections.

The segmentation for the scintillator is different for the forward and the large angle region. Since low energy photons dominate the trigger rate, the rejection factors in Fig. 108 are used to optimize the number of segmentation. The results are as follows:

- Large-angle SPD: A 10:1 photon rejection will bring the photon-induced calorimeter trigger rate down to below the electron-induced rate. The 10:1 rejection can be achieved by 60 azimuthal segments, with each segment covering 6 degrees.
- Forward SPD: 60 azimuthal and 4 radial segmentation will be necessary to provide a 5:1 photon rejection. This leads to a sub-dominant fake photon trigger rate in the SIDIS forward MIP and electron triggers. The azimuthal coverage of each SPD segment is 6 degrees and the radial coverages are increased from inner to outer pads, based on equal-rate considerations.

Readout of the SPD will be the same as for preshower: WLS fibers will be embedded in the scintillator to convert and carry out the light, then be connected to clear fibers and guided to 16-ch MAPMTs. Because the threshold is below MIP and is much lower than for preshower, a higher combined gain of PMT and the preamplifier is needed. We currently plan to use preamplifiers with gain ≈ 50 because it's the maximum comfortable gain that can be achieved on a pre-amplifier board. This will allow us to place the threshold around 20 mV, the minimal threshold that is above the noise level.

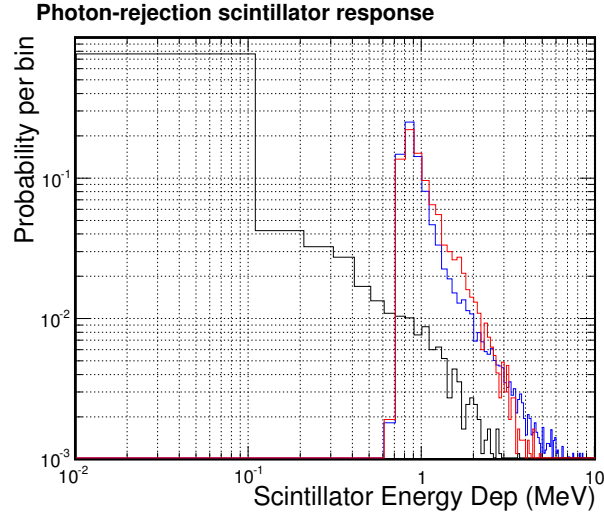


Figure 107: Typical probability for scintillator energy depositions in the SPD, for electron (blue), pion (red) and high energy photons (black).

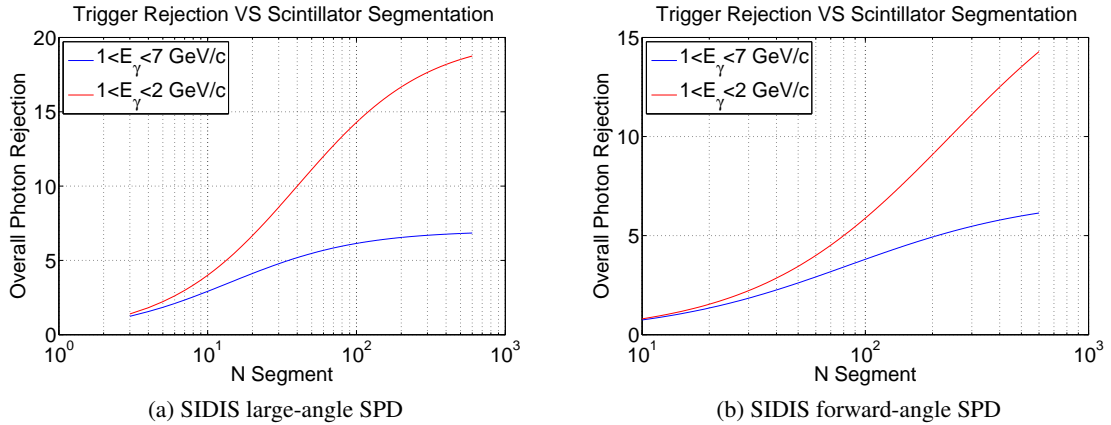


Figure 108: SPD high energy photon rejection vs. number of equal-rate segmentation. Two photon energy range were considered: $1 < E_\gamma < 2$ GeV (red curves) and $1 < E_\gamma < 7$ GeV (blue curves). A conservative 50 ns timing window was assumed for calculating the pile up effects.

References

- [1] G. Atoian, G. Britvich, S. Chernichenko, S. Dhawan, V. Issakov, et al., Nucl.Instrum.Meth. **A584**, 291 (2008), 0709.4514.
- [2] H. Avakian, N. Bianchi, G. Capitani, E. De Sanctis, P. Di Nezza, et al., Nucl.Instrum.Meth. **A417**, 69 (1998), hep-ex/9810004.
- [3] E. P. Olloqui (LHCb Collaboration), J. Phys. Conf. Ser. **160**, 012046 (2009).
- [4] Y. Kharlov et al., Nucl. Instrum. Meth. **A606**, 432 (2009), 0809.3671.

[5] D. Morozov et al., J. Phys. Conf. Ser. **160**, 012021 (2009).

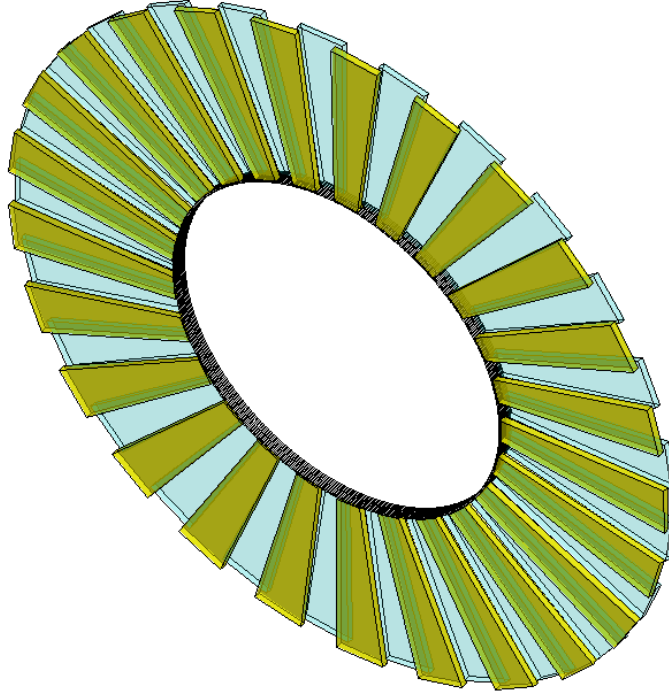


Figure 109: The layout of MRPC TOF

11 MRPC

The Multi-gap Resistive Plate Chamber (MRPC), which will be used as the time of flight (TOF) system, is located in front of the forward-angle calorimeter. Several MRPCs have been recently used in RHIC STAR and LHC ALICE as their TOF systems [1, 2, 3, 4] and the typical time resolution for these detectors is better than 80 ps. Most importantly, as a gas chamber, the MRPC does not need PMTs for readout so it can work inside a magnetic field. For SoLID-SIDIS configuration, the total path length is around 8 meters from the target and the flight time is calculated by comparing the timing signal to the beam RF signal. With a time resolution of 100 ps, we can identify pions from kaons at a rejection factor of 20:1 with their momenta up to 2.5 GeV/c. Compared with the MRPCs used at STAR and ALICE, the MRPC for SoLID receives higher flux rate which is approximately 10 kHz/cm². Tsinghua University has developed a new type of low-resistive glass with the bulky resistivity on the order of 10 Ωcm. The rate capability of the high rate MRPC assembled by this type of glass can reach 50 kHz/cm² [5, 6]. We proposed to construct the high rate SoLID-MRPCs assembled with this low resistive glasses.

11.1 Structure of the MRPC prototype

The layout of the MRPC is shown in Fig. 109. The inner diameter of the detector plane is about 1 meter and the outer diameter is 2 meters. The area of the disk is about 10 m². The whole detector consists of 50 super modules and each super module consists of 3 MRPC modules. There is overlap between MRPC modules and super modules to avoid blind area.

A prototype of the MRPC has been assembled and its structure is shown in Fig. 110. This trapezoidal module is assembled with our low-resistive glasses. The module has ten gas gaps and

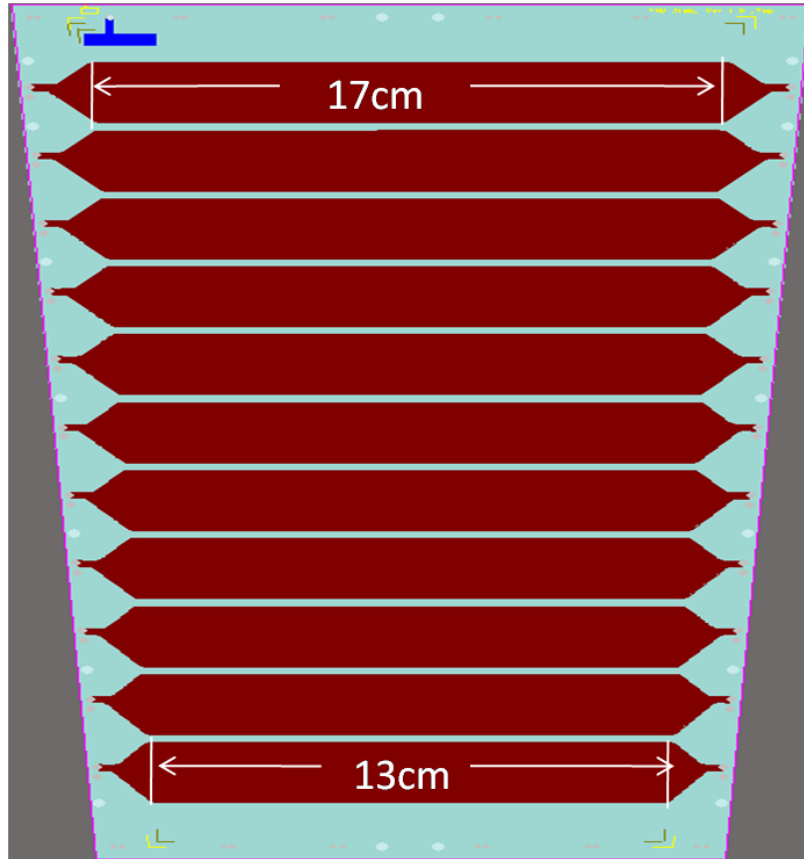


Figure 111: The structure of readout strip

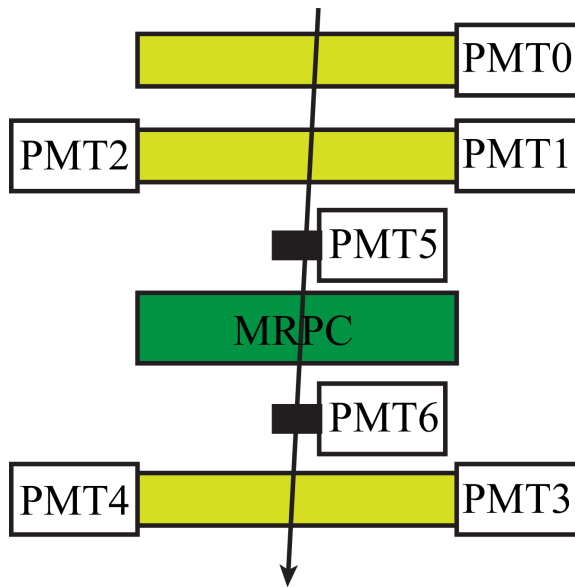


Figure 112: Layout of the test setup

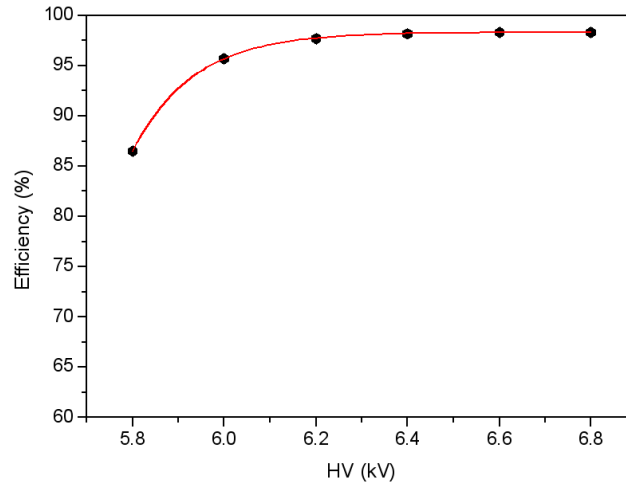


Figure 113: Efficiency plateau of the MRPC

were mainly soft photons, electrons and neutrons. The background intensity was stronger than the main electrons beam. A combined thick concrete shield was used to suppress background particles striking on MRPC. The diagram of DAQ is shown in Fig. 117. The trigger system was very similar to that of the cosmic test system. One small scintillator ($5 \text{ cm} \times 5 \text{ cm} \times 1 \text{ cm}$) was read out by PMT 0 and each of two long scintillators ($10 \text{ cm} \times 5 \text{ cm} \times 1 \text{ cm}$) was read out on both ends (by PMT 1-4). The coincidence of PMT0 and PMT4 provided the trigger signal of the system. The delayed coincident signal also acted as the gate signal of flash ADC and the stop signal of TDC. PMT1~PMT4 provided the reference time of the system. A CAEN V775 TDC was used to transfer time signal and a flash ADC, JLAB FADC 250, was used to record the charge signals. A VME scaler was used to record the time interval between two triggers. From this time interval we can get the signal rate to study the rate capability of the detector.

11.4 Beam test Results

11.4.1 HV Scan

MRPCs were conditioned under high voltage for a few hours in order to reach a stable, low dark-rate working region. The electronics threshold was set to 30 mV. The dark current was less than 8 nA and the rate of the module was less than 10 Hz/cm^2 at 108 kV/cm. The coincidence of PMT1-PMT4 provided the T0 of the test system, with a time jitter of about 100 ps. In order to find the optimum working voltage of the counters, the efficiency and time resolution were scanned as a function of the applied voltage for a 'low' flux of $\bar{\phi} \sim 1\text{-}4 \text{ kHz/cm}^2$. The results are summarized in Fig. 118. The counters showed large efficiency plateaus above 600 V, and time resolutions were as good as 75 ps. It can be seen that the time resolution obtained from cosmic ray is better than that from the electron beam test, because the time jitter of T0 in beam test was larger than that in the cosmic test.

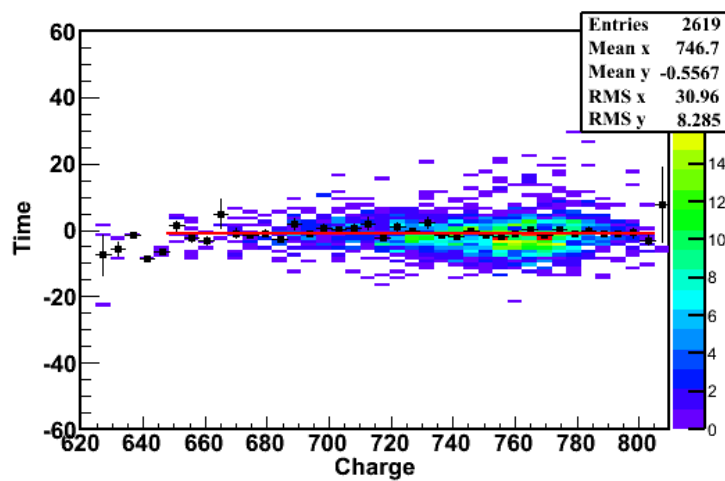


Figure 114: The relation between charge and time after slewing correction

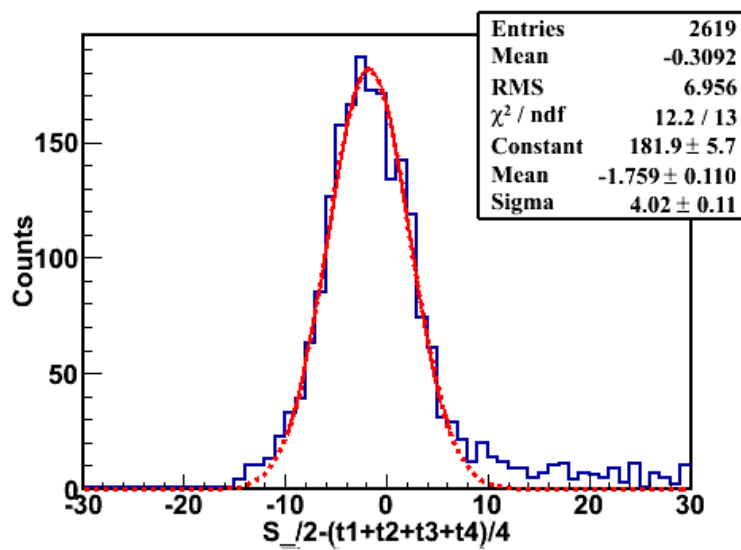


Figure 115: Time spectrum after correction

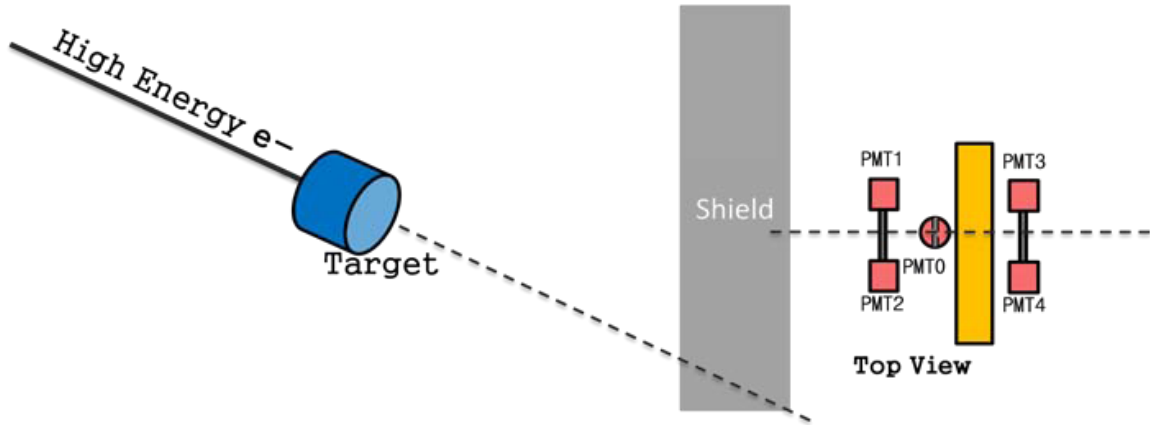


Figure 116: Setup of beam test in Hall A

11.4.2 Rate Scan

The rate depended on background intensity. From the scaler we can get the signal rate of MRPC. Fig. 119 show the signal rate change with time in RUN 188 and 193 respectively. The rate was not stable in each run. From these runs, we obtained different rates from 1 to 16 kHz/cm². These two runs were combined to analyze the rate performance. The results are shown in Fig. 120. It can be seen even when the flux rate reaches 16 kHz/cm², the efficiency is still higher than 94% and the time resolution is close to 80 ps. So this module meets the requirement of the SoLID TOF system.

The evolution of the charge distribution can be seen in Fig. 121 for this MRPC. The charge is obtained from the sum of its two ends. It can be seen that, with the increase of the flux, the average charge decreases and the spectrum shifts down to lower charges as expected.

11.5 Conclusions

A high rate MRPC was proposed to construct time of flight system for the SoLID-SIDIS program, and a prototype has been designed and constructed. The trapezoidal prototype module assembled with low resistive glasses has 10×0.25 mm gas gaps and 11 readout strips. The width of strips is 2.5 cm with an interval of 3 mm. This module was tested by cosmic ray and also tested by electron beams in Hall A of JLab. The results show its rate capability of larger than 16 kHz/cm². This module has a very promising time resolution. The time resolution can reach 50 ps in cosmic test and is about 75 ps in the beam test. The chambers behaved very stably during the experiment. These performances meet the requirement of the SoLID-TOF system. Detailed aging study has to be followed to assure the stability over a long running time.

References

- [1] Y. Wang, *et al.*, Nucl. Instr. and Meth. A 538 (2005) 425.
- [2] Y. Wang, *et al.*, Nucl. Instr. and Meth. A 537 (2005) 698.
- [3] A. Akindinov, *et al.*, Nucl. Instr. and Meth. A 602 (2009) 709.
- [4] A. Akindinov, *et al.*, Nucl. Instr. and Meth. A 533 (2004) 74.

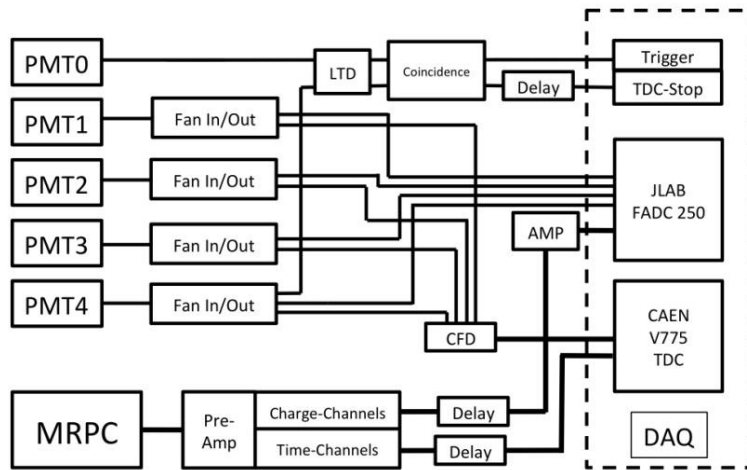


Figure 117: The diagram of DAQ system

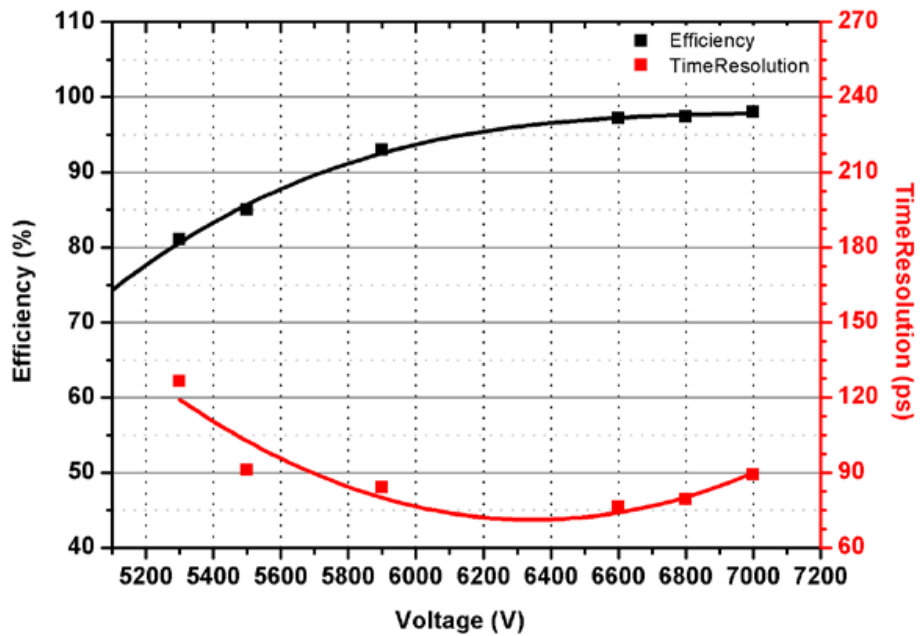


Figure 118: Time resolution and efficiency change versus applied voltage

- [5] Y.Wang, *et al.*, Chinese Physics C. 33 (2009) 374.
- [6] J.B. Wang, *et al.*, 2012 JINST 7 P10004.
- [7] JLab E-08-027, A. Camsonne, J. P. Chen, D. Crabb and K Slifer, spokespersons;
http://www.jlab.org/exp_prog/proposals/08/PR-08-027.pdf

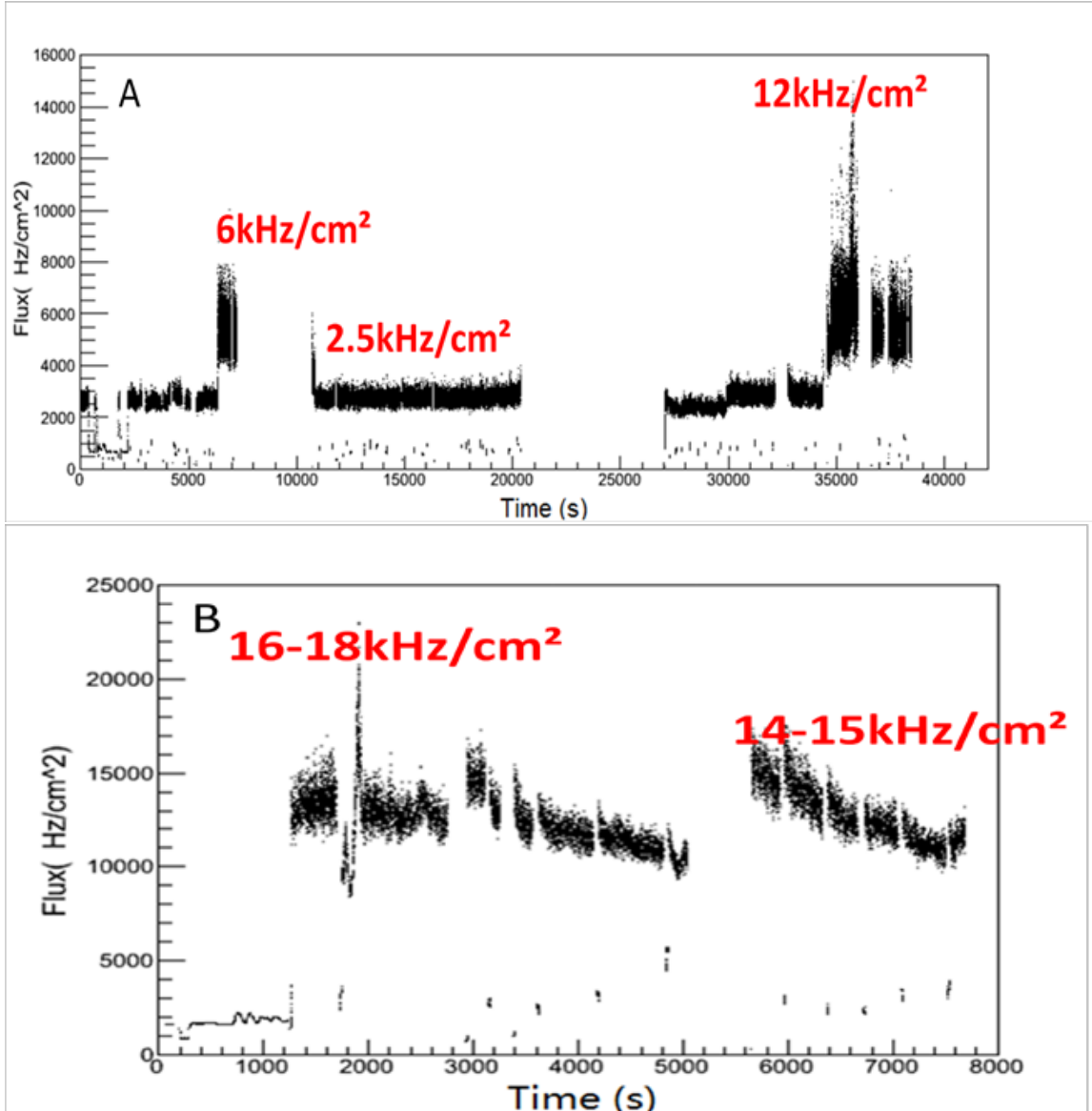


Figure 119: Signal rate changes with time. (A) shows RUN 188 and (B) shows RUN 193. MRPC located 5 meters from target. There is shield in front of the detector in (A) no shield in front of the detector in (B).

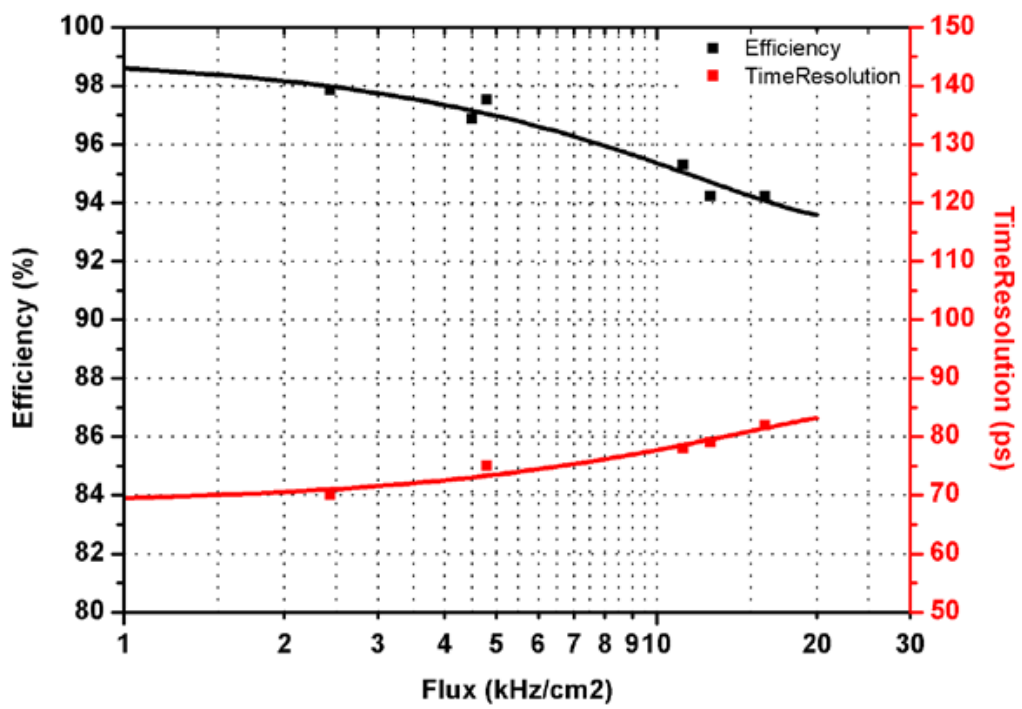


Figure 120: Measured efficiencies and time resolutions as a function of the particle flux.

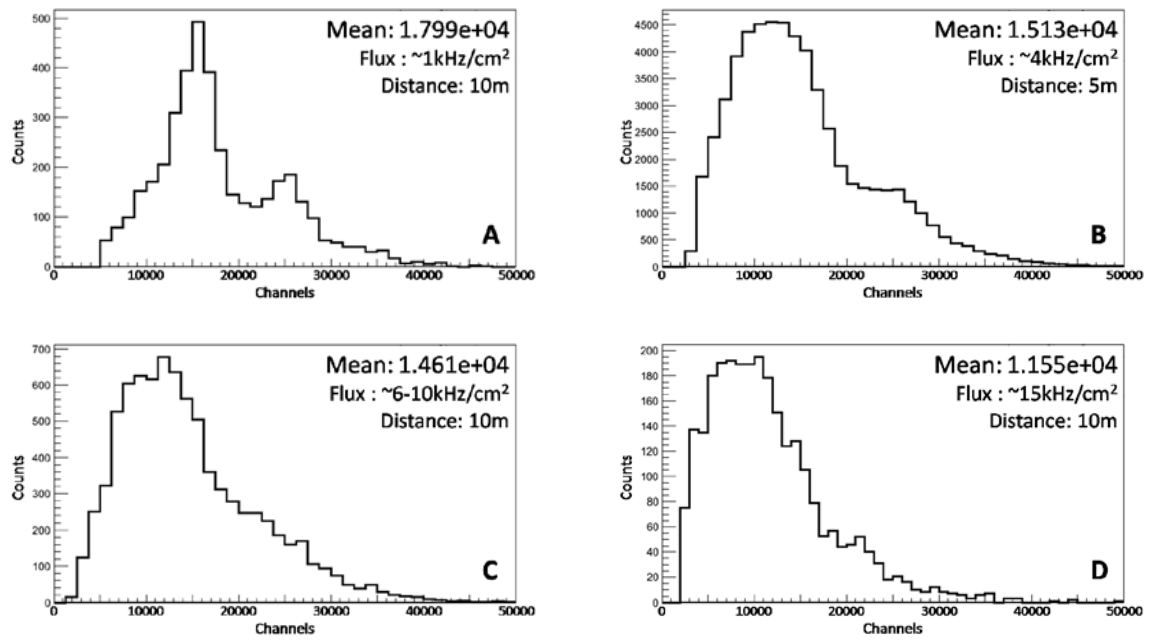


Figure 121: Charge distribution at various fluxes over one readout strip. Flux increases from figure A to D.

12 Data Acquisition

12.1 Introduction

The SoLID detector is a large acceptance detector designed to run at high luminosity. Several experiments are driving the project for the program of parity violation and transversity. The common point for these experiments are large background rates in the detector and trigger rates of the order of several tens of kilohertz. The detector will feature a few thousands of calorimeter channels, a few hundreds of channels of Cerenkov detectors and about hundred fifty thousands of channels for the GEM trackers.

Considering the large amount of channels, the rate requirements and the availability of new electronics developed for the Hall D GlueX detector, a pipelined electronics approach is chosen which consists of continuously digitizing the detector signals and keeping the data in large memory buffers to be looked back after the trigger is received. The data from the detectors being readily digitally available thanks to the Flash Analog to Digital Converter (FADC), one can directly generate the trigger from the FADC data. This gives a lot of flexibility on the First Level Trigger (L1) which can be changed by simply reprogramming the trigger algorithm based on the FADC data without the need of any re-cabling.

12.2 Jefferson Laboratory Hall D Flash ADC

The DAQ system of SoLID will use the modules recently developed by the Physics Division Fast Electronics group and Data Acquisition group of Jefferson Laboratory for Hall D. The central module for this system is the JLAB FADC250, a 16-channel 12-bit FADC sampling at 250 MHz. The input signals are continuously recorded into the memory with a memory depth up to 8 us. The system is thus dead timeless as long as the trigger is generated before the memory rolls over and the event of interest is overwritten. The Flash ADC has two separated data path. The first one uses the new high speed serialized VME standard called VME switched Serial (VXS). It allows full duplex point to point connection at up to 2.5 Gbps per lane using the backplane central connector. Currently the FADC is using two VXS lanes giving 5 Gbps of bandwidth. This allows to transfer a 16 bit word from each FADC to a Crate Trigger Processor (CTP) board every 4 ns. Each FADC being connected to The CTP via a 5 Gbps link, the CTP uses up to 16 FADC words from each FADC to form a 32-bit word every 4 ns which can be a lower resolution sum of all the channels or a bit pattern of the channel hit for example. The CTP board then sends the processed signals to a Sub-System Processor (SSP) board via a 10 Gbps optical link which puts together all the data from individual crates and computes the associated quantities which will be used in the trigger. All the SSP boards send their processed information to a Global Trigger Processor (GTP) which makes the L1 trigger. The GTP sends the trigger to the Trigger Supervisor (TS) which makes sure the system is ready to accept a trigger and sends the accepted signal to the Trigger Distribution boards in the VXS crates which are linked to the Trigger Interface boards in each crates via optical link as represented in Fig.122. The trigger and synchronization clock signals will then be sent back to individual crates and payload modules through Trigger Interface/Distribution (TID) boards and Signal Distribution (SD) boards which distributes the signals to the electronics such as the FADC. Once a trigger is generated, the full resolution data which is still in the pipeline is readout out using the VME320 protocol at an average data rate of 200 MB/s. The Flash ADC can run in different modes, it can either transfer all the samples of the waveform which can be useful to study pileup effect and background or process the data to give an integral over the length of the pulse.

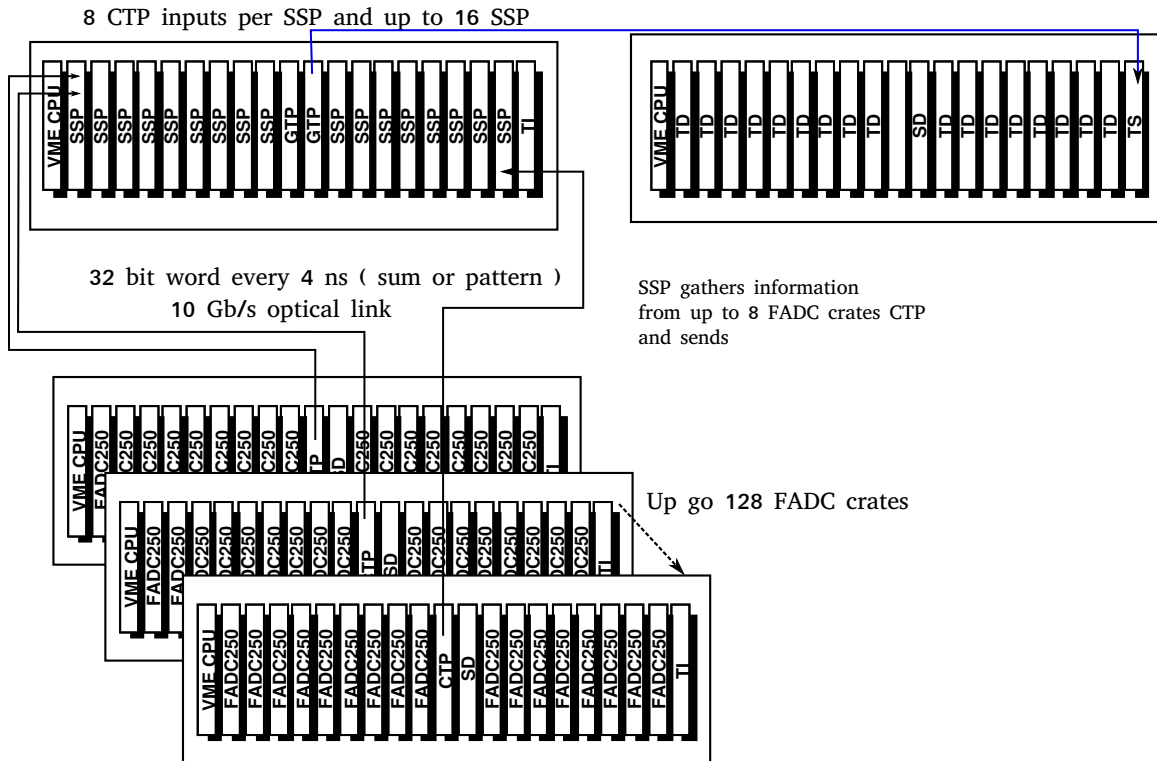


Figure 122: Standard Triggering scheme using the JLAB pipeline electronics

Table 13: Channel counts of individual detectors for PVDIS for one sector

Detector	Module Type	Number of Channels	Number of Modules
Electromagnetic Calorimeter (EC)	FADC	122	8
Light Gas Cherenkov (GC)	FADC	9	1
GEM	SRS	4700	1

12.3 PVDIS

The PVDIS measurement detects inclusive electrons to make a parity violation measurement. For such a measurement high rates are required to reach the needed statistical accuracy. The main trigger is going to be a coincidence of the electromagnetic calorimeter with the Gas Cherenkov trigger. The rate over the whole detector is expected to be of the order of 500 kHz, above the trigger rates that can be handled by the JLAB electronics which was tested up to 300 kHz for the FADC part. Since this measurement is inclusive, the detector will be split into 30 sectors giving a reasonable rate for each sector. From the simulation and the single rates from the EC 11 and CC 8.3.2 assuming a coincidence windows of 30 ns a coincidence rate of 20 kHz was determined.

12.3.1 Single electron Calorimeter trigger for PVDIS

Two options are available right now to generate a level 1 (L1) trigger. The standard one is the FADC computing the sum of all of its 16 channels and send the 16 bit sum value to the CTP every 4 ns.

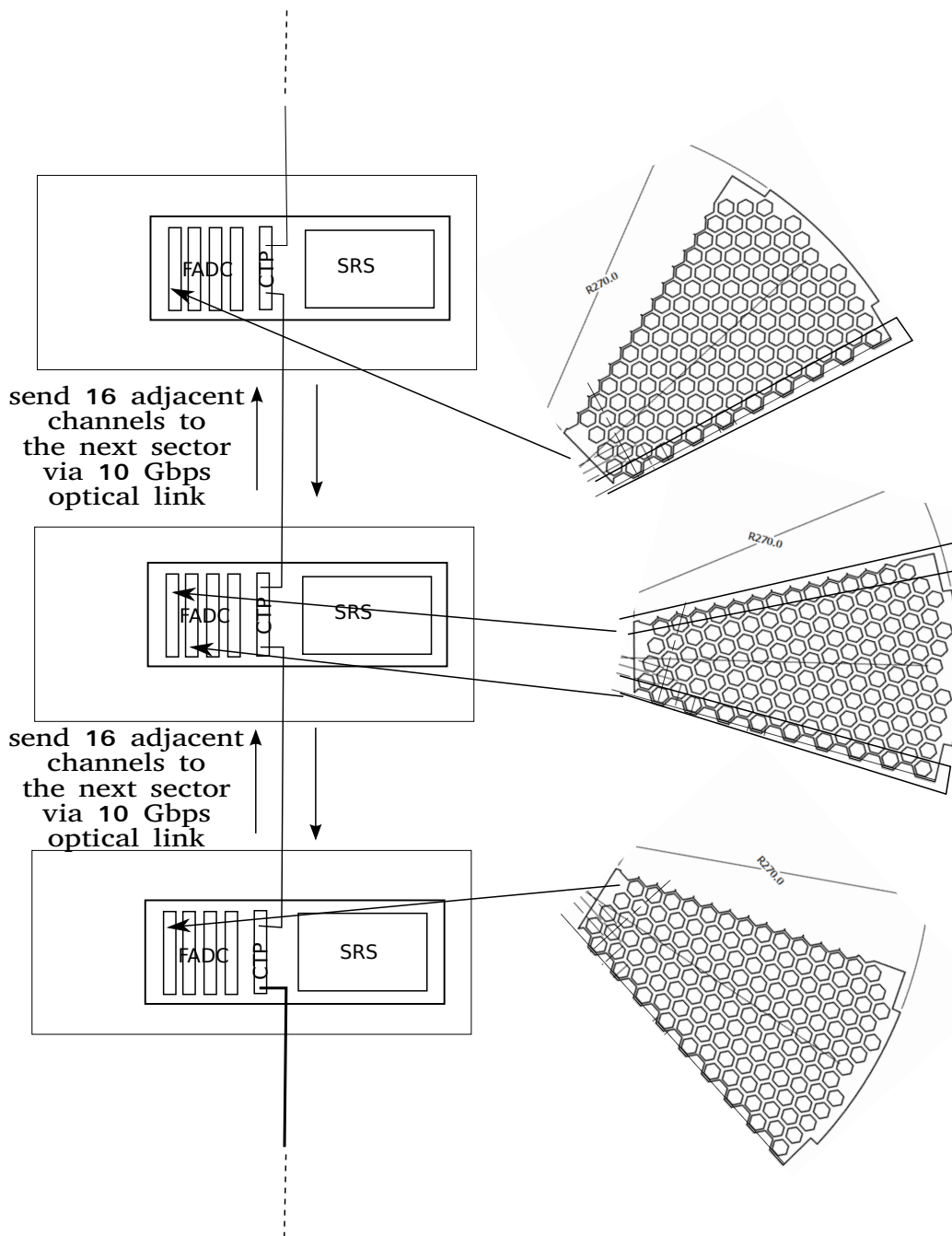


Figure 123: PVDIS specific electron trigger

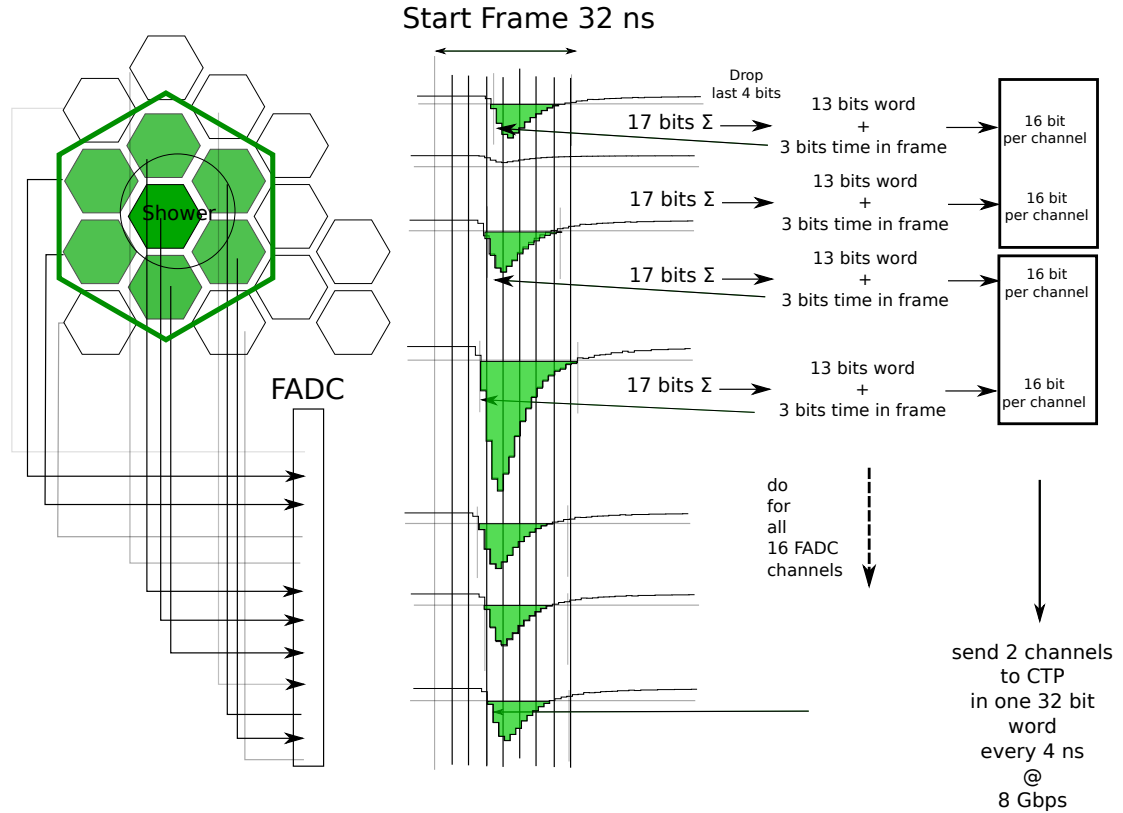


Figure 124: Calorimeter clustering scheme using the HPS algorithm. All calorimeter signals are sent to the FADC.

The CTP can sum all the FADC sums generating a global sum per crate. Another scheme was devised for the Heavy Photon Search experiment in Hall B. Each 32 bit word will carry the value of 2 channels and 8 of those words are sent giving all the channels every 32 ns as in Figure 124. The CTP having all the amplitude of all the calorimeter, it can compute all the sums of adjacent blocks. A sum of 3×3 blocks was implemented. In order to reduce the number of triggers coming from the background this summing approach is chosen to improve the online pion rejection. A sum over 1 central block and 6 surrounding blocks can be implemented in the same way as the HPS scheme.

In order to improve efficiency of hits shared between two sectors the amplitude recorded on a neighboring CTP are transferred through the bidirectional optical link between two CTPs as shown in Fig 123. Once the CTP received all the FADC data from its own crate and two adjacent crates, it either computes the total sum or performm cluster searching to generate trigger. A 64 bit pattern containing the FADC channels to be readout will be generated by the CTP and transferred to the Flash ADC using the trigger data path. A new firmware for the FADC will be developed to take this pattern into account allowing to only read the channels part of a cluster in order to reduce the sensitivity to background induced by usual pedestal suppression threshold.

12.3.2 Gas Cerenkov trigger

The gas Cerenkov detectors are both divided in sectors. The most straightforward way to generate a Cerenkov trigger is to put all 9 channels on one FADC board and generate the trigger from the CTP by putting a threshold on the sum of those 9 PMTs. To improve efficiency at interface between

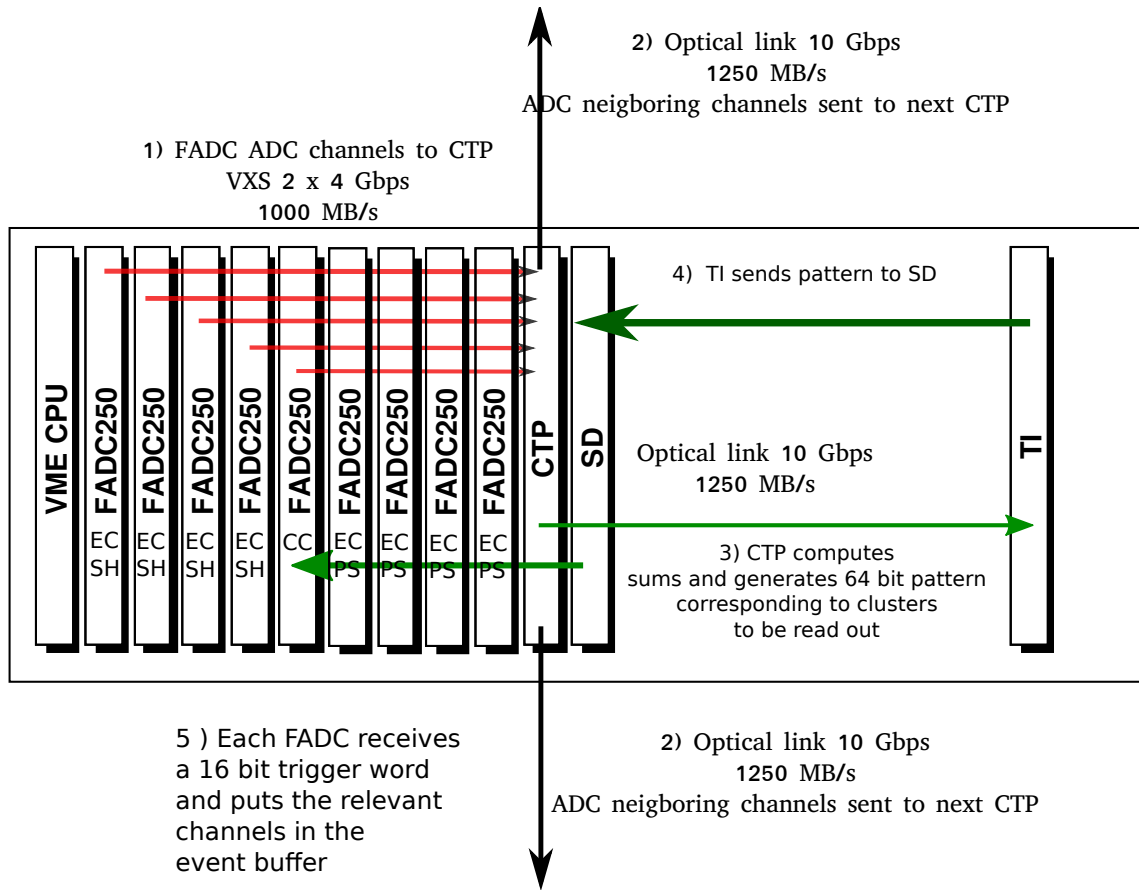


Figure 125: PVDIS FADC crate layout

two sectors one can put the threshold on the sum of two adjacent sectors. In case combinatory background is too big, one could switch to the clustering scheme similar to the calorimeter one. The efficiency and background of the different schemes was be evaluated in the full simulation of the digitized background. And it seems the summing is working and has good efficiency.

12.4 SIDIS and J/Ψ

12.4.1 SIDIS

Three experiments, E12-10-006 [1], E12-11-007 [2], and E12-11-108 [3], have been approved to measure single/double asymmetries through the semi-inclusive deep-inelastic scattering (SIDIS) ($e, e'\pi^\pm$) with the SoLID. With similar reaction channels, these experiments could share the same design of the DAQ system. The required overall luminosity of E12-10-006 and E12-11-007 is 10^{37} N/cm²/s, which is an order of magnitude higher than that of E12-11-108. Therefore, we will use E12-10-006 as an example to illustrate the requirement of the SIDIS DAQ. The goal of the SIDIS DAQ is to satisfy the requirement of ~ 100 kHz trigger rate, see Section 12.5 for more information about the limit.

The SIDIS process requires the detection of both the scattered electron and the leading pion. Therefore, a single electron trigger or a coincidence trigger of the electron and the hadron would satisfy the needs. The electron trigger at the large angle detector will be provided by the E&M

Detector	Channel
EC Shower	1800
EC Preshower	1800
SPD	300
Light Gas Cerenkov	270
Heavy Gas Cerenkov	360
MRPC	3300

Table 14: The numbers of detector channels for the SIDIS and J/Ψ experiment except for GEM.

calorimeter at a threshold of about 3 GeV. Such a trigger is sensitive to both high energy electrons and high energy photons (mostly from the π^0 decay). A set of scintillators is added in front of the calorimeter to reduce the trigger due to the photon by having it in coincidence with the calorimeter. With the scintillator paddles being incorporated into the trigger, the high energy photon triggers can be significantly suppressed.

The electron trigger at the forward angle detectors will be formed with a coincidence among the Gas Cerenkov detector, the E&M calorimeter, the scintillator paddel detector (SPD) and the Multigap Resistive Plate Chamber (MRPC). Considering the kinematics information of the scattered electrons from the DIS process (e.g. $Q^2 > 1 \text{ GeV}^2$), a position dependent energy threshold with a low limit at 1 GeV in E&M calorimeter will be used.

The single electron trigger rate was estimated from simulation to be 130 kHz for the forward angle calorimeter in coincidence with the Gas Cerenkov, SPD and MRPC. And it is 25.5 kHz for the large angle calorimeter in coincidence with the SPD. And the total rate of the single electron rate is 155.5 kHz. In order to control the level 1 trigger rate below the 100 kHz limit, we plan to form the coincidence trigger from the electron trigger and the charged hadron trigger. The charged hadron trigger using the calorimeter with the SPD and the MRPC is 14 MHz.

Hence the total accidental coincidence rate using a 30 ns time window will be :

$$155.5 \text{ kHz} \times 14 \text{ MHz} \times 30 \text{ ns} = 65.2 \text{ kHz}$$

With a physics coincidence rate of 2.8 kHz we get a coincidence trigger rate of 68 kHz. At the end, the coincidence trigger and the prescaled singles trigger will give a total trigger rate of 100 kHz.

12.4.2 J/Ψ

The E12-12-006 experiment is designed to measure the cross section of $p(e, e' J/\psi)p$ reaction at an unpolarized luminosity of $10^{37} \text{ N/cm}^2/\text{s}$ with a proton target. The primary trigger would be a triple coincidence of the scattered electron, and the decay electron and positron from J/Ψ . The scattered electrons are designed to be detected by the forward detector system with a momentum between 0.8 GeV/c and 2.5 GeV/c. The decay electrons and positrons are designed to be detected by either the forward detector system with momentum higher than 4.5 GeV/c or the large angle detector system with momentum higher than 2.5 GeV/c.

The design of electron triggers in both the large angle and forward angle detectors is similar to that of SIDIS. Due to the triple coincidences of lepton detection, the demand on DAQ from this experiment is much relaxed than that of SIDIS DAQ. For example, the position dependent threshold in the forward angle E&M calorimeter may not be required in the electron trigger.

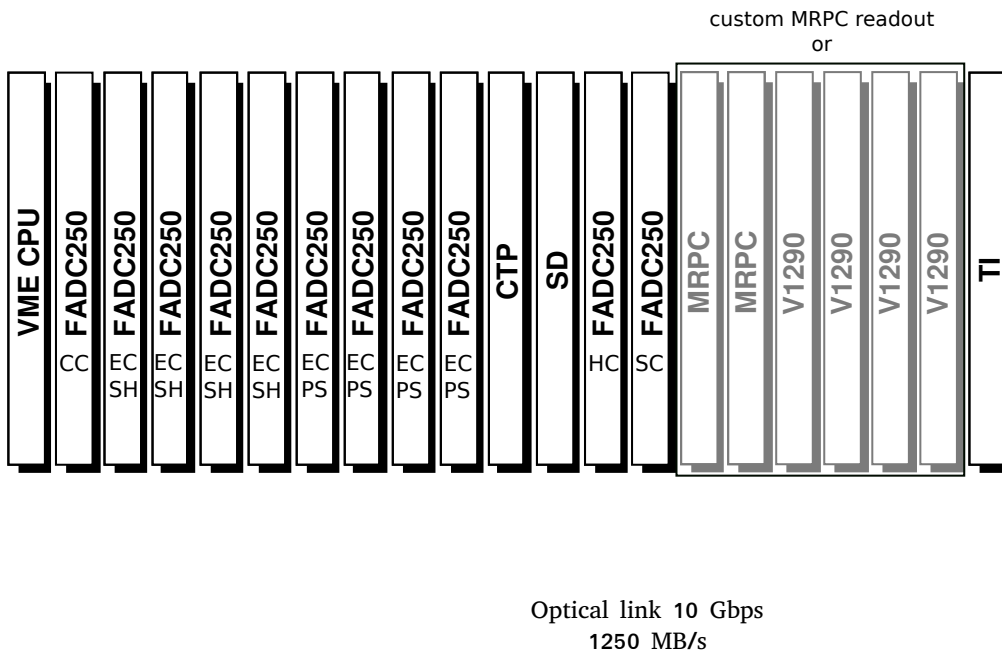


Figure 126: SIDIS FADC crate layout

12.4.3 Implementation SIDIS and J/Ψ

The SIDIS experiment will be reusing a similar detector setup as PVDIS by adding a few additional detectors. Scintillator planes are used to reduce the photon background since the baffles are removed. A Heavy Gas Cherenkov and a MRPC are also added for pi Kaon separation. The PVDIS crates will serve as base to the SIDIS DAQ, but the signals from the CTP will be sent to the SSP and GTP to be able to make coincidence trigger. Additional FADCs will be added for the additional detectors.

Based on our current simulation, the size of each event is expected to be about 3.1 kByte including signals from all detectors. So the 155.5 kHz singles rate and 68 kHz coincidence rate for SIDIS 3He will correspond to 482 MB/s and 210 MB/s aggregate DAQ rates of the total of 30 sub-crates.

The SIDIS experiment trigger formula is

forward angle electron trigger Forward Angle Calorimeter *AND* Light Gas Cherenkov *AND* SPD *AND* MRPC

large angle electron trigger Large Angle Calorimeter *AND* SPD

forward angle charged particle trigger Forward Angle Calorimeter *AND* SPD *AND* MRPC

coincidence electron trigger (large *OR* forward) *AND* forward angle charged particle trigger

The SIDIS experiment and J/Ψ use exactly the same detector configuration, cabling, DAQ and trigger hardware. The only difference is the trigger where one looks for a high energy electron and a pion for SIDIS and one looks for 3 high energy leptons for J/Ψ .

12.4.4 MRPC readout

So far the default solution is the development of a custom electronics module for the readout of 1550 strips of the MRPC. It will be a custom designed TDC receiving the 3300 channels of MRPC each strip being readout at both ends. Most likely solution will be to use a chip similar to the NINO chips which is an amplifier discriminator chip generating a discriminated signal with time resolution of the order of 10 ps and the width of the logic output is proportional to the time the pulse is above threshold allowing to have amplitude information for time walk correction. Rutgers University is proposing to use the GSI electronics and will help the integration into the DAQ this module is FPGA base with timing resolution better than 20 ps [?]. A new module is being developed by the JLAB electronics group to be able to use logic signals for the L1 which could be then used. The estimate price for this module is \$2000 for 96 channels, one would need 2 boards per sector which would add \$120k to add the MRPC in the trigger.

12.5 GEM readout

The GEM readout will be done with a specific chip. For now our studies are based on the APV25 chip which is suitable for the experiment requirements and we have a significant amount of channels available from other experiments. All the studies will hold for future chips which will be available later with better performances. The APV25 chip is a shaper amplifier circuit coupled with switched capacitor array chip to hold the data of 128 channels for 192 consecutive time samples of 25 ns. The data is continuously sampled at a 40 MHz frequency. When a trigger is issued the corresponding slice in time are frozen to be readout. This allows a look back in time of up to 4 μ s. With such a pipeline design the system is deadtimeless until all the samples are flagged to be readout which would occur with rates of several megahertz. The limiting factor of the system is the readout since the pipeline has to be emptied. The first stage of the readout is between the APV25 chip and the front end electronics. Readout of the chip is also done at 40 MHz. For each trigger 128 channels are readout, each channel has a 12 bit value with a 11 bit header which constitutes a 32 bit word, additional control words make a total of 141 signals to be transferred. The chip has the ability to record 1 sample per trigger or 3 samples in case of high background. The signal is transferred in an analog form which is digitized by an ad hoc FADC. In the case of one sample it will take :

$$141 * 25 = 3.6 \mu s$$

to transfer the data from the chip. This time is tripled to 10.6 μ s for 3 samples readout. This data transfer rate is ultimately limiting the rate capability of the chip to 91 kHz in 3 samples mode. The 3 samples mode can be used with on chip deconvolution effectively reducing the width of the pulse. All the data is digitized on board with pedestal subtraction and zero suppression. We are planning to use the CERN Scalable Readout System (SRS).

This system developed by the RD51 gathers all the common high level digital functions of a typical readout system : triggering, buffering, data transfer and event building. Only a chip specific interface is then needed to be developed. Such a board is available for several years for the hybrid boards holding APV25. Each hybrid board is linked to a Chip specific card using HDMI cables. This card has 8 FADC and can readout 8 APVs chips for 2048 channels of detectors per board. Those boards interface with the SRS Front-End Card (FEC). The FEC card processes the digitized data and transfers the data to a computer directly through Gigabit Ethernet. A Eurocrate can hold up to 8 FEC. For larger systems a Scalable Readout Unit (SRU) can be used then the FEC transfers the data to the SRU using DTCC a faster protocol than Ethernet allowing to distribute the clock and trigger as well as the data on the same Ethernet cable and the SRU sends the gathered data to the computer

Chamber	Hits	Hits>200	Hits with deconvolution	Offline treatment
0	316	199	23	160
1	303	147	12	116
2	283	107	9.4	104
3	280	102	8.9	72
Total hits	1182	555	53.3	452
Naive occupancy(%)	25.2	11.8	1.2	9.6
Event size 1 samples (Kbytes)	9.47	4.44	0.432	1.5
Event size 3 samples (Kbytes)	28.39	13.32	1.296	6.1
Data rates 20 kHz 3 samples (Mb/s)	567.84	266.4	25.92	30.6

Table 15: PVDIS GEM occupancies and event size for GEM

through 10 Gigabit Ethernet. Each FEC communicating individually to the computer or SRU, the system is highly Scalable and modular. As many FEC can be added to be able to readout all the detector channels. The performance of this system will be tested this year since UVA acquired a full read-out system but one can assume transfer speed will be the same as the internal bus of the PC, so we can expect at least 1 GB/s.

Some better chips (DREAM,CLAS12, SALTRO, VMM1, VFAT2) are foreseen to be available and should provide better performance for similar costs as the APV25 and will be adapted to the SRS system as they become available.

12.5.1 Background and GEM event size

In order to have a good evaluation of this size, the GEM signal and the APV25 digitization was modeled in the simulation, more details about this process is available in the simulation section 3.3 of this document. The total number of strips fired in a 25 ns window was computed in three different ways : one including all the hits having non zero energy, one with an arbitrary ADC threshold of 200, the third number is obtained by simulating the on chip deconvolution algorithm 3.3 in addition to the 200 channels threshold. The last column are the results coming from the tracking simulation Section 17. An optimization of the threshold with the background level and tracking efficiency will be done once the full simulation including background and tracking analyzing framework will be done.

12.5.2 PVDIS GEM rates

For PVDIS, we are interested in the data rate per sector. The numbers will be evaluated for 30 kHz (20 kHz rate + 50% safety margin). One can conclude that even if the occupancy is high, the data rates are manageable for PVDIS. The deconvolution and filtering are able to significantly reduce the occupancy and event size. We will plan to read out 3 samples to be able to do more treatment of the data offline in case the on chip deconvolution is affected by the high level off background. Using the SRS system, each FEC can transfer 1Gbps through its Ethernet link. Each sector has about 4700 strips so will need at least 3 FEC, by using an additional FEC, one can insure a 500 MB/s transfer rate. Each dedicated computer to will have 4 Gigabit Ethernet port and one 10 GigE Ethernet port to send the data to the L3 farm allowing transfers up to 500 MB/s which should be sufficient. We expect the combination of shower and PID cut in association with crude tracking to give us the factor of 4 data reduction needed. Testing of online data reduction will be studied using the simulation data we generated.

Chamber	Hits	Hits > 200	Hits with deconvolution
0	510	150	30
1	1890	450	60
2	1020	270	30
3	870	240	30
4	810	180	30
Total hits	5880	1470	210
Naive occupancy(%)	4.1	1.04	0.1
Event size 1 sample (Kbytes)	34.32	8.88	1.2
Data rates 100 kHz (Mb/s)	3432	888	120

Table 16: SIDIS GEM occupancies and event size for GEM

12.5.3 SIDIS GEM rates

For SIDIS, we need to have the data of all 30 sectors together since the leading pion can be anywhere in the detector. So the event size is very important to determine the data rate that can be recorded. The occupancy of the detector is fairly low when using the on-board deconvolution which is the default running mode for SIDIS. By reading in one sample mode with deconvolution, we expect the allowed trigger rate to be about 200 kHz which is very close to the theoretical limit of 270 kHz. But in trigger design for the SIDIS experiment, we put an additional safety factor of 0.5 to further reduce the allowed trigger rate to 100 kHz to tolerate any uncertainties in our rate estimation. We are planning to use a SRU to concentrate the signal from the SRS FEC, this module gathers all the FEC signals and send the data to a 10 Gbit Ethernet port which means around 1.2 GB/s. To have a safety margin a second SRU will be added for an additional \$4000 in case occupancies happen to be much higher than expected from Simulation.

12.6 Event size from FADC

The FADC samples are 12 bit at 250 MHz. In the case of PVDIS, since pile up is going to be significant, we plan to record all the waveform. The pulse signal is 40 ns wide, so we will be recording 10 samples for each detector channel. The event size per channels is per FADC : 4 bytes for block header, 4 bytes block trailer, 4 bytes for event header and two samples are packed in a 4 bytes word. For 10 samples each event is then $(12 + n * 10 / 2 * 4)$ bytes with n the number of channels firing.

The FADC simulation with digitization is still being developed. Given the size of a sector, the event size will be estimated with a maximum of 2 clusters of 7 for shower and 2 clusters of 3 preshower and assuming all 9 PMTs of the Cerenkov fire all the time. With this assumption the event size is 1160 bytes per event.

With the trigger rate of 20 kHz, this gives 23.2 MB/s data rate. As far as data rate are concerned VME320 backplane can transfer up to 200 MB/s.

In the case of SIDIS, the occupancy on the detector is small enough to only record the integral of the pulses, the estimated event size using the occupancies from the simulation is 1.9 KBytes, which give an aggregated data rate of 187 MB/s at 100 kHz for all 30 crate.

12.7 Data rates,event size and L3 Farm

Experiment	Event Size (kBytes)	L1 trig Rate (kHz)	L3 Data in Rate MByte/sec
PVDIS	47.76	20	955.2
SIDIS	3.1	100	310
JPsi	2.58	3	7.74

The L3 Farm will provide data reduction before putting it on tape since the amount of data generated by the electronics can be very large especially for the PVDIS experiment where the full waveform is recorded.

The trigger rate per sector in coincidence will be about 20 kHz per sector so L3 farm will be designed to handle 30 kHz to have a safety margin.

In addition to L1 farm based on the FADC information, the L3 Farm will do crude and quick reconstruction giving access to momentum.

The data reduction strategy will be based on region of interests by correlating GEM with calorimeter position and do crude tracking. This should significantly reduce the GEM data by discarding random hits. The timing will be refined by computing the time walk effect and taking into account path length and momentum correction. One can expect a resolution of the order of one nanosecond but to be conservative we will assume 10 ns for the data reduction estimates which gives a factor of 3 of reduction which already satisfies the limit of 250 MBytes/s put on tape.

The Flash ADC data will be further reduced by clustering on the calorimeter, considering the energy sharing between blocks we can expect a factor of 2 of reduction.

The simulation is being developed to generate digitized data including background. Once the full simulation is complete the different algorithm speed will be evaluated.

In order to have a first estimate of the processing, we will use the Hall D estimate for the L3 tracking. The Hall D forward detector has 24 detectors layers with 96 wires per plane and 3 readout channels per plane for a total of 6912 channels of tracker and 2800 channels of lead glass calorimeter. With wire based tracking speed of reconstruction is 27 Hz per CPU, without tracking the L3 trigger speed is tripled to 77 Hz. Each sector for PVDIS has about 4700 GEMs strips for 61 calorimeter blocks. Given the higher background and 3 samples treatment I will assume a slightly lower speed for tracking of 20 Hz. Most likely given the fewer number of blocks the non tracking speed should be faster but we will assume the same rate of 77 Hz for now.

Assuming a rate of 30 kHz per sector for PVDIS, we would require 1500 CPUs with tracking and 390 CPUs without wired base tracking.

12.8 Experiment switch over

It is not clear which experiment is going to go on the floor. But I will assume SIDIS experiment will go first, then switching to PVDIS will consist mostly of connecting the FEC of the SRUs directly to the sector dedicated PC for each sector and sending the L1A signal from the TI to the SRS. Additional FADCs for HC and SC will be uncabled and moved out from Hall to keep them as spare for PVDIS. GTP and SSP modules will be also removed.

12.9 Hall DAQ installation

The DAQ will be located in the hall, on the left side close to the entrance door from the counting house. A shield hut will be build to protect electronics from radiation. From QWeak experiment

experience estimated cost is about 10 days of designer time and 4 week / man of technician for installation. Including additional hardware this comes to a rough estimate of \$50k for cable tray and electric installation. It is assumed that all shielding blocks will be reused from the laboratory stockpile.

12.10 Cabling and rack

The SIDIS setup will have the most number of channels in use at the same time. Total number of cables needed for 4118 coaxial cables and 206 ribbon cables for the MRPC assuming we use NINO type time over threshold scheme. Since we are using pipeline electronics cable length does not need to be exactly the same. The BigCal calorimeter for the GeP III experiment used 1740 cables of about 100 meters and could be used if BigCal is not used at the same time. Assuming we can fit 3 VXS crate per rack as in Hall D, we will need 11 racks for the FADC and trigger. Depending if we use ATCA (14 FEC) or eurocrate (8 FEC), we will have 15 or 9 crates, the GEM cables being a bit less bulky than RG58, we will fit 4 crates per rack, so that would be 4 additional rack for a total of 15 racks. We might be able to reuse the SuperBigBite fastbus electronics weldment if the detector is not used which has 8 racks.

12.11 Pre R&D and tests

Right now we procured / loaned the VME APV25 readout, 4 FADC and 2 VXS crates. The readout software is being written for the APV25 to test the performances. A new version of the APV25 readout implement the VME 2eSST protocol. A CTP and a GTP are on order and should be available by May. This will allow to test PVDIS and SIDIS trigger in a smaller scale. A funding request for two additional VXS crates and FADC was made for fiscal year 2014.

References

- [1] E12-10-006, “Target Single Spin Asymmetry in Semi-Inclusive Deep-Inelastic ($e, e'\pi^\pm$) on a Transversely Polarized ^3He Target at 8.8 and 11 GeV”, Spokesperson: J.-P. Chen, H. Gao (contact), X. Jiang, J.-C. Peng, and X. Qian.
- [2] E12-11-007, “Asymmetries in Semi-Inclusive Deep-Inelastic ($e, e'\pi^\pm$) Reactions on a Longitudinally Polarized ^3He Target at 8.8 and 11 GeV”, Spokesperson: J.-P. Chen, J. Huang (contact), Y. Qiang, and W.-B. Yan.
- [3] E12-11-108 “Target Single Spin Asymmetry in Semi-Inclusive Deep-Inelastic ($e, e'\pi^\pm$) on a Transversely Polarized Proton Target”, Spokespersons: K. Allada, J.-P. Chen, H. Gao (contact), Z.-E. Meziani, and X.-M. Li.
- [4] L. W. Whitlow, SLAC-Report-357 (1990).
- [5] Developed by J. W. Lightbody and J. S. O’Connel in 1988.
- [6] D. E. Wiser, Ph. D. thesis, Univ. of Wiscosin (1977).
- [7] E12-12-006, “Near-threshold Electroproduction of J/ψ with a 11 GeV Beam”, Spokespersons: K. Hafidi, Z.-E. Meziani (contact), X. Qian, N. Sparveris, and Z.-W. Zhao.
- [8] E12-12-006, “Near-threshold Electroproduction of J/ψ with a 11 GeV Beam”, Spokespersons: K. Hafidi, Z.-E. Meziani (contact), X. Qian, N. Sparveris, and Z.-W. Zhao.

- [9] “Specifications for FADC-based HPS clusterer” Scott Kaneta
- [10] “THE UPGRADE PATH FROM LEGACY VME TO VXS DUAL STAR CONNECTIVITY FOR LARGE SCALE DATA ACQUISITION AND TRIGGER SYSTEMS”, Chris Cuevas, David Abbott, Fernando Barbosa, Hai Dong, William Gu, Edward Jastrzembski, Scott Kaneta, B. Moffit, Nick Nganga, Ben Raydo, Alexander Somov, William Mark Taylor, Jeff Wilson, Thomas Jefferson National Accelerator Facility, Newport News, Virginia, U.S.A JLAB-PHY-11-1458
- [11] “THE GLOBAL TRIGGER PROCESSOR: A VXS SWITCH MODULE FOR TRIGGERING LARGE SCALE DATA ACQUISITION SYSTEMS”, S. Kaneta, C. Cuevas, H. Dong, W. Gu, E. Jastrzembski, N. Nganga, B. Raydo, J. Wilson, Jefferson Lab, Newport News, VA, U.S.A. JLAB-PHY-11-1482
- [12] Hall D CDR
- [13] ”Implementation of a Level 1 Trigger System using High Speed Serial (VXS) Techniques for the 12GeV high luminosity experimental programs at Thomas Jefferson National Accelerator Facility”, C. Cuevas, B. Raydo, H. Dong, A. Gupta, F. J. Barbosa, J. Wilson, W. M. Taylor, E. Jastrzembski, D. Abbott Fast Electronics Group, Thomas Jefferson National Accelerator Facility, Newport News, United States, 2009 16th IEEE-NPSS Real Time Conference
- [14] “THE GLOBAL TRIGGER PROCESSOR: A VXS SWITCH MODULE FOR TRIGGERING LARGE SCALE DATA ACQUISITION SYSTEMS”, S. Kaneta, C. Cuevas, H. Dong, W. Gu, E. Jastrzembski, N. Nganga, B. Raydo, J. Wilson, Jefferson Lab, Newport News, VA, U.S.A. JLAB-PHY-11-1482
- [15] “Description and Technical Information for the VME Trigger Interface (TI) Module” J. William Gu <https://coda.jlab.org/wiki/Downloads/HardwareManual/TI//TI.pdf>
- [16] “Description and Technical Information for Version 4 Trigger Supervisor (TS) Module”, J. William Gu <https://coda.jlab.org/wiki/Downloads/HardwareManual/TS/TS.pdf>

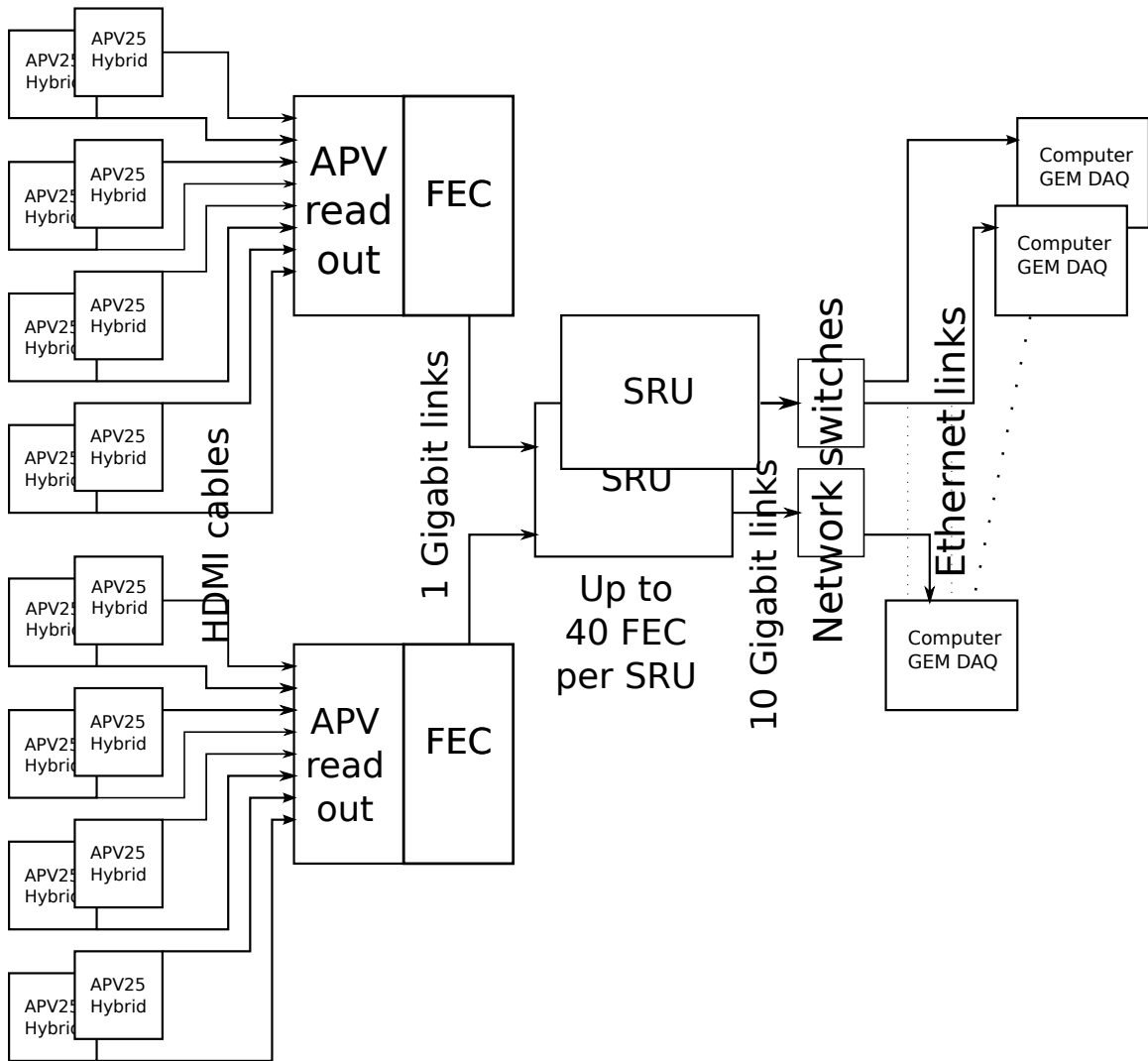


Figure 128: Standard SRS architecture which will be used for SIDIS experiment

13 Software and Tracking

At the time of this writing, development of the SoLID offline reconstruction software is at a very early stage. Although data taking is several years away, early planning is nevertheless important. This is especially true for the track reconstruction, where the usual feasibility questions arise. In the following, we describe the present conceptual design of the SoLID reconstruction chain and the status of the prototype track reconstruction software.

13.1 Software Framework

No decision has yet been made regarding the software framework to be used for SoLID analysis. One possible candidate is the present “Hall A C++ analyzer” [1]. This framework is object-oriented, highly modular and quite mature; it has in been in production use in Hall A since 2003. Currently, upgrades are underway to adapt the analyzer to the more demanding computing requirements of the 12 GeV era. In particular, automatic event-level parallelization will be implemented to take maximum advantage of current and future multicore processors, and a full library of decoder modules for the JLab-developed 12 GeV pipelined electronics is being written. These upgrades can be expected to be completed long before SoLID running, in part because they will already be needed for earlier experiments such as SuperBigBite (SBS).

Alternatively, SoLID might adopt one of the frameworks developed for the other Jefferson Lab halls for the 12 GeV era, *i.e.* the CLARA framework of Hall B and the JANA framework of Hall D. Both of these will have been extensively tested and optimized for very high data volume processing by the time of SoLID running and so should, in principle, be suitable for SoLID analysis as well. The main drawback of adopting a non-Hall A framework would be the lack of experience with such software within a collaboration mainly familiar with the Hall A environment.

Regardless of which framework is adopted, many existing detector analysis modules can most likely be reused for the development of SoLID software, for instance for the Cherenkov and calorimeter detectors. While the basic physics algorithms in these classes can be adopted without much change, code will need to be developed to support the cylindrical geometry of SoLID as well as the individual local detector geometries. Furthermore, a probability-based particle identification system would be desirable to have within the software framework, which may need development and/or refinement for SoLID. Development of calibration software tuned to the SoLID detectors will be necessary as well.

13.2 Track Reconstruction

Track reconstruction for SoLID, both in PVDIS and in SIDIS, is challenging for several reasons. High rates, up to on the order of 1 MHz/cm², lead to relatively high expected occupancies in the trackers. High occupancies, in turn, increase noise, hit ambiguities and combinatorics. Moreover, the level 3 data reduction envisioned for SoLID-SIDIS requires track reconstruction to run in real time, hence reconstruction speed is of the essence. Finally, systematics for SoLID-PVDIS must be kept especially low due to the parity-level asymmetries to be measured.

Extensive tracking simulations of GEM-based tracker systems were carried out in 2011 for the Hall A SBS project. In these studies [2], successful track reconstruction with > 90% efficiency was demonstrated even though the rates and occupancies in the GEMs exceeded the worst-case estimates for SoLID (see below). The main difference to SoLID is that, unlike SoLID, tracks in SBS will be straight since the tracking region is field-free. Handling track curvature is generally a matter of choosing and optimizing a proper reconstruction algorithm, whereas overall track reconstruction

feasibility is closely linked to the rates in and performance of the tracking hardware. Since both SBS and SoLID propose to use rather similar GEM trackers with comparable if not lower rates, the positive SBS results encourage us to believe that SoLID track reconstruction will not present a fundamental problem.

Currently, there are two candidate algorithms for track reconstruction that we plan to evaluate:

1. Xin Qian's "Progressive Algorithm" [3], which is essentially an implementation of a Kalman filter [4]. It allows for nearly arbitrary track curvature and was already shown, in a simplified approach, to be a feasible track reconstruction method for both PVDIS and SIDIS rates. However, it has not yet been tested with the full SoLID simulation data available now, nor has been implemented in the Hall A analyzer framework. Also, in general, progressive algorithms are computationally expensive and require a track starting point (seed). Finding track seeds from calorimeter hits is not difficult, but requires a calorimeter to be included in the simulation and reconstruction software, which is not presently the case.
2. The TreeSearch algorithm developed for the Hall A BigBite MWDCs [5]. This algorithm implements a global recursive template matching method [6], which is very fast, does not require a seed, has been integrated into the Hall A analyzer and demonstrated to work with both various BigBite data and SBS simulation data, the latter with very high occupancies. TreeSearch has also been used successfully in several other nuclear physics experiments, including HERMES, Qweak, and OLYMPUS. However, the algorithm may not fully solve the problem as it requires (nearly) straight tracks, which is not necessarily the case in SoLID, especially for SIDIS.

As a first attempt at SoLID track reconstruction, we decided to investigate the TreeSearch algorithm. The high speed of this algorithm is a major advantage, especially with a level-3 trigger in mind. Even if track curvature should turn out to be a problem for final track reconstruction, TreeSearch may still be useful as an effective noise filter for a subsequent tracking step.

Figure 129 illustrates the TreeSearch track reconstruction chain. Several key items are explained in the following:

1. Deconvolution & Clustering: Computes the signal amplitude for each GEM readout strip via a simple deconvolution algorithm [7] operating on the three amplitude samples provided by the GEM readouts. Additionally, this step rejects noise, identifies clusters of adjacent strips with over-threshold amplitudes and calculates the charge-weighted centroid of each cluster, as illustrated in Figure 130.

These pre-processing steps are independent of the track finding algorithm used. Some of the pre-processing could be performed by front-end firmware, as discussed in the DAQ section.

2. TreeSearch: This step implements the recursive template matching method proper described in [6]. TreeSearch operates independently for each readout strip coordinate ("projection").
3. 2D Decloning: TreeSearch frequently finds multiple patterns consistent with a single track. With GEM trackers, this occurs because of the finite hit position resolution and noise. Such clone patterns are merged as much as possible at this stage to improve speed and to suppress clone tracks. This part of the algorithm represents a clustering problem in computer science terminology.
4. Projection Matching: Track projections found in prior steps are matched to form 3-d tracks. Hits in the two coordinates of the 2-d GEM readout planes can be matched through correlation

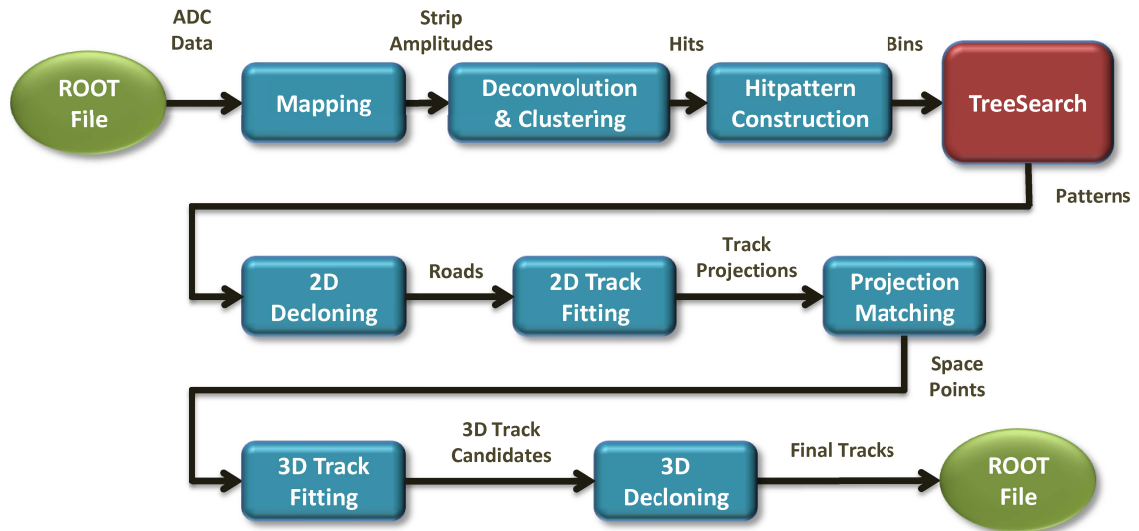


Figure 129: Schematic of the TreeSearch track reconstruction algorithm. Green boxes represent files, blue and red boxes, software modules, and text above arrows, the type of data passed between modules.

of their ADC amplitudes. In doing so, one correlation value is found for each chamber, yielding a very high matching probability even if amplitudes in a single readout plane are relatively loosely correlated.

5. 3-d Decloning: Clone tracks surviving at this stage are rejected by requiring that no tracks may share any hits. Of tracks with common hits, only the one with the best χ^2 of the 3-d straight line fit survives.

13.3 Simulation Results

The performance of the TreeSearch algorithm in the SoLID-PVDIS environment is currently being studied with simulation data. Figure 131 depicts the components of the analysis chain. The first box in this figure represents the simulation framework described in Sec. 3.1 and the second, the GEM digitization discussed in Sec. 3.3. The output ROOT file of the digitization is analyzed using the standard Hall A analyzer [1], described earlier, in the same fashion as actual experimental data. The final ROOT file for interactive analysis contains the reconstructed quantities as well as MC truth data for reference.

The Monte Carlo data sets were generated using the DIS generator and the PVDIS detector configuration with a 40 cm long liquid deuterium target. Five GEM chambers were configured, with parameters similar to the ones detailed in Table 4, however using only a 10° stereo angle and $400 \mu\text{m}$ strip pitch throughout. In the data sets used to date, muons were propagated as the primary scattered particles through the spectrometer to minimize interactions and multiple scattering. (Electrons will be used in future studies.) These muon data represent the “signal” to be reconstructed. Signal runs were performed without a magnetic field in the spectrometer to obtain straight tracks. (As discussed earlier, the *feasibility* of reconstructing straight and curved tracks, respectively, should be similar, although each track class calls for a different algorithm.)

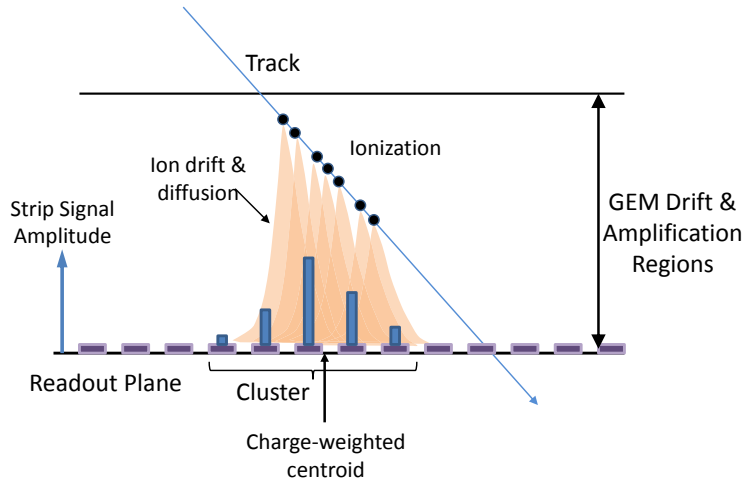


Figure 130: Ionization, charge collection, and clustering in a GEM readout plane. GEM foils have been omitted for simplicity (cf. Fig. 56).

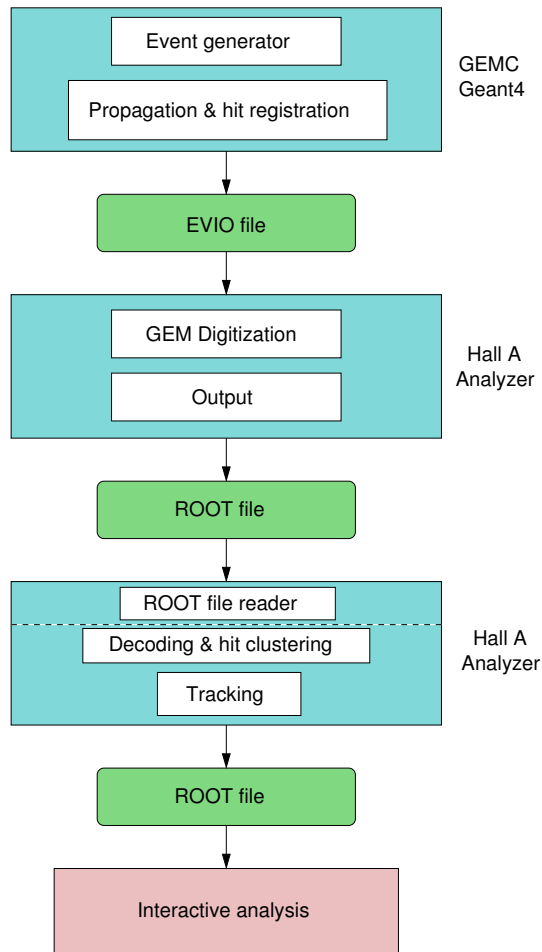


Figure 131: Flowchart of the SoLID track reconstruction simulation

Background from non-DIS processes was added to the signal runs at the digitization stage, using a 300 ns wide uniform random distribution of event times relative to the primary interaction. This time window roughly equals the effective gate time of the tracker electronics. Each background event added in this manner corresponds to one beam electron passing through the target within 300 ns of the primary interaction. Hence, to simulate 100% background intensity, so many events must be added to a single signal event as electrons pass the target during this time window at the expected production beam current, $50 \mu\text{A}$. This is approximately $9.4 \cdot 10^7$. To study 10^4 signal events, then, one needs approximately 10^{12} background events, which are obviously unrealistic to obtain under constrained time. For this study, a smaller set of $2 \cdot 10^8$ background events was generated, of which the fraction corresponding to the desired background intensity was added to the signal using the above-mentioned time randomization. This procedure ensured a different background hit topology and timing profile for every signal event. Due to limited computing time available, only background intensities up to 25% have been studied so far.

Unlike the signal runs, background data were simulated assuming the presence of a magnetic field, resulting in proper simulation of the field's sweeping effect for low-energy particles. However, any true secondary tracks present in the background would likely only be reconstructed with low efficiency since they would fail the straight-line requirement of TreeSearch. We estimate the rate of such secondaries to be small and expect that most secondary tracks, if reconstructed, could be rejected using Cherenkov and calorimeter data or by simply not being in the trigger sector. On the other hand, the presence of the field is not expected to have a significant effect on the rate of ghost tracks, which typically result from combinatorics of randomly-distributed noise hits.

13.3.1 GEM Occupancies

Average occupancies obtained for each readout plane coordinate with simulation data at 25% background intensity are listed in Table 17. Here, average occupancy is defined as the total number of readout strips with signal ("active strips") divided by the total number of strips in the plane. Before considering a strip active, its signal was subjected to the deconvolution and noise filtering procedure described in Section 3.3 and in [7]. Only pulses within an approximately 25 ns wide time window successfully pass this step, reducing noise by about one order of magnitude.

One observes that the noise-filtered occupancies are below 15% in all planes, and below 10% for all but the first chamber. As mentioned, simulations of SBS [2] have demonstrated track reconstruction in GEMs to be feasible with high efficiency at filtered occupancies up to 20%.

13.3.2 Track Reconstruction & Efficiency

Track reconstruction has been studied for background intensities up to 10% so far. These simulations employed 4 GEM planes and a less optimized shielding configuration in the spectrometer than is now available.

The overall tracking efficiency for very clean muon-only data (no background) was found to be about 88%. The 12% inefficiency was found to be partly due to an effective 90% single hit efficiency and partly due to various χ^2 cuts in the reconstruction. With 10% background, the efficiency drops to 63%. However, for that study, the noise filtering algorithm described above was ineffective and so the study is actually representative of a higher, but difficult-to-quantify background intensity.

Figure 132 illustrates the residuals obtained in the 10% background study. Despite the low statistics, one observes good resolutions and centered, approximately Gaussian distributions in all coordinates, indicating a functioning reconstruction chain.

Filtered occupancies, 5 GEM setup, 25% background				
Plane	Mean # active strips	Total # strips	Occupancy @ 25% bg (%)	Est. Occupancy @ 100% bg (%)
u1	19.3	753	2.6	10.2
v1	20.1	627	3.2	12.8
u2	13.8	945	1.5	5.8
v2	14.8	659	2.2	9.0
u3	12.2	921	1.3	5.3
v3	13.1	657	2.0	8.0
u4	8.5	1271	0.67	2.7
v4	8.8	1271	0.69	2.8
u5	8.1	1309	0.62	2.5
v5	8.5	1309	0.65	2.6

Table 17: Average occupancies (number of readout strips with signal *after noise filtering* divided by total number of strips in the readout plane) obtained at 25% background intensity and scaled to 100% intensity (rightmost column). The asymmetry between the u and v coordinates for the first three chambers is due to geometric effects.

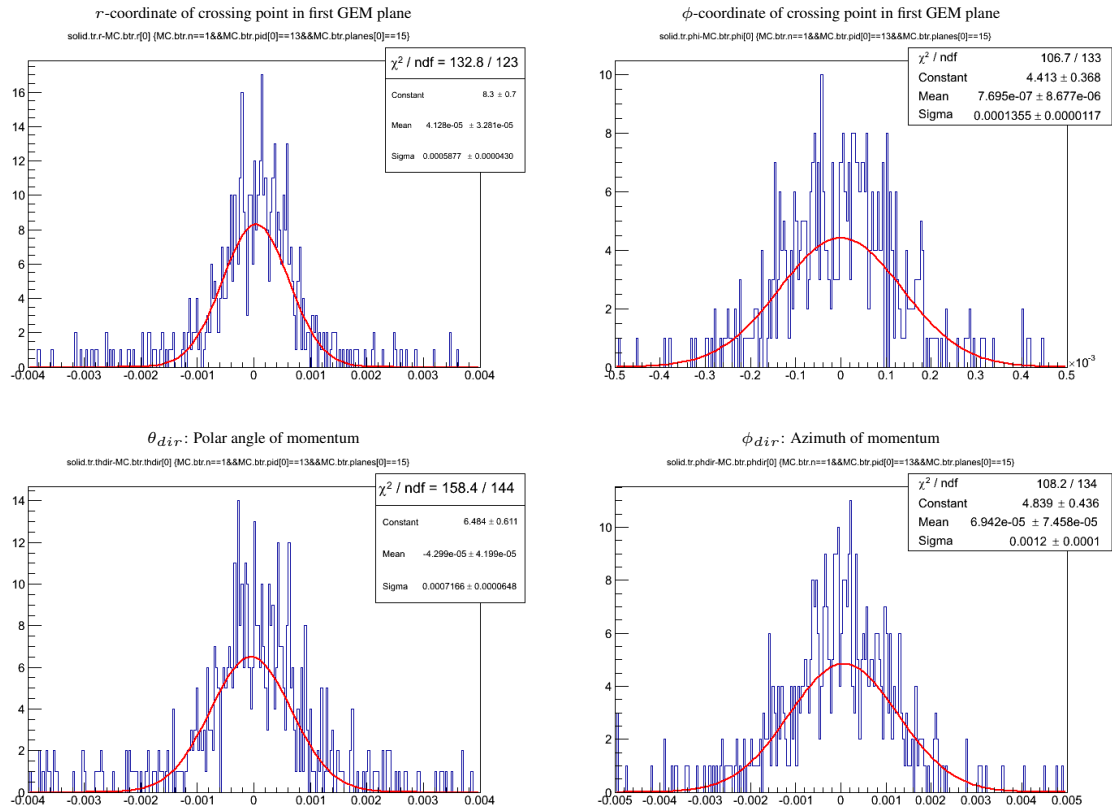


Figure 132: Track reconstruction residuals for 10% simulated background intensity and four GEM planes. The actual effective background level in this study may be higher than 10% (see text).

A second round of track reconstruction studies are in progress at the time of this writing. These simulations are configured with five GEM planes instead of four, have a better-optimized detector geometry, improved digitization and cover higher background levels.

References

- [1] The Hall A C++ Analyzer, <http://hallaweb.jlab.org/podd>.
- [2] *Progress Report on the SuperBigbite Project*, G. Cates, K. deJager, J. LeRose and B. Wojtsekhowski, eds., July 13, 2011, http://hallaweb.jlab.org/12GeV/SuperBigBite/SBS_CDR/Response_TR2.pdf,
- [3] Xin Qian, *Progressive Tracking Algorithm for SoLID*, https://hallaweb.jlab.org/wiki/index.php/Xin's_progressive_tracking
- [4] R. E. Kalman, *A New Approach to Linear Filtering and Prediction Problems*, Transactions of ASME Journ. Basic Engineering **82**, 35 (1960).
- [5] J.-O. Hansen in *Hall A Status Report 2008*, p. 23, <http://hallaweb.jlab.org/publications/AnnualReports/AnnualReport2008.pdf>.
- [6] M. Dell'orso and L. Ristori, Nucl. Instr. Meth. in Phys. Res. A **287**, 436 (1990).
- [7] S. Gadomski *et al.*, Nucl. Instr. Meth. in Phys. Res. A **320**, 217 (1992).

14 Electron Beam Polarimetry

The interpretation of the measurement of the parity-violating asymmetry relies on precise correction for finite beam polarization, with an accurate absolute normalization to 0.4% accuracy at both 11 GeV and 6.6 GeV. This will be achieved using two independent measurement techniques with independent sources of calibration errors, which can be directly cross-checked to high precision. This is an ambitious goal. The most precision electron beam polarimetry result to date in a physics publication is the 0.5% Compton polarimetry result by the SLD collaboration [1]. Compton polarimetry is well-suited for the energy and intensity of the upgraded Jefferson Lab beam. Plans for upgrading the existing Hall A Compton polarimeter to achieve 0.4% precision are described below.

The best candidate for a second, high-precision, independent measurement is Møller polarimetry. The use of iron foils in high magnetic fields can provide a precision well better than 1%, and may prove to be more precise to the level of 0.5%.

14.1 Compton Polarimetry

Compton polarimetry is a very promising technique for high precision polarimetry at beam energies above a few GeV. Beam interactions with a photon target are non-disruptive, so Compton polarimetry can be employed at high currents as a continuous polarization monitor. The photon target polarization can be measured and monitored with a very high precision, and the scattering between a real photon and free electron has no theoretical uncertainty, such as the atomic or nuclear effects which can complicate other measurements. Radiative corrections to the scattering process are at the level of 0.3% and are very precisely known. While the SLD collaboration result, with a precision of 0.5%, demonstrates the feasibility of very high accuracy Compton polarimetry, that measurement was ultimately limited by the inability to detect individual scattered particles (due to the pulsed beam) and the high Bremsstrahlung background in the photon detector due to the proximity to the interaction region. Conditions at JLab are favorable for both of these concerns. The existing apparatus and plans for future improvements are described below.

14.2 The Hall A Compton Polarimeter Baseline Upgrade

As pictured in Fig. 133, the Hall A Compton polarimeter [2] is located in a chicane, about 15 meters long, just below the beamline. After modification of the bend angle to accommodate 11 GeV running with the existing chicane magnets, the electron-photon interaction point will be 21 cm below the primary (straight-through) beamline. After passing the electron-photon interaction point, the electron beam is bent about 3.5 degrees by the third chicane magnet and then restored to the main beamline. The scattered electrons are separated from the primary beam and detected using silicon microstrips, just before the fourth chicane magnet. Scattered photons pass through the bore of the third chicane magnet to be detected in a calorimeter.

The photon target is a 0.85 cm long Fabry-Perot cavity crossing the electron beam at an angle of 1.4° . The laser system can be configured for infrared (1064 nm) or green (532 nm) light, and has achieved power levels of 10 kW of green light for polarimetry measurements. The laser light is polarized using a quarter-wave plate, and can be toggled between opposite polarizations of highly circularly polarized light. The feedback loop which locks the laser to the cavity resonance can be disabled to enable backgrounds from all non-Compton-scattering processes. To reduce overhead from the time required to re-lock the cavity, the transition between laser states is typically performed with a period of 1-2 minutes. The polarization of the transmitted light from the locked cavity and

the reflected light from the unlocked cavity are each monitored and can be used to characterize the laser polarization at the interaction point.

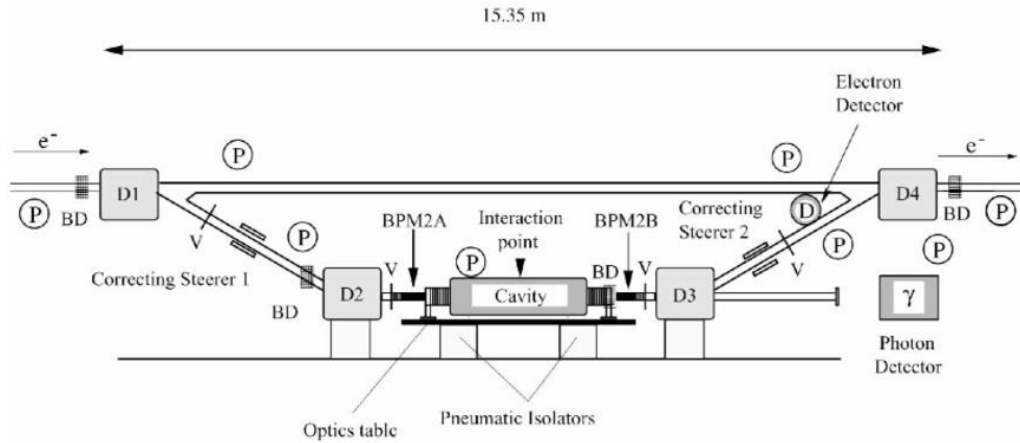


Figure 133: Schematic of the Hall A Compton polarimeter. Figure from [2].

The vacuum in the interaction region is at the level of few $\times 10^{-8}$ torr, implying a photon background rate due to Bremsstrahlung scattering from residual gas of around $5 \text{ Hz}/\mu\text{A}$. The dominant source of background in the photon detector is thought to be tails of the beam halo distribution interacting with the apertures in the interaction region. In contrast, for the electron detector the dominant background is thought to be dominated by energy tail or position halo of the primary beam since electrons from aperture scattering would presumably not cleanly transit the third dipole. When well-tuned, the background rates in the photon and electron detectors have been seen to be roughly similar: around $<100 \text{ Hz}/\mu\text{A}$ in recent use. At 11 GeV, with a 10 kW IR cavity, the Compton-scattered rates would be approximately $20 \text{ kHz}/\mu\text{A}$ and the asymmetry will range from 17.8% to -4% over the energy spectrum. At 6.6 GeV, a 10 kW green cavity will be used, which will provide a rate of $13 \text{ kHz}/\mu\text{A}$ with an asymmetry ranging from 20.9% to -4.7%. If backgrounds remain comparable to recent operation, statistical precision of 0.4% would be possible in less than 5 minutes, depending on the specific detection and analysis approach which is considered.

Electrons are detected in a set of 4 planes of silicon microstrips located just before the 4th dipole. Each microstrip instrument has 192 strips with a pitch of $240 \mu\text{m}$. Custom readout electronics pre-amplify and discriminate signals from the microstrips, implement a simple tracking algorithm to reduce non-directional backgrounds, and count hits in each strip over specified integration gates corresponding to the helicity pattern of the electron beam. Presently, this system is operating at low efficiency with poor signal size for a minimum ionizing track compared to environmental noise on individual strips. The baseline upgrade would include an improvement in this system to achieve high efficiency and high signal-over-noise for the microstrip readout. The use of diamond microstrips, such as were recently successfully used for the Hall C Compton polarimeter [3], is under consideration. Such diamond microstrips are more difficult to procure and in principle are more challenging to instrument than silicon strips, however, they are more radiation hard and less susceptible to low-energy photon backgrounds.

The calorimeter for detecting scattered photons lies about 7 meters downstream of the interaction point. The strong forward boost of scattered photons leads to a tightly collimated photon beam ($<1 \text{ mrad}$), so the calorimeter size determined by consideration of energy resolution through shower

loss. The photon calorimeter is a GSO crystal scintillator of 6 cm diameter and 15 cm length, with a single photomultiplier tube. The PMT signal is split between two parallel data acquisitions: one with a fast-counting, buffered ADC self-triggered on pulses from the photon detector, and the other utilizing a 250MHz flash ADC (fADC) to integrate the total signal over periods corresponding to the helicity pattern of the electron beam. The fADC system can also record a very low rate of individual pulses for calibration. Each of these dual readouts can be analyzed independently. The fast counting ADC readout and the sample pulses in the fADC system can both be triggered using the electron detector, providing an electron-photon coincidence spectrum for calibration.

14.3 Upgrades Beyond the Baseline

There are several issues which must be addressed, related either to operation at the higher beam energy or to the very high level of precision which is proposed.

- The electron beam halo - a term meant to describe a long tail on the momentum or position distribution of the beam - is expected to be larger at 11 GeV compared to 6 GeV operation, due to synchrotron light emission in the recirculation arcs which will increase the momentum-normalized beam emittance. For Compton polarimetry, a tail on the beam energy distribution is directly responsible for the dominant backgrounds in electron detection, while scattering of beam halo from narrow apertures in the interaction region is thought to dominate backgrounds in photon detection.
- The measurement of the laser polarization must be performed with very high precision.
- The total power of synchrotron radiation emitted by the beam in the chicane arcs will be more than an order of magnitude higher compared to Compton measurements in the 6 GeV era, and this radiation spectrum will be significantly stiffer. Dilution from this radiation would complicate photon and electron detection.
- Photon detection must provide a well-characterized and linear response for photons in an energy range from about 3 GeV to low energies and over a large variation in signal rate, while being radiation hard and also insensitive or shielded from the synchrotron radiation power.

These issues are addressed by several modifications which go beyond the baseline 11 GeV upgrade, listed below and described in the following sections. These improvements are expected to allow us to achieve the precision goals listed in Table 18.

- **Laser system** A larger crossing angle for the photon and electron beams would allow larger electron beam apertures, and reduce backgrounds in the photon detector. This increase in crossing angle comes at the expense of lower luminosity, leading to a tradeoff in signal rate and background rate. With the high cavity power that has been achieved with this laser system, we do not expect to be limited by laser power even at increased crossing angle. The decision on crossing angle can be made when more is known about beam conditions at 11 GeV. The beamline through the chicane magnets is one inch inner diameter, which is about a factor of three larger than the aperture required by the present laser crossing angle. The luminosity would drop roughly linearly with crossing angle, and even with a factor of 1/3 the statistical power of the signal rate for a 10 kW cavity would still be sufficient assuming a reduced background fraction.

In addition to the option to increase this crossing angle, a system for measuring laser polarization inside the resonant optical cavity (although not while locked to resonance) must

Relative error (%)	electron	photon
Position asymmetries*	-	-
E_{Beam} and λ_{Laser} *	0.03	0.03
Radiative Corrections*	0.05	0.05
Laser polarization*	0.20	0.20
Background / Deadtime / Pileup	0.20	0.20
Analyzing power Calibration / Detector Linearity	0.25	0.35
Total:	0.38	0.45

Table 18: *Goals for systematic errors for the Hall A Compton polarimeter at 11 GeV. Topics marked * are a common systematic error between the photon and electron analyses, while the other are largely independent between the detector systems.*

be developed and used, along with a thorough study of all optical components, to improve knowledge of the photon polarization.

- **Chicane Modification** The synchrotron light power on the photon detector will be significantly reduced by installing shims to increase the fringe fields of the chicane dipole magnets in the interaction region. This would also soften the synchrotron energy spectrum, making shielding more effective. The effect of synchrotron light on the electron detector is being investigated, with the possibility to add some baffeling to limit reflection into the detector.
- **Photon Detector** The photon detection system used for recent running will be replaced with a detector better matched to the Compton photon energy spectrum for 11 GeV operation.

These upgrades are described in more detail below.

14.3.1 Laser System and Luminosity

As described above, in the current configuration of the Hall A Compton, the electron beam interacts with green (532 nm) light in a resonant optical cavity at a crossing angle of about 1.4° . After accounting for the length of the optical cavity (about 85 cm) and the finite size of the cavity mirror, it is necessary to enforce an aperture on the electron beam of ± 5 mm. It is thought that this narrow aperture is the dominant source of background for 6 GeV running. At higher energies, synchrotron light emission in the accelerator recirculation arcs will increase the beam emittance and presumably lead to significantly larger backgrounds from this aperture scattering. In present use of the Compton polarimeter, frequent beam tuning is required to maintain operation with the signal-over-background > 10 . A large background signal is often associated with large fluctuations over the period of time in the laser on/off cycle used to measure backgrounds. This reduces the measurement precision, and potentially introduces a significant systematic error through instability in the phototube under large variations in rate. For this reason, it is desirable to keep the signal-over-background ratio large.

The aperture can be widened only by increasing the laser crossing angle which would also lower the luminosity. Although the baseline upgrade plans do not make provision for changing this crossing angle, operability at 11 GeV may require larger apertures. At a finite crossing angle α , the luminosity for a continuous-wave electron and photon beam, with intersecting electron and photon

waists sizes σ_e and σ_γ , is given by:

$$\mathcal{L} \approx \frac{1 + \cos \alpha}{\sqrt{2\pi}} \frac{I_e P_\gamma}{ek_0 c} \frac{1}{\sqrt{\sigma_e^2 + \sigma_\gamma^2}} \frac{1}{\sin \alpha} \quad (18)$$

Here P_γ is the power of the photon beam, I_e is the current in the electron beam, and k_0 is the photon energy scattered at the kinematic maximum limit of colinear backscattering. As an example: at 10000 W stored power at 532 nm, the Compton scattering rate would be about 12 kHz/ μ A at 1.4° crossing angle and about 4.8 Hz/ μ A at 3.5°. At the expense of approximately a factor of 2.5 in luminosity, that larger crossing angle would allow a ± 0.5 inch aperture, comparable to the maximum aperture allowed by the 1" beam pipe diameter in the bore of the existing dipole magnets in the chicane.

With an available laser power of 10 kW, the polarimeter is not expected to be limited by low signal rates even at the larger crossing angles. However, the drop in luminosity with increasing crossing angle suggests that any change must be optimized from the point of view of signal-over-background. Until beam tests at higher beam energies are performed to form reliable estimates of background levels, it is prudent to design for both large crossing angle and large luminosity.

We propose the use of an infrared cavity storing 10 kW of optical power at 1064 nm for operation at beam energy above 8.8 GeV, and a cavity storing 10 kW of optical power at 532 nm for beam energies at 6.6 GeV and below. The primary disadvantages to the longer photon wavelength are the reductions in analyzing power and softening of the energy spectrum (17% analyzing power and 1.8 GeV maximum photon energy for IR at 11 GeV, compared to 32% and 3 GeV for 532 nm). The advantages for the IR system would be a greater available luminosity and system reliability. While the cross-section is very similar between the two photon energies, at 1064 nm there are twice as many photons per unit energy. At 10 kW, an IR cavity would provide a rate of 9 kHz/ μ A at the increased crossing angle to allow the full ± 0.5 " electron beam aperture, or 23 kHz/ μ A at the original design 1.4° crossing angle. The 532 nm system requires an additional stage to frequency-double the original 1064 laser light. Without this doubling stage, the IR system can inject higher power to the cavity, enabling higher cavity power or the same cavity power with reduced cavity gain. A lower gain cavity will typically be more robust, and less sensitive to radiation damage of the cavity optics. At beam energies below 8.8 GeV, the improvement in analyzing power and higher scattered photon energy endpoint are worth the possible trade-off in ease of operability.

Precision electron beam polarimetry also requires precise determination of the polarization of the photon target. This has proved to be the dominant systematic error contribution in recent Hall A Compton polarimeter measurements, in part because the use of a high-gain resonant cavity significantly complicates this determination. In a resonant cavity, the polarization state of the stored light can not be directly measured without destroying the resonance. For the present Hall A polarimeter, the laser polarization is inferred from measurements of the light that transmits through the cavity. A transfer function, relating the polarization of light in the Compton Interaction Region (CIP) to the polarization measured in the transmitted beam outside the vacuum vessel, is determined from measurements with an un-locked cavity. The highly-reflective cavity mirrors must be removed for these measurement, and the cavity must be open to air, which implies a relaxation of stress-induced birefringence of the vacuum entrance and exit windows. Contributions from birefringence in the cavity mirror substrate and stress on the vacuum windows can be characterized separately, but as a practical matter these corrections are difficult to determine with high precision. For the Hall A polarimeter, previous studies have quoted the uncertainty in beam polarization to be 0.35%, but in recent operation the uncertainty could not be bounded to better than 0.7%.

An improved technique has been used in Hall C to control the laser polarization uncertainty.

The polarization of light arriving at the cavity entrance can be inferred from light reflected back from the cavity and analyzed with the same apparatus used to create the initial polarization state, measuring a single power level [4]. This technique was employed in Hall C to maximize the circular polarization of light injected in the cavity and to monitor the polarization during the run. It was verified to work by two methods. In the first, with the cavity under vacuum in running conditions, a scan over a broad range of initial polarization states was performed, and the recorded analyzed reflected power was shown to be well described by the simple hypothesis of optical reversibility. A more direct verification was made with the cavity opened, directly measuring the polarization of the injected light in the cavity and correlating this with the analysis of the reflected light. The correlation is shown over the full range of the scan, and zoomed in for measurements at maximum circular polarization, in Fig. 134. In operation, the Hall C Compton polarimeter ran with the reflected light very near minimum, with an implied uncertainty on the circular polarization within the cavity of 0.1%.

These studies demonstrate that this technique may provide knowledge and monitoring of the circular polarization in the cavity to the level of 0.1%. An *in situ* measure of the polarization would be a valuable confirmation of this procedure. Modifications to the interaction region will be made to allow an insertable, vacuum-compatible analysis assembly for measurements of the beam in the CIP. The power level for such measurements will necessarily be very low, as the highly reflective mirrors of the cavity will attenuate incident light, but such a direct measurement would include all effects of birefringence and depolarization in the injection of optical power into the cavity.

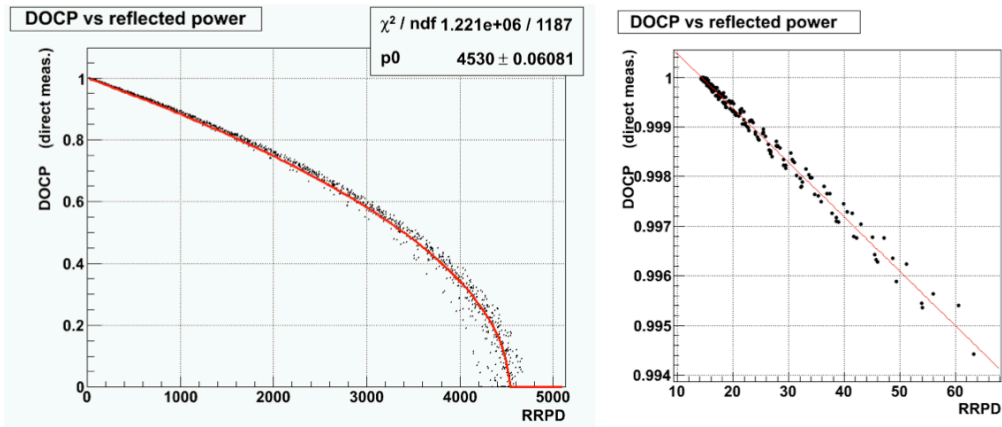


Figure 134: Measured degree of circular polarization in the Hall C Compton laser cavity vs. the polarization-analyzed reflected light, measured over a broad scan of initial polarization states. The figure on the right is zoomed in the region of maximum circular polarization.

14.3.2 Alternative Laser System

An alternative laser system has also been considered, based on the use of a short-pulse RF laser synchronized to the electron bunch frequency. Such a system would concentrate laser power on the electron bunches, in effect creating an electron-photon collider. For a laser with narrow pulse structure (≈ 10 ps) and repetition frequency sub-harmonic to the electron beam ($f_{laser} = 499$ MHz

/ n with integer n), the the ratio of luminosity for the same average power goes as:

$$\frac{\mathcal{L}_{pulsed}}{\mathcal{L}_{CW}} \approx \frac{c}{f_{beam} \sqrt{2\pi}} \frac{1}{\sqrt{\sigma_{e,z}^2 + \sigma_{\gamma,z}^2 + \frac{1}{\sin^2 \alpha/2} (\sigma_e^2 + \sigma_\gamma^2)}}. \quad (19)$$

Here f_{beam} is the electron repetition rate and $\sigma_{e,z}$ ($\sigma_{\gamma,z}$) is the longitudinal size of the electron (laser) pulse. For the parameters relevant to the proposed system, this corresponds to an enhancement of luminosity per unit power of between 20-50. Commercially available mode-locked laser systems has been identified providing 45 W at 1064 nm, with 100 MHz repetition rates and 10 ps pulse widths. Assuming an average injected power of 30 W at the 3.6° crossing angle, such a pulsed laser would provide 330 Hz/ μ A with a single-pass beam, that is, without the resonant optical cavity.

Although the relatively low rates would be expected to be a disadvantage, it may turn out to be operable depending on the characteristics of the 11 GeV electron beam. The statistical precision (0.4% in about 3 hours) would be sufficient for a high precision measurement. The primary advantage of such a system would be a more straightforward determination of the laser polarization, relative to a high-gain optical cavity. There are other advantages as well. Locking and unlocking a cavity takes time, so to maintain a high duty factor for a cavity system the locked and un-locked periods used to determine backgrounds are long (≈ 1 minute) relative to the fluctuations in the background. On the other hand, a laser can be turned off or deflected to a dump quickly, so background measurements for such a single pass system could take place quickly, potentially providing superior control of background fluctuations even if the signal-over-background ratio is smaller. Similarly, without the requirement to maintain the delicate balance of signal levels necessary to robustly lock a high-gain cavity, systematic studies varying laser power or position would be simplified.

Should the rate from such a system be unmanageably small relative to backgrounds, it could be roughly doubled using a ‘‘butterfly’’ cavity to recirculate the exit beam through the interaction point. A more powerful option would be a hybrid system in which the RF pulses are stored in a resonant optical cavity. A moderate cavity gain ≈ 20 would double the Compton signal rate compared to the 10 kW, gain ≈ 3000 CW default design. At such a low gain, the cavity lock would be relatively easy to acquire, potentially enabling more rapid background measurements than the high-gain system. The polarization measurement would also likely be simpler than for a high-gain cavity system, as the injection beam in the interaction region would still be similar to the beam stored through relatively few resonant reflections.

Such a cavity would require the dual resonance condition of being both an integral number of optical and RF wavelengths. This is not a particularly difficult condition to maintain. The injection laser must be mode-locked to ensure coherence between pulses. Locking mode-locked lasers to Fabry-Perot cavities has been actively pursued over the last decade in development studies for Compton-based X-ray sources [5, 6] and for a polarized positron source for the ILC [7, 8], with significant technical success beyond the requirements for this proposed system.

The above discussion demonstrates the utility and technical feasibility of the alternative proposal for a 10 ps pulse length, 100 MHz, 1064 nm laser system operating either as an injection laser for a gain ≈ 20 resonant cavity or as a 30 W single-pass system. This alternative proposal would require new investment for acquisition of the injection laser and high-power optics. In addition, the possibility of time-dependent polarization in the short RF laser pulse may additionally complicate the laser polarization determination. The alternative system remains as a backup should complications in determining the laser polarization inside the high-gain laser cavity prove to be insurmountable.

14.3.3 Chicane Magnet Modification

At 11 GeV, significant synchrotron radiation is emitted when the electron beam is bent in a magnetic field. The total radiated power rises as β^4 for the same bend radius. At 11 GeV, this radiation load will be a significant background in the photon detector and may overwhelm the signal from Compton scattering. Figure 135 shows the energy spectrum of synchrotron light attenuated by lead shielding between 1–5 mm thick, depending on the beam energy. On the left, the spectrum for 11 GeV with unmodified magnets is compared to calculations for the recent runs of HAPPEX-III (3 GeV) and PV-DIS (6 GeV). On the right, the energy spectrum (“Fringe 2”) is shown when iron extensions, 15 cm in length, are added to the dipole magnets in order to provide an extended region of reduced field. This reduced magnetic field produces synchrotron light with lower energy range and with reduced intensity, for the portion of the electron beam trajectory that projects to the photon detector. With this modification, the bending strength of the magnet remains the same but the synchrotron light radiated into the detector is reduced by a factor of 10^4 , to a level comparable to HAPPEX-III. The magnetic field extensions were modeled using TOSCA, and have been constructed. Field measurements have been taken to verify the magnetic model for both the integral Bdl and the shape of the fringe field with and without the field extensions. These field extension pieces have been built and will be ready for installation at the start of 11 GeV operations.

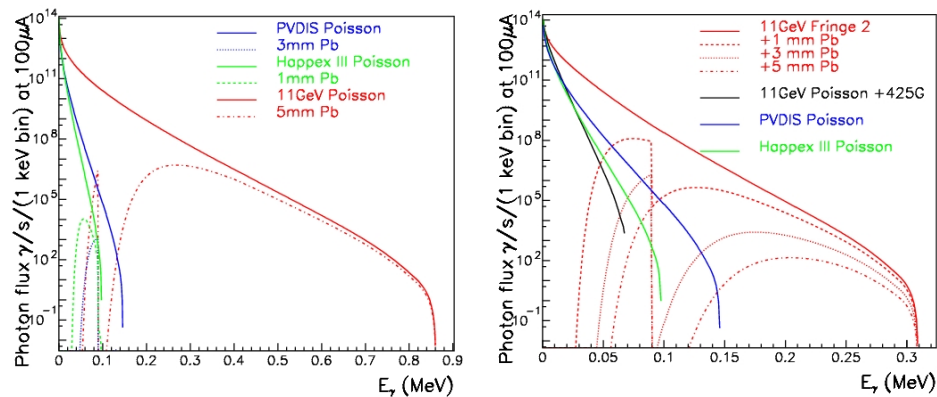


Figure 135: Energy spectrum of synchrotron radiation penetrating lead shielding of thickness listed. Plot on left shows unmodified chicane magnets, plot on right shows energy spectrum for proposed magnetic shims which reduce the field for the bend radiating into the Compton photon detector acceptance. Note the different horizontal scales between the plots.

14.3.4 Photon Detection

The specific calorimeter to be employed is not yet determined. The present calorimeter is a GSO crystal scintillator, which has excellent light yield suitable for measurements at low energies. The crystal is too small to contain most showers at higher energies, and a new calorimeter will be required for precision measurements at 11 GeV. In the past, Hall A has used an undoped lead tungstate (PbWO_4) array. This may be suitable for 11 GeV operation; the relatively low light yield for PbWO_4 is not an issue for higher photon energies of the proposed measurements or for the integrating measurements, and the high speed of this material reduces pile-up issues in counting measurements. Designs for multi-layer sampling calorimeters, using either scintillation or Cherenkov light, will also be considered.

14.4 Systematic Uncertainties

While the proposed system should assure operability and sufficient statistical precision at 11 GeV, the challenge will be achieving an absolute measurement of beam polarization with a precision of 0.4%. Table 18 summarizes the goals for various contributions to systematic uncertainty. The first four rows list sources of uncertainty which are highly or completely correlated between the electron and photon analyses. Other potential systematic errors arise in detector readout or calibration and are mostly or entirely decorrelated between the analyses. Each of these separate categories of potential systematic uncertainty: correlated, electron-only, and photon-only, will be discussed in the following sections.

14.4.1 Sources of Correlated Error

Any error associated with the Compton scattering process will be a common source of systematic error between the electron- and photon-detector analyses. One example lies in the energy normalization of the scattering process. The analyzing power is a function of both electron energy and photon energy, so these must be precisely determined. The photon wavelength will be determined to better than 0.1 nm and the electron energy to 0.05%, which leads to an uncertainty at the level of 0.03%. A similarly small uncertainty will come from radiative corrections, which are calculable [9] with high precision and will contribute at the level of 10^{-3} .

Helicity-correlated changes in luminosity of the laser/electron interaction point can introduce a false asymmetry. Various causes of luminosity variation must be considered, such as electron beam intensity, beam motion or spot-size variation. The control of helicity-correlated beam asymmetries is now a standard technology at Jefferson Lab, and typically achievable results (few part per million intensity, 10's of nanometers beam motion, $<10^{-3}$ spot size changes) will suitably constrain the electron-photon crossing luminosity variations. Another possible source of false asymmetry would be electronics pickup of the helicity signal, which could potentially impact an integrating photon analysis. However, the demands of the primary experiment for isolation of the helicity signal exceed those for polarimetry by several orders of magnitude. In addition, the laser polarization reversal provides an additional cancellation for asymmetries correlated to the electron beam helicity. For these reasons, beam asymmetries are expected to be a negligible source of uncertainty in this measurement.

A more significant potential source of error comes from the uncertainty in the photon polarization. As described above, the determination of photon polarization will be improved with the analysis of light reflected from the cavity input mirror, which will allow precise control and measurement of the polarization state injected into the cavity. This will be supplemented by an insertable stage to measure the polarization in the interaction region directly. The circular polarization of the laser will be determined and cross-checked with a precision of 0.2%. If studies do not demonstrate that this can be achieved within the high-gain cavity, the alternative laser system will need to be developed.

14.4.2 Systematic Errors for the Electron Detector

The electron detector is composed of 4 planes of silicon microstrips normal to the electron beam trajectory and positioned on the low-energy side of the beam trajectory in the dispersive chicane. Electrons which have given up energy to a scattering process are separated from the primary beam by the third chicane dipole, and the energy of a detected electron is implied by the distance of the track from the primary beam with a dispersion of about 0.45% of the beam energy per millimeter. Models of the chicane magnets are used to calculate the electron energy as a function of position

in the detector. The effects of electronics noise and non-directional backgrounds are reduced by triggering on tracks which are restricted to very small angles relative to the beam. The trigger can be adjusted for the range of track angles and number of planes used in the track, including a single plane trigger. The efficiency of individual strips can also be measured using data from the multiple planes.

The silicon detector may also be sensitive to synchrotron light, and while the detector is not in line-of-sight to synchrotron emission in dipole 3, synchrotron photons rescattered in the beam pipe may be a problem. The 11 GeV upgrade includes a gate valve installed on the straight-through beam pipe, to block synchrotron light from the first dipole of the chicane during operation of the polarimeter.

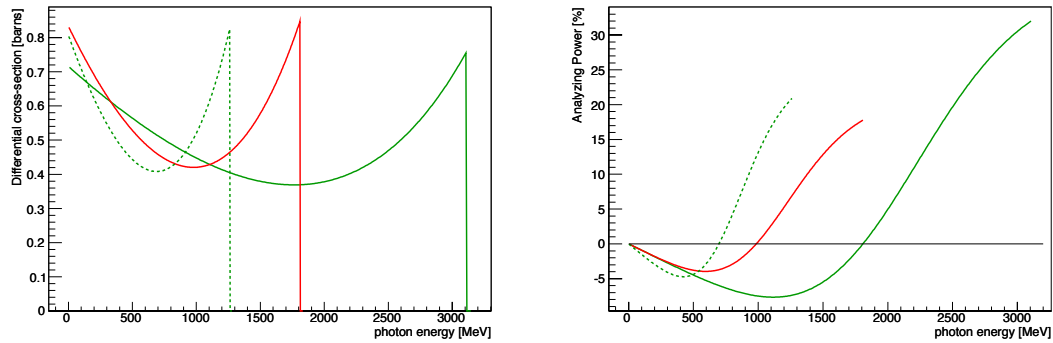


Figure 136: *The cross-section and asymmetry plotted versus Compton scattered photon energy for the Hall A polarimeter at 11 GeV for 532 nm (green solid line) and 1064 nm (red line) laser options, and at 6.6 GeV for the 532 nm laser (green dotted line).*

The cross-section and asymmetry as a function of Compton scattered photon energy is plotted in Figure 136 for 11 GeV electron beam. The Compton edge (the kinematic endpoint of the Compton energy spectrum) is observed in the electron detector and used to calibrate the distance of the detector from the primary beam. In addition, the asymmetry as a function of photon energy k exhibits a zero crossing. Determining the location of this asymmetry zero crossing (0xing) provides a second absolute energy calibration point, so together the Compton edge and 0xing can be used to calibrate two parameters: the detector location relative to the beam and the strength of the magnetic field in dipole 3. In this way, survey results and magnetic field maps serve as a cross-check to a beam-based self-calibration of the Compton energy spectrum. The precision of this calibration is limited by delta-ray production in the microstrips, which distorts the measured spectrum, and efficiency variations between the microstrips.

In operation at low beam energies, the 0xing is close to the primary beam: for HAPPEX-II, the separation was approximately 5 mm. At this proximity, background rates were extremely sensitive to beam tuning in the injector and RF phase corrections in the linacs, presumably due to energy tails. At 11 GeV with the IR laser, the 0xing will be around 16mm from the primary beam, which should allow for robust operation. The analyzing power for the measured electron distribution can be very accurately determined with use of this self-calibration, with the systematic error dependent upon the specifics of the analysis approach.

For an example of a specific analysis technique, consider an asymmetry measured from the Compton edge to some selected cut-off in the electron spectrum. This would need to be compared to the theoretically expected average asymmetry, which would be sensitive to the energy cut-off

threshold. In an analysis that computed a single count-rate asymmetry from the integrated rate from the Oxing to Compton edge, an error in determining the Oxing would act approximately as a dilution effect (as the asymmetry is small in the neighborhood of the Oxing). While there may be statistical variation in determining the Oxing, this would be merely a source of statistical noise. If the systematic bias in determining the Oxing is estimated to be within $1/10$ μ strip width (about $25 \mu\text{m}$), this would imply a systematic bias in the analyzing power of about 0.15%. While this is a useful estimate of the error due to energy calibration, this analysis relies on integrating the rate-weighted average asymmetry over the accepted energy range, and so would likely suffer a larger contribution of systematic error due to efficiency variations in the μ strips.

Other analysis techniques which would be less sensitive to efficiency variations would rely on averaging asymmetries over a range of strips, rather than averaging the count rate. In this case, both energy calibration points are needed to determine the expected asymmetry at each μ strip. Because the Compton edge will be extracted from the rate spectrum, efficiency variation between the silicon strips must be minimized and well-known to avoid biasing this determination. In addition, careful study of the contribution of delta-ray production, which distorts the asymmetry spectrum at the Oxing and the rate spectrum at the Compton edge, will also be important. Here also, a high strip efficiency will be helpful, by providing a high-efficiency for vetoing events with multiple tracks. Strip-by-strip efficiencies can be calculated by comparing track-hit efficiency between the multiple planes of the μ strip detector, and comparisons between planes can also help benchmark corrections for delta-ray production. A uniform and high-efficiency detector will be an important component of this system.

It is worth noting a measurement using only the last, single silicon strip at the Compton edge will be capable of 0.4% statistical precision on time-scales of around one hour. The rate of change of the asymmetry in this region is only 0.5% / mm. Locating this strip, relative to Compton edge, to a little better than half its own width should provide a robust accuracy on the analyzing power better than 0.4%. This technique would be sensitive to determination of the location of the Compton edge, but otherwise very insensitive to other calibration parameters.

Similarly, if the electron detector can be moved close to the primary beam (about 9 mm from the primary beam for the IR laser at 11 GeV) the asymmetry minimum could be detected. The statistical power is much lower in this region, with a single strip requiring 20 hours to achieve 0.4% statistical precision on the polarization (assuming signal-noise ratio of 10:1). However, here the asymmetry is not changing with position, so there is minimal calibration error in selecting a strip in this minimum. Beam position and angle may vary the asymmetry minimum over hundreds of microns during this time span, but such changes can be tracked using beam position monitors or the Compton edge, and the analyzing power varies by only about 0.4% of itself over a range of $\pm 300 \mu\text{m}$, suggesting minimal corrections will be necessary.

Cross-checks between calibrations and techniques should provide convincing evidence that the system is well understood. Given these considerations, it seems likely that the calibration of the electron detector will be understood at the level of 0.3% or better.

Regardless of the analysis, contributions from deadtime and pileup will need to be understood. The fast-counting DAQ can take very high rates with low deadtimes, and deterministic deadtime intervals are enforced in readout and acquisition electronics stages. While the total Compton-scattered data rates may as high as 1 MHz, rates in individual strips will be reduced by segmentation to $< 15 \text{ kHz}$, which will allow dead-time and pile-up systematic errors to be controlled at the level of 0.2%. The high statistical power of the measurement is of significant use here; high precision studies can be performed to benchmark models of the readout system against changes the laser power or the parameters of the triggering (preamp levels, logical gate lengths, coincidence levels, etc).

Backgrounds are also a potential but small source of systematic uncertainty. Backgrounds are

studied with the laser cavity unlocked, allowing both the background level and asymmetry to be well determined. However, high backgrounds could impact the systematic error due to deadtime or pile-up corrections. There is also the possibility of backgrounds from Compton-scattered electrons, which can produce delta rays when scattering in the detector or in its shielding. These tracks can themselves be sufficiently forward-going to pass the trigger, thus changing the analyzing power as a function of energy. Simulation will be used to avoid such problems, and studies of track distribution and electron-tagged photon energy spectra can be used to identify such effects in the data.

Finally, it is perhaps obvious, but worth stating, that beam properties at 11 GeV will be important for the precision of the electron detector analysis. If simulations reveal that halo backgrounds for the electron detector are likely to be large in the region ~ 15 mm from the primary beam, then the green laser option would be required for high precision polarimetry. Using 532 nm light in a cavity would put the zero-crossing about 33 mm from the primary beam. It is also worth noting that the single-strip analyses would be also improved with the higher resolution and larger asymmetries (and larger distances from the primary beam) available from a green laser.

14.4.3 Systematic Errors for the Photon Detector

The precise determination of the analyzing power as a function of energy is more difficult for the photon calorimeter than for the electron detector due to the width and shape of the detector response function. In order to fit the asymmetry as a function of detected photon energy, the analyzing power must be calculated as a convolution of the response function with the theoretical analyzing power curve. The response function shape and energy calibration can be simulated, and studied using the photon tagging through coincidence triggers with the electron detector.

In general, determining the effect of a low-energy threshold on the analyzing power depends sensitively on the shape of the response function; at low energies this is a major source of uncertainty. At high energies, the improved resolution and consistency of the response function shape over the range of interest should significantly reduce this problem. As noted above, the photon calorimeter will be upgraded to better contain showers from high energy photons, with the primary objective to provide a response function which scales linearly over a broad range of energy.

The pulse-counting analysis in the photon detector is also sensitive to pile-up, which distorts the asymmetry distribution. Background and rate distributions will serve as inputs to simulation for corrections to the analyzing power. In the current Hall A analysis, pile-up corrections are estimated at the level of 1%, and the effect can be controlled at a level better than 10% of itself. Deadtime corrections, which can vary significantly with background conditions, will also represent a potential systematic uncertainty.

Uncertainties related to the threshold, response function shape, absolute energy calibration, deadtime and pile-up can also be eliminated by integrating the photon calorimeter signal, without threshold [10]. These previous problems are then replaced with a requirement on the linearity of the average response to the photon energy. Because the analyzing power integral is energy-weighted, the statistical figure-of-merit is not badly degraded by the negative asymmetry region at low photon energies.

The PREX experiment, with a beam energy near 1 GeV, relied on the integrating photon method for polarimetry at the level of 1% precision. Simulations of the photon response function were sufficient to control the analyzing power uncertainties for those measurements. The dominant uncertainty in the asymmetry measurement arises from variation in the photomultiplier response with changes in average rate which introduces a systematic error through background subtraction.

At high energies, with the ability to study response function with the electron-detector-tagged photon beam over a large fraction of the energy range, the photon detector analyzing power nor-

malization uncertainty in the range of 0.3% should be achievable. Characterization of the phototube response as a function of rate and pulse-size will also be important. As described above, Bremsstrahlung scattering from apertures in the interaction region, coupled with the characteristics of the 11 GeV electron beam, present a possible source of background.

14.5 Summary of Compton Polarimetry

The prospects for 0.4% Compton polarimetry are excellent. This ambitious goal will require vigorous and dedicated efforts to reduce sources of systematic uncertainty. It is expected that some significant fraction of data production time will be used for studies of the Compton polarimeter system which are not disruptive to the experiment, for example, scans of detector positions, laser power and polarization, and data acquisition parameters. The scattering asymmetry at 11 GeV is relatively large which, for some analysis approaches, will provide statistical precision at the level of $\sim 0.5\%$ in a few minutes of data collection. Given this high statistical power, these studies will be an effective method for constraining many of the possible experimental systematic uncertainties.

The future use of the Hall A polarimeter at 11 GeV will be a very different situation from the recent operation. The dominant systematic errors in recent operation lay in the determination of the analyzing power and laser polarization. Operating at lower energies the asymmetries were significantly lower and therefore the statistical power was worse. In addition, the limits of systematic uncertainty had not been pushed by demands of the experiment precision.

The 0-Xing “self-calibration” of the electron detector was attempted for the first time for the HAPPEX-II and HAPPEX-He measurements. The situation was complicated due to the low beam energy of around 3 GeV, which not only reduced the average asymmetry but also reduced the ratio of Compton-scattered photon energies and the electron energies. At 3 GeV, the zero-crossing was about 5 mm from the primary beam, which was as close as the electron detector could get to the beam. Geometric efficiency at the edge were a significant complication in this approach. In addition, the microstrip detector was damaged and displayed low and uneven efficiency, which complicated the analysis. The estimated systematic errors for that analysis which were not associated with these efficiency issues are consistent with Table 18. A similar technique has been successfully employed in the Hall C Compton polarimeter at 1 GeV, where a larger chicane and green laser were used to optimize for the low beam energy during the Qweak experiment. While analysis is ongoing, the current status indicates that the ultimate precision will be significantly better than 1%.

For the photon detector, the integration readout method has been successfully used in the HAPPEX-3 and PREX experiments, with the primary limitations being the characterization of the phototube response over the range of signal levels. The rapid access to high statistical power expected for 11 GeV operation, which is so powerful for cross-checking potential sources of systematic uncertainty, has never before been available to the Hall A Compton. Coincidence measurements between the photon and electron detectors will also provide a significant cross-check to the response function and energy calibrations. As described above, recent improvements in available laser power, analysis techniques, laser polarization measurements, and the favorable kinematics of the higher electron beam energy have opened the door to 0.4% precision Compton polarimetry for the SOLID program.

14.6 Møller Polarimetry

This section describes our plans for precision Møller polarimetry in Hall A. Møller polarimetry will provide a useful cross check on beam polarization measurements performed with Compton scattering, gathering high statistics in a short amount of time and with different attendant systematic

error. The principal challenge is to achieve high precision ($\sim 0.5\%$ on the beam polarization) through careful control of the systematic effects.

Electron-electron scattering, with arbitrary spin orientation for the beam and target, has been calculated in lowest order QED by many authors [11, 12, 13, 14], and the basic formulas for (non parity-violating) polarized Møller scattering are given in many places. For example, following [15], the cross section at high energies in the center of mass frame can be written as

$$\frac{d\sigma}{d\Omega_{cm}} = \frac{\alpha^2}{s} \frac{(3 + \cos^2 \theta)^2}{\sin^4 \theta} [1 - P_{\text{long}}^{\text{B}} P_{\text{long}}^{\text{T}} A_{\text{long}}(\theta) - P_{\text{tran}}^{\text{B}} P_{\text{tran}}^{\text{T}} A_{\text{tran}}(\theta) \cos(2\phi - \phi_B - \phi_T)] \quad (20)$$

Here, $s = (2E)^2$ for electron energy E , θ is the scattering angle, $P_{\text{long,tran}}^{\text{B,T}}$ are the longitudinal and transverse polarizations of the beam and target electrons, ϕ is the azimuthal scattering angle, and $\phi_{\text{B,T}}$ are the azimuthal angles of the beam and target polarizations. The analyzing powers are

$$A_{\text{long}}(\theta) = \frac{(7 + \cos^2 \theta) \sin^2 \theta}{(3 + \cos^2 \theta)^2} \quad \text{and} \quad A_{\text{tran}}(\theta) = \frac{\sin^4 \theta}{(3 + \cos^2 \theta)^2} \quad (21)$$

which are maximized at $\theta = 90^\circ$ with $A_{\text{long}}(90^\circ) = 7/9$ and $A_{\text{tran}}(90^\circ) = 1/9$. The electron laboratory scattering angle for $\theta = 90^\circ$ is $(2m/E)^{1/2}$, rather small for GeV electron beams.

A Møller polarimeter makes use of Eq. 20 to measure the beam polarization vector $\vec{P}^{\text{B}} = (P_{\text{long}}^{\text{B}}, P_{\text{tran}}^{\text{B}})$ by incorporating a target with a known electron polarization vector $\vec{P}^{\text{T}} = (P_{\text{long}}^{\text{T}}, P_{\text{tran}}^{\text{T}})$ into a spectrometer to detect one or both of the scattered electrons. By reversing the beam polarization vector $\vec{P}^{\text{B}} \rightarrow -\vec{P}^{\text{B}}$, one can deduce its magnitude, and perhaps its direction, through the analyzing powers (21). The ideal Møller polarimeter, for determining longitudinal beam polarization $P_{\text{long}}^{\text{B}}$, is set at $\theta = 90^\circ$ with maximal (minimal) target longitudinal (transverse) polarization $P_{\text{long(tran)}}^{\text{T}}$.

We describe two techniques for getting as close as possible to the ideal Møller polarimeter. One is based on iron foil targets, in which the outer atomic electrons are polarized, and the other is based on an atomic hydrogen target. In the case of the iron foil target design, polarimeters at Jefferson Lab have already described control of systematic errors near the 0.5% level. We describe upgrades already in progress in Hall A in preparation the general 12 GeV program at Jefferson Lab which will enable that level of performance. While potentially very precise, such a polarimeter requires calibration from a body of magnetization studies with iron, and this normalization has never been cross-checked to the required precision. In addition, iron foil polarimeters require dedicated measurements at low current, and so measured polarization must be interpolated between spot measurements and extrapolated to the high currents used for production. Møller polarimetry with an atomic hydrogen target, in contrast, would be able to provide a continuous, non-invasive polarization measurement and would not require external calibration for accuracy at the few 10^{-3} level, but would be a new technology requiring significant technical R&D.

The strategy for Møller polarimetry, therefore, is to complete the upgrade of the Hall A iron foil polarimeter and seek to maximize the accuracy of this device. A cross-calibration with the upgraded Compton polarimeter should demonstrate that normalization of the target foil polarization is under control. The atomic hydrogen polarimeter option could be pursued if it is needed to confirm results of those studies.

14.7 The Hall A Upgrade: “High Field” Iron Foil Targets

Nearly all high energy Møller polarimeters operated to date [19, 20, 23, 24, 25, 26, 27, 28] make use of tilted ferromagnetic foil targets. High permeability alloys coupled with \sim few hundred Gauss

Variable	Hall C	Hall A:	
		High Field Foil	Hydrogen
Target polarization	0.25%	0.25%	0.01%
Target angle	‡	‡	*
Analyzing power	0.24%	0.20%	0.10%
Levchuk effect	0.30%	0.20%	*
Target temperature	0.05%	0.05%	*
Dead time	‡	0.10%	0.10%
Background	‡	0.10%	0.10%
Others	0.10%	0.10%	0.30%
Total	0.47%	0.42%	0.35%

*: Not applicable ‡: not estimated

Table 19: Systematic error summary for Møller polarimeters at JLab, including anticipated uncertainties for future prospects. The Hall C polarimeter [16] uses a high field pure iron target [17, 18] with a simple two-quadrupole spectrometer. Uncertainties quoted for that system are taken from a publication detailing calibration of the analyzing power. The current Hall A Møller polarimeter [19, 20] uses a tilted ferromagnetic allow target, and a spectrometer with a dipole magnet following three quadrupoles. A high-field pure iron target upgrade is underway with plans for an additional quadrupole in the spectrometer for high energy operation. Uncertainties for this system are the expected performance after the upgrade. Research and development for a hydrogen gas target [21, 22] provides the basis for a second continuously-running high precision polarimeter to complement the Compton apparatus.

magnetic fields preferentially polarize in the plane of the foil, so tilting the foil at a moderate angle gives a substantial longitudinal target polarization. Calculating the effective polarization, however, is typically the limiting systematic error, and such devices cannot ultimately do better than several percent precision.

A different approach [16], implemented in Hall C at Jefferson Lab, using a high magnetic field perpendicular to the foil plane [17, 18], has reported 1% precision on the beam polarization. It is this target design that we are adopting for SOLID, and indeed are already preparing to implement in Hall A.

Below we describe the principles of “high field” iron foil targets, the plans for redesign of the scattering chamber, and modifications to the existing spectrometer including simulations for operation at high energy.

14.7.1 Ferromagnetic Foil Targets

Materials respond to external magnetic fields because atomic electrons, with spin and orbital angular momentum, align themselves to an applied field. However, with a Bohr magneton equal to 5.8×10^{-5} eV/Tesla, the magnetic energy at several Tesla is still much smaller than the thermal energy at room temperature, so the effects of magnetic fields in most materials (“diamagnetism” and “paramagnetism”) are quite small.

Ferromagnetism, on the other hand, is a quantum mechanical phenomenon in which a subset of atomic electrons in some elements and alloys spontaneously align. These alignments happen in localized domains, which themselves are randomly oriented. However, the application of relatively

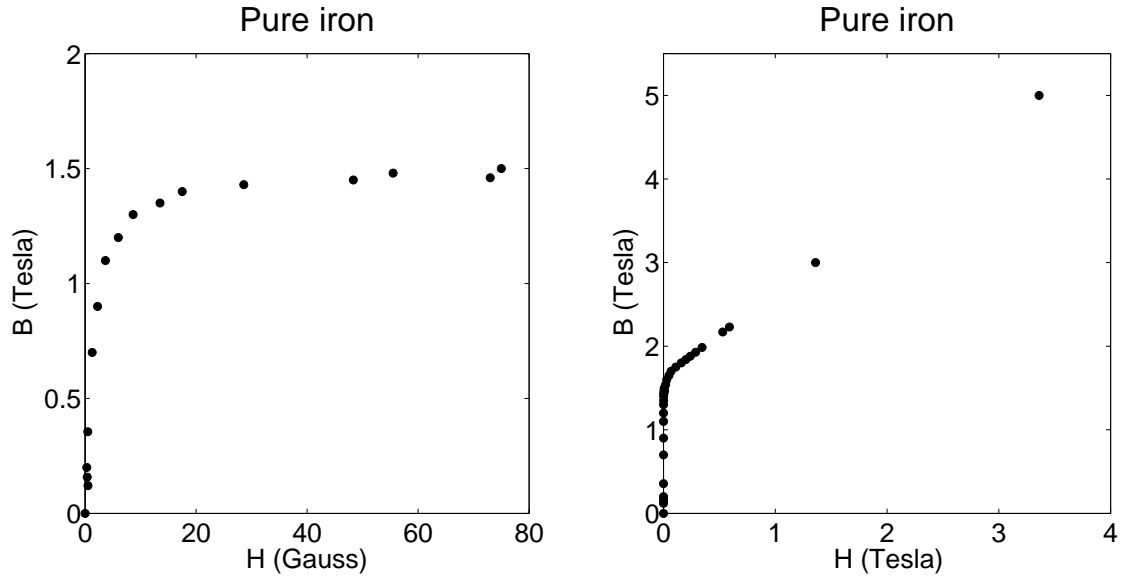


Figure 137: Magnetization curves for pure iron, from <http://www.fieldp.com/magneticproperties.html>. We use CGS units, so both B and H are properly measured in Gauss, but 1 Tesla = 10^4 Gauss. Both plots are of the same data set, but the horizontal scale is much expanded on the right.

small magnetic fields cause the domains themselves to line up, leading to large induced magnetic fields.

Magnetostatics (in CGS units) is governed by the equations $\vec{\nabla} \cdot \vec{B} = 0$ and $\vec{\nabla} \times \vec{H} = 4\pi\vec{j}/c$ where \vec{B} is the magnetic field, \vec{j} is the free current density, and \vec{H} absorbs the magnetic response of the medium. To be precise, $\vec{H} \equiv \vec{B} - 4\pi\vec{M}$ where the magnetization \vec{M} is the magnetic dipole moment per unit volume. It is the magnetization \vec{M} that we interpret, ultimately, as the polarization of target electrons.

For *linear* materials (which *do not* include ferromagnets), we define the magnetic permeability μ through $\vec{B} = \mu\vec{H}$. It is nevertheless a habit to speak of μ for ferromagnetic materials in terms of vector magnitudes, that is $B = \mu H$. For most materials, μ is a constant slightly larger than unity. In ferromagnets, however, μ is a strong function of H and can be very large.

Figure 137 shows magnetization data for pure iron. At several tens of Gauss of “applied” field H , the magnetic field B saturates at ~ 1.5 Tesla because the domains are aligned. The resulting magnetization corresponds to ~ 2 Bohr magnetons per iron atom, that is, roughly two electrons worth of magnetic dipole moment in *each* iron atom. As H reaches and exceeds several Tesla, the magnetization field simply adds directly to the applied field. The value of μ rises to several thousand for a few Gauss, and then decreases to unity for fields much greater than saturation.

Møller polarimeters using “low field tilted” foil targets operate in the region where $\mu \gg 1$. In fact, they generally make use of special alloys that have exceptionally high values of μ , that is, saturate at relatively low values of H . In this case $\vec{B} = 4\pi\vec{M}$ to a very good approximation. Since $\vec{\nabla} \cdot \vec{B} = 0$ implies that perpendicular components of \vec{B} are continuous across the foil surface, and since $B = H$ outside the foil is hundreds of times smaller than the magnetization, the only way to meet the boundary condition is for \vec{M} to point in the plane of the foil. (Of course, this argument breaks down if the foil is at right angles to the applied field.) Thus a target tilted at some angle, say $\sim 20^\circ$ provides a dominantly longitudinally polarized target for an incident electron beam in the

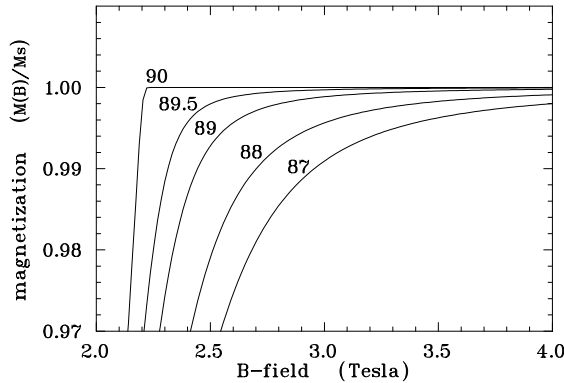


Figure 138: Simulations of foil magnetization for angles between the foil plane and the B-field direction close to 90 degrees. Errors due to imperfect alignment or a slight warp of the foil could produce such a result. Taken from [17, 18], which uses a calculation [33] of magnetization curves for uniformly magnetized prolate ellipsoidal domains.

same direction as the applied field.

The limiting precision of polarimeters using such targets, however, is extracting the target electron spin polarization from the magnetization. The ratio of “spin” magnetization M_s to the total can be written as [29] $M_s/M = 2(g' - 1)/g'$, with g' close to, but somewhat less than 2. The attendant uncertainties in g' for the alloys used in tilted target applications, limit one’s knowledge of the target polarization to several percent.

Measurements in *pure* iron or nickel, however, point to very precise knowledge of their magnetization parameters [30, 31]. The approach used by the Basel/Hall C group [16, 17, 18] is to not only use pure iron foil targets, but to polarize them with a very high (several Tesla) field, provided by superconducting coils. This overcomes limitations of a not-so-large value of μ for pure iron.

It is important to note that the magnetization of the foils in the strong longitudinal field has not been measured, but is taken from published data on the properties of bulk iron, which claims an accuracy of $\sim 0.1\%$. The orbital contributions to the magnetization of about 5% can be evaluated and subtracted using the magneto-mechanical factor, measured by other dedicated experiments [32]. With strong external fields of 3-4 T several additional correction of about 0.5% have to be made to compensate for extra orbital momenta and other complex effects. These corrections are temperature dependent. It will be important to carefully evaluate the literature on these measurements and their interpretation to verify that the uncertainty is not larger than a few 10^{-3} . For example, it is apparent that the anomalous magnetic moment of the electron has not been accounted for in recent publications, amounting to a correction of more than 0.2% to the target electron spin polarization.

Calculations of the longitudinal magnetization of a foil placed perpendicular (or nearly so) to an applied field, are quite difficult. Figure 138, taken from [17, 18], shows the magnetization (relative to its maximum value) of a pure iron foil as a function of applied magnetic field, for different angles between the field and the normal to the foil. To be sure, this calculation is in fact of a model of non-interacting prolate ellipsoidal domains [33], and the extent to which it applies to a pure iron foil is not clear.

A polarimeter based on this “high field” target was constructed in Hall C at Jefferson Lab [16]. The device has performed well, with experimenters claiming accuracy of 1% or better on the longitudinal beam polarization. Much of the updated design of the Hall A Møller polarimeter is based on the Hall C experience.

14.7.2 Simplified Møller Scattering Target Assembly

Quite a number of small, systematic effects need to be considered in order to achieve 0.5% uncertainty on the longitudinal beam polarization. For example, Figure 138 gives an idea of the tolerance

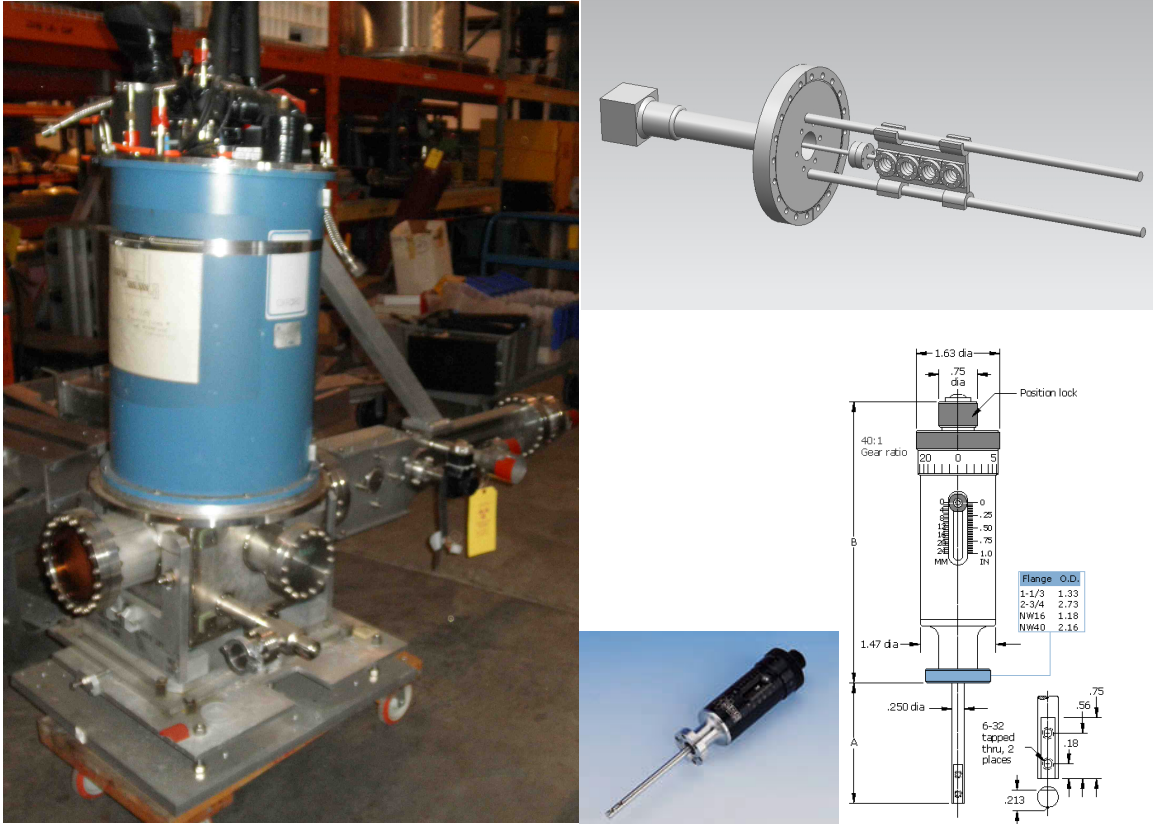


Figure 139: *Left*: Existing Hall A target chamber with ladder actuator extending off to the right. The magnet cryogenic system sits on top of the chamber. Our plan is to replace the actuator assembly, here shown supported by a boom attached to the cryo system. *Right*: Design concept for a new ladder actuator system, based on the Hall C design, along with a photo and schematic of the MDC660034 linear motion feedthrough.

needed on iron target alignment. In order to be assured of at least 99.8% of the maximum target polarization for a field of ~ 3 T, the tolerance on the foil angle misalignment is $\sim 1^\circ$.

Figure 139 includes a photograph of the high-field foil target chamber previously in place in Hall A, and some details of our current plans for the upgrade. Our plan is to retain the cryogenic magnet system and the target chamber and overall adjustment mechanism, but to replace the target actuator assembly. Originally designed to provide adjustments in many degrees of freedom, the existing actuator assembly proved unwieldy for regular use. It was also very heavy, and required stabilization through a connection to the dewar for the cryogenes. The redesign relies on precision construction with fewer adjustable degrees of freedom, and will be much lighter.

In order to interpret the target polarization to high precision, it is imperative that the foil be saturated. This can be confirmed by studying the Møller scattering asymmetry as a function of applied magnetic field. The cryogenic magnet is limited to fields less than 4 T, so according to Fig. 138 we need to have the target angle precise to about 1° . It would be useful to in fact confirm the behavior suggested by the figure, by making these measurements with the target arm rotated by various angles close to 90° .

References

- [1] K. Abe *et al.* [SLD Collaboration], Phys. Rev. Lett. **84**, 5945 (2000) [arXiv:hep-ex/0004026].
- [2] N. Falletto *et al.*, “Compton scattering off polarized electrons with a high finesse Fabry-Perot cavity at JLab,” *Nucl. Instrum. Meth.*, A459, 212-425, 2001.
- [3] A. Narayan, D. Dutta, V. Tvaskis and J. W. Martin, Nuovo Cim. C **035N04**, 134 (2012).
- [4] N. Vansteenkise, P. Vignolo, and A. Aspect, “Optical Reversibility Theorems for Polarization: Application to Remote Control of Polarization”, J. Opt. Soc. Am. A, Vol. 10, No. 10, (1993) 2240.
- [5] R.J. Loewen, “A compact light source: Design and technical feasibility study of a laser-electron storage ring X-ray source,” SLAC-R-0632 (2003).
- [6] S. Miyoshi *et al.*, Photon generation by laser-Compton scattering at the KEK-ATF, NIM A623 (2010) 576.
- [7] A. Variola *et al.*, The LAL Compton Program,, NIM A608 (2009) S83.
- [8] V. Brisson *et al.*, High finesse Fabry-Perot cavities in the picosecond regime, NIM A608 (2009) S75.
- [9] A. Denner and S. Dittmaier, “Complete $\mathcal{O}(\alpha^2)$ QED corrections to polarized Compton scattering”, Nucl. Phys. B **540** 58 (1999).
- [10] M. Friend *et al.*, “Upgraded photon calorimeter with integrating readout for Hall A Compton Polarimeter at Jefferson Lab”, [arXiv:1108.3116 [physics.ins-det]].
- [11] G. W. Ford and C. J. Mullin, “Scattering of Polarized Dirac Particles on Electrons,” Phys. Rev. **108**, 477 (1957); Erratum, Phys. Rev. **110**, 1485(E) (1958).
- [12] A. M. Bincer, “Scattering of Longitudinally Polarized Fermions,” Phys. Rev. **107**, 1434 (1957).
- [13] P. Stehle, “Calculation of Electron-Electron Scattering,” Phys. Rev. **110**, 1458 (1958).
- [14] A. Raćzka and R. Raćzka, “Møller Scattering of Arbitrarily Polarized Electrons,” Erratum, Phys. Rev. **110**, 1469 (1958).
- [15] G. Alexander and I. Cohen, “Møller scattering polarimetry for high-energy e^+e^- linear colliders,” Nucl. Instrum. Meth. A **486**, 552 (2002) [hep-ex/0006007]. This paper contains the basic formulas for Møller polarimetry, as well as references to calculations of higher order QED corrections.
- [16] M. Hauger *et al.*, “A high-precision polarimeter,” *Nucl. Instrum. Meth.*, vol. A462, pp. 382–392, 2001, nucl-ex/9910013.
- [17] Matthias Loppacher, “Møller Polarimetry for CEBAF Hall C”, Inaugural Dissertation, Universität Basel (1996).
- [18] L. V. de Bever, J. Jourdan, M. Loppacher, S. Robinson, I. Sick, J. Zhao, “A Target for Precise Møller Polarimetry”, Nucl. Instrum. Meth. A **400**, 379 (1997).

- [19] A. V. Glamazdin, V. G. Gorbenko, L. G. Levchuk, R. I. Pomatsalyuk, A. L. Rubashkin, P. V. Sorokin, D. S. Dale and B. Doyle *et al.*, “Electron beam Møller polarimeter at JLab Hall A,” *Fizika B* **8**, 91 (1999) [hep-ex/9912063].
- [20] E. A. Chudakov, A. V. Glamazdin, V. G. Gorbenko, L. G. Levchuk, R. I. Pomatsalyuk, P. V. Sorokin, “Electron beam Møller polarimeter at Hall A, JLab”, *Prob.Atom.Sci.Tech.* **40**, 43 (2002)
- [21] E. Chudakov and V. Luppov, “Møller polarimetry with atomic hydrogen targets,” *IEEE Trans. Nucl. Sci.*, vol. 51, pp. 1533–1540, 2004.
- [22] E. Chudakov and V. Luppov, “Moeller polarimetry with atomic hydrogen targets,” *Eur. Phys. J.*, vol. A24S2, pp. 123–126, 2005.
- [23] P. S. Cooper, M. J. Alguard, R. D. Ehrlich, V. W. Hughes, H. Kobayakawa, J. S. Ladish, M. S. Lubell and N. Sasao *et al.*, “Polarized electron Electron Scattering at GeV Energies,” *Phys. Rev. Lett.* **34**, 1589 (1975).
- [24] B. Wagner, H. G. Andresen, K. H. Steffens, W. Hartmann, W. Heil and E. Reichert, “A Møller polarimeter for CW and pulsed intermediate-energy electron beams,” *Nucl. Instrum. Meth. A* **294**, 541 (1990).
- [25] J. Arrington, E. J. Beise, B. W. Filippone, T. G. O’Neill, W. R. Dodge, G. W. Dodson, K. A. Dow and J. D. Zumbro, “A Variable energy Møller polarimeter at the MIT Bates Linear Accelerator Center,” *Nucl. Instrum. Meth. A* **311**, 39 (1992).
- [26] K. B. Beard, R. Madey, W. M. Zhang, D. M. Manley, B. D. Anderson, A. R. Baldwin, J. M. Cameron and C. C. Chang *et al.*, “Measurement of the polarization of a pulsed electron beam with a Møller polarimeter in the coincidence mode,” *Nucl. Instrum. Meth. A* **361**, 46 (1995).
- [27] H. R. Band, G. Mitchell, R. Prepost and T. Wright, “A Møller polarimeter for high-energy electron beams,” *Nucl. Instrum. Meth. A* **400**, 24 (1997).
- [28] P. Steiner, A. Feltham, I. Sick, M. Zeier and B. Zihlmann, “A high-rate coincidence Moller polarimeter,” *Nucl. Instrum. Meth. A* **419**, 105 (1998).
- [29] G. G. Scott and H. W. Sturmer, “Magnetomechanical Ratios for Fe-Co Alloys,” *Phys. Rev.* **184**, 490 (1969).
- [30] J. Crangle and G. M. Goodman, “The Magnetization of Pure Iron and Nickel,” *Proceedings of the Royal Society of London, Series A*, **321**, 477 (1971).
- [31] C. D. Graham, Jr., “Iron and Nickel as Magnetization Standards,” *J. Appl. Phys.* **53**, 2032 (1982).
- [32] G. G. Scott, “Review of gyromagnetic ratio experiments,” *Rev. Mod. Phys.*, vol. 34, pp. 102–109, Jan 1962.
- [33] E. C. Stoner and E. P. Wohlfarth, “A Mechanism of Magnetic Hysteresis in Heterogeneous Alloys,” *Phil. Trans. Royal Soc. London, Series A* **240**, 599 (1948).

- [34] L. G. Levchuk, “The Intraatomic motion of bound electrons as a possible source of a systematic error in electron beam polarization measurements by means of a Møller polarimeter,” *Nucl. Instrum. Meth.*, vol. A345, pp. 496–499, 1994.
- [35] M. Swartz, H. R. Band, F. J. Decker, P. Emma, M. J. Fero, R. Frey, R. King and A. Lath *et al.*, “Observation of target electron momentum effects in single arm Møller polarimetry,” *Nucl. Instrum. Meth. A* **363**, 526 (1995) [hep-ex/9412006].
- [36] D. Gaskell, D. G. Meekins, and C. Yan, “New methods for precision Møller polarimetry,” *Eur. Phys. J.*, vol. A32, pp. 561–564, 2007.
- [37] E. Chudakov and V. Luppov, “Møller polarimetry with atomic hydrogen targets,” tech. rep., JLab, 2005. http://www.jlab.org/~gen/hyd/loi_3.pdf.
- [38] I. F. Silvera, “Ultimate fate of a gas of atomic hydrogen in a liquid-helium chamber: Recombination and burial,” *Phys. Rev. B*, vol. 29, pp. 3899–3904, Apr 1984.
- [39] I. F. Silvera and J. T. M. Walraven, “Stabilization of atomic hydrogen at low temperature,” *Phys. Rev. Lett.*, vol. 44, pp. 164–168, Jan 1980.
- [40] I. F. Silvera and J. T. M. Walraven, “Spin polarized atomic hydrogen,” *Progress in Low Temperature Physics*, vol. X, pp. 139–370, 1986.
- [41] T. Roser *et al.*, “Microwave driven extraction of stabilized spin polarized atomic hydrogen,” *Nucl. Instrum. Meth.*, vol. A301, pp. 42–46, 1991.
- [42] M. Mertig, V. G. Luppov, T. Roser, and B. Vuaridel, “Continuous density measurement of atomic hydrogen by means of a bolometer,” *Rev. Sci. Instrum.*, vol. 62, pp. 251–252, 1991.
- [43] M. D. Miller and L. H. Nosanow, “Possible ”new” quantum systems. ii. properties of the isotopes of spin-aligned hydrogen,” *Phys. Rev. B*, vol. 15, pp. 4376–4385, May 1977.
- [44] M. Poelker, J. Grames, J. Hansknecht, R. Kazimi, J. Musson, *Phys. Rev. ST Accel. Beams* **10**, 053502 (2007).

15 Supports and Infrastructure

15.1 Magnet Support

The initial plan used for estimating the cost is to build a stationary frame and distribute the approximate 1000 ton load of the modified CLEO-II magnet section using eight 200 ton enerpac jacks. Steel plates and large steel blocks and/or large I-beams will be used to distribute the load out over a safe area. The 200 ton jacks will be used for vertical alignment and have locking rings which allow for a full mechanical connection and not rely on hydraulic pressure for stationary support.

15.2 Endcap Support Structure and Motion Mechanism

The endcap will have a support structure that cradles each half the cylindrical ring. The structure will be integrated into a track system that is mounted to steel plates resting upon the concrete floor. The initial design concept for the track system requires a set of longitudinal (downstream direction) tracks for moving the endcap away from the magnet. A second set of tracks that would separate the endcap halves in the lateral direction would ride on top of the longitudinal tracks. The endcap support structure would then be attached to the top lateral track system. Motion can be achieved by using hydraulic or electric cylinders to push and pull the entire system into position.

15.3 Support Structure for Equipment Located Inside Cryostat Bore

The magnet will be located adjacent to the existing Hall A center pivot/target mount area and will have limited access to the front of the magnet. The insertion of the large angle detector packages that will reside internal to the cryostat will be accomplished from the downstream side of the magnet using a supporting framework to roll the packages in and out. This will require the detector hut to be moved downstream to allow access to the cryostat.

An internal frame system is needed to mount the lead baffles in the PVDIS experiment. See Figure 140. The frame cannot come into contact with the inside bore of the cryostat. This requires the frame to span the entire length of the cryostat and mount to the return yoke iron. The rails of the frame will be fabricated from 4 inch diameter schedule 80 welded stainless steel pipe. Either 304 or 316 grade stainless is acceptable. The downstream end of the rails will have a hemispherical cap and a stainless steel foot welded on and will be bolted to the downstream collar. The upstream end of the rail will either be bolted or welded to an annular stainless steel plate. The upstream end of the frame will be mounted to the frontcup (magenta body inside the red front collar). Since the frontcup has to be movable to balance the magnetic field on the coils the annular plate will be attached to the frontcup with studs. This will allow the rail framework to remain stationary if the frontcup has to be adjusted. The same rail system can be used for the SIDIS experiment for mounting the large angle calorimeter and GEM's.

15.4 Power Requirements

The projected electrical power load is 1.6MVA, maximum current for magnet at 3266A. The present power consumption for Hall A is less than 1 MVA. So upgrade to the Hall substation to have 2 MVA is required. (Moeller Experiment has included the cost (\$300k)for this in their MIE).

The CLEO-II magnet is designed to have a low cryogenic heat load with passive cooling. The HRS arms will not be operational during SoLID, so it is expected that the refrigeration heat load will be less than needed for HRS. The refrigeration need for the cryotarget is discussed in the target section (Section 5).

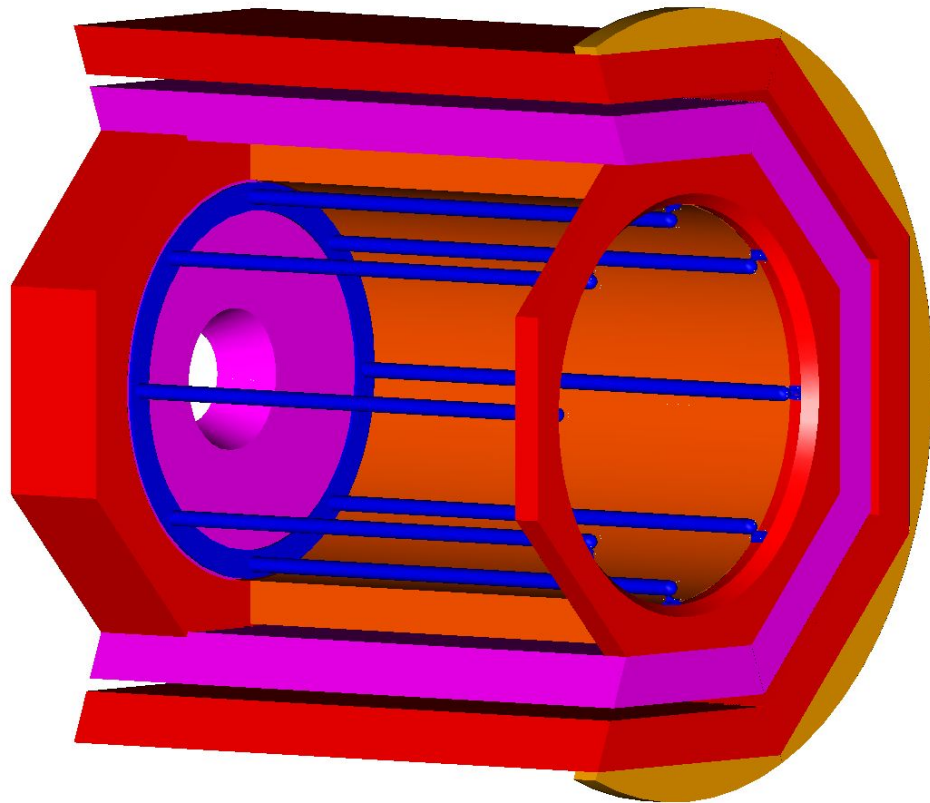


Figure 140: The internal rail system will be used to mount all parts inside the barrel, including PVDIS baffle, SIDIS large angle calorimeter and GEM's

16 Installation

16.1 Experimental Layout

An initial check of the experimental equipment layout in Hall A has been done and no major obstructions have been found. The experiment layout puts the HRS arms at 90 degrees to the beamline on the left and right. The target is at the nominal pivot location with the center of the CLEO-II magnet 350 cm downstream of the target center. The SoLID magnet and detectors encompass an area of 5.8 meters in diameter and 7.3 meters long. With the magnet on beamline center, clearance to the Hall floor ranges from 10 to 38 cm. This is sufficient area to support the load. The weight of the CLEO-II magnet, detector hut and detectors is estimated to be 1300 tons. The floor in this installation region is designed for 250 tons for a 12 square foot pad.

16.2 Magnet Moving and Placement

In evaluating the use of the CLEO magnet for SoLID consideration is given to how the CLEO magnet can be transported into Hall A and how Hall A structurally meets the requirements of CLEO. The footprint of SoLID utilizing the CLEO magnet will be approximately a 1000 ton load with dimensions of 24 feet long by 19 feet in diameter. Hall A is 164 feet in diameter. In the area required to install SoLID, the floor is constructed to carry 250 to 500 tons per 12 square feet.

The existing Hall A equipment consists of the two High Resolution Spectrometers mounted at the center pivot and all related infrastructure. To accommodate installation of SoLID the target will need to be mounted 115 cm downstream from the existing support location in order for the magnet to clear the HRS bearing assembly. Placing the CLEO magnet on beamline height gives 15 inches clearance to the floor for adequate support and alignment. The location of the HRS arms during SoLID have two options: remove the existing beam line and move both HRS arms to beam left locations or place both HRS arms 90 degrees to the beam line. The second option allows more clearance for SoLID during operation but requires more planning and infrastructure modifications during installation. These options will be studied further.

The bird's eye view Figure 141 and the back side Figure 142 show the SoLID in Hall A with two HRS arms on the side. The SoLID detector hut is cut in half and the right side of the return yoke layers are removed showing the cryostat in orange color.

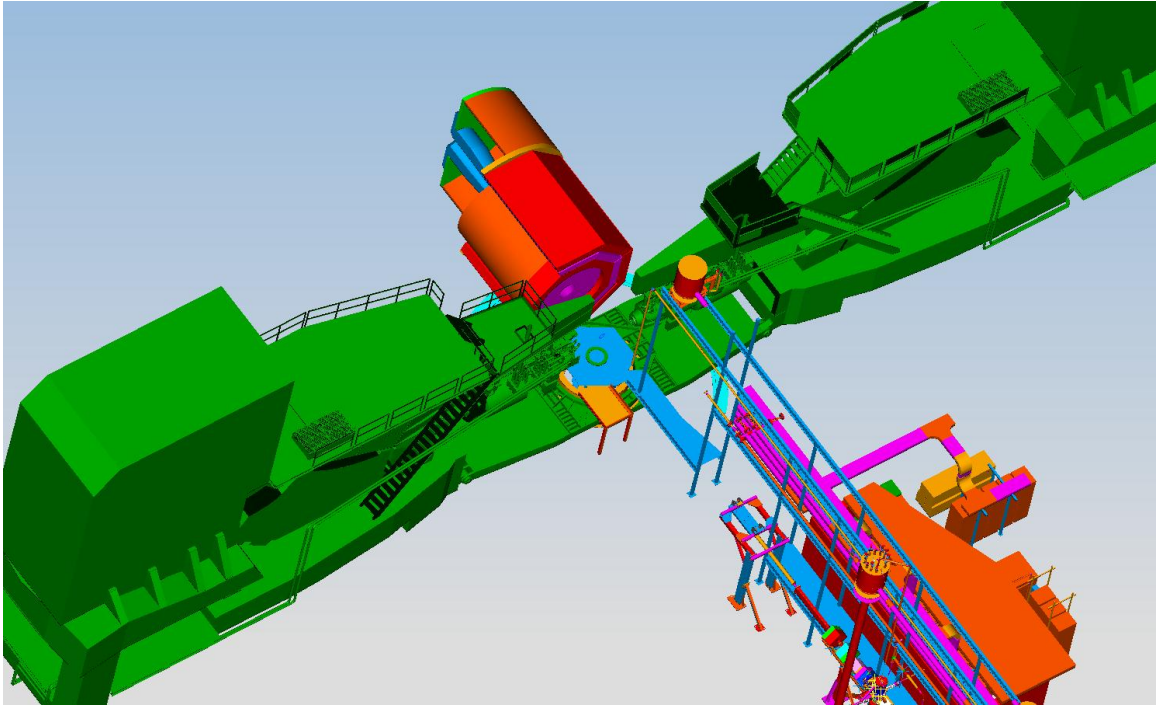


Figure 141: The bird's eye view of SoLID in Hall A

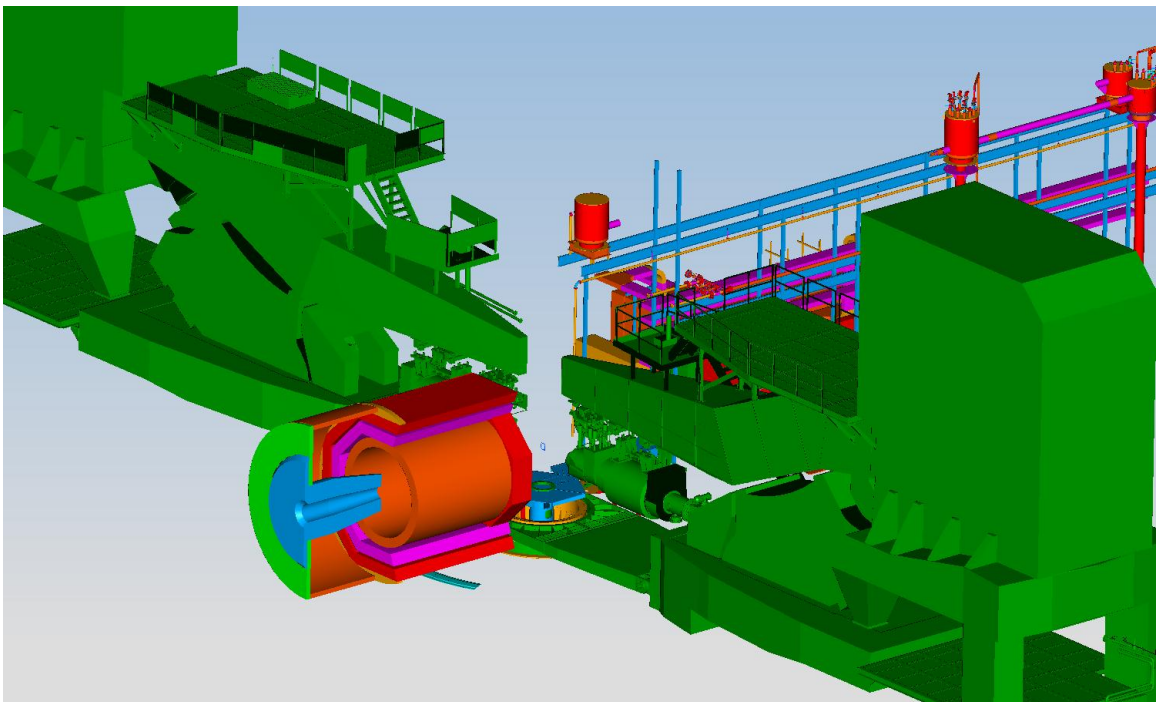


Figure 142: The back side view of SoLID in Hall A

The CLEO-II magnet will be disassembled and loaded on trucks for shipping by the Cornell personnel with oversight by Jefferson Lab. It will require 52 trucks to transport the magnet and related equipment.

We have identified all of the parts of the CLEO magnet, with sizes and weights, anticipating a need for storage of these parts at Jefferson Lab starting Summer 2016. We have identified specifically the parts to reuse in building the SoLID magnet, and these have a total weight of 1,053k lbs. The cryostat (35k lbs) and power supply will need to be stored in an environment-controlled area of approximately 400 square feet. Jefferson Lab projects the use of the CMSA site for storage of all parts.

In developing the installation plan for SoLID, the largest part to transport is the cryostat. The cryostat is 12.3 feet long, 11.8 feet in diameter and weighs 22 tons. The height of the truck ramp into Hall A is limited to 17 feet in height. This will require the cryostat to be moved into the Hall on a roller structure rather than a flatbed type truck. This type of procedure has been completed several times at Jefferson Lab. See Figure 143, Figure 144, and Figure 145.

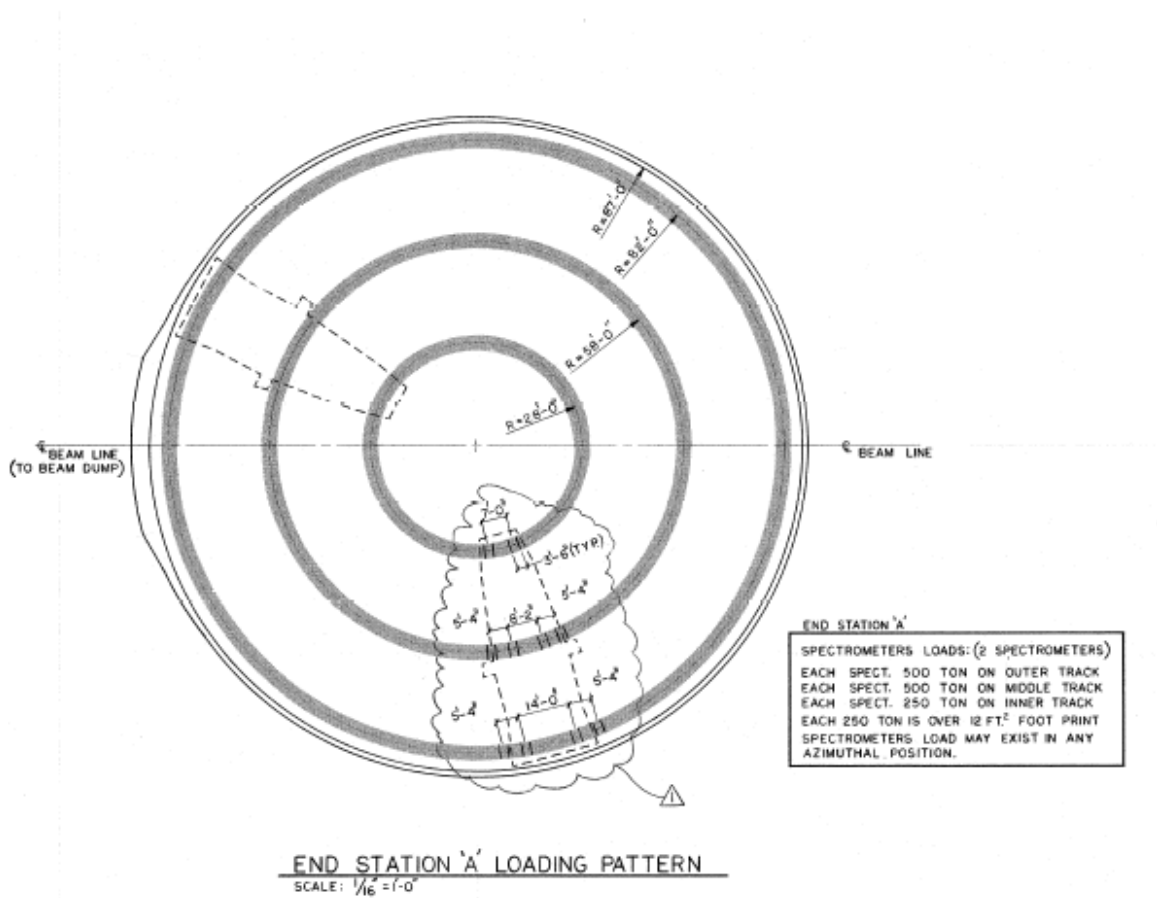


Figure 143: Hall A loading pattern.

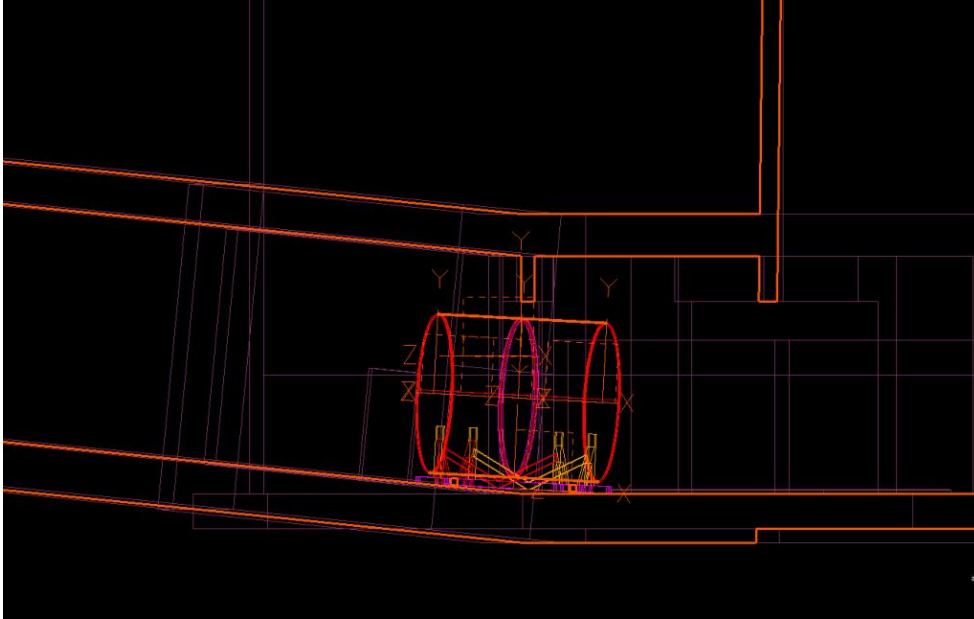


Figure 144: The plan of moving CLEO cryostat through Hall A ramp.

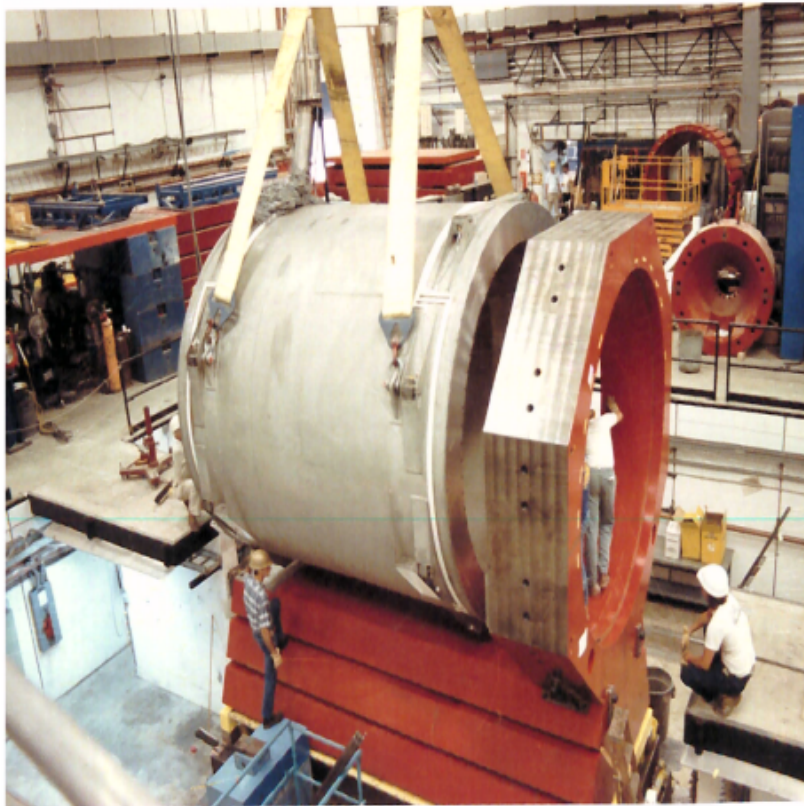


Figure 145: CLEO cryostat lifted during the installation at Cornell.

16.3 Helium Dewar Support and Upper Access Platform

An upper personnel access platform that is capable of supporting the helium dewar will be mounted to the top of the magnet. A similar platform was used for the CLEO II experiments. See Figure 146.

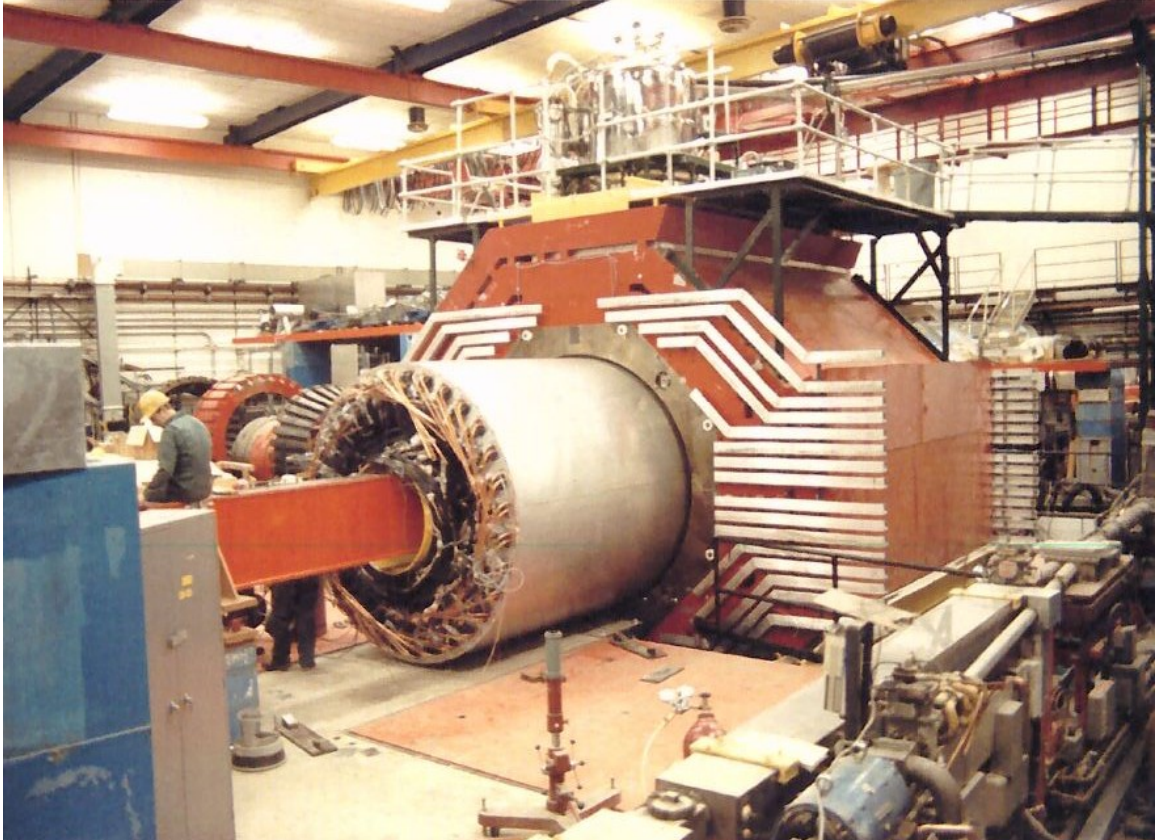


Figure 146: Helium dewar support upper access platform and detector loading inside of cryostat.

16.4 Endcap Forward Angle Detector Package Installation Structure

The basic design concept for the detectors mounted inside the endcap will have them supported by individual rails mounted to the inner circumference of the cylindrical ring and on rails attached to the outer horizontal circumferential surface of the nose if needed. The heavy gas Cherenkov will be separated into six sections with each section utilizing two rails to attach the section to the outer circumference of the endcap. A counterweight balanced installation device that is slung from the crane can be used to orient and position each section onto the rails. Personnel access to the endcap will be through man lifts and/or a specialized scaffolding as needed.

16.5 Large Angle Detector and Baffle Installation Mechanism

An installation mechanism is needed to load the large angle detector packages and baffle system into the internal support structure mentioned in the last section. This mechanism will likely be mounted to the longitudinal track system used for the endcap movement and can utilize the tracks for rolling the detectors and baffles into the cryostat and transferring the load to the internal frame. Depending

on the final design of the detectors and baffle system the support could be a simple beam that runs through the middle of the detectors and baffles. See Figure 146 for similar approach at BNL

16.6 Light Gas Cherenkov Installation Structure

The light gas Cherenkov will mount to the external downstream end of the magnet and will not traverse with endcap. When the endcap is in the operational position the light gas Cherenkov will be enclosed within the cylindrical ring along with the rest of the forward angle detectors. The light gas Cherenkov detector will be made up of six pie shaped sections that will need to be bolted to the downstream side of the magnet. A space frame similar to a scaffolding system would hold and position each section while being attached to magnet. The space frame would attach to the rail system and could be movable along the rails if needed. The space frame will be suitable for personnel access to allow workers to perform the installation and maintenance of the detectors.

17 Integration, Calibration, and Systematics

17.1 Assembly and PID Integration

System integration incorporates several tasks : 1) Quality control of the engineering of the apparatus so that all the pieces fit and so that the system satisfies *all* of the experimental program with minimal turnover between experiments; 2) Integration of the detectors so that they work together and form efficient triggers, and so that we can predict the combined PID performance; and 3) Control of calibrations and systematic errors; and 4) Commissioning plans.

In a preliminary engineering study done at Argonne National Lab by Paul Reimer, scenarios for assembling and disassembling of the apparatus have been developed which allow for switching rapidly between PVDIS and SIDIS, as well as for allowing other experiments to share Hall A during the SoLID running era. We believe we can switch between running setups in approximately three months.

For the second topic, we have made a study of the combined particle ID using the gas Cherenkov and the calorimeters, see fig 147 where the resulting π/e ratios are shown. A similar PID performance was achieved by the Hermes spectrometer [1]. Our study was performed by using the pion rejection factor and electron efficiency as a function of the scattered angle and momentum for both detectors for both the PVDIS and SIDIS configurations based on Geant simulations of the current detector designs. The results here, shown for PVDIS, are preliminary since the detector designs and the analysis strategies are still evolving. Nevertheless, the preliminary results are encouraging and show that we can likely meet the requirements for the error in the pion contamination, which is 10^{-3} for entire experimental program. We believe it may be possible to combine some information with the shower shape in a multi-variable analysis to further improve the pion rejection. We are also still considering the issues of rate dependence and pileup on the pion rejection factor.

17.2 Kinematics, Resolution and Calibration for PVDIS with SoLID

17.2.1 Introduction

In this section, we describe the general method of measuring the momentum p and the scattering angle θ of each track. In addition, we discuss the resolution of x , and Q^2 , the relevant variables for the analysis. Finally, we discuss the calibration of the average value of Q^2 . The most critical requirements are the the x resolution is on the order of 0.01 to avoid kinematic smearing and that the average Q^2 , which is proportional to the asymmetry, is calibrated to 0.1%.

17.2.2 Approximate Method

The method that we use to reconstruct the tracks, determining the scattering angle and momentum, is easiest to understand in the approximation of a uniform field. Based on this method, we can explain our alignment tolerances and systematic errors. We then show how to make the corrections for the realistic case. These corrections do not alter most of the tolerances.

17.3 Uniform field case

First, we look at the track in the x - y plane. This is given in Figure 148. All we require is hits in two GEM detectors. The one closest to the target is labeled GEM_i and the other is GEM_j . Since the beam is small ($300 \mu\text{m}$ by $250 \mu\text{m}$), it provides a third point which is sufficient to determine the radius of curvature ρ of the helix. The transverse momentum of the electron is then κ/ρ , where κ

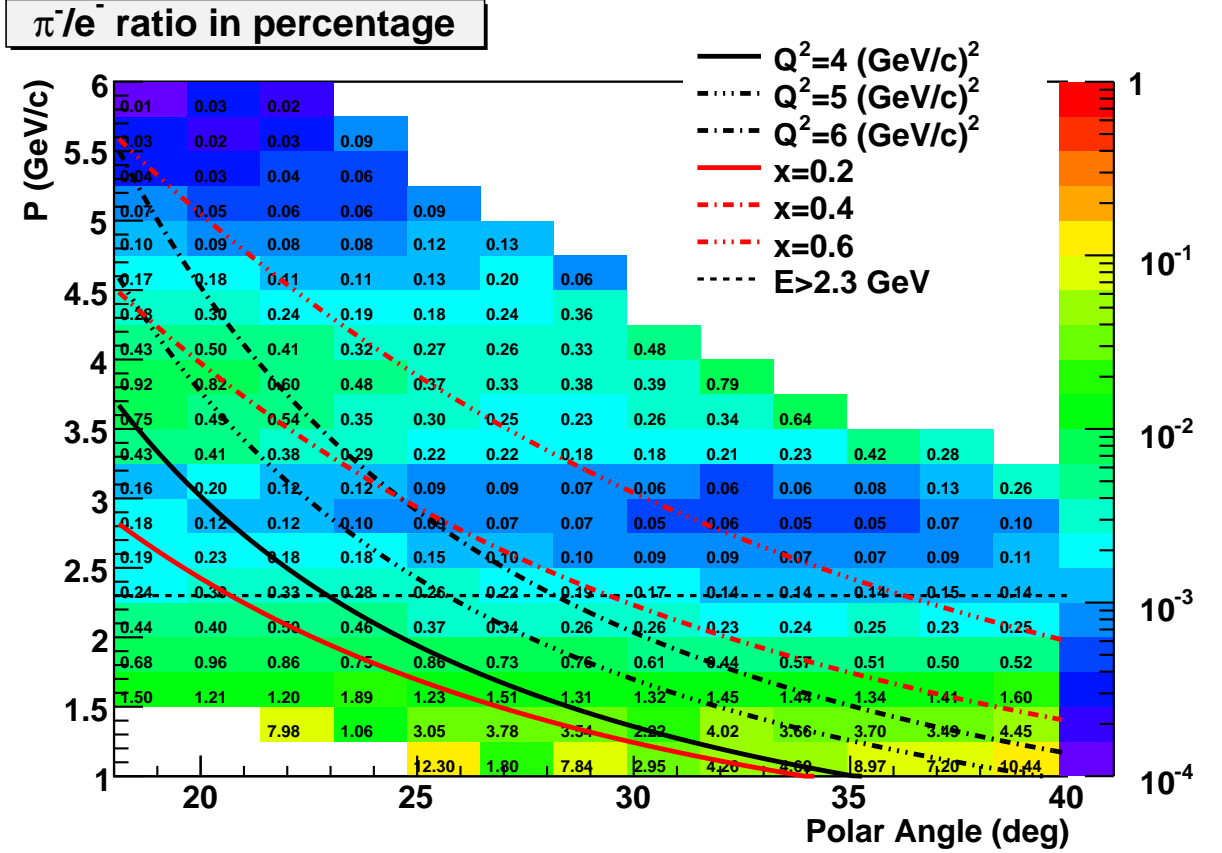


Figure 147: The π/e ratio from combined Cherenkov and Calorimeter detector performance as a function of the scattered momentum P and polar angle θ . The numerical values are the ratios corresponding to that cell in (P, θ) . The curves indicate various regions of $Q^2 x$ or scattered energy E .

is a constant proportional to the magnetic field. The transverse distance between the beam and the first GEM is R and between the two GEM's is D . The angle between the line segments R and D is $(\psi + \delta)/2$. From the diagram, we have

$$\frac{1}{\rho} = \frac{2(\sin(\psi/2) + \sin(\delta/2))}{(R + D)} \approx \frac{\psi + \delta}{R + D}, \quad (22)$$

where the approximation is for small angles. Since

$$\frac{\sin(\psi/2)}{\sin(\delta/2)} = \frac{R}{D}$$

and $(\psi + \delta)/2$ is measured, Eq. 22 can be evaluated exactly.

For the helix, the angle θ between the trajectory and the z -direction is constant, and thus is the scattering angle. If Δz is the difference in the z -coordinates of the GEM's, then

$$\tan \theta = \frac{\rho}{\Delta z} \sin^{-1} \frac{D}{\rho} \approx \frac{D}{\Delta z}. \quad (23)$$

From the approximation, we see that the error in ρ contributes little to the error in θ .

Finally, we note that

$$Q^2 = 4E \frac{\kappa}{\rho} \tan(\theta/2).$$

Thus the fractional error in Q^2 is the sum in quadrature of the fractional errors in ρ and θ .

Thus with two GEM points and a narrow beam, we can reconstruct the important variables for DIS. In addition, the distance r from the first GEM to the beam line in the x - y plane and the azimuthal angle of the first GEM hit are measured. The first can be used to determine the z -coordinate of the interaction, which can be used as a check that the track is valid and also determine if it came from the front or rear target windows.

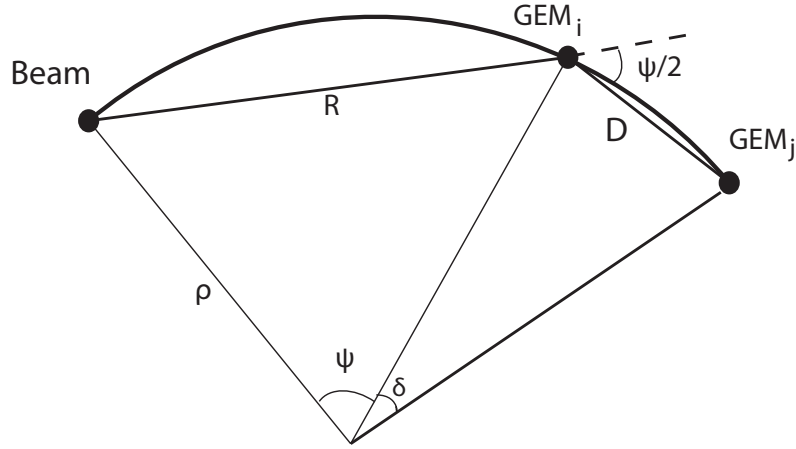


Figure 148: Projection of the track in the $x - y$ plane. The projected radius of curvature is ρ .

17.4 Realistic Case

For realistic magnetic fields, we generated with our Monte Carlo many trajectories and determined the discrepancies with Eqs. 22 and 23. These discrepancies could be parameterized in terms of the measured variables $\psi + \delta$, D , R , and r and used as corrections. With the corrections, ρ and θ can be determined from the GEM hits with a precision better than 0.1%.

Rather than $\psi + \delta$, we used the angle α between the line segment R and the line joining the beam with the hit in GEM_j . Then

$$\alpha \approx \frac{\psi + \delta}{2} \frac{D}{R + D},$$

and

$$\frac{1}{\rho} = \frac{2\alpha}{D}.$$

Thus our precise and realistic equation for ρ is

$$\frac{1}{\alpha\rho} = \frac{2}{D} + F_\rho(R, D, r, \Delta z). \quad (24)$$

An important feature is that the angle α only appears in the left side. This feature is useful for our momentum calibration method shown below. For θ ,

$$\tan \theta = \frac{D}{\Delta z} + F_\theta(R, D, r, \Delta z, \alpha). \quad (25)$$

There are two effects that contribute to F_θ . The first is the approximation in Eq. 23. The second is the fact that radial components of the magnetic field change the angle that the trajectory makes with the z -axis. Thus F_θ depends slightly on α .

Since F_ρ and F_θ are small, the errors in their arguments do not contribute significantly to the errors in ρ or θ . The requirements for calibration can be obtained from the leading approximations.

17.4.1 Resolution

The momentum resolution, which is dominated by multiple scattering, mostly in the air, is about 1%, independent of momentum. The angular resolution, dominated by GEM resolution, is about 0.5%. The resolution in Q^2 is 1.5% and in x is 1%. The z -resolution is 7 mm. These numbers are obtained with our simulation with realistic GEM signals.

17.4.2 Calibration

There are two calibrations. The first the alignment of the GEM's. The method is to move one of the baffles to obtain some straight-through tracks from a thin C target with the magnetic field off.

The first step is to assure that $\langle \alpha \rangle = 0$. This calibrates assures that $\alpha = 0$ corresponds to $\rho = \infty$. The radial coordinates can be calibrated by

1. Checking that the z of the target is correct and independent of sector. The resolution of a thin target is about 5 mm.
2. Installing a ‘‘sieve slit’’. In our case, the slot would be slots instead of holes. Tracks passing through the slot would be identified by a good Cerenkov signal and the reconstructed energy of the track matching the energy in the calorimeter.
3. A second sieve slit at a different z would provide redundancy and check the position of the target. Only one or two sectors would require the second slit.

The magnetic field is calibrated as follows. First a map is obtained with a precision of about 1%. With this map the radial fields are known well enough so that F_θ can be precisely determined. To improve the calibration of the momentum to the 0.1% level, we lower the beam to 4 GeV and observe elastic events. Since the beam energy is known to better than 0.1% and the angle can be measured to that precision, the location of the elastic peak provides a calibration of the magnetic field. One issue is that for one beam energy, there is only one track energy at each angle, whereas for DIS, the angle and energy are much less correlated. However, the correction F_ρ in Eq. 24 is independent of α , so a single momentum at each angle is sufficient. In other words, the importance difference between two similar fields is the value of $\int B_z ds_\perp$ which is a scale factor for all momenta. Hence a single momentum from the elastic scattering is sufficient to make a precise correction. The fact that $1/\rho$ in Eq. 24 is independent of α makes this possible.

References

- [1] H. Avakian *et.al* Nucl. Instrum. Meth. **A417** (1998) 69.

18 Project Status and Proposed Management Organization

The SoLID spectrometer was initially proposed in 2009 for two experiments: SIDIS experiment (PR12-09-014, later became E12-10-006) and the PVDIS experiment (PR12-09-012, later became E12-10-007). Both experiments aim to achieve high precision which require very high statistics. A spectrometer/detector system with a large acceptance and also able to handle high luminosity is needed. Therefore SoLID is designed to have a large solid angle and broad momentum acceptance and can handle luminosity up to $10^{39}\text{s}^{-1}\text{cm}^{-2}$ with a baffel system in the PVDIS configuration and $10^{37}\text{s}^{-1}\text{cm}^{-2}$ without a baffel system in the SIDIS configuration. With these unique features, SoLID is ideal for inclusive and semi-inclusive DIS experiments and is also good for measurements of certain exclusive reactions. The SoLID base equipment consists of a solenoid magnet (CLEOII magnet), tracking detectors (GEMs), electron PID detectors (electromagnetic calorimeter and light gas Čerenkov detector) and hadron PID detectors (MRPC, heavy gas Čerenkov and EC), DAQ system, supporting structure and infrastructure needed for the spectrometer. Leveraging the unique capabilities of SoLID, currently, there are five high impact (four “A” rating and one “A⁻”) experiments approved using SoLID and three more proposed for the upcoming PAC.

The conceptual design has gone through many iterations, including careful studies, detailed simulations, pre-R&D testings and a number of internal reviews. Of the various internal reviews, it is worth mentioning the two brainstorming sessions in September 2011 and January 2012, organized by the JLab physics division, and the dry run review in June 2012 with external experts (outside SoLID collaboration, including people from outside JLab). These reviews helped greatly in optimizing, improving and finalizing the conceptual design. Detailed simulations with realistic background (including neutron backgrounds) and pre-R&D activities focusing on the major challenges have significantly improved the reliability of the conceptual design.

18.1 Collaboration and Organization

The SoLID collaboration has more than 200 members from over 50 institutions over 9 countries. SoLID has attracted international attention with many groups committed to make significant contributions, including noticeably the commitments to large detector projects (GEMs and MRPC) from several Chinese groups.

The proposed SoLID Organization Chart is shown in Figure 149.

Project Manager

Function: The Project Manager (PM) will be in charge of executing the project and report to JLab management. The collaboration will provide advice and oversight, and members of the collaboration will work under the PM in various roles to execute the project. For example, all subsystems coordinators will report to the PM. The PM has the authority and responsibility to manage the SoLID project.

Jian-ping Chen is the initial PM.

Executive Board

Function: The Executive Board (EB) makes decisions on scientific and organizational choices, and provides high level oversight on all matter pertaining to preparation and operation of the SoLID project.

The Chair of EB is the science leader, and is the principle contact between the collaboration and the lab management/DOE. The Chair will provide oversight and input to the PM for the SoLID project. The Chair, together with the PM, is responsible for the performance and assessment of all subsystems.

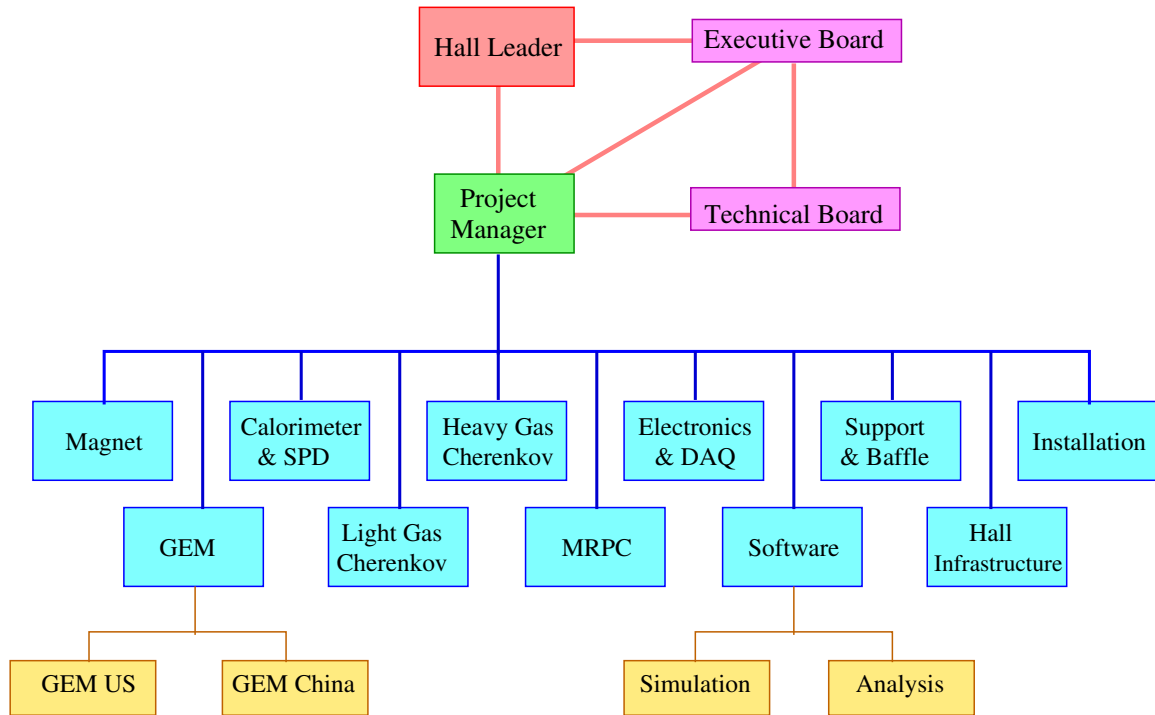


Figure 149: SoLID Organization Chart

Initial members are the senior spokespeople plus the Hall Leader (ex-officio) and the PM (ex-officio): Paul Souder (PVDIS), Haiyan Gao (SIDIS), Zein-Eddine Meziani (J/Psi), Thia Keppel (Hall Leader, ex-officio) and Jian-ping Chen (PM, ex-officio).

Paul Souder is the 1st Chair. It is expected that the Chair position will rotate.

Technical Board

Function: The technical Board (TB) advises the PM on all aspects of the Project, including any changes in cost, scope or schedule.

The TB will have a group of (usually senior) collaborators who represent the full range of required technical expertise and usually a representative from each subsystem is expected to be on this board. This group will be appointed by the EB. In addition, the TB will include the PM and also project engineers when they are appointed. The membership of the TB can be periodically adjusted by the EB as the situation warrants.

The chair of the TB will be the PM. All EB members who are not already in the TB are ex-officio members, along with the Hall leader.

Initial members: Jian-ping Chen (Chair), Paul Souder, Haiyan Gao, Zein-Eddine Meziani, Thia Keppel (ex-officio); Alexandre Camsonne, Eugene Chudakov, Tom Hemmick, Xiaodong Jiang, Nilanga Liyanage, Bob Michaels, Xin Qian, Paul Reimer, Yi Wang, Zhengguo Zhao, Xiaochao Zheng

Sub-System Lead Coordinators and Institutions

- **Magnet:** Robin Wines / Paul Reimer; JLab, Argonne
- **GEM-US:** Nilanga Liyanage / Bernd Surrow ; UVa, Temple
- **GEM-China:** Zhengguo Zhao / Xiaomei Li; USTC, CIAE, Lanzhou, Tsinghua, IMP

- **Calorimeter:** Xiaochao Zheng / Wouter Deconick / Chufeng Feng; UVa, W&M, Shandong (China), Argonne, Los Alamos
- **Light Gas Cherenkov:** Zein-Eddine Meziani / Michael Paolone; Temple
- **Heavy Gas Cherenkov:** Haiyan Gao / Mehdi Meziane; Duke
- **MRPC:** Yi Wang / Alexandre Camsonne; Tshinhua (China), JLab, Duke, Rutgers
- **DAQ/Electronics:** Alexandre Camsonne / Rory Miskimen / Ron Gilman ; JLab, UMass,Rutgers
- **Simulation:** Seamus Riordan / Zhiwen Zhao ; UMass, UVa, Duke, Syracuse
- **Reconstruction and Analysis:** Ole Hansen; JLab
- **Supporting Structure and Baffle:** Robin Wines / Seamus Riordan; JLab, Argonne, UMass
- **Hall Infrastructure Modification:** Robin Wines / Ed Folts; JLab
- **Installation:** Ed Folts / Robin Wines; JLab, all user groups.

The names listed are the coordinators for sub-systems. Institutions working on and responsible for the sub-systems are also listed. Details of the responsibilities are described in the summary for each sub-system. The list reflects the current situation and it is expected to be modified as more groups join the effort as the SoLID project moves forward.

18.2 Cost estimation

Cost estimation has gone through many iterations in the last few years. Procurement cost and manpower estimations were first performed by the coordinators of subsystems. There are variations in assumptions, including the number of years to complete the project. The final estimation made adjustments to keep consistency for all subsystems in the assumptions. The length of the project is assumed to be 4 years. Most of the procurement costs were estimated based on quotations from vendors. Manpower were estimated from comparison with similar projects. JLab manpower was estimated initially based on the estimation of similar projects from other halls. They were revised later using the actual manpower used at the end of project completion in Hall D. The JLab budget office provided valuable assistance in the cost estimation. Details of cost break down are in Appendix A.

Appendix A Summary of Subsystems

In responding to the recommendations from JLab physics division, we add this section, aiming to provide a brief description of the key assumptions for each subsystem, namely where the subsystem will be built, which groups will build it, where the fund comes from, how long it will take and what is needed from JLab to support it. Anything unique to the system which drives the project will also be listed.

A.1 Magnet

The solenoid magnet provides the magnetic field required for measuring the momentum of the track in the experiment. The detectors for SoLID will be mounted on the magnet yoke. The collaboration has identified the CLEO-II magnet as the one to be used for SoLID after modifications. The magnet will be transported to JLab and the modifications will be done at JLab. The JLab Hall A engineering team, with assistance from JLab Engineering Division and also from the SoLID collaboration, will be responsible for the transportation and modification of the magnet.

The transportation (disassembling and shipping) the magnet from Cornell to JLab and initial refurbishing to verify the magnet is in good state for specific modifications for physics experiments will be covered from the JLab Physics Division (operation fund). The cost for refurbishing and modifications specific to SoLID is to be part of the SoLID MIE to DOE.

The transportation of the magnet is planned, in coordination with CLEO, to be in the summer of 2016. The refurbishing and modification specific to SoLID will take 2.5 years.

JLab will perform most of the work. Will need space at JLab for refurbishing, modification and storage. We will also need JLab support for the cryogenic and control systems.

Breakdown of the cost is in the next section (Section A.1) on Cost Estimations.

A.2 GEM

- **Where the system will be built and who will build it:** It is assumed that the SoLID GEM tracker will be built in China by the five member institutions of the Chinese SoLID GEM collaboration: CIAE, LZU, THU,USTC and IMP. The GEM module development, design prototyping and benchmarking would be done in collaboration with the GEM detector groups at the University of Virginia (Liyange) and Temple University (Sorrow). The GEM module and Electronics fabrication activities would be divided among the Chinese collaboration as follows:

- USTC: The main institution for GEM module fabrication, readout electronics development and fabrication.
- CIAE: GEM foil fabrication and GEM module fabrication.
- LZU: GEM module fabrication
- THU and IMP: GEM module fabrication and testing.

- **Who will fund it ?**

The funding for the SoLID GEM tracker will be sought from the Chinese funding agencies. Only the pre R&D funds and R&D funds (of the order of \$ 400 k) for the activities conducted at the University of Virginia and Temple University will be requested from the US DoE.

- **How long will it take ?**

The pre-R&D phase of the project would take at least 2 years. This would be especially true if the GEM foils fabricated in China are to be used for the project as assumed. A well focused and intense pre-R&D program in China is required to ensure that the manufacturing capabilities and capacities for full size GEM foils, and that GEM module assembly facilities setup and several full size prototype module constructed and tested at each of the five institutions.

After the successful conclusion of the pre-R&D program, it would take at least two more years for the R&D, construction, testing, installation and the commissioning phase.

- **what is needed from JLab to support it ?**

Jlab engineering support will be needed for the design of the GEM module mounting structure, and DAQ support will be needed to integrate the GEM readout into the hall A DAQ framework.

A.3 Light Gas Čerenkov

The light gas Čerenkov prototyping and construction will be done by the Temple University Nuclear Physics Group. All of the construction will be done at Temple, with the possible exception of any specific materials needed to adapt and integrate the subsystem into the larger SoLID detector. Funds for the project will be requested by the group from DOE and/or NSF. The light gas Čerenkov detector will also be designed at Temple University with the expectation that communication with the SoLID project engineers at Jefferson Lab, as well as access to schematics and documentation, will be made available concerning interfacing the sub-detector design with the larger SoLID design.

A.4 Heavy Gas Čerenkov

The Heavy Gas Cherenkov (HGC) will provide the required particle identification of pions in a background of kaons and protons. It will be built at Duke University, mostly by the Medium Energy Physics group with engineering and technical help from the Triangle Universities Nuclear Laboratory (TUNL).

A.5 Electromagnetic Calorimeter and Scintillator-Pad Detector

The Electromagnetic Calorimeter (EC), in combination with other detectors, provides the main trigger and the particle identification for the SoLID experiments. The EC consists of a Preshower and a Shower portion. The technologies that we chose for the EC: WLS-fiber-embedded scintillator for the Preshower, and the Shashlyk-type modules for the Shower, have both been used in collider experiments. The main goal of the pre-R&D is thus to optimize the design configuration of the EC to meet the physics requirement of SoLID.

The Scintillator Pad Detector (SPD) is only needed by the SIDIS program of SoLID. It will serve as a photon veto in order to reduce the photon background to a manageable level. Design of the SPD is very similar to the Preshower detector of the EC; thus R&D effort of the SPD can be combined with the EC.

The pre-R&D stage of EC and SPD will likely take up to two years. We will focus on optimizing the fiber-embedding method for the Preshower and the SPD; characterizing the performance of Preshower, SPD, and Shower modules; and testing fibers and fiber connectors. The use of multi-anode PMTs (MAPMTs) will be studied in order to reduce the readout cost. These pre-R&D work

will be carried out mostly at JLab, University of Virginia (UVa), and College of William and Mary (WM),

The Shashlyk modules (Shower) will be built by IHEP, Russia. Manufacturing of all the modules will likely take two years. Individual Shashlyk modules will be shipped to our collaboration groups at other laboratories and universities for testing. This includes UVa, WM, Los Alamos National Laboratory (LANL), and possibly Shandong University, China (SDU). The SPD and the Preshower modules will likely be built by IHEP, but the SDU group is also developing the technique of manufacturing fiber-embedded scintillators and could produce some of the SPD or Preshower modules. After initial testing, pre-assembling of Shower, Preshower, and SPD modules can be done at WM, which has a high-bay area for assembling large detectors. The support system of EC and SPD will be designed by the engineering group of Argonne National Lab (ANL), with help from the JLab engineering group. Testing of all readout PMTs will be performed at SDU.

A.6 MRPC

The Multi Gap Resistive Plate Chamber (MRPC) will be used by the SIDIS experiment for particle identification by means of time of flight. A MRPC can achieve a timing resolution of 50 ps. Under more realistic conditions with large background rates, timing resolution of 80 ps has been demonstrated.

- Who will build it :
Tsinghua University
- Where the system will be built:
In Tsinghua University, Beijing
- Rutgers university will take care of the readout electronics.
- Who will fund it :
NSFC (China) for the detector; the front end electronics will be funded by the DOE, and also the NSF through Rutgers University.
- How long will it take :
Two and half years
- What is needed from JLab to support it:
Beam tests will be needed at Jlab including electronics and DAQ system in order to test the detector and optimize it under realistic beam conditions. Since it is planned to include the MRPC in the trigger to reduce the background, a special board from JLAB will be required to send the logic signals to the L1 trigger.
- Anything unique to that system that's a project driver : This is the first high rate TOF system in hadron physics experiments and is need for the particle identification.

A.7 DAQ

The SoLID experiment is a large acceptance detector designed to run at high luminosities. The trigger rates expected for PVDIS are of the order of 600 KHz and for SIDIS up to 100 KHz. This pipelined electronics is crucial to generate a selective trigger in the very large background present in the detector.

- Where the system will be built and who will build :
Two universities are collaborating on the SoLID DAQ :
 - The Rutgers University with the group of Pr. Ronald Gilman group will be in charge of the high resolution timing measurement aspects of the development and production for the electronics.
 - The University of Massassuchets group led by Prof. Rory Miskimen will help in the testing of the Flash ADCs similar to what was done for Hall D.
- Who will fund it ?
The electronics will be funded by the DOE request.
- How long it will take
The project will take 2 years of preRD, 4 years of R%D, production and testing, and installation.
- What is needed from JLAB to support it
Since SoLID will be using the Jefferson Laboratory Pipelined Electronics, the JLAB Fast electronics group will be largely involved in the development, tests and deployment of the electronics. An estimate of the electronics and DAQ group is summarized in the table in addition of the JLab physics staff person.

Appendix B Rates and Background Simulation

B.1 DIS e^- and π^-/e^- ratio

Pion electro- and photo-productions are a significant background for both SIDIS and PVDIS experiments. Rates of DIS e^- and the π^-/e^- ratio from the targets are shown in Figs. 150 and 151 respectively for the PVDIS and the SIDIS running conditions.

B.2 GEM Background Rates

Accidental background from low energy electromagnetic processes can be simulated by processing individual electrons through the target and tracking any resulting particles. A significant background process are from real photons emanating from the target, producing electrons through Compton scattering, and cause ionization in the GEM drift region. The PVDIS experiment, with such a high luminosity, requires good blockage of line-of-sight photons. For the SIDIS experiment, the luminosity is lower, but the GEM planes reach more forward angles and the background rates depend on the exact running conditions. Hit rate densities are shown in Fig. 152 for PVDIS and Fig. 153 for the ^3He SIDIS experiment.

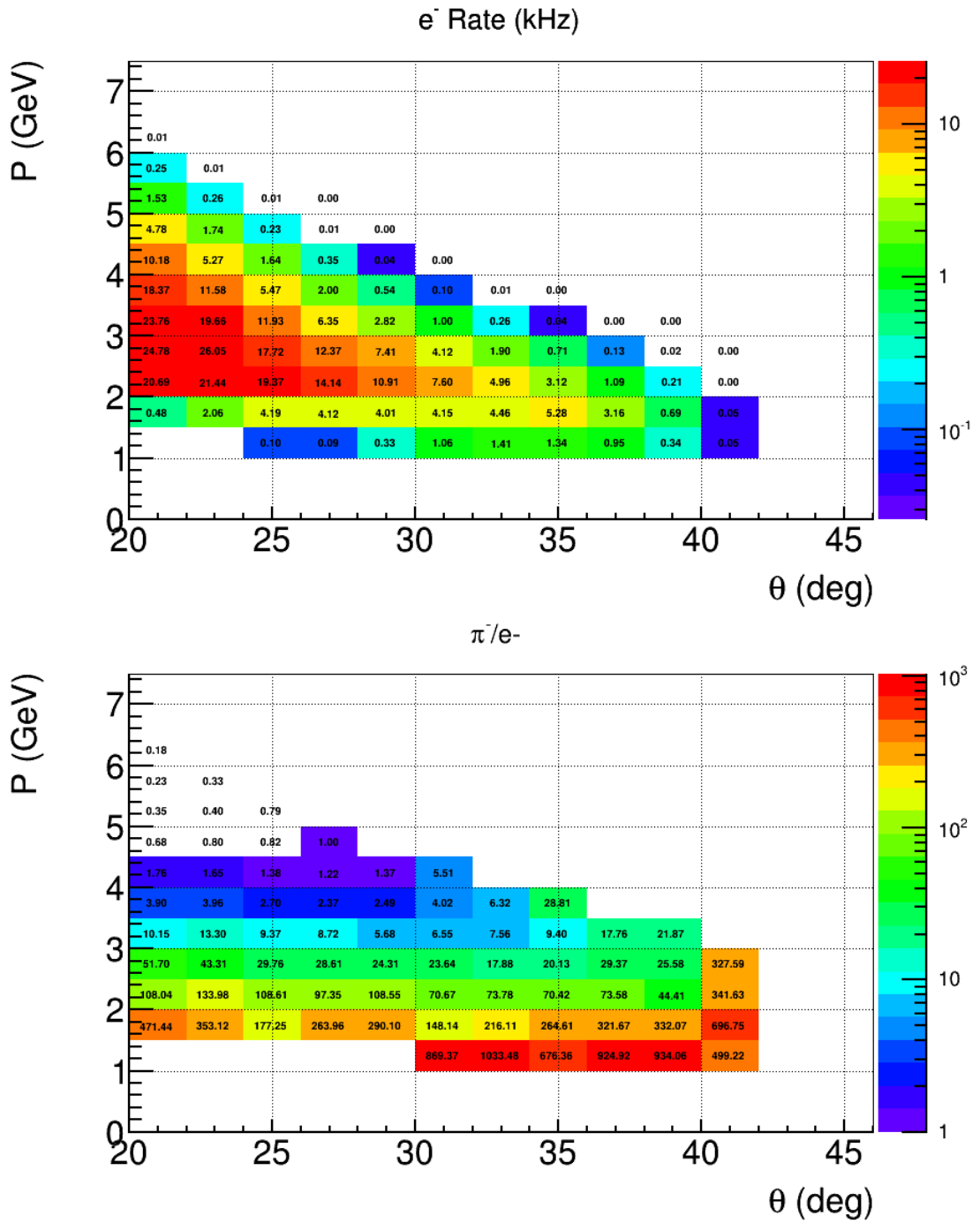


Figure 150: DIS scattering rates and the π^-/e^- ratio for the PVDIS experiment with a $50 \mu\text{A}$ beam on a 40 cm LD_2 target. The momentum and polar angles are at the vertices in the target where particles are created.

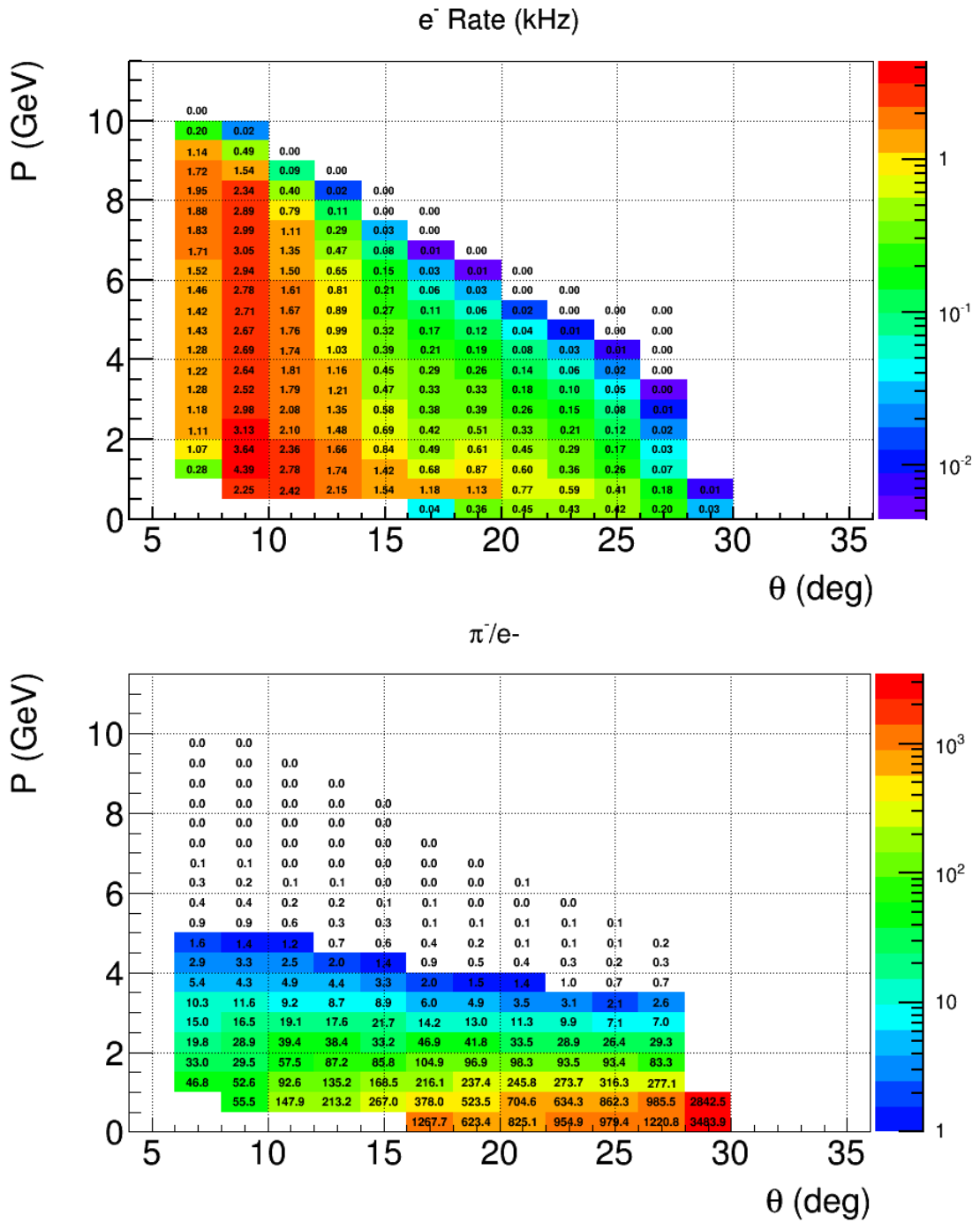


Figure 151: DIS scattering rates and the π^-/e^- ratio for the SIDIS experiment with a $15 \mu\text{A}$ beam on a 40 cm ^3He target. The momentum and polar angles are at the vertices in the target where particles are created.

EM background

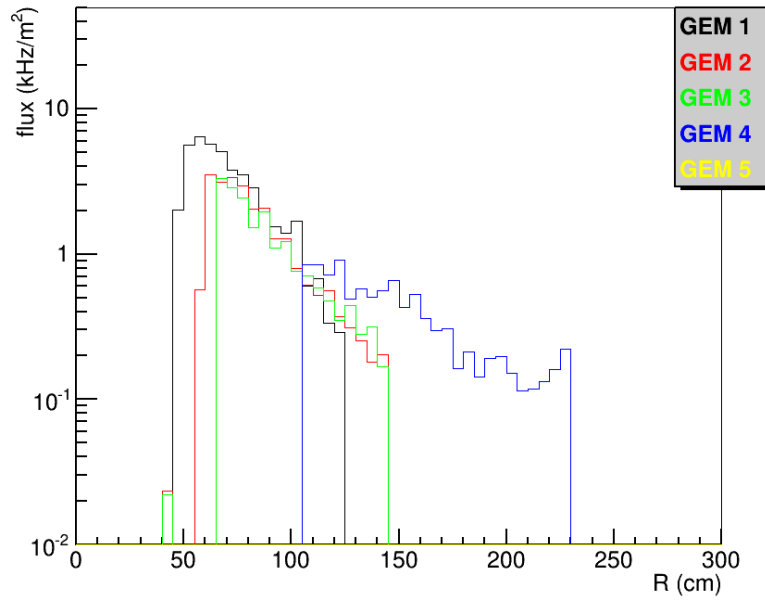


Figure 152: Projected hit rates on GEM chambers in the PVDIS configuration with baffles.

EM background

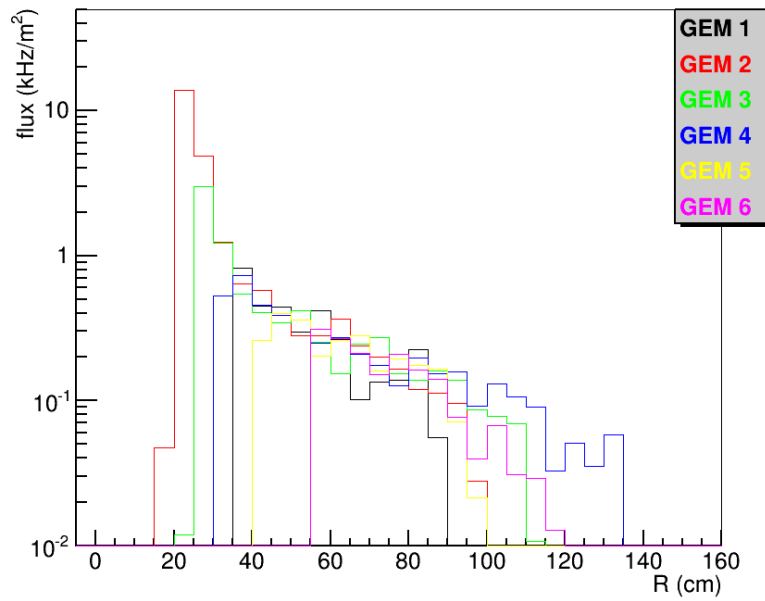


Figure 153: Projected hit rates on GEM chambers in the open SIDIS configuration.

Appendix C Magnet Choice

Comparing to the cost of 8-10M\$ of making a new magnet just for SoLID, reusing an existing magnet represents significant saving. There are several magnets might satisfy the need SoLID solenoid requirement.

Table 20: Magnet Choices

	BaBar	CLEO	CDF	ZEUS
Inner radius (cm)	142	144	150	86
Length (cm)	351.35	347.6	500	245
Central field (T)	1.5	1.5	1.47	1.8
Compact Flux return	Yes	Yes	No	No

CDF is too large in length and ZEUS is too small in radius, thus they will harm the SIDIS kinematic space (mostly 4-momentum transfer Q^2 and transverse hadron momentum P_T). BaBar and CLEO magnets have very similar geometry and field. They are right in the middle range of the SoLID requirement and could be used by SoLID. We have studied both magnets carefully.

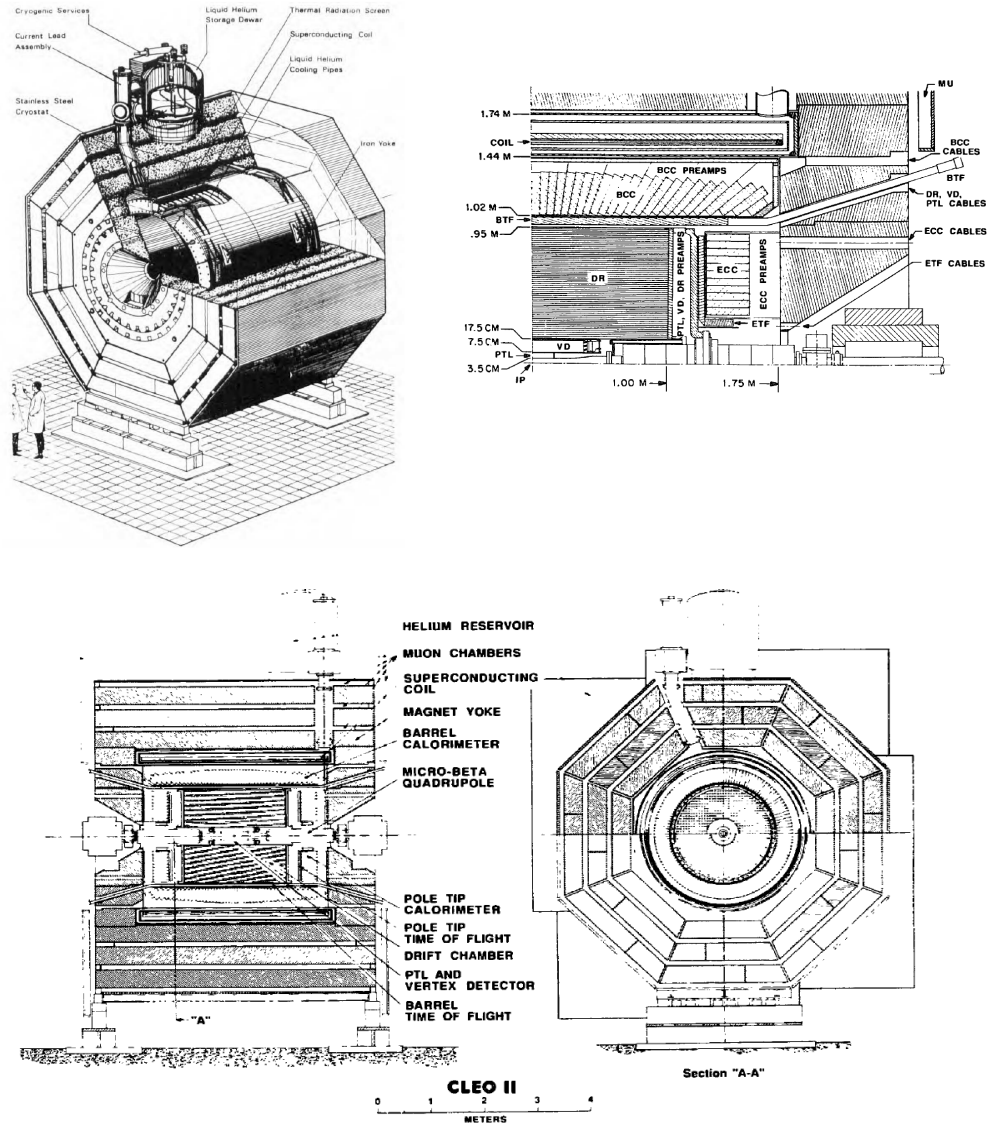


Figure 154: CLEO-II detector

The BaBar magnet, as shown in Figure 155 was seriously considered. It was built by Ansaldo Energia in Italy and installed in late 1990s. It contains an aluminium stabilized, thin superconducting solenoid and a return yoke, providing an axial central field of 1.5 T. The current density is graded to meet the field uniformity requirements of 2%. The cooling system uses liquid helium thermosyphon technique similar to CLEO. Automatic cooldown and cryogen supply to the coil and its 40 K radiation shield is done by a helium liquefier/refrigerator via coaxial, return gas screened, flexible transfer lines. A hexagonal flux return, comprised of a barrel and two end doors provides the external flux path for the field. To accommodate the muon detectors, the barrel and end caps are segmented into 18 plates of different thickness. The gaps between the plates are about 3 cm wide. The solenoid center is 3.5 m above the floor. To fit with Jlab Hall A 3m beamline height with enough clearance, the bottom supporting structure of the flux return needs to be modified and the most outer layer of barrel flux return needs to be removed. Unfortunately, removing material

at large diameters would seriously compromise the mechanical strength of the yoke, and a major redesign and construction project would be required. The CLEO II magnet was then chosen because it was simpler and cheaper to install in Hall A at JLab.

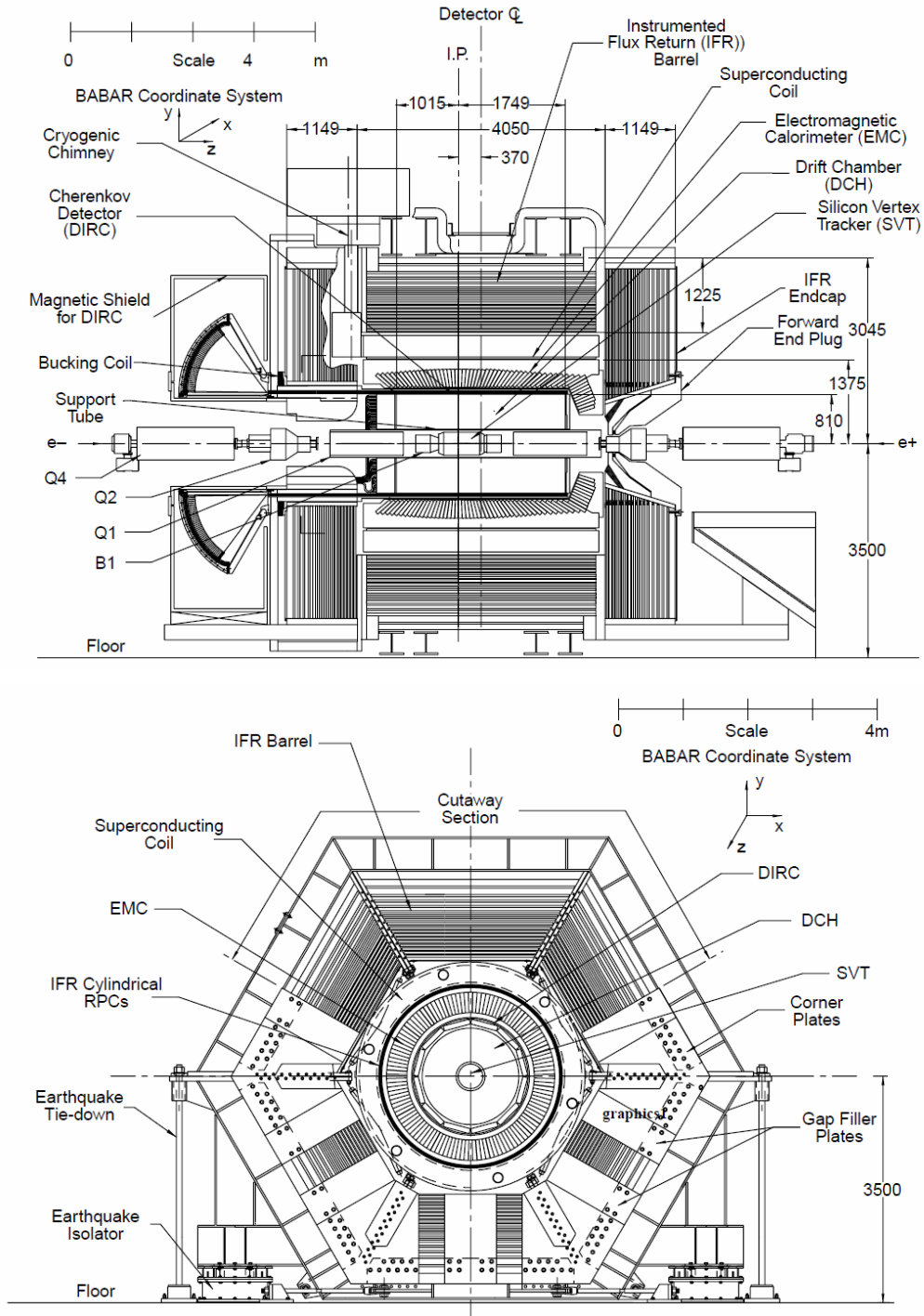


Figure 155: BaBar detector